Design, Synthesis and Application of Cylindrical Polymer Brushes: From Nanostructures to Advanced Materials

DISSERTATION

zur Erlangung des akademischen Grades eines

Doktors der Naturwissenschaften (Dr. rer. nat.)

an der Bayreuther Graduiertenschule für Mathematik und

Naturwissenschaften der Universität Bayreuth

vorgelegt von

Zhicheng Zheng

Geboren in Fujian, VR China

Bayreuth, 2013

Die vorliegende Arbeit wurde in der Zeit von April 2010 bis September 2013 in Bayreuth am Lehrstuhl für Makromolekulare Chemie II unter Betreuung von Herrn Prof. Dr. Axel H. E. Müller angefertigt.

Vollständiger Abdruck der von der Bayreuther Graduiertenschule für Mathematik und Naturwissenschaften (BayNAT) der Universität Bayreuth genehmigten Dissertation zur Erlangung des akademischen Grades eines Doktors der Naturwissenschaften (Dr. rer. Nat.).

Dissertation eingereicht am: 18.09.2013
Zulassung durch das Leitungsgremium: 09.10.2013
Wissenschaftliches Kolloquium: 29.11.2013

Amtierender Direktor: Prof. Dr. Franz Xaver Schmid

Prüfungsausschuss:
Prof. Dr. Axel H. E. Müller (Erstgutachter)
Prof. Dr. Mukundan Thelakkat (Zweitgutachter)
Prof. Dr. Josef Breu (Vorsitz)
Prof. Dr. Birgit Weber

Where there is a Will there is a Way

To My Family and My Fiancée Zhuying

Table of Contents

Summary

This thesis focuses on the design, synthesis and application of cylindrical polymer brushes (CPBs). Herein, we investigated the scission behavior of polyelectrolyte CPBs on different surfaces, developed novel synthetic pathways for well-defined CPBs *via* reversible addition-fragmentation chain transfer (RAFT) polymerization, designed and prepared complex functional CPBs for light-harvesting and energy transfer, and utilized CPBs as templates for the synthesis of novel one-dimensional (1D) organic/inorganic hybrid nanostructures.

The 'grafting-from' approach was chosen as the general method to synthesize well-defined CPBs with various chemical and structural compositions. The linear polymer backbones (polyinitiators) were obtained by anionic polymerization or RAFT polymerization, whereas the side chains were grafted by atom transfer radical polymerization (ATRP) or RAFT polymerization. The obtained CPBs possess a narrow molecular weight distribution in both the backbone and the side chains.

The polymer backbone of core-shell CPBs consisting of a poly(oligo(ethylene glycol) methyl ether methacrylate) (POEGMA) core block and a poly(2-(dimethylamino)ethyl methacrylate) (PDMAEMA) shell block was ruptured upon drying on solid surfaces, when sufficient Coulombic interactions between the shell block and the surface were formed. We controlled this scission behavior by tuning the surface interactions through switching the surface nature, shell quaternization, varying pH, or adding multivalent counterions. This study demonstrates that core-shell CPBs serve as a tool to directly compare the weak intermolecular forces with the strong carbon-carbon covalent bonds.

A novel 'grafting-from' approach was developed to overcome the challenges of synthesizing well-defined CPBs from a linear polymer backbone with a high density of RAFT functionalities. In this so-called "CTA-shuttled" R-group approach, a certain amount of low-molecular-weight chain transfer agent (CTA) was added to the polymerization system, serving as shuttles to transfer active radicals among the individual growing

CPBs. Well-defined CPBs with polystyrene or poly(*tert*-butyl acrylate) branches and core-shell CPBs with polystyrene-*block*-poly(*N*-isopropylacrylamide) branches were synthesized, with the molecular weight distribution much narrower than that from the conventional R-group approach. Monte Carlo simulations confirmed that the advantage of the "CTA-shuttled" R-group approach consists in the release of the active radicals from the trapping CPB systems.

Imitating the natural "energy cascade" architecture, we developed single-molecular, rod-like nano-light harvesters (NLHs) on the basis of CPBs. Herein, a number of block copolymer side chains carrying light absorbing antennae groups (9,9-diethylfluorene, energy donors) were tethered to a linear polymer backbone containing emitting groups (anthracene, energy acceptors). These NLHs provide very efficient energy absorption and energy transfer from antennae to energy acceptors. Furthermore, we were able to manipulate the efficiency of energy transfer by tuning the distance between energy donors and energy acceptors in physical and/or chemical ways. This CPB-based NLH architecture presents a novel concept to design light harvesting materials and can readily be transplanted to any other applications in photoelectronic devices.

Core-shell CPBs with a poly(acrylic acid) (PAA) core block and a PDMAEMA shell block were employed as templates for the preparation of various rare-earth metal cations (Ln^{3+}) incorporated silica hybrid nanoparticles (NPs). A tight chelation of Ln^{3+} ions in the PAA core and a crosslinked silica layer deposited on the shell provide a very stable encapsulation of Ln^{3+} ions within the hybrid NPs and thus a high biocompatibility. The silica hybrid NPs obtain unique and diverse properties from the incorporated Ln^{3+} ions, such as visible photoluminescence, paramagnetic behavior, and a longitudinal relaxation time (T_1) shortening effect. This novel template-directed approach succeeds in combining different functional centers *via* loading *in-situ* mixed Ln^{3+} ions into individual CPBs resulting in multicomponent hybrid NPs, which possess both visible photoluminescence and T_1 contrast enhancement and can thus be applied as multimodal bioimaging probes.

Zusammenfassung

Die vorliegende Arbeit befasst sich mit dem Entwurf, der Synthese und den Anwendungen von zylindrischen Polymerbürsten (CPBs). Dabei haben wir das Bruchverhalten von Polyelektrolyt-Polymerbürsten auf verschiedenen Oberflächen untersucht, neuartige Synthesewege mittels der *Reversible Addition-Fragmentation Chain Transfer* (RAFT) Polymerisation für wohldefinierte CPBs entwickelt, komplexe funktionale Polymerbürsten für Lightharvesting und Energieübertragung entworfen und synthetisiert, sowie CPBs als Template für die Herstellung von eindimensionalen organisch-anorganischen Hybrid-Nanostrukturen eingesetzt.

Der ‚*grafting-from*'-Ansatz wurde als die allgemeine Methode gewählt, um wohldefinierte Polymerbürsten mit verschiedenen chemischen und strukturellen Zusammensetzungen zu synthetisieren. Die linearen Polymerrückgrate (Polyinitiatoren) wurden durch die anionische Polymerisation oder die RAFT-Polymerisation hergestellt, während die Seitenketten durch die *Atom Transfer Radical Polymerization* (ATRP) oder die RAFT-Polymerisation gepfropft wurden. Die erhaltenen CPBs besaßen eine enge Molekulargewichtsverteilung sowohl in der Hauptkette als auch in den Seitenketten.

Das Polymerrückgrat von Kern-Schale-Polymerbürsten mit einem Poly(oligo(ethylen-glycol)methylether-methacrylat)-Kernblock (POEGMA) und einem Poly(2-(dimethyl-amino)ethylmethacrylat)-Schaleblock (PDMAEMA) zerbrach nach dem Trocknen auf festen Oberflächen, sobald sich ausreichend Coulomb-Wechselwirkungen zwischen dem Schaleblock und der Oberfläche gebildet haben. Wir überprüften dieses Bruchverhalten durch eine Variation der Oberflächenwechselwirkungen durch den Einsatz verschiedener Substrate, die Quarternisierung des Schaleblocks, die Variierung des pH-Werts, oder die Zugabe von mehrwertigen Gegenionen. Diese Studie hat gezeigt, dass Kern-Schale Polymerbürsten als Hilfsmittel dienen können, um die schwachen intermolekularen Kräfte mit den starken kovalenten Kohlenstoff-Kohlenstoff-Bindungen direkt zu vergleichen.

Eine neuartige ‚*grafting-from*'-Methode wurde entwickelt, um die Herausforderungen der Synthese wohldefinierter Polymerbürsten aus einem linearen Polymerrückgrat mit einer hohen Dichte von RAFT-Funktionalitäten zu überwinden. In diesem sogenannten „CTA-shuttled" R-Gruppe-Ansatz wurde eine bestimmte Menge an niedermolekularem Kettenüberträger (CTA) in das Polymerisationssystem hineingegeben, welches die Übertragung von aktiven Radikalen unter den einzelnen wachsenden Polymerbürsten steuert. Wohldefinierte Homopolymerbürsten mit Polystyrol- oder Poly(*tert*-butylacrylat)-Seitenketten und Kern-Schale-Polymerbürsten mit Polystyrol-*block*-poly(*N*-isopropylacrylamid)-Verzweigungen wurden synthetisiert, welche eine wesentlich engere Molekulargewichtsverteilung aufwiesen als mit dem herkömmlichen R-Gruppe-Ansatz erhaltenen. Monte Carlo-Simulationen bestätigten, dass der Vorteil des „CTA-shuttled" Ansatzes in der Freisetzung der aktiven Radikale aus den Polymerbürsten-Fallen besteht.

Durch Nachahmung der natürlichen Energie-Kaskade-Architektur wurden einzelmolekulare, stäbchenförmige Nano-Lightharvester (NLHs) auf Basis von CPBs entwickelt. Dabei wurde eine große Menge von Blockcopolymerseitenketten mit lichtabsorbierenden Antennengruppen (9,9-Diethylfluoren, Energiedonator) an ein lineares Polymerrückgrat angebunden, welches emittierende Gruppen (Anthracen, Energieempfänger) enthielt. Diese NLHs boten sehr effiziente Energieabsorption and -übertragung von Antennen zu Emitteren. Darüber hinaus waren wir durch das Abstimmen des Abstands zwischen den Energiedonatoren und den Empfängern in der Lage, die Effizienz der Energieübertragung auf physikalische und chemische Weise zu manipulieren. Diese Polymerbürsten-basierte NLH-Architektur stellt ein neuartiges Konzept für Lightharversting-Materialien dar und kann leicht in andere photoelektronische Anwendungen integriert werden.

Kern-Schale-Polymerbürsten mit einem Polyacrylsäure-Kernblock (PAA) und einem PDMAEMA-Schaleblock wurden als Template für die Herstellung von Silika-Hybrid-Nanopartikeln eingesetzt, die verschiedene Seltenerdmetallkationen (Ln^{3+}) enthielten. Eine enge Chelatbildung von Ln^{3+}-Ionen mit dem PAA-Kern und eine

vernetzte Silikaschicht auf der Schale gewährleisteten eine sehr stabile Verkapselung von Ln^{3+}-Ionen in den Hybrid-Nanopartikeln und damit eine hohe Biokompatibilität. Die Silika-Hybrid-Nanopartikeln erhielten durch die eingebauten Ln^{3+}-Ionen einzigartige und vielfältige Eigenschaften, wie sichtbare Photolumineszenz, paramagnetisches Verhalten und Verkürzung der longitudinalen Relaxationszeit (T_1). Mehrkomponenten-Hybrid-Nanopartikel mit verschiedenen funktionellen Zentren (gemischte Ln^{3+}-Ionen) besitzen sowohl eine sichtbare Photolumineszenz als auch eine T_1-Kontrastverstärkung und können somit als multimodale Bioimaging-Sonden angewandt werden.

Glossary

1D	one-dimensional
2D	two-dimensional
3D	three-dimensional
^{1}H-NMR	proton nuclear magnetic resonance
AFM	atomic force microscopy
ATRP	atom transfer radical polymerization
CD	cyclodextrin
CPB(s)	cylindrical polymer brush(es)
CRP	controlled radical polymerization
Cryo-TEM	cryogenic transmission electron microscopy
CTA	chain transfer agent
CuAAC	copper-catalyzed azide-alkyne cycloaddition
DLS	dynamic light scattering
DP_n	number-average degree of polymerization
EDX	energy dispersive X-ray spectroscopy
Eu	europium
FRET	Förster resonance energy transfer
Gd	gadolinium
H_2SO_4	sulfuric acid
HCl	hydrogen chloride
HF	hydrogen fluoride
HMTETA	1,1,4,7,10,10-hexamethyltriethylenetetramine
HR-TEM	high resolution transmission electron microscopy
ICP-OES	inductively coupled plasma optical emission spectrometry
IPEC	interpolyelectrolyte complex
IR	infrared
l_m	length per monomer unit
Ln^{3+}	rare-earth metal cations
l_p	persistence length
Me_6TREN	tris(2-aminoethyl)amine
MALS	multi-angle laser light scattering
M_n	number-average molecular weight
MRI	magnetic resonance imaging
M_w	weight-average molecular weight
MWD	molecular weight distribution
Nd	neodymium
NLH	nano-light harvester

NMP	nitroxide mediated polymerization
NP(s)	nanoparticle(s)
OsO_4	osmium tetroxide
P2VP	poly(2-vinylpyridine)
PAA	poly(acrlyic acid)
PAnMA	poly(9-anthracenemethyl methacrylate)
PAPTS	poly(3-acryloylpropyl trimethoxysilane)
PB	polybutadiene
PBIEM	poly(2-(bromoisobutyryloxy)ethyl methacrylate)
PCEVE	poly(chloroethyl vinyl ether)
PCL	poly(ε-caprolactone)
PDI	polydispersity index
PDMAEMA	poly(2-(dimethylamino)ethyl methacrylate)
PE	polyethylene
PEG	polyethylene gylcol
PFlMA	poly((9,9-diethylfluoren-2-yl)methyl methacrylate)
PFS	poly(ferrocenyldimethylsilane)
PHEMA	poly(hydroxyethyl methacrylate)
PI	polyisoprene
PLA	poly(lactic acid)
PMDETA	*N,N,N′,N″,N‴*-pentamethyldiethylenetriamine
PMETAI	poly((2-(methacryloyloxy)ethyl) trimethylammonium iodide)
PMMA	poly(methyl methacrylate)
P*n*BA	poly(*n*-butyl acrylate)
PNIPAAm	poly(*N*-isopropylacrylamide)
POEGMA	poly(oligo(ethylene glycol) methyl ether methacrylate)
POEGA	poly(oligo(ethylene glycol) methyl ether acrylate)
PS	polystyrene
PSS	poly(styrenesulfonate)
P*t*BA	poly(*tert*-butyl acrylate)
PTMS-HEMA	poly(2-(trimethylsiloxy)ethyl methacrylate)
PVBC	poly(vinylbenzyl chloride)
QD	quantum dot
RAFT	reversible addition fragmentation transfer polymerization
RE	rare-earth
R-group	the reinitiating group of a chain transfer agent
R_h	hydrodynamic radius
RI	refractive index
ROMP	ring-opening metathesis polymerization
ROP	ring-opening poylmerization
SDS	sodium dodecyl sulphate
SEC	size exclusion chromatography
SEM	scanning electron microscopy

$SiO_{1.5}$	silsesquioxane
SiO_2	silica
SLS	static light scattering
SQUID	superconducting quantum interference device
T_1	longitudinal (or spin-lattice) relaxation time
T_2	transverse (or spin-spin) relaxation time
Tb	terbium
TEM	transmission electron microscopy
TGA	thermogravimetric analysis
THF	tetrahydrofuran
TiO_2	titanium dioxide, titania
TMOS	tetramethyl orthosilicate
Z-group	the stabilizing group of a chain transfer agent

Chapter 1

Introduction

Cylindrical Polymer Brushes

In the year 1991, Milner introduced 'polymer brushes' as "long-chain polymer molecules attached by one end to a surface or interface by some means, with a density of attachment points high enough so that the chains are obliged to stretch away from the interface, sometimes much farther than the typical unstretched size of a chain".[1] Nowadays, the term 'polymer brushes' refers to assemblies of polymer chains which are tethered by one end to a linear backbone, a planar or a spherical surface. Depending on the architectures, polymer brushes can be classified as 1-dimensional (1D) cylindrical polymer brushes (CPBs), 2-dimensional (2D) planar polymer brushes (PPBs) and 3-dimensional (3D) spherical polymer brushes (SPBs).[2,3]

Cylindrical polymer brushes (CPBs), also known as 'molecular bottlebrushes', are composed of a linear main chain (backbone) and a large number of linear side chains or high-generation dendritic side groups densely grafted on this linear backbone (ideally each monomer unit of the main chain carries one side chain). Generally, the backbone can be a linear polymer chain or a cross-linked polymeric cylindrical domain with a radius much smaller than the length of the side chains.[4] Over the past decade CPBs have attracted considerable attention from both experimental and theoretical scientists, due to their unique properties in solution, in bulk and in thin films, and especially the possibility of forming extended cylindrical or worm-like conformation due to the intramolecular excluded-volume interactions between the densely grafted side chains.

CPBs have a densely branched compact architecture and can thus reach a gigantic dimension of hundreds of nanometers. Therefore, CPBs provide a suitable platform for microscopic investigation of single molecular behavior, such as ordering, spreading, de-

wetting, collapsing and other responsive transitions. The intrinsic 1D conformation makes CPBs highly interesting for the application as unimolecular templates for the preparation of well-defined anisotropic hybrid nanomaterials or inorganic nanostructures.[4,5]

In recent years, research activities on CPBs have mainly focused on developing new synthetic methods, designing complex and functional nanostructures, studying physico-chemical properties in solution and bulk, conducting theoretical simulations, and finding applications in materials science and engineering. This chapter explores the various synthetic approaches for preparing CPBs, their diverse architectures and properties in different states, and their ingenious applications.

1.1 Synthesis of Cylindrical Polymer Brushes

The characteristic cylindrical or worm-like conformation of CPBs is attributed to the high density of polymer side chains (grafting density) and the resulting crowding and stretching. This branched architecture is achieved by two general strategies differing in the composition of the backbone: (i) the fabrication of lateral branching of a linear polymer main chain, and (ii) the crosslinking of polymeric cylindrical domains in block copolymer self-assemblies. The first strategy is also known as classic grafting approaches,[2-4] including 'grafting-through' (the polymerization of macromonomers, Scheme 1–1A), 'grafting-onto' (the attachment of monochelic side chains to a functional backbone, Scheme 1–1B), and 'grafting-from' (the polymerization of side chains from a polyinitiator backbone, Scheme 1–1C). The second strategy takes advantage of self-assembly of block copolymers and is achieved in two possible approaches: (i) crosslinking of the core domain of cylindrical micelles assembled by block copolymers in solution (Scheme 1–1D)[6-8] or (ii) crosslinking of the cylindrical domain of microphase-separated bulk morphologies followed by dispersing in a solvent (Scheme 1–1E).[9-12] Furthermore, brush-like micelles with a cylindrical crystalline domain as backbone were prepared by crystallizing one block of linear block copolymers.[13-17] However, the core of these brush-like micelles is linked by supramolecular interactions and is thus less stable as compared to the classical CPBs.

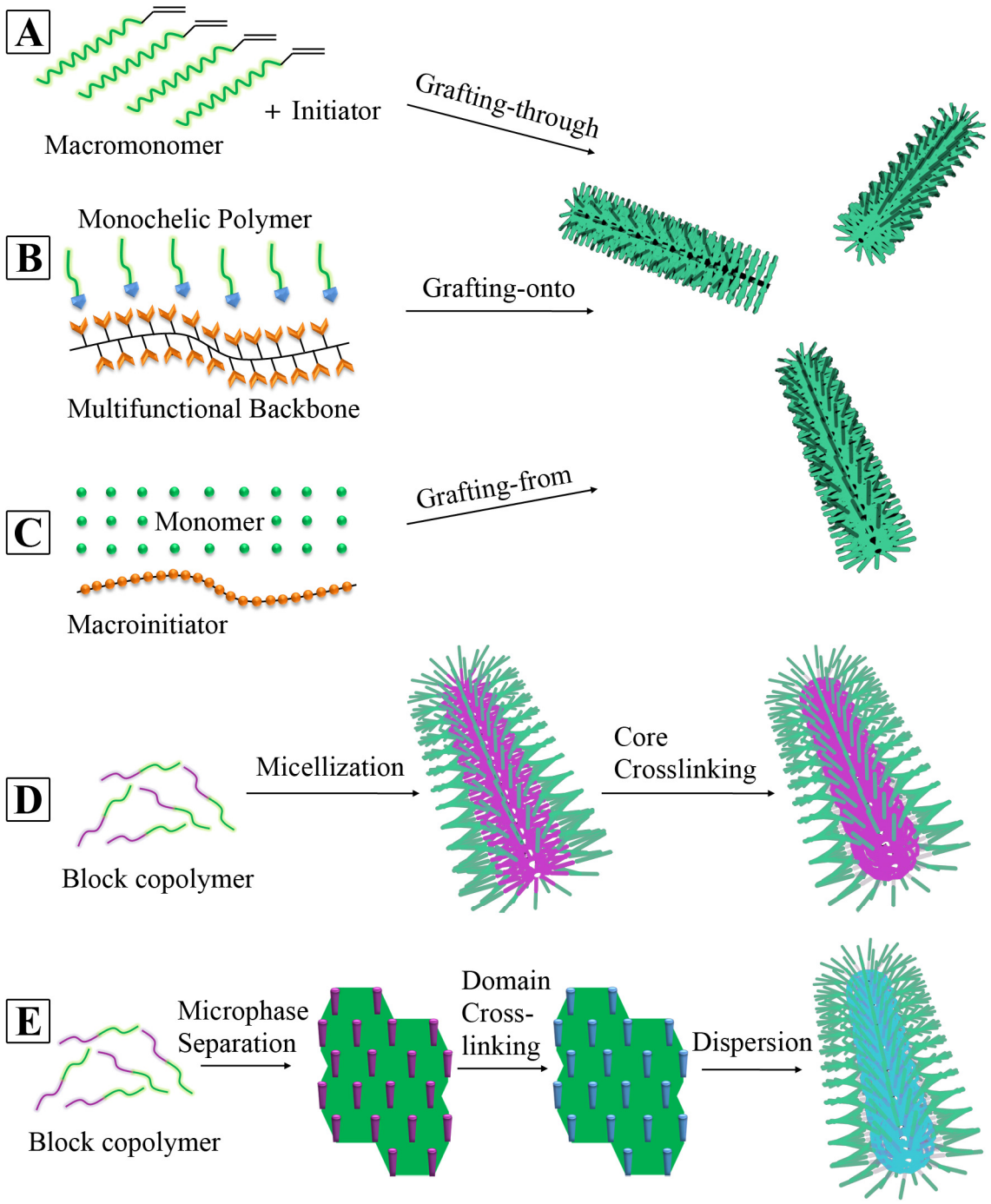

Scheme 1-1. Various synthetic approaches to CPBs: **(A)** 'grafting-through', **(B)** 'grafting-onto', **(C)** 'grafting-from', **(D)** core-crosslinking of cylindrical micelles assembled by block copolymers in solution, and **(E)** crosslinking of the hexagonally packed cylindrical domains of microphase-separated bulk morphologies followed by dispersing in solvent.

In the synthesis of CPBs, various aspects can be designed and controlled, such as grafting density, chemical composition, uniformity, length and sequence of backbone and side chains. Each of the mentioned synthetic approaches demonstrates distinct advantages

and limitations in governing these structural parameters. In the following, different synthetic approaches are described with particular attention paid to the classic grafting approaches employing controlled radical polymerization (CRP) techniques, as these are most widely applied in the preparation of well-defined CPBs.

1.1.1 Grafting-through

The 'grafting-through' approach achieves CPBs *via* the polymerization of macromonomers, which are linear polymer chains with polymerizable terminal groups, as illustrated in Scheme 1–1A. The macromonomers are prepared in mainly two pathways: (i) modifying the end-groups of polymer chains to polymerizable functionalities or (ii) growing polymer chains from initiators carrying polymerizable groups (in a different polymerization mechanism). The polymerization of the polymerizable terminal groups through macromonomers results in a covalently bonded linear polymer backbone. In the last two decades, various polymerization techniques have been applied to polymerize macromonomers, such as conventional free radical polymerization,[18-22] controlled radical polymerization (CRP),[23-25] anionic polymerization[26,27] and ring-opening metathesis polymerization (ROMP).[28-34] However, the application of conventional free radical polymerization is limited by its poor control over molecular weight. In the case of CRP techniques, such as atom transfer radical polymerization (ATRP), reversible addition fragmentation chain transfer (RAFT) polymerization and nitroxide-mediated polymerization (NMP), the low radical concentration limits the macromonomer conversion and thus the backbone length. In contrast, the ROMP technique for norbornene end-functionalized macromonomers succeeds in synthesizing CPBs with acceptable backbone length and molecular weight distribution. So far, various CPBs have been prepared *via* ROMP of norbornenyl-terminated macromonomers, such as polystyrene (PS),[28,32] poly(ethylene oxide) (PEO),[30] poly(ε-caprolactone) (PCL),[31] poly(*n*-butyl acrylate) (P*n*BA), poly(*tert*-butyl acrylate) (P*t*BA), and polylactide (PLA).[32] The synthesis of well-defined CPBs with poly(acrylic acid) (PAA) side chains *via* ROMP of RAFT-prepared macromonomers[33] is shown in Figure 1–1. The most important advantage of the 'grafting-through' approach is

the full grafting density on the backbone, that is, each repeating unit of the backbone carries a side chain. Secondly, 'grafting-through' approach allows the preparation of side chains prior to the grafting process, which provides the possibility to exactly characterize the composition and distribution of the side chains. On the other side, the 'grafting-through' approach has some significant drawbacks: (i) the low degree of polymerization (DP) of the backbone induced by the high steric hindrance in the polymerization of macromonomers and (ii) the difficult removal of excess macromonomers from the formed polymer brushes after the grafting process.

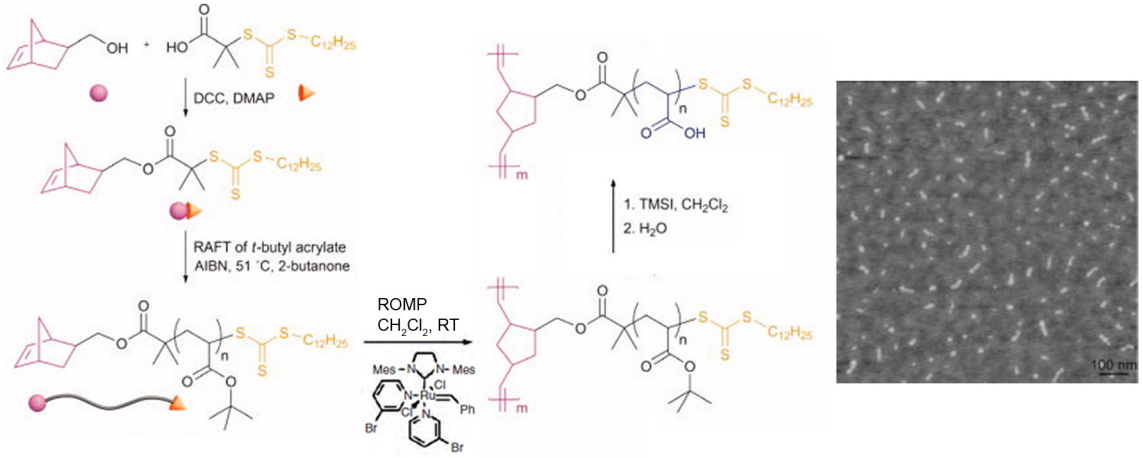

Figure 1-1. 'Grafting-through' synthetic route to CPBs bearing poly(acrylic acid) side chains *via* ROMP.[33] Reprinted with permission of Wiley Periodicals, Inc.

1.1.2 Grafting-onto

In the 'grafting-onto' approach, a linear polymer main chain carrying functional groups on each repeating unit is employed as the backbone, with end-functional polymer chains serving as grafts (Scheme 1–1B). Both backbone and side chains are prepared independently prior to the grafting process and can be exactly characterized for DP and molecular weight distribution (MWD), which is the main advantage of the 'grafting-onto' approach. CPBs are achieved by a coupling reaction between the pendant reactive sites of the backbone and the end-functional groups of grafts. So far, various coupling reactions have been employed for the synthesis of CPBs *via* the 'grafting-onto' approach. The first representative is the nucleophilic substitution method based on living anionic polymerization.

Herein, active polymer anions are quenched in a controlled manner onto a polymer backbone carrying functional groups susceptible to nucleophilic attack, such as poly(chloroethyl vinyl ether) (PCEVE)[35-44] and poly(vinylbenzyl bromide) (PVBB),[45-47] forming the polymer brushes. In the last decade, the great development of the 'click chemistry' enables another efficient, robust and modular synthetic pathway under ambient conditions for the 'grafting-onto' approach.[48] The most well-known 'click reaction', the copper(I)-catalyzed azide-alkyne cycloaddition (CuAAC)[49] has been widely applied to the 'grafting-onto' approach.[50-54] An example of the synthesis of CPBs using CuAAC is demonstrated in Figure 1–2, where a post-polymerization alkyne-functionalized poly(hydroxyethyl methacrylate) (PHEMA) was used as the backbone and azido- functionalied PEO, PS, P*n*BA and P*n*BA-*b*-PS were used as grafts.[50] Furthermore, brush-like supramolecular architectures have been generated *via* the 'grafting-onto' approach utilizing non-covalent interactions, such as hydrogen bonding,[55-59] ionic interactions[60,61] and coordination bonding.[62]

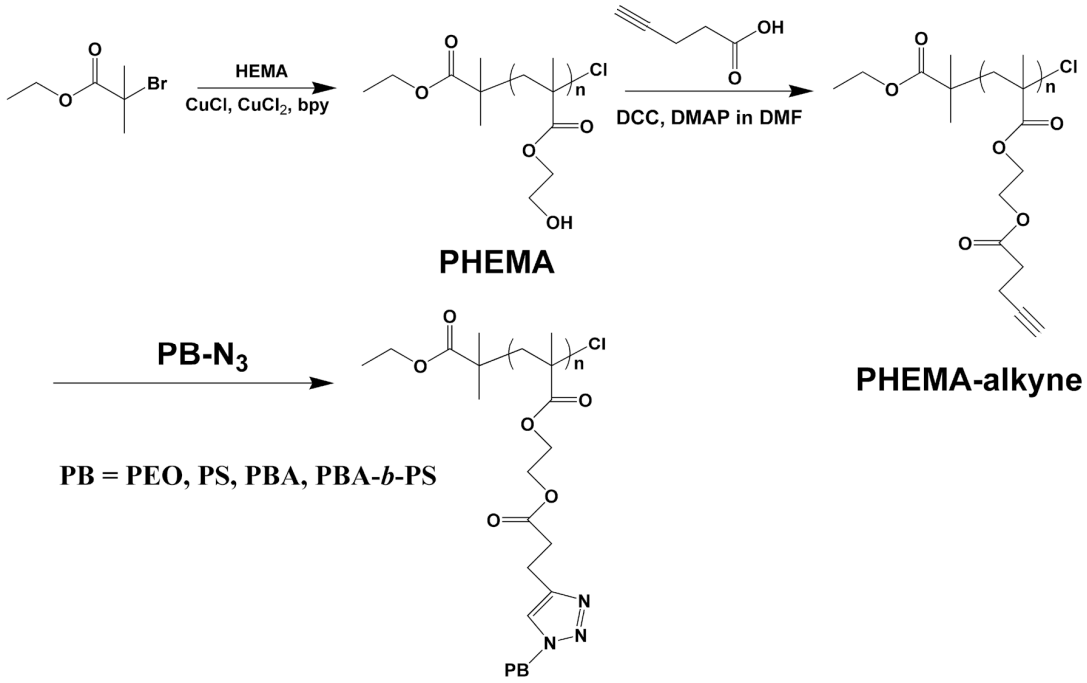

Figure 1-2. 'Grafting-onto' synthetic route to CPBs bearing various side chains *via* 'click reaction'.[50] Reprinted with permission of ACS.

The main limitation of the 'grafting-onto' approach, regardless of the employed coupling reaction, is the low grafting density of 20 – 40% induced by both thermody-

namic and kinetic obstacles. On the one hand, the attachment of side chains onto the backbone leads to entropically unfavorable changes of their conformation from random coils into more stretched ones. On the other hand, the increasing steric hindrance resulting from the increasing grafting density restricts the diffusion of the to-be-attached grafts to functional groups on the backbone. Therefore, the end-functionalized grafts are typically fed in a large excess with respect to the reactive sites on the backbone to increase the grafting density, which leads to another drawback of the 'grafting-onto' approach, that is, the post-reaction purification, *i.e.* the complete removal of unreacted grafts, is very difficult.

1.1.3 Grafting-from

The 'grafting-from' approach is the most prevailing grafting approach for synthesizing polymer brushes. This approach involves a linear polymer main chain (polyinitiator) with initiating sites on each monomer unit, from which side chains are subsequently grown. The first advantage of the 'grafting-from' approach is the employed backbone polymer, which is prepared prior to the grafting process and can be fully characterized. As the molecular weight distribution of the backbone is crucial to the length distribution of the latterly synthesized CPBs, the backbone is prepared by living/controlled polymerization techniques, such as anionic polymerization,[63,64] RAFT,[65,66] ATRP,[67,68] NMP[69,70], ring-opening polymerization (ROP)[71] or ROMP,[72,73] to achieve a narrow MWD. Especially, the backbone polymer deriving from anionic polymerization can reach a very high DP of up to several thousands, which is impossible for the 'grafting-through' approach mentioned above. There are mainly two pathways to prepare the polyinitiator backbone: (i) polymerization of inimers (monomers carrying initiating sites for the grafting process)[66,69,74] and (ii) post-polymerization modification to introduce initiating sites.[63,65,67] The second merit of the 'grafting-from' approach is the tolerance to many functional moieties, as various polymerization techniques can be utilized in the grafting process depending on the monomer for side chains. So far, ATRP,[25,63,67,68,74-77] RAFT,[65,78-80] NMP[81-83] and ROP[84-88] have been applied in the 'grafting-from' approach. More generally,

ATRP is the most widely used polymerization technique in the 'grafting from' approach with perfect control over the growth of side chains from styrene, acrylate, methacrylate, acrylamide, acrylonitrile, etc. An example of the synthesis of CPBs by ATRP is demonstrated in Figure 1–3, where a postpolymerization functionalized PHEMA with ATRP initiating sites was used as the backbone and PS-*b*-P*t*BA were grafted as side chains, which were subsequently hydrolyzed to PS-*b*-PAA.[67] The third advantage of the 'grafting-from' approach is the sufficiently high grafting density, which reaches 50 – 90% depending on the monomer and the polymerization technique chosen for the grafting process.

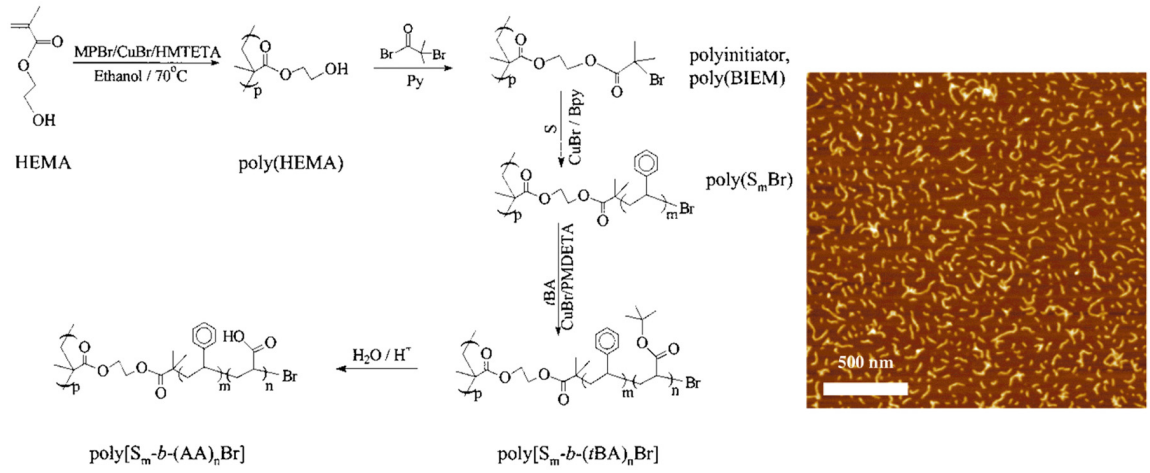

Figure 1-3. 'Grafting-from' synthetic route to CPBs bearing polystyrene-*block*-poly(acrylic acid) side chains *via* ATRP.[67] Reprinted with permission of ACS.

The determination of the initiation efficiency and the exact DP of the side chains provides the main limitation of the 'grafting-from' approach. Since the side chains are tethered on the backbone after grafting, cleavage of the side chains is necessary for the analysis of the DP of the side chains and, thus, the initiation efficiency. In the case of an ester functionality, this cleavage step is always carried out under acidic or basic conditions, resulting in linear polymer chains being individual side chains or their hydrolyzed compounds. Size exclusion chromatography (SEC) analysis of these linear polymer chains or their transesterified products indicates the MWD of the side chains. Combined with the absolute molecular weight of the brush or the monomer conversion, the initiation efficiency can be further determined.

1.1.4 Self-assembly of Block Copolymers

Beside the grafting approaches, self-assembly of block copolymers provides another pathway for fabrication of CPBs or rather brush-like polymeric cylinders. It is well known that block copolymers with chemically distinct immiscible polymer blocks self-assemble into micelles in a selective solvent or into microphase-separated morphologies in bulk. By varying the volume fraction ratio of the different polymer blocks, cylindrical micelles can be achieved in solution.[6,89,90] When the core domains of the cylindrical micelles are subsequently crosslinked, brush-like polymeric cylinders with side chains tethered to a stable core can be generated. As an example, Liu *et al.* have prepared long brush-like cylinders (> 1 μm) by utilizing the micellization of PS-*b*-poly(2-cinnamoyloxyethyl methacrylate) (PS-*b*-PCMEMA) block copolymers in cyclopentane and the following UV-crosslinking of the PCMEMA core (see Figure 1–4A).[7] Similarly, block copolymers with suitable volume fractions can self-assemble into regular microphase-separated hexagonal cylinder bulk morphologies.[9,11,12] By crosslinking the cylindrical domains and subsequently dispersing the morphologies into solution, brush-like polymeric cylinders can also be achieved. An example of synthesis of brush-like cylinders with poly(2-vinyl pyridine) (P2VP) branches and crosslinked polybutadiene (PB) core is illustrated in Figure 1–4B.[91] Here, PB-*b*-P2VP diblock copolymers formed a bulk morphology of PB cylinders embedded in P2VP matrix. The unsaturated PB cores were cross-linked using a commercial photoinitiator to lock the cylindrical structure. The following dissolution in solvent assisted by ultrasonication resulted in brush-like polymeric cylinders.

Alternatively, block copolymers with a crystallizable block can be used to form brush-like polymeric cylinders. The crystallization-driven micellization of these block copolymers upon cooling in solution results in worm-like nanostructures with a crystalline cylindrical core and amorphous grafts. So far, brush-like polymeric cylinders have been generated from diblock copolymers poly(ferrocenyldimethylsilane)-*block*-poly(isoprene) (PFS-*b*-PI)[13] and triblock co- and terpolymers

PS-*b*-polyethylene-*b*-PS (PS-*b*-PE-*b*-PS),[17] PS-*b*-PE-*b*-poly(methyl methacrylate) (PS-*b*-PE-*b*-PMMA),[15,16] where the PFS and the PE block crystallize into the cylindrical core, respectively.

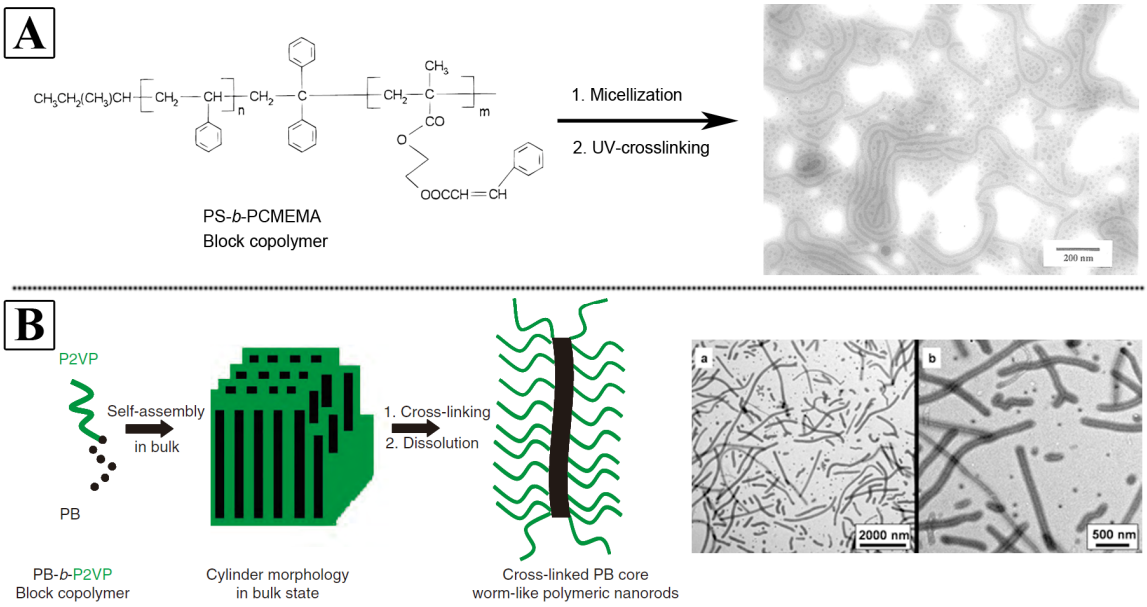

Figure 1-4. (A) Synthesis of brush-like polymeric cylinders with PS side chains and crosslinked PCMEMA core by utilizing the micellization of diblock copolymers PS-*b*-PCMEMA in cyclopentane.[7] Reprinted with permission of ACS. **(B)** Preparation of brush-like polymeric cylinders with P2VP side chains and crosslinked PB core from the microphase-separated bulk morphology.[91] Reprinted with permission of RSC.

1.2 Architectures of Cylindrical Polymer Brushes

At the mesoscopic scale, a polymer brush represents the assembled structure of the side chains tethered to a backbone. Therefore, the architecture of the polymer brush depends on the chemical composition and the block sequence of the side chains as well as the geometry of the backbone. The architecture of polymer brushes is of prominent importance for their physicochemical properties in solution and bulk and for their applications as templates for preparation of hybrid nanomaterials. In the last decade, various architectures of CPBs have been designed and synthesized. Scheme 1–2 summarizes the twelve representative architectures of CPBs.

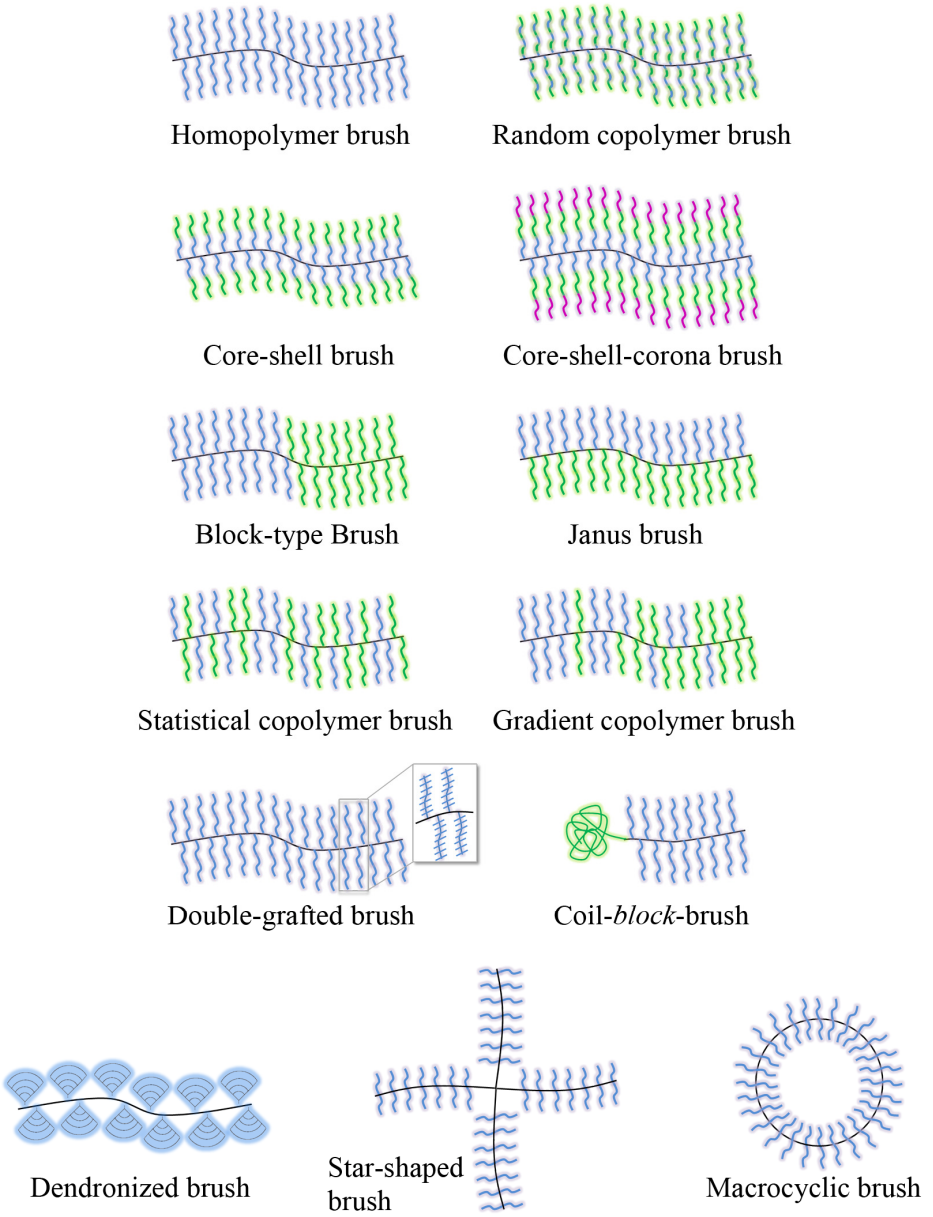

Scheme 1-2. Various architectures and structural compositions of CPBs.

From the synthetic aspect, homopolymer brushes and random copolymer brushes are the simplest architectures, as they can be achieved in one grafting step. The architectures with block copolymer side chains, *i.e.* core-shell brushes and core-shell-corona brushes, are the most common templates for preparing 1D hybrid nanoparticles. Block-type brushes, Janus brushes, and coil-*block*-brushes[92,93] demonstrate unique asymmetric characteristics. Heterogeneous side chain distribution along the backbone can be found in statistical copolymer brushes and gradient copolymer brushes. More complicated architectures are demonstrated by double-grafted brushes and dendronized brushes, where

each monomer unit of the side chains carries an oligomer chain on itself[94-96] and each side chain is a high-generation dendrimer,[97-101] respectively. Furthermore, by utilizing backbones with nonlinear geometries, nonlinear polymer brush topologies can be generated, such as star-shaped brushes and macrocyclic brushes. In the following, the synthesis and the visualization of some representative polymer brush architectures are described in details.

1.2.1 Core-shell and Core-shell-corona Polymer Brushes

CPBs show core-shell or core-shell-corona architectural features, when the side chains are diblock copolymers or triblock terpolymers, as the side chains assemble in a way to divide the brushes into two or three concentric cylindrical compartments. So far, core-shell and core-shell-corona CPBs have been synthesized *via* the 'grafting-through' approach of block copolymer macromonmers[102-105], *via* a sequential 'grafting-from' approach of different monomers[29,63,67,68,79,84,106-108] or *via* a 'grafting-onto' approach of block copolymer side chains.[109] As discussed above, the 'grafting-from' approach demonstrates significant advantages in preparing backbone polymers with narrow molecular weight distribution and high DP as well as in purifying the obtained CPBs. Therefore, the sequential 'grafting-from' approach is much more favored in the synthetic design of core-shell and core-shell-corona CPBs. Herein, a linear polymer main chain with initiating sites on each monomer unit is used as polyinitiator to stepwise graft side chain blocks according to the core-shell(-corona) sequence. By employing living/controlled polymerization techniques, such as ATRP and ROP, the initiating sites can be retained after each grafting step as end-groups of the side chains and can be utilized to grow further side chain blocks. An example of a sequential 'grafting-from' approach *via* two-step ATRP for preparing amphiphilic core-shell CPBs with a PAA core and a P*n*BA shell is illustrated in Figure 1–5A.[63] Müllner *et al.* have used a combination of sequential ROP and ATRP to prepare core-shell CPBs with PCL-*block*-poly(2-(dimethylamino)ethyl methacrylate) (PCL-*b*-PDMAEMA) side chains (see Figure 1–5B).[110]

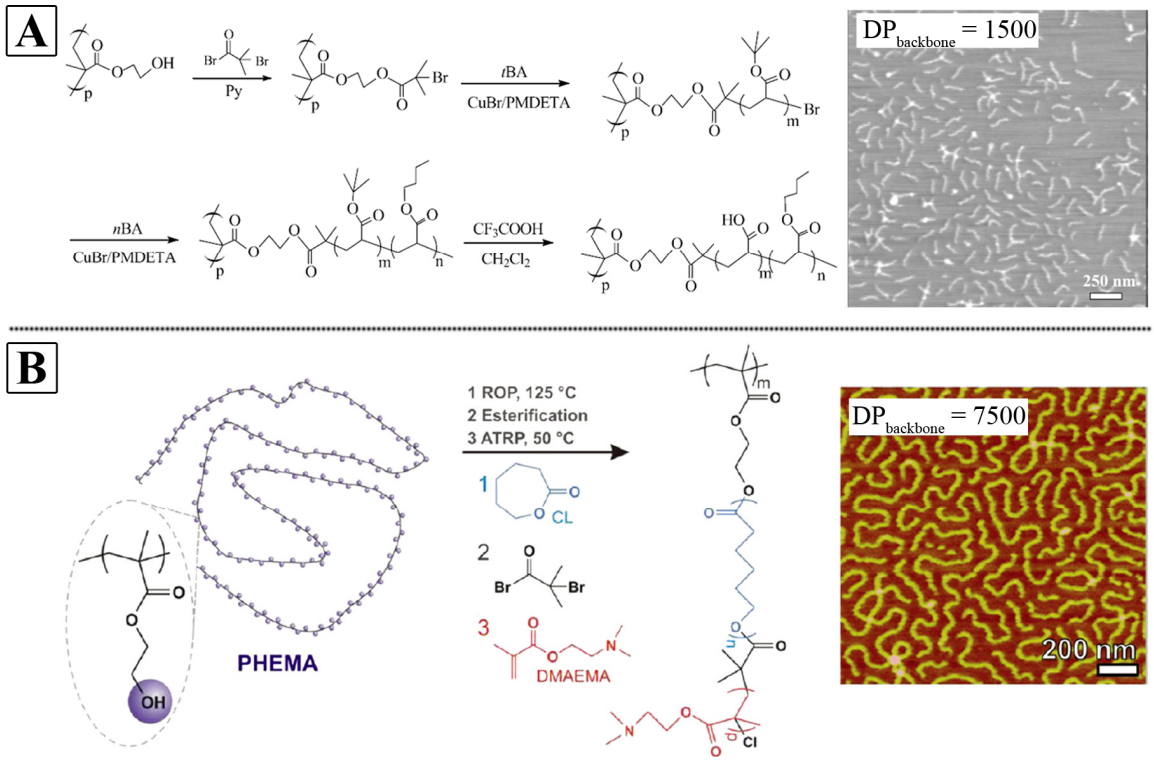

Figure 1-5. (A) Core-shell CPBs with PAA-*b*-P*n*BA side chains obtained *via* sequential 'grafting-from' approach by two-step ATRP.[63] Reprinted with permission of Elsevier. **(B)** Core-shell CPBs with PCL-*b*-PDMAEMA side chains obtained *via* sequential 'grafting-from' approach by the combination of ROP and ATRP.[110] Reprinted with permission of ACS.

Compared with the core-shell brushes, the core-shell-corona brushes have a more complicated architecture by possessing one more side chain block. So far, only the sequential 'grafting-from' approach has been reported for synthesizing well-defined core-shell-corona CPBs. Herein, three grafting steps are conducted according to the sequence of side chain blocks by using ATRP[111,112] or a combination of ROP and CRP.[88,113] Figure 1–6 shows an example of preparation of core-shell CPBs with PCL-*block*-PDMAEMA-*block*-poly(oligo(ethylene glycol) methyl ether methacrylate) (PCL-*b*-PDMAEMA-*b*-POEGMA) side chains by using a combination of sequential ROP and ATRP.[113]

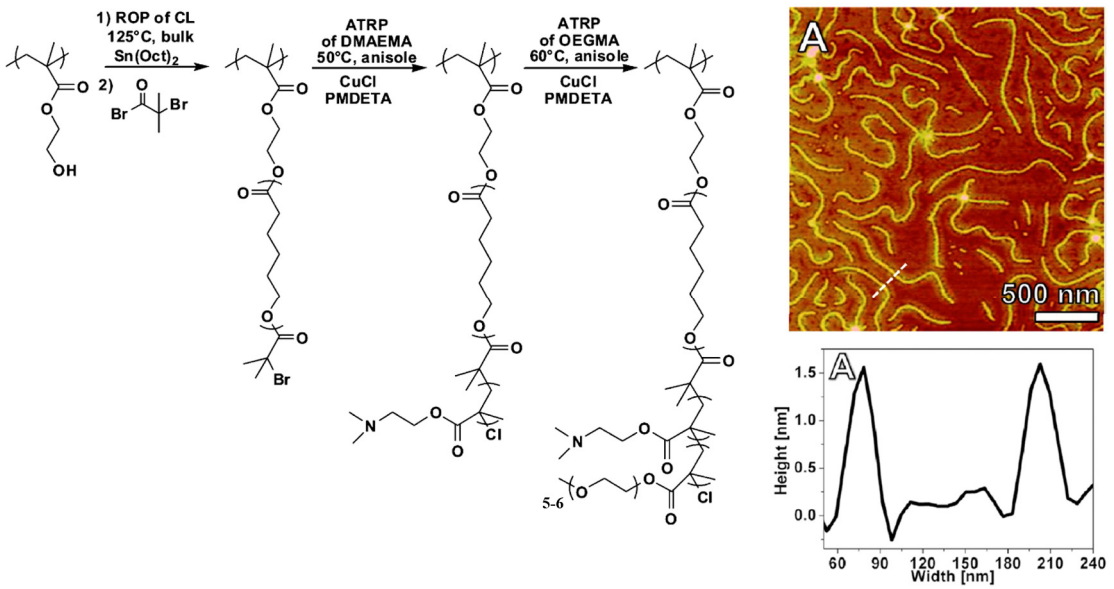

Figure 1-6. Core-shell-corona CPBs with PCL-*b*-PDMAEMA-*b*-POEGMA side chains obtained *via* sequential 'grafting-from' approach by the combination of ROP and ATRP.[113] Reprinted with permission of ACS.

Core-shell brushes and core-shell-corona brushes are the most important representatives among various polymer brush architectures. They not only show very interesting physicochemical behavior in solution or on surface, but also provide outstanding application possibilities in template-directed synthesis of diverse 1D hybrid nanoparticles. The properties and applications of these two architectures are discussed in Section 1.3 and 1.4, respectively.

1.2.2 Block-type and Janus Polymer Brushes

Both block-type polymer brushes and Janus polymer brushes demonstrate asymmetric characteristics. Block-type CPBs possess two blocks of different side chains, dividing the brushes perpendicular to the backbone into two cylindrical compartments. Janus CPBs consist of two hemi-cylinders of different side chains, with the interface along the backbone. In both cases, the differences in the chemical nature and the physicochemical properties between the two different side chain types induce special and interesting behavior of CPBs in solution, bulk and thin films (see Section 1.3). However, the hetero-grafted features lead to great challenges from the synthetic aspect, especially for the block-type

CPBs. So far, only few research groups have reported successful preparation of well-defined block-type CPBs by using complicated synthetic methods, such as the combination of 'grafting-through' and 'grafting-from' approaches,[25,81,114,115] the sequential 'grafting-from' approach *via* a combination of two different polymerization techniques[116-118] and the sequential 'grafting-through' approach of different macromonomers.[32,119] An example of synthesizing block-type CPBs *via* the sequential 'grafting-from' approach is illustrated in Figure 1–7A.[116] Herein, a diblock copolymer poly(2-(2-bromoisobutyryloxy)ethyl methacrylate)-*block*-PHEMA (PBIEM-*b*-PHEMA) was prepared and used as the backbone. The ROP of monomer CL from the PHEMA units formed the first side chain block, while the subsequent ATRP of monomer *n*BA from the PBIEM segments built the second side chain block. By using atomic force microscopy (AFM), the two side chain blocks can be clearly observed.

In the fabrication of Janus polymer brushes, the self-assembly of block copolymers shows the best pathway, as triblock terpolymers with appropriate volume fraction ratios can microphase-separate into regular patterned morphologies with cylinders embedded in alternate lamellae.[11,120,121] Figure 1–7B demonstrates an example of preparing Janus brushes from PS-*b*-PB-*b*-PMMA triblock terpolymers.[120] In bulk, the terpolymers form PB cylinders located between alternate PS and PMMA lamellae. By crosslinking the PB domains, the cylindrical scaffolds are locked. The following ultrasonication-supported dispersion of the bulk morphologies in solvent results in Janus cylinders with PS side chains on one side and PMMA grafts on the other side, as observed in the transmission electron microscopy (TEM) image.

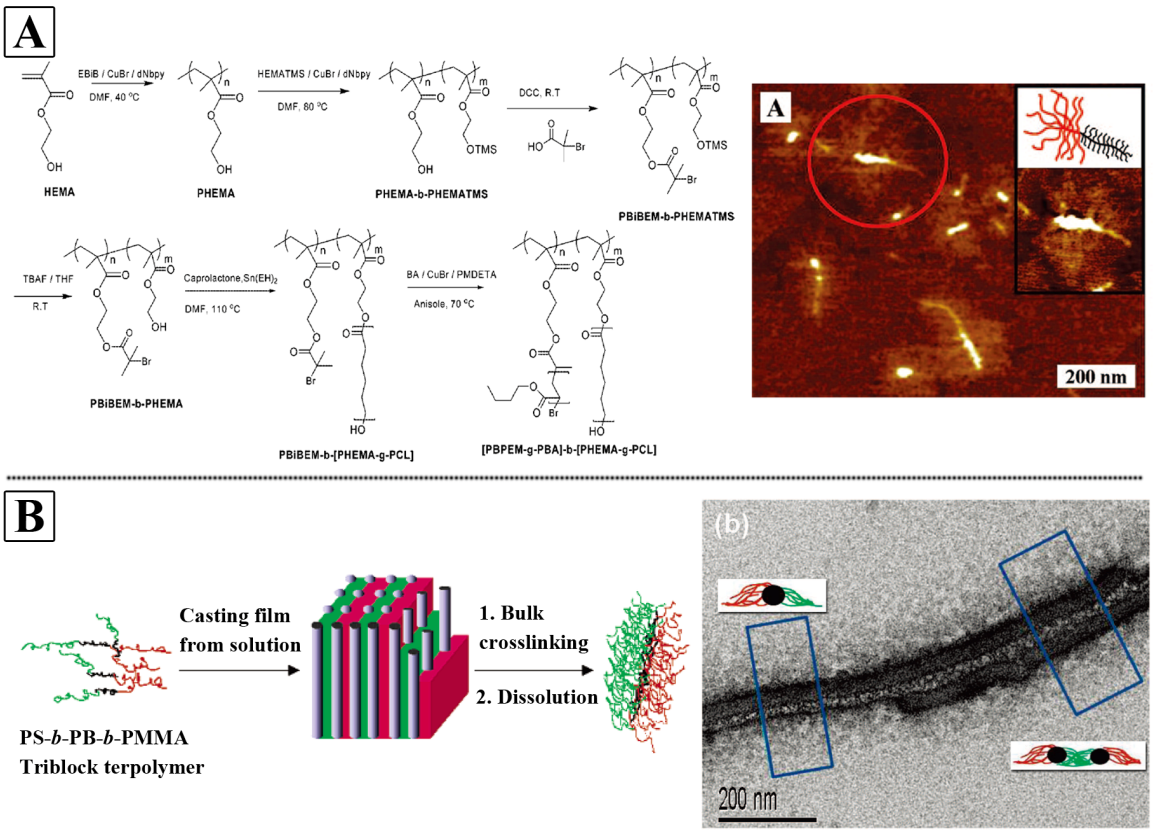

Figure 1-7. (A) Block-type CPBs with PCL and P*n*BA side chains obtained *via* sequential 'grafting-from' approach by a combination of ROP and ATRP.[116] Reprinted with permission of ACS. **(B)** Janus CPBs with PS and PMMA side chains obtained *via* self-assembly of triblock terpolymers in bulk and subsequent cross-slinking.[120] Reprinted with permission of ACS.

1.2.3 Statistical and Gradient Copolymer Brushes

Both statistical copolymer brushes and gradient copolymer brushes are hetero-grafted, consisting of two types of chemically distinct homopolymer side chains. However, the side chains are herein not divided into two different compartments as in block-type CPBs or Janus CPBs (see Section 1.2.2). In the case of statistical copolymer brushes, different polymer side chains are randomly distributed along the backbone, while gradient copolymer brushes have a gradually changing distribution of side chains along the backbone. So far, statistical copolymer brushes have been prepared *via* the 'grafting-through' approach by random copolymerization of two different macromonomers[32,122,123] or *via* the sequential 'grafting-from' approach by using a linear polymer main chain with statistically distributed initiating sites for different polymerization mechanisms.[124,125] An example

of statistical CPBs consisting of P2VP and PMMA side chains fabricated *via* the 'grafting-through' approach is illustrated in Figure 1–8A, where the different macromonomers with comparable reactivity are copolymerized by random free radical copolymerization.[122]

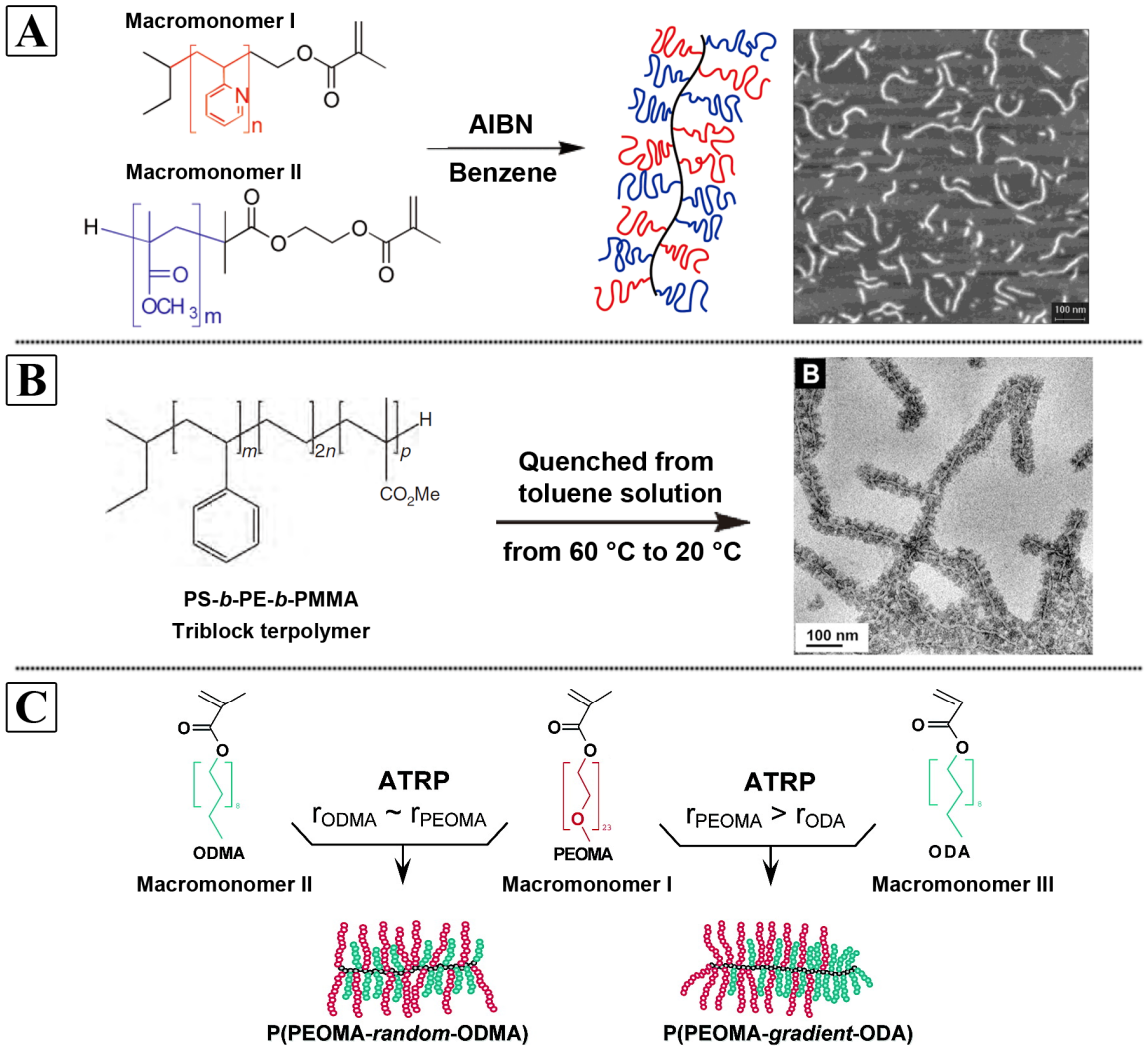

Figure 1-8. (A) Statistical copolymer brushes with P2VP and PMMA side chains obtained *via* 'grafting-through' approach by random copolymerization of different macromonomers.[122] Reprinted with permission of ACS. **(B)** Worm-like patchy brushes synthesized by crystallization-driven micellization of triblock terpolymer PS-*b*-PB-*b*-PMMA.[15] Reprinted with permission of ACS. **(C)** Statistical copolymer brushes with PPEOMA and PODMA side chains and gradient copolymer brushes with PPEOMA and PODA side chains prepared *via* 'grafting-through' approach. The reactivity ratio of the macromonomers decides the type of obtained brushes.[126] Reprinted with permission of ACS.

Alternatively, crystallization-induced micellization of triblock terpolymer PS-*b*-PB-*b*-PMMA can be employed to fabricate worm-like patchy brushes,[15] as illu-

strated in Figure 1–8B. Herein, the crystallizable PE block forms cylindrical crystalline cores of the brushes, which are however not as stable as the classic CPBs with a covalently bonded backbone. In the synthesis of gradient copolymer brushes, the 'grafting-through' approach by random copolymerization of two different macromonomers is again of dominant important. However, the side chain distribution in gradient CPBs changes gradually along the backbone. Therefore, an appropriate combination of macromonomers should be chosen, so that the reactivity ratio of the copolymerization can result in gradient copolymer brushes.[126,127] Neugebauer *et al.* have prepared gradient copolymer brushes by ATRP copolymerization of poly(ethylene glycol) methyl ether methacrylate (PEGMA) and octadecyl acrylate (ODA), with the latter having a lower reactivity (see Figure 1–8C).[126] With the hetero-grafted architectures, statistical copolymer brushes and gradient copolymer brushes demonstrate interesting and unique properties, especially the intramolecular phase separation behavior in solution, which is discussed in Section 1.3.

1.2.4 Star-shaped and Macrocyclic Polymer Brushes

Polymer brushes of nonlinear topologies also received great research attention in the last decade. Star-shaped brushes and macrocyclic brushes are the most important representatives of the nonlinear geometries. So far, star-shaped brushes have been synthesized *via* the 'grafting-onto' approach by coupling end-functional polymer chains onto a star-shaped multifunctional backbone[38,128] or *via* the 'grafting-from' approach by growing side chains from a star-like polyinitiator backbone.[129] Matyjaszewski *et al.* have fabricated well-defined three- and four-armed star-shaped brushes by utilizing the 'grafting-from' approach.[129] Herein, three- and four-armed star-like polymer main chains with ATRP initiating sites on each monomer unit were prepared and used as polyinitiator for the grafting process to produce star-shaped brushes with P*n*BA branches (see Figure 1–9A). AFM images confirmed the successful preparation.

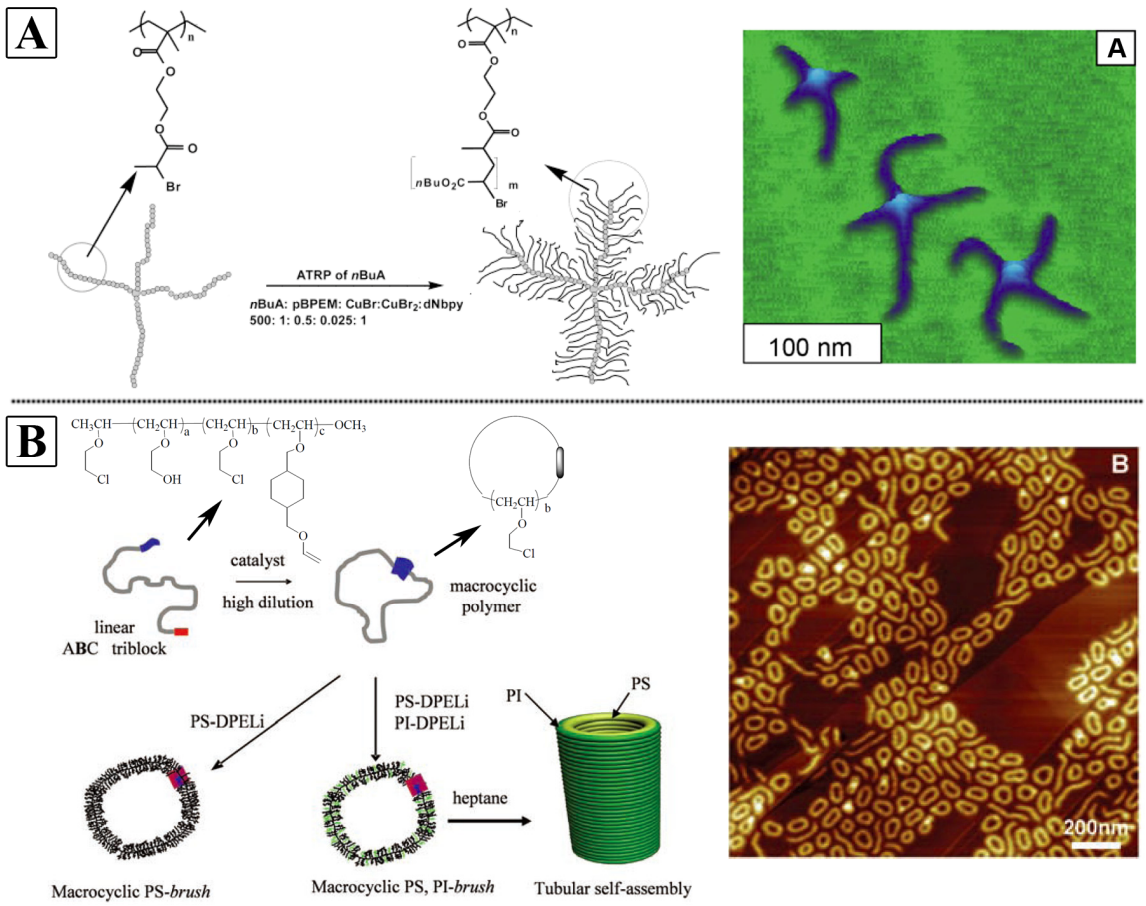

Figure 1-9. (A) Four-armed star-shaped brushes with P*n*BA side chains obtained *via* 'grafting-from' approach by ATRP.[129] Reprinted with permission of ACS. **(B)** Macrocyclic brushes obtained *via* 'grafting-onto' approach by coupling PS and PI with living anionic chain ends onto macrocylic backbone with electrophilic pendant groups.[130] Reprinted with permission of the American Association for the Advancement of Science.

Another interesting architecture is demonstrated by macrocyclic brushes, which consist of side chains tethered to a macrocyclic polymer backbone. In contrast to other polymer brush architectures, the main challenge in the synthesis of macrocyclic brushes is the preparation of well-defined macrocyclic backbones.[130,131] There are several reasons for the synthetic difficulties of the polymer macrocycles: (i) highly selective coupling reactions are necessary for the end-closing of a linear polymer chain, (ii) an increased DP and corresponding end-to-end distance of the linear polymer chain reduces drastically the efficiency of ring formation, and (iii) high dilution conditions are required to avoid intermolecular coupling reactions. Schappacher and Deffieux have employed an ABC-type triblock terpolymer to construct the macrocyclic backbone, where the blocks A and C bear

reactive antagonist functions and can undergo coupling reaction to enclose the polymer chain into a macrocycle. Subsequently, PS and PI chains with living anionic chain ends were grafted onto the block B, which carries an electrophilic chloroethyl pendant group on each monomer unit (see Figure 1–9B). The obtained macrocyclic brushes self-assemble into cylindrical tubes of up to 700 nanometers in a selective solvent for the PI branches.[130]

1.3 Properties of Cylindrical Polymer Brushes

As mentioned above, a single CPB represents an assembly of a large number of polymeric side chains, which are grafted on the backbone at a very high density and are thus suffering from great steric repulsion between each other.[132] However, a dissociation of this side-chain assembly is restrained by the covalently bonded backbone. Therefore, an extended cylindrical worm-like conformation of CPBs is the result of the competition between the lateral repulsion among side chains and the axial confinement of the backbone.

The unique molecular architecture of CPBs results in their special and interesting physicochemical properties and behavior. In contrast to linear polymers, polymer brushes are effectively 'self-disentangled' even in concentrated solutions and melt.[78] On the single-molecular scale, CPBs provide a perfect platform to investigate single-molecular behavior in solution or on surfaces, as any conformational transition of CPBs is limited to individual brushes and can be visualized by various modern microscopy techniques,[3,4,133,134] such as AFM, TEM and SEM. On the supramolecular scale, polymer brushes can form hierarchical self-assemblies in solution or in bulk, containing domains of much larger dimension than that from linear polymers. The properties of polymer brushes are determined and affected by various parameters, such as grafting density, chemical composition, nature and sequence of backbone and side chains. In the last decade, various CPBs with different chemical and structural compositions have been prepared and investigated for their structure-property relationships. In the following, representative studies exploring the properties and behaviors of CPBs in solution, in bulk and on surfaces are described in details.

1.3.1 Cylindrical Polymer Brushes in Solution

In solution, CPBs adopt the conformation of a worm-like object and can be characterized by the length per monomer unit of the backbone, l_m) the brush diameter, D, and the persistence length, l_p. These molecular dimensions and the overall conformation depend on the length and stiffness of the side chains, the grafting density and the interactions between the side chains and the solvent molecules. So far, many theoretical calculations,[135-137] computer simulations[138-141] and experimental studies[19,142-144] have been performed to investigate the effect of these structural parameters on the molecular conformation. However, the results are contradictory on how much the side chain length and stiffness affects the l_p and the brush morphology.[145] Some theories predict that stiffening the backbone cannot induce ordering of CPBs,[139,146] while some simulations and experiments show ordering behavior of CPBs stiffened by increased side chain length.[147,148]

The solution behavior of the side chains decides the solubility and morphology of the CPBs in solution. Homopolymer CPBs dissolved in a good solvent for the side chains demonstrate the most typical conformation, *i.e*. extended homogeneous worm-like cylinders. In the case of core-shell CPBs with a more complex architecture, various conformations depending on the solvent quality for the core and the shell are expected.[149-151] AFM images of core-shell CPBs with PAA-*b*-P*n*BA branches from toluene solution on mica show an interesting 'pearl-necklace' structure in the core part (Figure 1–10A).[149] This conformation is induced by the different dissolving properties of the core and the shell in toluene. On one hand, the in toluene well-dissolved P*n*BA shell ensures the solubility and the cylindrical shape of the whole CPB. On the other hand, the poor solubility of the PAA polyelectrolyte core leads to the collapse of the core and the formation of individual 'pearls'. This dissolving mechanism is confirmed by Monte Carlo simulations (Figure 1–10A). Another 'pearl-necklace' conformation is demonstrated by core-shell CPBs with a P*n*BA shell and a core of polychelates built up by PAA and Cd^{2+} cations in methanol/chloroform (v/v = 1/1) (Figure 1–10B).[152] Herein, the formation of the 'pearl-necklace' structure is attributed to the crosslinking of side chains by Cd^{2+} cations.

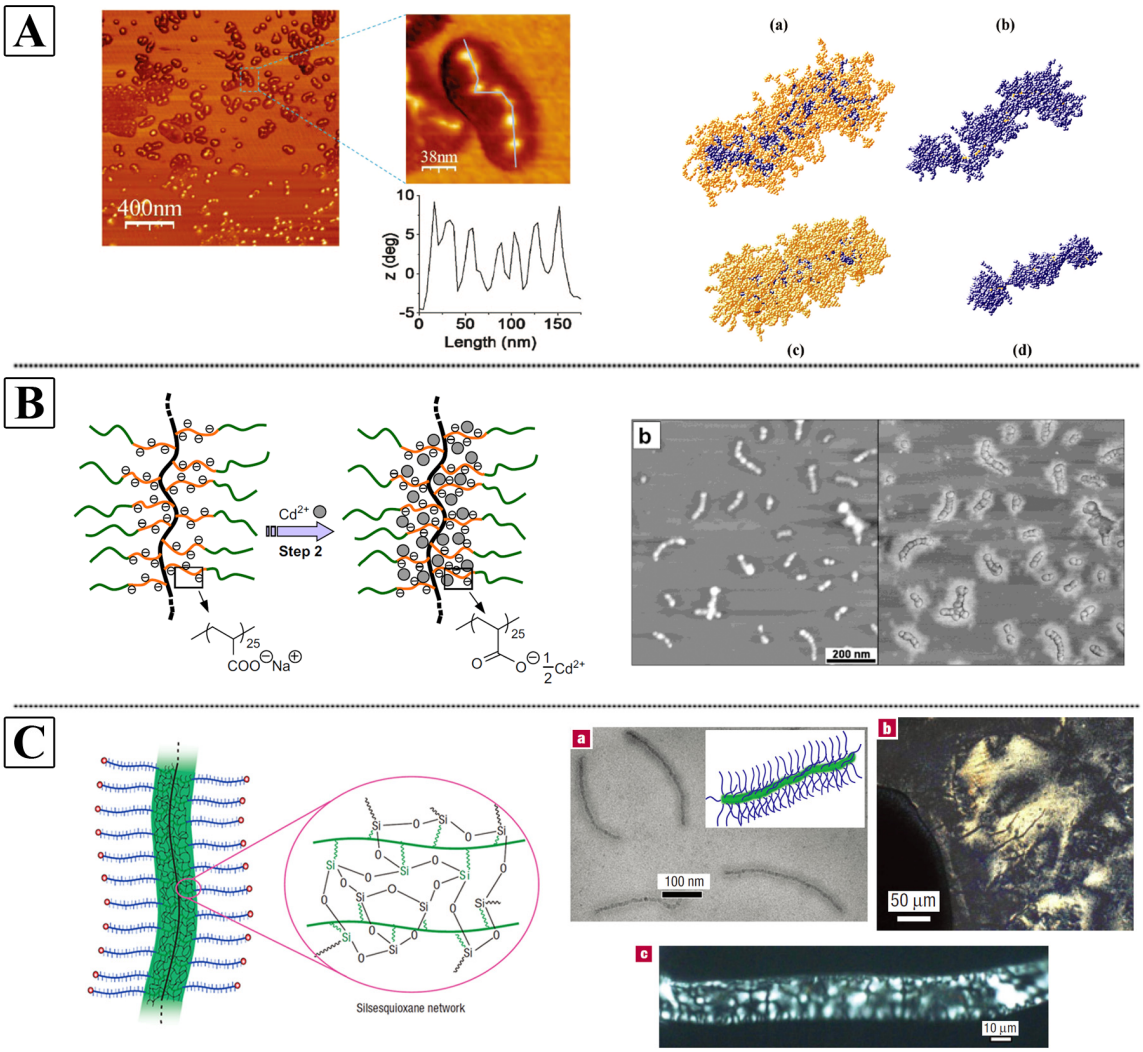

Figure 1-10. (A) AFM images showing 'pearl-necklace' conformation of PAA-P*n*BA core-shell brushes from a toluene solution. Snapshots of typical conformations obtained by Monte Carlo simulations: (a) and (b) show the conformation in a good solvent for the corona (orange) and the core (blue); (c) and (d) show the conformation in a bad solvent for the core (blue).[149] Reprinted with permission of ACS. **(B)** Another 'pearl-necklace' conformation demonstrated by core-shell CPBs with a P*n*BA shell and a polychelate core built up by PAA and Cd^{2+} cations in methanol/chloroform (v/v = 1/1).[152] Reprinted with permission of ACS. **(C)** Hybrid core-shell CPBs with a stiff silsesquioxane core and POEGMA shell form lyotropic liquid-crystalline phases upon concentrating.[108] Reprinted with permission of Nature Publishing Group.

Another interesting behavior of CPBs in solution is the possible formation of a lyotropic liquid-crystalline phase. In the case of stiff CPBs, a competition of orientational entropy and excluded-volume interaction leads to this lyotropic ordering. An example of a liquid-crystalline phase formed by polymer brushes with a stiff core of silsesquioxane is given in Figure 1–10C, where the liquid-crystalline phase is verified by the birefringence patterns emerging from the solution.[108]

Stimuli-responsive linear polymers and polymer micelles have received great research attention in last decades, as they undergo reversible conformational transitions in response to external stimuli in a controlled manner and can be applied in biomedical processes, membrane materials and sensor technologies. When polymer brushes carry stimuli-responsive segments, they are expected to respond conformationally to environmental changes. So far, various CPBs responsive to temperature,[153-155] pH value,[156-158] salt,[156,159] surfactants[160], polyelectrolytes[161], mechanical compression[162,163] and light[164] have been prepared and probed for their behavior in solution.

Temperature-sensitive CPBs consisting of side chain segments with a lower critical solution temperature (LCST) collapse upon heating above a certain temperature, since the side chains become dehydrated and insoluble. An example of molecular brushes with side chains consisting of thermoresponsive DMAEMA and hydrophobic MMA is illustrated in Figure 1–11A.[155] Herein, an unusual concentration-dependent LCST was observed. In dilute solutions (0.1 w/v %), single-molecular collapse was observed. However, at higher concentrations (1.0 w/v %), intermolecular aggregation occurred.

pH-sensitive CPBs are constructed by building ionizable polymer segments with a pK_a between 3 and 10 (weak acids and bases) into the side chains. A change in the ionization state upon pH variation leads to a conformational change of the brush. Figure 1–11B shows pH-sensitive CPBs with side chains consisting of PAA, which has a pK_a of 6.8 – 7.[158] By increasing the pH of the solution from 4.8 to 8.9, the brush undergoes a transition from a compact collapsed globule to a fully stretched cylinder.

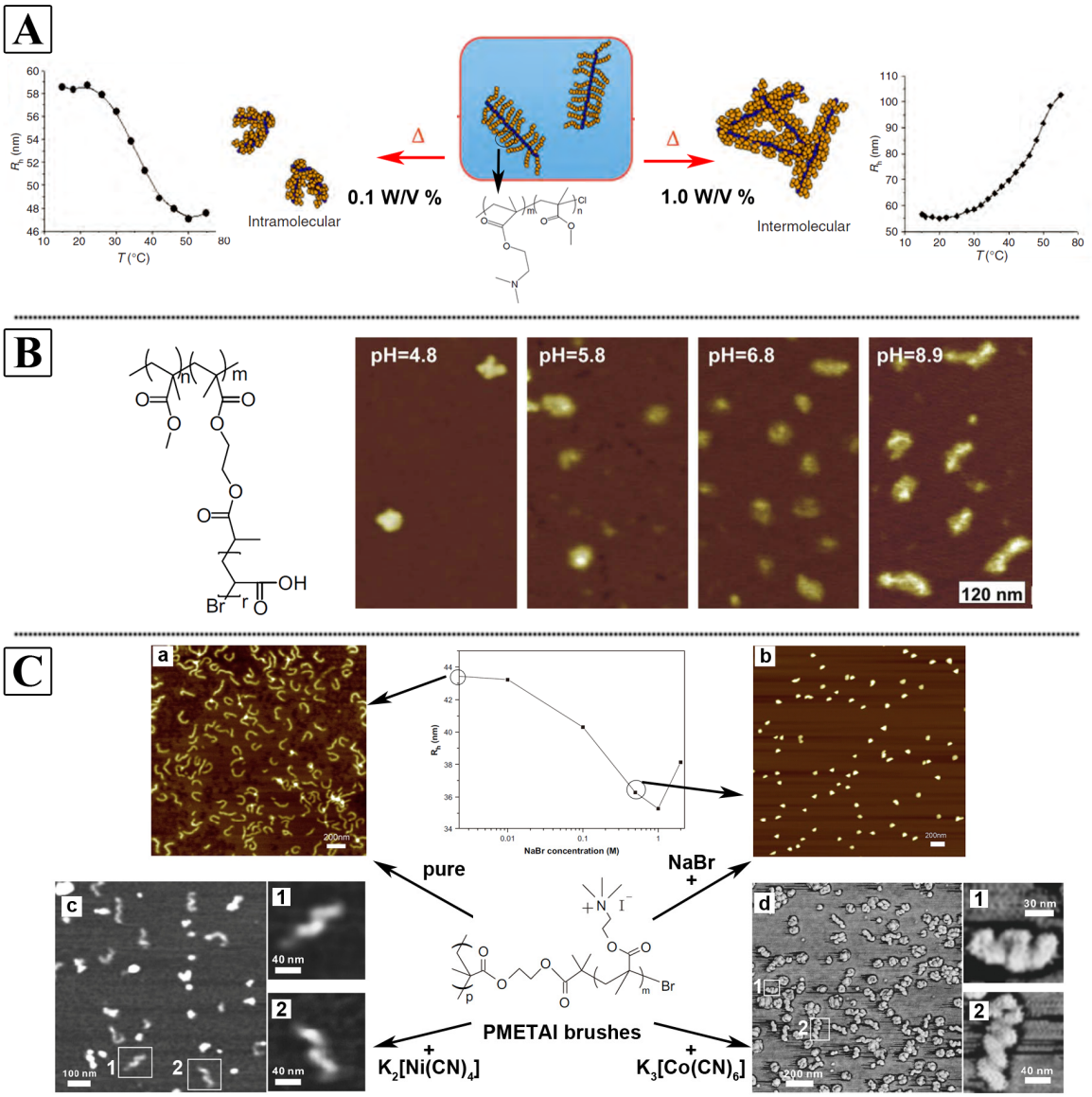

Figure 1-11. (A) Temperature-responsive CPBs consisting of PDMAEMA segments with a lower critical solution temperature (LCST) in side chains. Both intra- and intermolecular aggregation upon heating can be induced through appropriate selection of brush concentration.[155] Reprinted with permission of Wiley-VCH. **(B)** pH-responsive CPBs consisting of PAA segments in side chains show a transformation from a compact globule to an extended conformation with an increase in pH.[158] Reprinted with permission of Elsevier. **(C)** CPBs with cationic polyelectrolyte PMETAI side chains demonstrate salt-sensitive behavior.[156,159] AFM images of CPBs from (a) salt-free, (b) monovalent salt NaBr, (c) divalent salt $K_2[Ni(CN)_4]$ and (d) trivalent salt $K_3[Co(CN)_3]_6$ aqueous solution. Reprinted with permission of Elsevier and RSC.

CPBs with polyelectrolyte side chains always demonstrate salt-sensitive behavior in aqueous solution. Xu *et al.* prepared CPBs with the cationic polyelectrolyte poly((2-(methacryloyloxy)ethyl) trimethylammonium iodide) (PMETAI) branches and investigated their responses to salts with different counterions (Figure 1–11C).[156,159] In a

salt-free solution, the cationic brushes show an extended cylindrical conformation due to the strong Coulombic repulsion of the charged side chains. The addition of monovalent salt (NaBr) screens the electrostatic interaction within the polyelectrolyte branches and thus induces a collapse of the brush conformation with an obvious decrease in the hydrodynamic radius, R_h, of the brush. In the presence of a divalent ($K_2[Ni(CN)_4]$) or trivalent salt ($K_3[Co(CN)_6]$), this collapse passes through an intermediate state in which the cylindrical polymer brushes assume a helical conformation (Figure 1–11C). The formation of the helix is prompted by the contraction of the polymer molecules along the long axis by the presence of the multivalent counterions.

Ionic surfactants act as a further trigger of the CPBs with polyelectrolyte side chains. Xu *et al.* found that the anionic surfactant sodium dodecyl sulfate (SDS) forms an ionic complex with the cationic PMETAI CPBs, leading to the collapse of the brushes from worms to spheres (Figure 1–12A).[160] Both α-cyclodextrin (α-CD) and β-cyclodextrin (β-CD) form supramolecular inclusion complexes with SDS and thus liberate the CPBs back to the worm-like conformation. In the case of β-CD used for complex formation with SDS, a more competitive inclusion agent, 1-adamantylammonium chloride (AdAC), can remove the β-CD from the SDS-β-CD complex, causing the recollapse of the brushes. Polyelectrolyte CPBs also show conformational response to the presence of oppositely charged linear polyelectrolytes. Figure 1–12B illustrates an example of the conformational transition of cationic PMETAI brushes upon addition of linear poly(styrenesulfonate) (PSS), where extended CPBs collapse through worm-like and 'pearl-necklace' into spherical interpolyelectrolyte complexes (IPECs).[161]

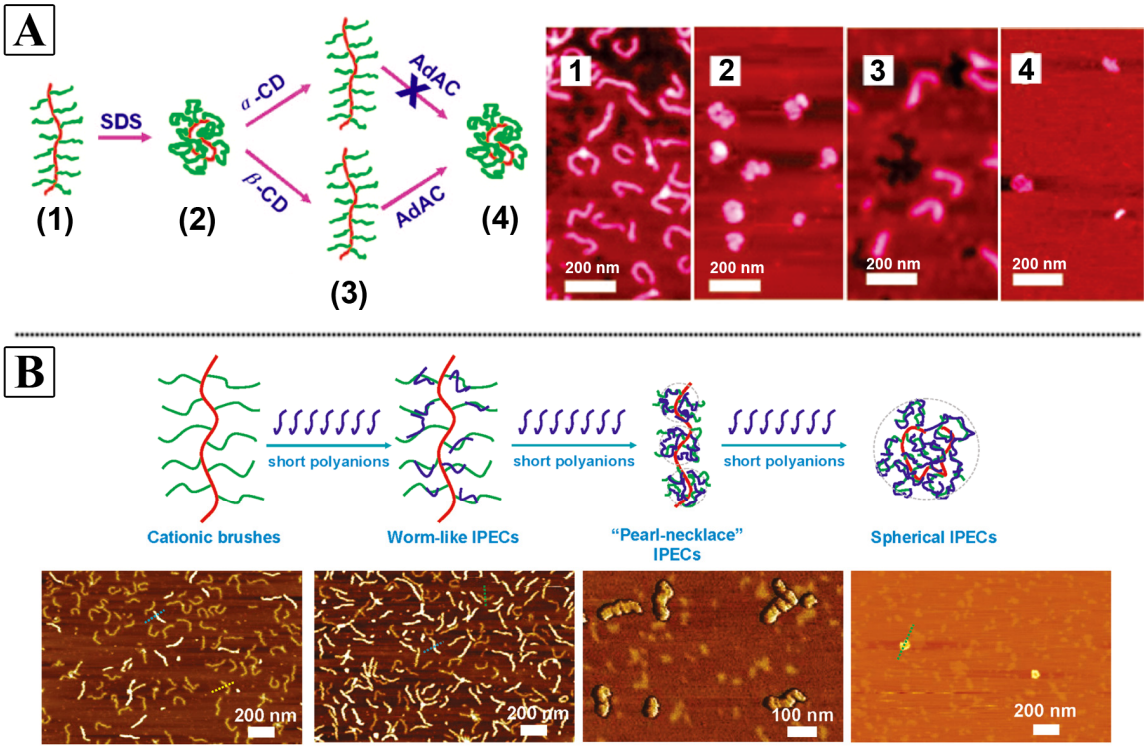

Figure 1-12. (A) Conformational transitions of cationic polyelectrolyte PMETAI brushes induced by surfactants.[160] SDS: sodium dodecyl sulfate; α-CD: α-cyclodextrin; β-CD: β-cyclodextrin; AdAC: 1-adamantylammonium chloride. Reprinted with permission of ACS. **(B)** IPECs formed by cationic polyelectrolyte PMETAI brushes and linear polyelectrolyte poly(styrenesulfonate) (PSS).[161] Reprinted with permission of ACS.

Another interesting behavior of CPBs in solution is that they can self-assemble into hierarchical structures. The self-assembly occurs on both intramolecular and intermolecular level. Statistical copolymer brushes with quaternized P2VP and PMMA side chains adopt horseshoe conformation in chloroform or meander-like structure in water (Figure 1–12A).[122] Herein, the solvent nature induces the intramolecular self-assembly. Polymer brushes with amphiphilic compartmentalized characteristics demonstrate intermolecular self-assembling behavior. Block-type CPBs with PAA and PS side chains form global micelle-like structures in water (Figure 1–12B).[119] Janus brushes with PS and PMMA hemicylinders assemble into elongated bundles in acetone (Figure 1–12C), where the polystyrene part is shielded from the poor solvent within the center.[120] Coil-*block*-brush polymers with a coil part of PS and a brush part of PAA adopt flower-like morphology in water (Figure 1–12D).[93] The common condition for the formation of the intermolecular

self-assemblies mentioned above is the choice of a selective solvent, which provides different dissolving abilities toward different building blocks of the brush polymers.

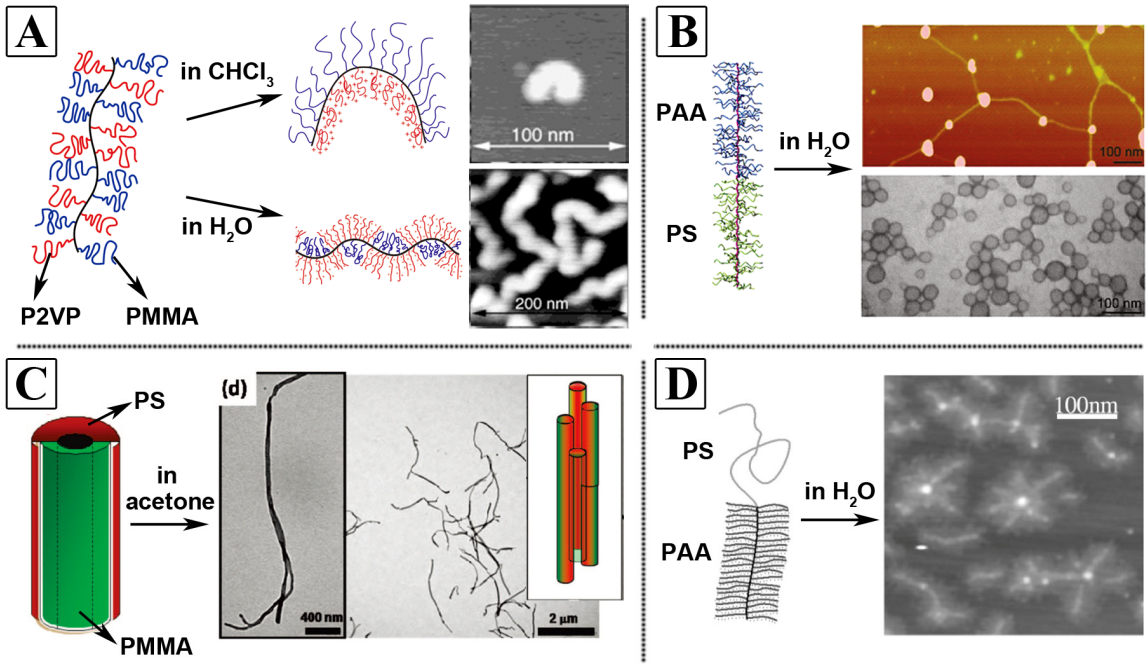

Figure 1-13. (A) Intramolecular phase separation of statistical copolymer brushes with quaternized P2VP and PMMA side chains in different solvents.[122] Reprinted with permission of ACS. **(B)** Micelle-like structures formed by block-type PAA-PS CPBs in water.[119] Reprinted with permission of ACS. **(C)** Self-assembly of Janus brushes with PS and PMMA hemicylinders into elongated fiber-like bundles in acetone.[120] Reprinted with permission of ACS. **(D)** Flower-like morphology assembled by coil-*block*-brush polymers with a coil part of PS and a brush part of PAA in water.[93] Reprinted with permission of Wiely-VCH.

1.3.2 Cylindrical Polymer Brushes in the Bulk

Similar to the solution behavior, molecular brushes 'self-disentangle' in the bulk state due to the steric repulsion of the densely grafted side chains. This self-disentanglement results in unique bulk morphologies and thus special mechanical, optical and thermal properties.[4,94,107,165] As systematically understood, linear block copolymers with incompatible segments self-assemble into microphase-separated morphologies in bulk. In the case of molecular brushes, as the side chains cannot leave the backbone, one more structural requirement besides the incompatibility of building blocks is necessary for the formation of microphase-separated bulk morphologies. That is, the side chains must be constructed into compartmentalized blocks on the single-molecular level. Therefore,

block-type polymer brushes represent good candidates for microphase-separation. Rzayev *et al.* reported the preparation and microphase-separation of block-type CPBs with PS and PLA side chain blocks.[117,166] By controlling the volume fraction ratio through varying the length of backbone and side chains, different microphase-separated bulk morphologies, *i.e.* lamellae and cylinder patterns, were fabricated (Figure 1–14A). Uniquely, the dimensions of the formed microphase domains (> 100 nm) are much larger than those from analogous linear diblock copolymers with similar volume fraction ratio. A subsequent selective etching of the PLA cylinders from the cylindrical morphology generated nanoporous materials with an average cylindrical pore diameter of 55 nm.

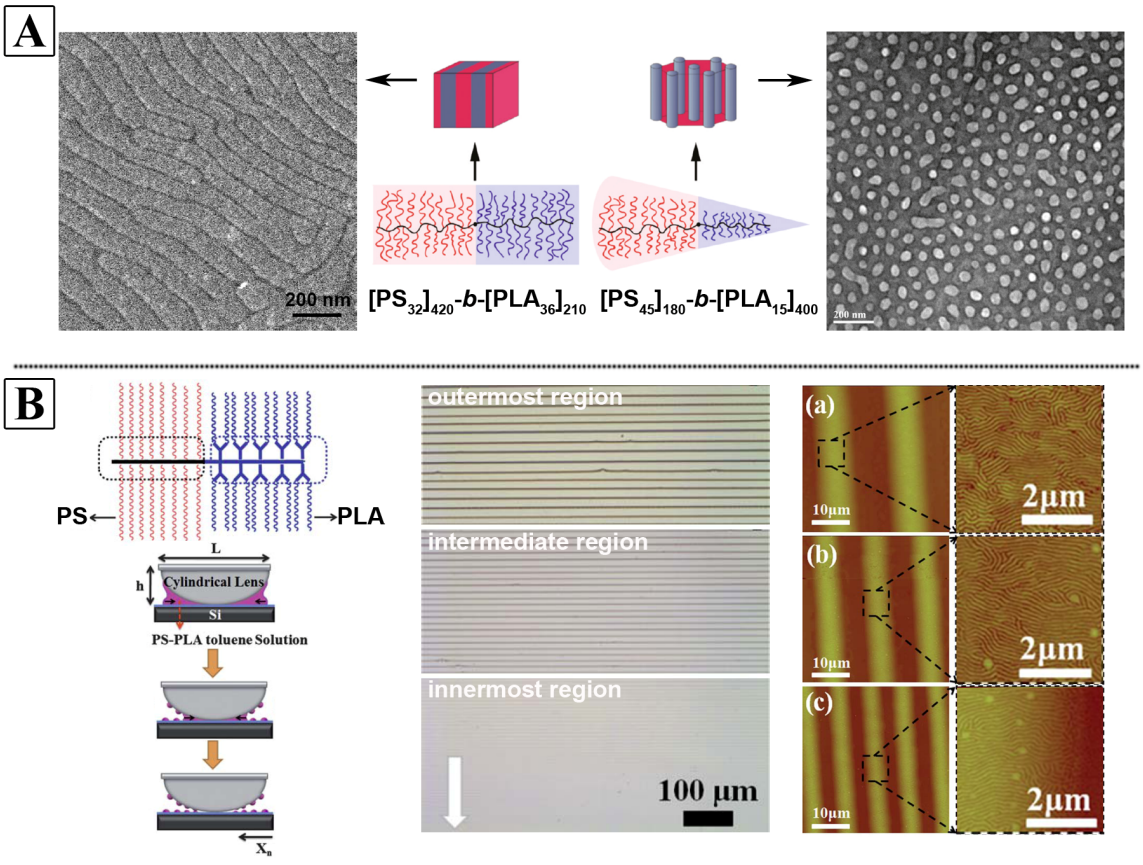

Figure 1-14. (A) Microphase-separated lamellae and cylinder bulk morphologies formed by block-type PAA-PS CPBs with different structural compositions.[117,166] Reprinted with permission of ACS. **(B)** Hierarchically structured gradient stripes of block-type PS–PLA CPBs with internal lamellar phase-separation obtained by controlled evaporative self-assembly in a cylinder-on-flat geometry.[167]

Furthermore, the block-type PS–PLA CPBs were hierarchically structured by combining controlled evaporative self-assembly in the cylinder-on-flat geometry, which

yielded microscopic gradient stripes over large areas, with spontaneous self-assembly of PS–PLA at the nanoscale, which was facilitated by selective solvent vapor annealing (Figure 1–14B).[167] The enzymatic removal of PLA branches in PS–PLA rendered the formation of nanochannels within the stripes.

1.3.3 Cylindrical Polymer Brushes on Surfaces

Generally, the behavior of molecular brushes on surfaces is determined by the surface quality. The overall brush conformation and the local dimensions, such as contour length, brush width, backbone curvature, and persistence length, can be influenced by tuning the surface nature, the interaction between the brush and the surface and the lateral surrounding conditions. The first research focus of the surface properties was the adsorption of brushes on a flat substrate, which breaks the cylindrical symmetry and induces partitioning of the side chains.[162,168-170] As illustrated in Figure 1–15A, the conformation of adsorbed brush depends on the fraction of adsorbed side chains, ϕ_a, and the uneven distribution of the side chains with respect to the backbone, ϕ_L and ϕ_R.[3] When ϕ_a is large and $\phi_L \neq \phi_R$, the brush adopts a spontaneous curvature conformation. A ribbon conformation is expected for large ϕ_a and $\phi_L = \phi_R = 0.5$. When the side chains are no longer strongly adsorbed to the surface ($\phi_a < 1$) and desorbed side chains repel each other, the brush assumes a cylindrical conformation. In the case of low adsorption ($\phi_a < 1$) and desorbed side chains attract each other, a globular conformation of the brush should be formed. Further research focused on the spreading behavior of CPBs on surfaces and the related surface coverage, brush conformation and orientation.[171,172] It was found that flowing brushes become more extended with decreasing film pressure (increasing distance from the drop center) and occupy a larger area per molecule during spreading (Figure 1–15B).[173]

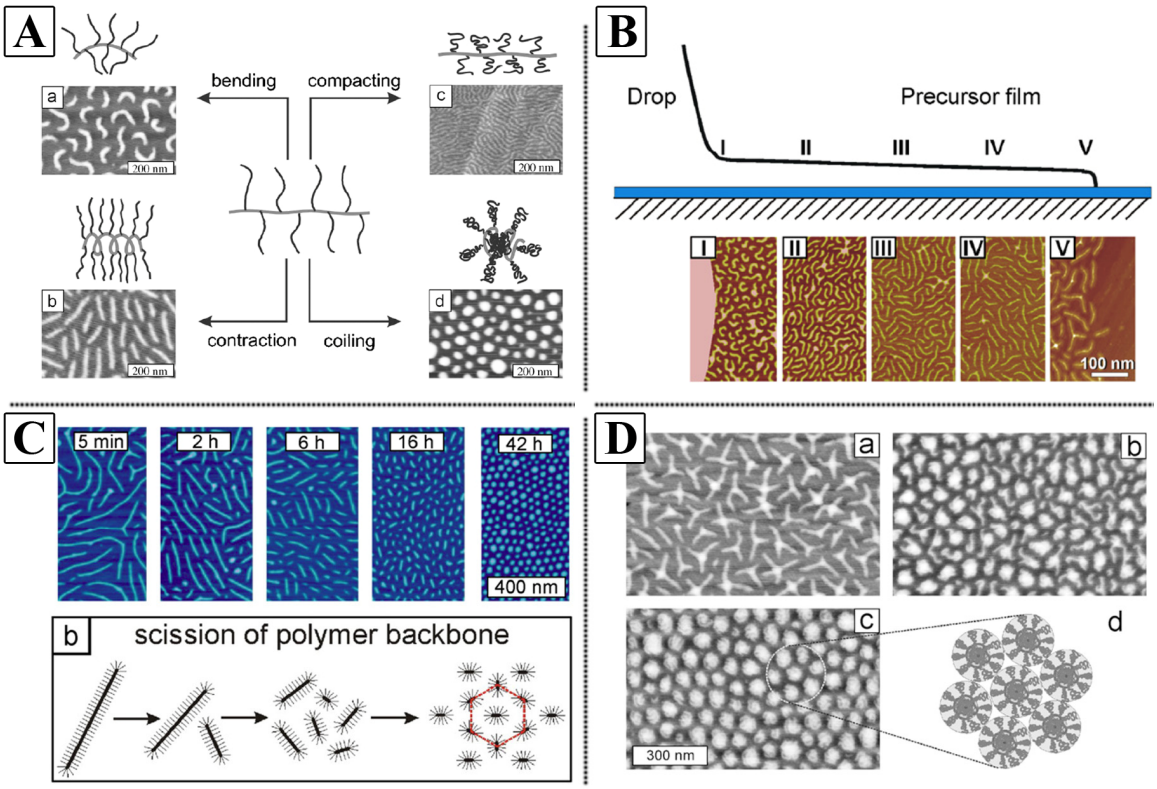

Figure 1-15. (A) AFM height images along with schematics demonstrate four distinct conformations observed for molecular brushes adsorbed on different surfaces: (a) spontaneous curvature, (b) ribbons, (c) cylindrical, and (d) globular.[3] Reprinted with permission of Elsevier. **(B)** Conformational transitions of molecular brushes with P*n*BA side chains during their spreading on a mica surface.[3,173] In the flow direction, the brushes change from a densely packed state to a loosely packed extended state. Reprinted with permission of Elsevier and Wiley-VCH. **(C)** Random scission of the backbones of CPBs with P*n*BA side chains on a water/propanol (99.8/0.2 wt-%/wt-%) substrate.[3,174] Reprinted with permission of Elsevier and Nature Publishing Group. **(D)** AFM observes the transition of the four-arm star brushes from a star-like to a disk-like conformation caused by lateral compression of monolayer films on the surface of water.[175] Surface pressure: (a) 7 mN/m, (b) 22.5 mN/m, and (c) 23.5 mN/m. Reprinted with permission of ACS.

The underlying substrates that can interact with CPBs are not restricted to solid surfaces. An impressive behavior of molecular brushes is also observed on liquid surfaces. The backbones of CPBs with P*n*BA side chains undergo a random scission on water/propanol (99.8/0.2 wt-%/wt-%) surface upon transforming *via* very slow expansion (in hours or in days) from a 3-dimentional cylindrical conformation into a 2-dimentional flat one driven by a confinement-induced passive exclusion of densely grafted side chains (Figure 1–15C).[174] Furthermore, lateral compression of four-arm star-like P*n*BA brushes on water surface causes a transition from an extended dendritic-like conformation to a

compact disk-like conformation with local hexagonal ordering (Figure 1–15D).[175]

1.4 Application of Cylindrical Polymer Brushes

The unique molecular architectures and the versatile properties enable plenty promising applications of CPBs in the fields of chemistry, physics, biology, medicine and materials science. First of all, the distinct cylindrical shape and the corresponding high aspect ratio of CPBs render them suitable templates for the fabrication of anisotropic 1D organic/inorganic hybrid nanoparticles. Secondly, CPBs can serve as effective vehicles for drug delivery or gene transfection in biomedical applications. The multiple functionalities and 1D structure make the CPBs advantageous in cell entry. Furthermore, molecular brushes as assemblies of many side chains provide visualizable platforms for the investigation of elementary reactions. Moreover, the bulk morphologies obtained by self-assembly of CPBs construct different kinds of advanced materials, such as supersoft elastomers and photonic materials. In the following, prominent applications of CPBs are described in details.

1.4.1 Cylindrical Polymer Brushes as Templates for One-dimensional Hybrid Nanostructures

In recent years, 1D organic/inorganic hybrid nanostructures, such as nanowires, nanorods and nanotubes, with their unique size- and shape-dependent optical, magnetic, biological and electrical properties have drawn increasing attention to the field of materials science. Various ‘bottom-up’ or ‘top-down’ approaches have been developed to overcome the preparation challenge of the 1D nanomaterials. Utilization of molecular templates to direct the synthesis of 1D nanoparticles has proved to be a simple, intuitive, versatile and straightforward method. Herein, surfactants, block copolymers, molecular brushes, biological superstructures as well as inorganic porous membranes are used as templates, which allow a direct translation of a desired topology from the template into the hybrid nanoparticles.[145] So far, template-directed preparation routes based on core-shell,

core-shell-corona and homopolymer CPBs have been reported, demonstrating several significant advantages: (i) uniform and tunable dimension of the 1D nanostructures. The CPB templates prepared from living/controlled polymerization techniques ensure the low polydispersity of the obtained 1D nanostructures in dimension. (ii) Encapsulation of (toxic) functional centers within the 1D nanostructures. Core-shell(-corona) CPBs with multiple separated compartments provide possibility to encapsulate functional centers like metal cations and nanoparticles within the inner compartment (core) *via* coupling or chelating. (iii) Solubility of the 1D nanostructures. All 1D hybrid nanoparticles templated from core-shell(-corona) molecular brushes are colloidally stable in the solvents of their outer block (shell or corona) regardless of the solubility of the inner block.

The most straightforward template-directed preparation method of 1D organic/inorganic hybrid nanostructures based on CPBs is the introduction of external inorganic precursor into the pure organic templates. The molecular brush templates used here always consist of a block of polyelectrolyte, such as PAA, P2VP, PDMAEMA and PMETAI, which can form complex with metal ions. So far, semiconducting nanowires of CdS[152] and CdSe,[176] superparamagnetic nanocylinders of γ-Fe_2O_3,[177,178] crystalline TiO_2 (anatase) nanowires[179] and linearly aligned gold[150] or platinum[180] nanoparticles have been fabricated with this method. Figure 1–16A illustrates an example of the preparation of superparamagnetic γ-Fe_2O_3 nanocylinders, where amphiphilic CPBs with a PAA core and a P*n*BA shell were utilized as templates.[177] Fe^{3+} or Fe^{2+} cations were coordinated with the carboxylic acid groups (or carboxylate groups, after neutralization) in the core. Subsequent redox reactions yielded ultrafine superparamagnetic nanoparticles, as confirmed by SQUID measurements.

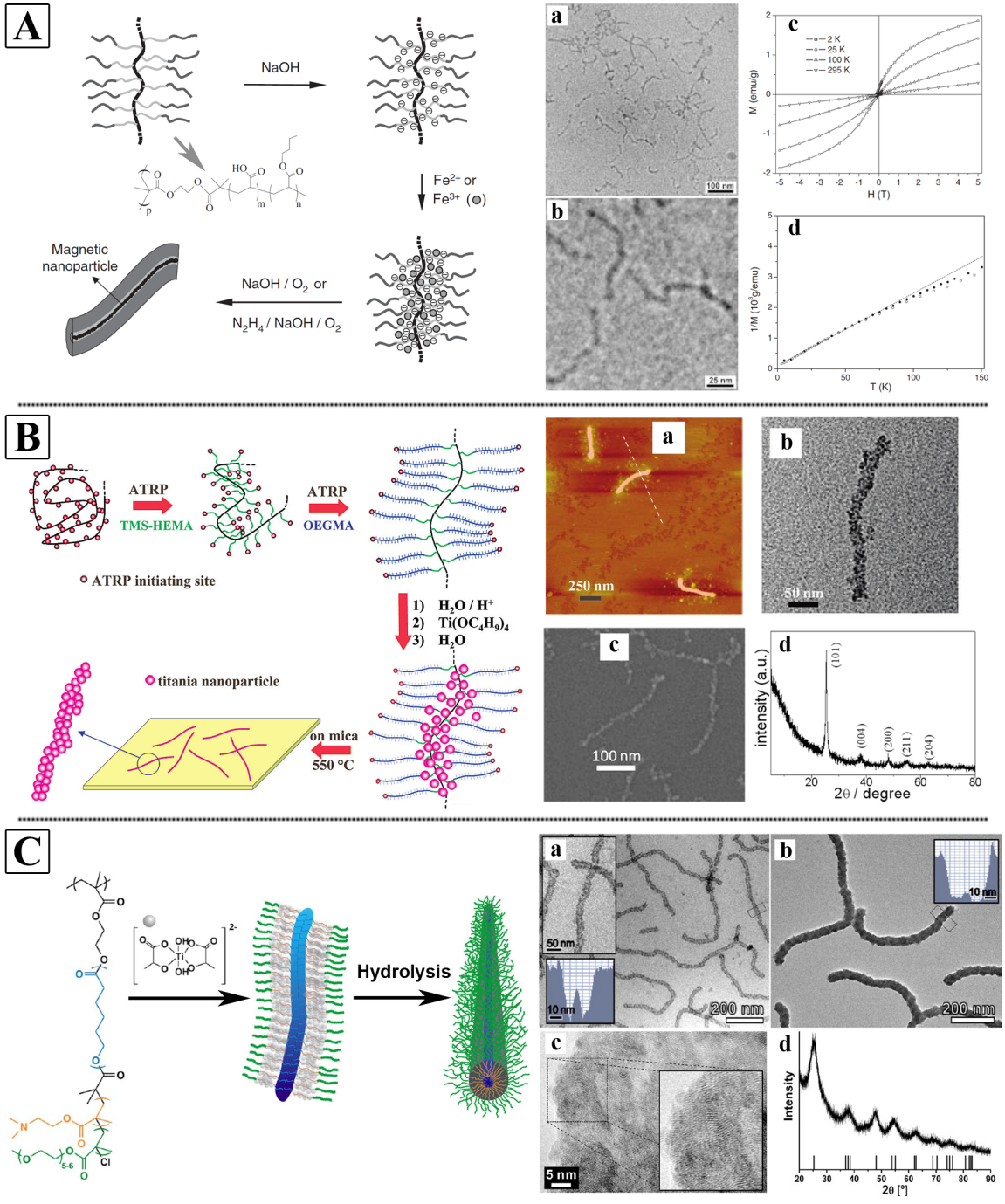

Figure 1-16. (A) Template-directed synthesis of superparamagnetic γ-Fe_2O_3 nanocylinders by utilizing PAA-P*n*BA core-shell CPBs.[177] (a, b) TEM images, (c, d) magnetization curves of hybrid magnetic nanocylinders. Reprinted with permission of Wiley-VCH. **(B)** Synthesis of anatase nanowires *via* PHEMA-POEGMA core-shell CPBs.[179] (a) AFM and (b) TEM images of titania-CPB hybrids; (c) SEM image and (d) XRD pattern of titania nanowires after pyrolysis. Reprinted with permission of ACS. **(C)** Synthesis of anatase nanotubes by using PCL-PDMAEMA-POEGMA core-shell-corona CPBs.[113] (a, b) TEM, (c) HR-TEM images and (d) XRD pattern of titania hydrid nanotubes. Reprinted with permission of ACS.

By utilizing well-defined core-shell CPBs with a poly(2-hydroxyethyl methacrylate) (PHEMA) core and a POEGMA shell as templates, Yuan *et al.* successfully prepared water-soluble titania-polymer hybrid nanowires (Figure 1–16B).[179] Herein, the titania precursors $Ti(OC_4H_9)_4$ were doped into the brush core *via* a transalcoholysis reaction. The titania-CPB hybrid nanowires can form pure inorganic titania nanowires by pyrolysis at 550 °C. XRD measurements confirmed the anatase phase in the pure titania nanowires. Furthermore, crystalline anatase hybrid nanotubes were synthesized *via* a similar template-directed approach using core-shell-corona CPBs with a PCL core, a PDMAEMA shell and a POEGMA corona as templates (Figure 1–16C).[113] The weak polyelectrolyte shell complexed an oppositely charged titania precursor, namely titanium(IV) bis(ammonium lactate) dihydroxide (TALH), and then acted as a nanoreactor for the hydrolysis and condensation of TALH, resulting in crystalline TiO_2. The POEGMA shell provides solubility in aqueous and organic solvents. The phase purity of the crystalline nanostructures was verified by powder XRD.

An alternative template-directed strategy to prepare 1D hybrid nanostructures is to construct CPB templates carrying hybridizable building blocks. In such a 'self-templating' route, the fabrication of the CPB template is completed simultaneously with the introduction of the inorganic precursor. Core-shell CPBs with a precursor-containing core of poly(3-acryloylpropyl trimethoxysilane) (PAPTS) and a POEGMA shell were prepared as templates to fabricate organo-silica hybrid nanostructures (Figure 1–17A).[108] A simple hydrolysis and condensation of the trimethoxysilyl moieties yielded a crosslinked silsesquioxane core, forming water-soluble organo-silica hybrid nanowires. They show lyotropic liquid-crystalline behavior and can be pyrolyzed to pure silica nanowires at 700 °C. A further example of this 'self-templating' method is demonstrated by the utilization of core-shell-corona CPBs consisting of a P*t*BA core, a PAPTS shell and a POEGMA corona.[112] Herein, the precursor-containing monomers constructed the shell whose base-catalyzed condensation led to the formation of water-soluble organo-silica hybrid nanotubes (Figure 1–17B).

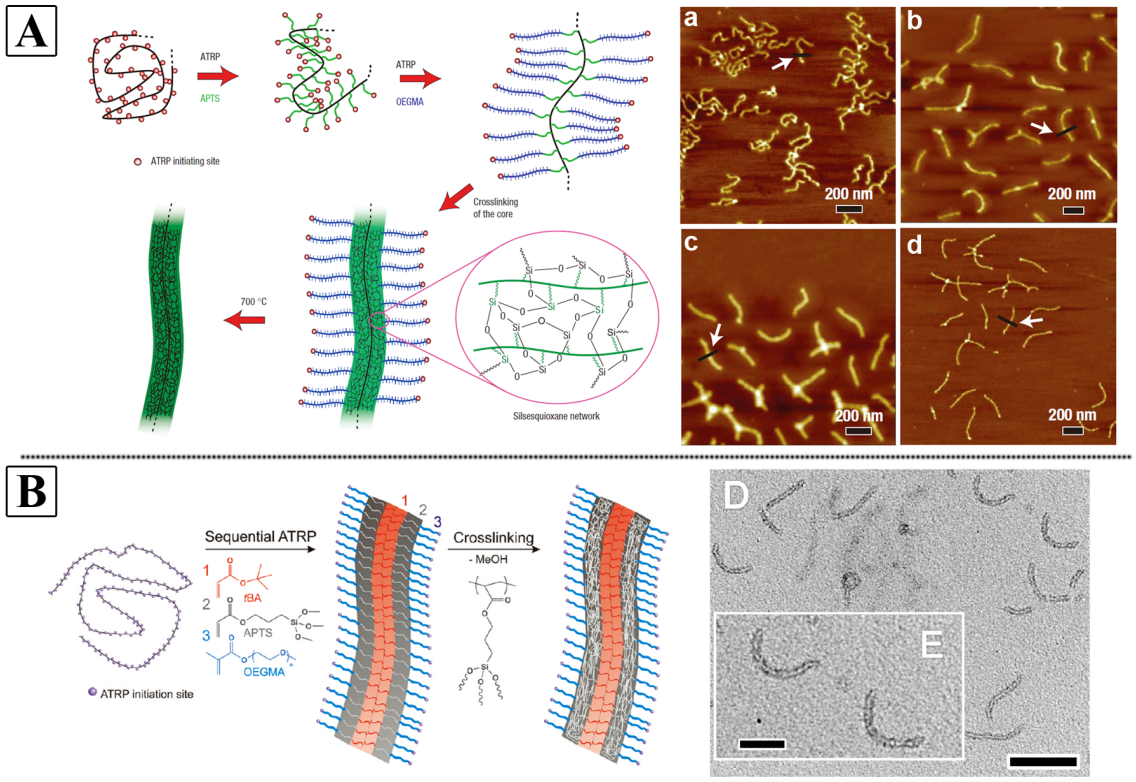

Figure 1-17. (A) 'Self-templated' synthesis of soluble organo-silica and inorganic silica nanowires by using PAPTS-POEGMA core-shell CPBs.[108] AFM images of (a) PAPTS homopolymer brush precursor, (b) PAPTS-POEGMA core-shell CPBs, (c) organo-silica hybrid nanowires, and (d) inorganic silica nanowires. Reprinted with permission of Nature Publishing Group. **(B)** Synthesis of organo-silica hybrid nanotubes *via* P*t*BA-PAPTS-POEGMA core-shell-corona CPBs.[112] Reprinted with permission of ACS.

Besides the classic molecular brushes, brush-like cylinders obtained from self-assemblies of various building blocks, such as surfactants and block copolymers, serve as versatile templates for the preparation of 1D hybrid nanostructures.[181-189] As described in previous sections, block copolymers can self-assemble into nanomorphologies both in bulk and in solution. Figure 1–18A illustrates an example of template-directed preparation of hybrid nanofibers based on self-assembly of block copolymer in bulk.[190] The preparation involved the self-assembly of triblock copolymer PS-*b*-PCEMA-*b*-P*t*BA in thin films into concentric PCEMA and P*t*BA cylinders dispersed in a matrix of PS. The cylindrical structures were then locked by photo-crosslinking the PCEMA shells. Dissolving the films in THF yielded individual nanocyclinders with a PS corona, a PCEMA shell, and a P*t*BA core. Cleaving the *tert*-butyl groups from the P*t*BA segments lead to nanotubes with a PAA lined core, into which Fe^{2+} cations were loaded. A subsequent oxi-

dation yielded solvent-dispersible superparamagnetic Fe_2O_3 hybrid nanofibers. Brush-like cylindrical micelles assembled by block copolymers can also be used as templates. As illustrated in Figure 1–18B, core-shell cylindrical micelles with a PFS core and a P2VP shell were formed by diblock copolymer PFS-*b*-P2VP in a selective solvent.[191] The P2VP shell was then quaternized by iodomethane into a positively charged block. Triblock co-micelles were grown by adding uncharged PFS-*b*-P2VP unimers into the solution of these quaternized cylinders. Subsequently, negatively charged gold nanoparticles or PbS quantum dots were selectively bonded to the positively charged P2VP units of the central block of the triblock co-micelles to afford hybrid nanofibers. Dark-field TEM confirmed the preparation of the micelle-nanoparticles hybrids (Figure 1–18B).

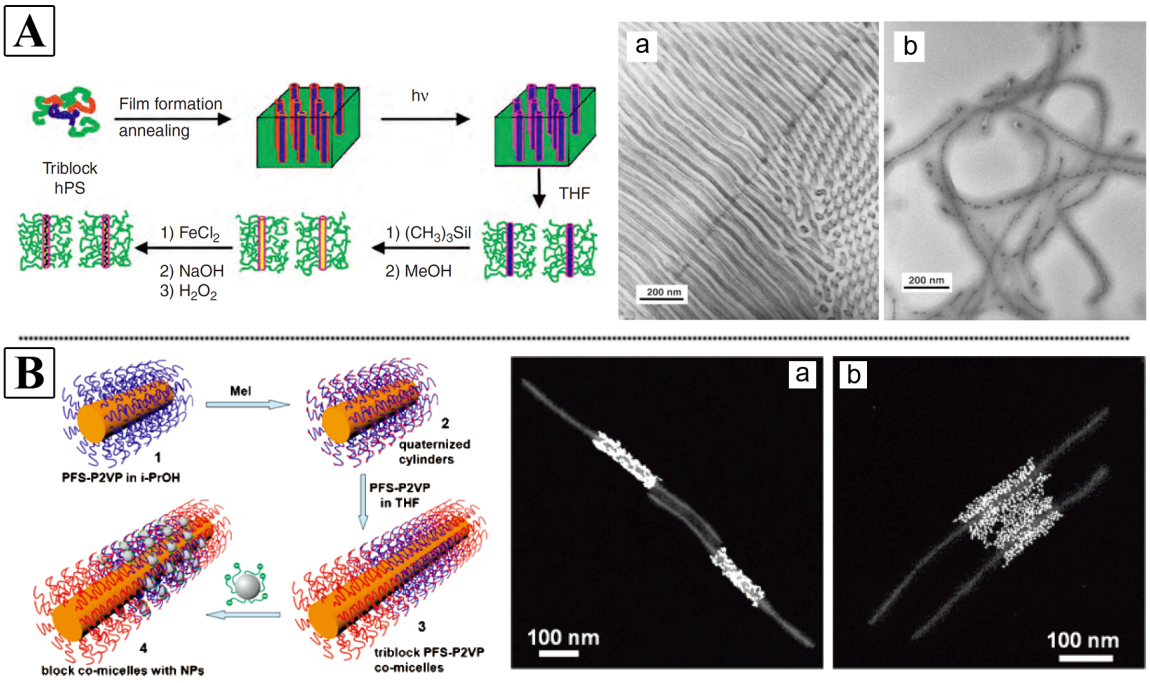

Figure 1-18. (A) Synthesis of γ-Fe_2O_3 magnetic hybrid nanofibers based on self-assembly of PS-*b*-PCMEMA-*b*-PAA triblock terpolymer.[190] TEM images of (a) micro-phase separated bulk morphology and (b) hybrid nanofibers. Reprinted with permission of Wiley-VCH. **(B)** Synthesis of hybrid nanofibers by utilization of core-shell cylindrical micelles with a PFS core and a P2VP shell.[191] Dark-field TEM images of (a) micelle-gold nanoparticles hybrids and (b) micelle-PbS quantum dots hybrids. Reprinted with permission of ACS.

1.4.2 Cylindrical Polymer Brushes as Drug Delivery Vehicles

Recently, various polymeric micelle systems have been developed as delivery vehicles for

drug release or gene transfection in biomedical applications. It is found that the cell entry and the retention in the body circulation depend on the shape of the delivery vehicles.[192] Under fluid flow conditions, 1D cylindrical nanoobjects are taken up by cells less readily and more persistent than spheres because the former are extended by the flow. Therefore, CPBs with intrinsic 1D topology are good candidates as delivery vehicles. Moreover, another advantage of molecular brushes is their multiple functionalities, which ensure a high capacity to load drugs. Johnson *et al.* demonstrated the utilization of branched PEG-*branch*-azide bivalent-brushes as drug delivery vehicles. In the first case, the drugs were loaded by coupling photo-cleavable doxorubicin (DOX)-alkyne derivatives to the azide groups in the core (Figure 1–19A).[34] A UV photolysis of the resulting DOX-loaded materials yielded free DOX that was therapeutically effective against human cancer cells. In the second case, the drugs were loaded onto PEG-based macromonomers prior to the 'grafting-through' process (Figure 1–19B).[193] This ensures a complete loading of the CPBs with drugs, which are released from the materials by exposure to UV-light.

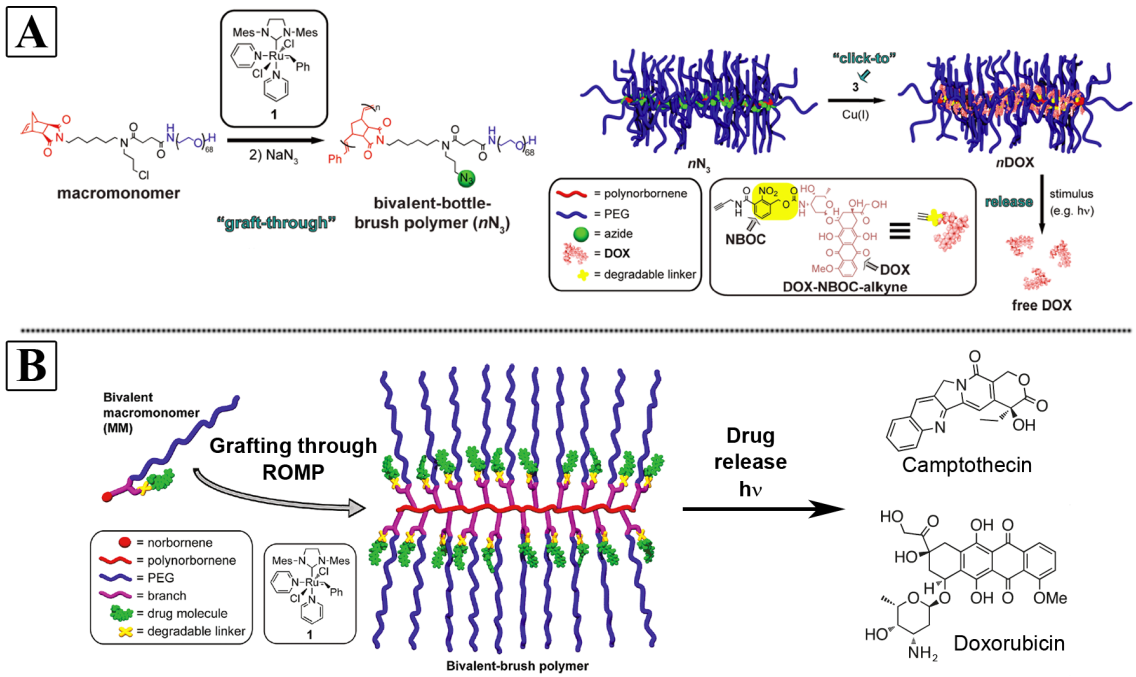

Figure 1-19. CPBs applied as 1D delivery vehicles for drug release. The drugs were loaded **(A)** after or **(B)** before the 'grafting-through' process.[34,193] Reprinted with permission of ACS.

1.4.3 Polymer Brushes Applied to the Investigation of Elementary Reactions

As described in previous sections, polymer brushes can reach a dimension of up to several hundred nanometers, when the lengths of the backbone and the side chains are large enough. Structures on this length scale are feasible to be characterized by various modern microscopy techniques, such as AFM, TEM and SEM. Thereby, molecular brushes can serve as platforms to visualize elementary reactions, which is hardly possible for small molecules or linear polymers. Schappacher *et al.* employed four-arm star-shaped polymer brushes to investigate the initiation efficiency of chloroethyl vinyl ether (CEVE) monomers from acetal groups of 4-branch star backbone precursor *via* controlled cationic polymerization (Figure 1–20).[38] A statistic analysis of the star brush structures in terms of the number of arms and the length of each arm based on the AFM images pointed out that the initiation of CEVE polymerization is not quantitative and that some transfer or termination also takes place during the propagation reaction. As shown by AFM, although the contribution of each of these two side processes is relatively small (less than 10% contribution for each), they already significantly affected the purity of the targeted four-arm star-shaped brushes.

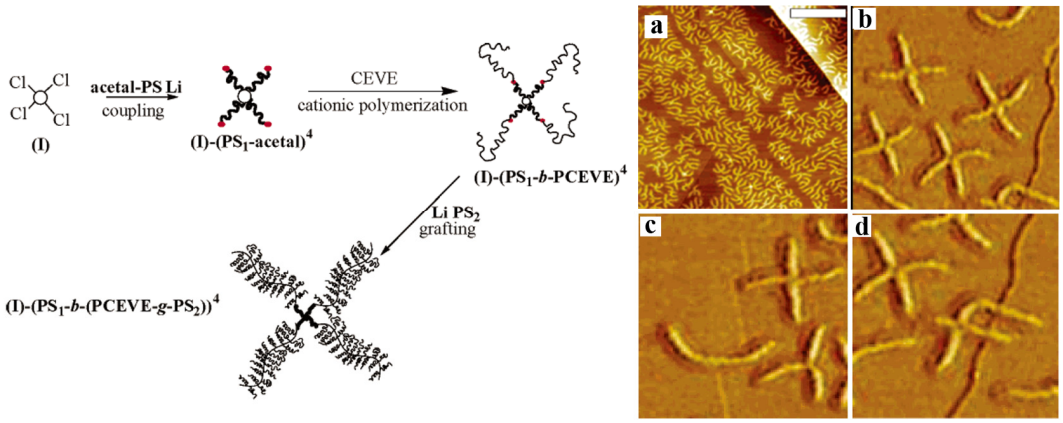

Figure 1-20. Application of four-arm star-shaped brushes as platforms to investigate the initiation efficiency of CEVE monomers from 4-branch star backbone precursor *via* controlled cationic polymerization.[38] Overview AFM image of the star-shaped brushes (a) with scale bar of 300 nm. Zoomed AFM images of regular four-arm stars (b), and stars exhibiting structural defects like (c) three- and two-arm stars, and (d) four-arm star with an aborted arm. Reprinted with permission of ACS.

1.4.4 Advanced Materials from Bulk Morphologies of Cylindrical Polymer Brushes

Further utilizations of bulk morphologies of CPBs as advanced materials have also been reported. One important application is the fabrication of photonic materials from micro-phase-separated bulk morphologies of block-type CPBs.[32,117] These highly ordered morphologies with domain sizes up to 200 nm can interact with visible light and thus show reflection of different colors. Another interesting application is the construction of super-soft elastomers based on crystallization-induced crosslinking of star-shaped polymer brushes.[107,126]

1.5 Aim of the Thesis

The motivation of this thesis was to explore the physicochemical behavior of CPBs on surfaces, to develop new synthetic methods for well-defined CPBs, to design and prepare complex and functional CPBs, and to apply CPBs as templates for the preparation of novel 1D hybrid nanostructures.

Core-shell CPBs consisting of a hydrophilic core block and a polyelectrolyte shell block were to be designed and synthesized for the investigation of their properties on different surfaces. The tunable interactions between the CPBs and the surface can result in unique behavior of the CPBs.

A novel 'grafting-from' approach was to be developed in order to overcome the challenges of synthesizing well-defined CPBs from a linear polymer backbone with a high density of RAFT functionalities. Experimental studies and Monte Carlo simulations should confirm the advantage of the new approach.

Core-shell CPBs with functional components were to be designed and prepared for the construction of light-harvesting nanostructures. It was intended that the formed systems can harvest and transfer light energy within one single macromolecule.

Various well-defined rare-earth metal cations (Ln^{3+}) incorporated silica hybrid nano-

particles (NPs) were to be synthesized *via* a template-directed approach based on core-shell CPBs. The silica hybrid NPs were of great interest, as they can obtain the unique and diverse properties from the incorporated Ln^{3+} ions.

1.6 References

1. Milner, S. T. *Science* **1991,** *251*, 905-914.
2. Zhang, M.; Müller, A. H. E. *J. Polym. Sci. Part A: Polym. Chem.* **2005,** *43*, 3461-3481.
3. Sheiko, S. S.; Sumerlin, B. S.; Matyjaszewski, K. *Prog. Polym. Sci.* **2008,** *33*, 759-785.
4. Yuan, J.; Müller, A. H. E.; Matyjaszewski, K.; Sheiko, S. S., In *Polymer Science: A Comprehensive Reference*, Vol. 6, Müller, A. H. E; Wooley K. L., Eds., Elsevier: Amsterdam, **2012**, pp 199-264.
5. Yuan, J.; Müller, A. H. E. *Polymer* **2010,** *51*, 4015-4036.
6. Won, Y.-Y.; Davis, H. T.; Bates, F. S. *Science* **1999,** *283*, 960-963.
7. Tao, J.; Stewart, S.; Liu, G.; Yang, M. *Macromolecules* **1997,** *30*, 2738-2745.
8. Ishizu, K.; Tsubaki, K.; Mori, A.; Uchida, S. *Prog. Polym. Sci.* **2003,** *28*, 27-54.
9. Liu, G. *Adv. Mater.* **1997,** *9*, 437-439.
10. Liu, G.; Qiao, L.; Guo, A. *Macromolecules* **1996,** *29*, 5508-5510.
11. Liu; Abetz, V.; Müller, A. H. E. *Macromolecules* **2003,** *36*, 7894-7898.
12. Ishizu, K.; Ikemoto, T.; Ichimura, A. *Polymer* **1999,** *40*, 3147-3151.
13. Wang, X.; Guerin, G.; Wang, H.; Wang, Y.; Manners, I.; Winnik, M. A. *Science* **2007,** *317*, 644-647.
14. Gadt, T.; Ieong, N. S.; Cambridge, G.; Winnik, M. A.; Manners, I. *Nat. Mater.* **2009,** *8*, 144-150.
15. Schmalz, H.; Schmelz, J.; Drechsler, M.; Yuan, J.; Walther, A.; Schweimer, K.; Mihut, A. M. *Macromolecules* **2008,** *41*, 3235-3242.
16. Schmelz, J.; Karg, M.; Hellweg, T.; Schmalz, H. *ACS Nano* **2011,** *5*, 9523-9534.
17. Schmelz, J.; Schedl, A. E.; Steinlein, C.; Manners, I.; Schmalz, H. *J. Am. Chem. Soc.* **2012,** *134*, 14217-14225.
18. Tsukahara, Y.; Mizuno, K.; Segawa, A.; Yamashita, Y. *Macromolecules* **1989,** *22*, 1546-1552.
19. Wintermantel, M.; Gerle, M.; Fischer, K.; Schmidt, M.; Wataoka, I.; Urakawa, H.; Kajiwara, K.; Tsukahara, Y. *Macromolecules* **1996,** *29*, 978-983.
20. Vogt, A. P.; Sumerlin, B. S. *Macromolecules* **2006,** *39*, 5286-5292.
21. Nomura, E.; Ito, K.; Kajiwara, A.; Kamachi, M. *Macromolecules* **1997,** *30*, 2811-2817.
22. Ishizu, K.; Toyoda, K.; Furukawa, T.; Sogabe, A. *Macromolecules* **2004,** *37*, 3954-3957.
23. Yamada, K.; Miyazaki, M.; Ohno, K.; Fukuda, T.; Minoda, M. *Macromolecules* **1998,** *32*, 290-293.
24. Ohno, S.; Matyjaszewski, K. *J. Polym. Sci. Part A: Polym. Chem.* **2006,** *44*, 5454-5467.
25. Qin, S.; Matyjaszewski, K.; Xu, H.; Sheiko, S. S. *Macromolecules* **2003,** *36*, 605-612.
26. Pantazis, D.; Chalari, I.; Hadjichristidis, N. *Macromolecules* **2003,** *36*, 3783-3785.
27. Ishizu, K.; Satoh, J. *J. Appl. Polym. Sci.* **2003,** *87*, 1790-1793.
28. Heroguez, V.; Breunig, S.; Gnanou, Y.; Fontanille, M. *Macromolecules* **1996,** *29*, 4459-4464.
29. Cheng, C.; Khoshdel, E.; Wooley, K. L. *Macromolecules* **2007,** *40*, 2289-2292.
30. Breunig, S.; Héroguez, V.; Gnanou, Y.; Fontanille, M. *Macromol. Symp.* **1995,** *95*, 151-166.

31. Mecerreyes, D.; Dahan, D.; Lecomte, P.; Dubois, P.; Demonceau, A.; Noels, A. F.; Jérôme, R. *J. Polym. Sci. Part A: Polym. Chem.* **1999,** *37*, 2447-2455.
32. Xia, Y.; Olsen, B. D.; Kornfield, J. A.; Grubbs, R. H. *J. Am. Chem. Soc.* **2009,** *131*, 18525-18532.
33. Li, Z.; Zhang, K.; Ma, J.; Cheng, C.; Wooley, K. L. *J. Polym. Sci. Part A: Polym. Chem.* **2009,** *47*, 5557-5563.
34. Johnson, J. A.; Lu, Y. Y.; Burts, A. O.; Lim, Y.-H.; Finn, M. G.; Koberstein, J. T.; Turro, N. J.; Tirrell, D. A.; Grubbs, R. H. *J. Am. Chem. Soc.* **2010,** *133*, 559-566.
35. Deffieux, A.; Schappacher, M. *Macromolecules* **1999,** *32*, 1797-1802.
36. Schappacher, M.; Deffieux, A. *Macromol. Chem. Phys.* **1997,** *198*, 3953-3961.
37. Bernard, J.; Schappacher, M.; Ammannati, E.; Kuhn, A.; Deffieux, A. *Macromolecules* **2002,** *35*, 8994-9000.
38. Schappacher, M.; Deffieux, A. *Macromolecules* **2005,** *38*, 4942-4946.
39. Schappacher, M.; Deffieux, A. *Macromolecules* **2005,** *38*, 7209-7213.
40. Lanson, D.; Schappacher, M.; Deffieux, A.; Borsali, R. *Macromolecules* **2006,** *39*, 7107-7114.
41. Lanson, D.; Schappacher, M.; Borsali, R.; Deffieux, A. *Macromolecules* **2007,** *40*, 5559-5565.
42. Lanson, D.; Ariura, F.; Schappacher, M.; Borsali, R.; Deffieux, A. *Macromolecules* **2009,** *42*, 3942-3950.
43. Schappacher, M.; Bernard, J.; Deffieux, A. *Macromol. Chem. Phys.* **2003,** *204*, 762-769.
44. Schappacher, M.; Billaud, C.; Paulo, C.; Deffieux, A. *Macromol. Chem. Phys.* **1999,** *200*, 2377-2386.
45. Pitsikalis, M.; Sioula, S.; Pispas, S.; Hadjichristidis, N.; Cook, D. C.; Li, J.; Mays, J. W. *J. Polym. Sci. Part A: Polym. Chem.* **1999,** *37*, 4337-4350.
46. Hirao, A.; Kawano, H.; Ryu, S. W. *Polym. Adv. Technol.* **2002,** *13*, 275-284.
47. Ryu, S. W.; Hirao, A. *Macromolecules* **2000,** *33*, 4765-4771.
48. Kolb, H. C.; Finn, M. G.; Sharpless, K. B. *Angew. Chem. Int. Ed.* **2001,** *40*, 2004-2021.
49. Rostovtsev, V. V.; Green, L. G.; Fokin, V. V.; Sharpless, K. B. *Angew. Chem. Int. Ed.* **2002,** *41*, 2596-2599.
50. Gao, H.; Matyjaszewski, K. *J. Am. Chem. Soc.* **2007,** *129*, 6633-6639.
51. Engler, A. C.; Lee, H.-i.; Hammond, P. T. *Angew. Chem. Int. Ed.* **2009,** *48*, 9334-9338.
52. Shi, Y.; Zhu, W.; Chen, Y. *Macromolecules* **2013,** *46*, 2391-2398.
53. Zhao, P.; Yan, Y.; Feng, X.; Liu, L.; Wang, C.; Chen, Y. *Polymer* **2012,** *53*, 1992-2000.
54. Jiang, X.; Lok, M. C.; Hennink, W. E. *Bioconjugate Chem.* **2007,** *18*, 2077-2084.
55. Ruokolainen, J.; Torkkeli, M.; Serimaa, R.; Komanschek, E.; ten Brinke, G.; Ikkala, O. *Macromolecules* **1997,** *30*, 2002-2007.
56. de Wit, J.; van Ekenstein, G. A.; Polushkin, E.; Korhonen, J.; Ruokolainen, J.; ten Brinke, G. *Macromolecules* **2009,** *42*, 2009-2014.
57. Valkama, S.; Ruotsalainen, T.; Nykänen, A.; Laiho, A.; Kosonen, H.; ten Brinke, G.; Ikkala, O.; Ruokolainen, J. *Macromolecules* **2006,** *39*, 9327-9336.
58. Tal'roze, R. V.; Kuptsov, S. A.; Sycheva, T. I.; Bezborodov, V. S.; Plate, N. A. *Macromolecules* **1995,**

28, 8689-8691.

59. Huh, J.; Ikkala, O.; ten Brinke, G. *Macromolecules* **1997,** *30*, 1828-1835.
60. Ikkala, O.; Ruokolainen, J.; ten Brinke, G.; Torkkeli, M.; Serimaa, R. *Macromolecules* **1995,** *28*, 7088-7094.
61. Bazuin, C. G.; Tork, A. *Macromolecules* **1995,** *28*, 8877-8880.
62. Ruokolainen, J.; Tanner, J.; ten Brinke, G.; Ikkala, O.; Torkkeli, M.; Serimaa, R. *Macromolecules* **1995,** *28*, 7779-7784.
63. Zhang, M.; Breiner, T.; Mori, H.; Müller, A. H. E. *Polymer* **2003,** *44*, 1449-1458.
64. Mori, H.; Wakisaka, O.; Hirao, A.; Nakahama, S. *Macromol. Chem. Phys.* **1994,** *195*, 3213-3224.
65. Quinn, J. F.; Chaplin, R. P.; Davis, T. P. *J. Polym. Sci. Part A: Polym. Chem.* **2002,** *40*, 2956-2966.
66. Venkatesh, R.; Yajjou, L.; Koning, C. E.; Klumperman, B. *Macromol. Chem. Phys.* **2004,** *205*, 2161-2168.
67. Cheng, G.; Böker, A.; Zhang, M.; Krausch, G.; Müller, A. H. E. *Macromolecules* **2001,** *34*, 6883-6888.
68. Börner, H. G.; Beers, K.; Matyjaszewski, K.; Sheiko, S. S.; Möller, M. *Macromolecules* **2001,** *34*, 4375-4383.
69. Gromadzki, D.; Makuška, R.; Netopilík, M.; Holler, P.; Lokaj, J.; Janata, M.; Štěpánek, P. *Eur. Polym. J.* **2008,** *44*, 59-71.
70. Gromadzki, D.; Filippov, S.; Netopilík, M.; Makuška, R.; Jigounov, A.; Pleštil, J.; Horský, J.; Štěpánek, P. *Eur. Polym. J.* **2009,** *45*, 1748-1758.
71. Guo, S.; Wang, W.; Deng, L.; Xing, J.; Dong, A. *Macromol. Chem. Phys.* **2010,** *211*, 1572-1578.
72. Nomura, K.; Abdellatif, M. M. *Polymer* **2010,** *51*, 1861-1881.
73. Kriegel, R. M.; Rees, W. S.; Weck, M. *Macromolecules* **2004,** *37*, 6644-6649.
74. Beers, K. L.; Gaynor, S. G.; Matyjaszewski, K.; Sheiko, S. S.; Möller, M. *Macromolecules* **1998,** *31*, 9413-9415.
75. Börner, H. G.; Matyjaszewski, K. *Macromol. Symp.* **2002,** *177*, 1-16.
76. Börner, H. G.; Duran, D.; Matyjaszewski, K.; da Silva, M.; Sheiko, S. S. *Macromolecules* **2002,** *35*, 3387-3394.
77. Lee, H.-i.; Matyjaszewski, K.; Yu, S.; Sheiko, S. S. *Macromolecules* **2005,** *38*, 8264-8271.
78. Nese, A.; Kwak, Y.; Nicolaÿ, R.; Barrett, M.; Sheiko, S. S.; Matyjaszewski, K. *Macromolecules* **2010,** *43*, 4016-4019.
79. Nese, A.; Li, Y.; Averick, S.; Kwak, Y.; Konkolewicz, D.; Sheiko, S. S.; Matyjaszewski, K. *ACS Macro Lett.* **2011,** *1*, 227-231.
80. Bernard, J.; Favier, A.; Davis, T. P.; Barner-Kowollik, C.; Stenzel, M. H. *Polymer* **2006,** *47*, 1073-1080.
81. Zehm, D.; Laschewsky, A.; Gradzielski, M.; Prévost, S.; Liang, H.; Rabe, J. P.; Schweins, R.; Gummel, J. *Langmuir* **2009,** *26*, 3145-3155.
82. Cheng, C.; Qi, K.; Khoshdel, E.; Wooley, K. L. *J. Am. Chem. Soc.* **2006,** *128*, 6808-6809.
83. Fan, X.; Wang, G.; Zhang, Z.; Huang, J. *J. Polym. Sci. Part A: Polym. Chem.* **2011,** *49*, 4146-4153.

84. Lee, H.-i.; Jakubowski, W.; Matyjaszewski, K.; Yu, S.; Sheiko, S. S. *Macromolecules* **2006,** *39*, 4983-4989.
85. Zhang, N.; Steenackers, M.; Luxenhofer, R.; Jordan, R. *Macromolecules* **2009,** *42*, 5345-5351.
86. Zhang, N.; Huber, S.; Schulz, A.; Luxenhofer, R.; Jordan, R. *Macromolecules* **2009,** *42*, 2215-2221.
87. Huang, K.; Rzayev, J. *J. Am. Chem. Soc.* **2009,** *131*, 6880-6885.
88. Huang, K.; Canterbury, D. P.; Rzayev, J. *Chem. Commun.* **2010,** *46*, 6326-6328.
89. Liu, G.; Li, Z.; Yan, X. *Polymer* **2003,** *44*, 7721-7727.
90. Liu, G. *Macromol. Symp.* **1997,** *113*, 233-248.
91. Yelamanchili, R. S.; Walther, A.; Müller, A. H. E.; Breu, J. *Chem. Commun.* **2008,** *0*, 489-491.
92. Du, J.-Z.; Chen, D.-P.; Wang, Y.-C.; Xiao, C.-S.; Lu, Y.-J.; Wang, J.; Zhang, G.-Z. *Biomacromolecules* **2006,** *7*, 1898-1903.
93. Khelfallah, N.; Gunari, N.; Fischer, K.; Gkogkas, G.; Hadjichristidis, N.; Schmidt, M. *Macromol. Rapid Commun.* **2005,** *26*, 1693-1697.
94. Neugebauer, D.; Zhang, Y.; Pakula, T.; Sheiko, S. S.; Matyjaszewski, K. *Macromolecules* **2003,** *36*, 6746-6755.
95. He, L.; Huang, J.; Chen, Y.; Xu, X.; Liu, L. *Macromolecules* **2005,** *38*, 3845-3851.
96. Xu, Y.; Becker, H.; Yuan, J.; Burkhardt, M.; Zhang, Y.; Walther, A.; Bolisetty, S.; Ballauff, M.; Müller, A. H. E. *Macromol. Chem. Phys.* **2007,** *208*, 1666-1675.
97. Schlüter, A. D.; Rabe, J. P. *Angew. Chem. Int. Ed.* **2000,** *39*, 864-883.
98. Zhang, B.; Wepf, R.; Fischer, K.; Schmidt, M.; Besse, S.; Lindner, P.; King, B. T.; Sigel, R.; Schurtenberger, P.; Talmon, Y.; Ding, Y.; Kröger, M.; Halperin, A.; Schlüter, A. D. *Angew. Chem. Int. Ed.* **2011,** *50*, 737-740.
99. Guo, Y.; van Beek, J. D.; Zhang, B.; Colussi, M.; Walde, P.; Zhang, A.; Kröger, M.; Halperin, A.; Dieter Schlüter, A. *J. Am. Chem. Soc.* **2009,** *131*, 11841-11854.
100. Ouali, N.; Méry, S.; Skoulios, A.; Noirez, L. *Macromolecules* **2000,** *33*, 6185-6193.
101. Zhang, A.; Shu, L.; Bo, Z.; Schlüter, A. D. *Macromol. Chem. Phys.* **2003,** *204*, 328-339.
102. Djalali, R.; Hugenberg, N.; Fischer, K.; Schmidt, M. *Macromol. Rapid Commun.* **1999,** *20*, 444-449.
103. Ishizu, K.; Tsubaki, K.-i.; Ono, T. *Polymer* **1998,** *39*, 2935-2939.
104. Tsubaki, K.; Ishizu, K. *Polymer* **2001,** *42*, 8387-8393.
105. Dziezok, P.; Fischer, K.; Schmidt, M.; Sheiko, S. S.; Möller, M. *Angew. Chem. Int. Ed.* **1997,** *36*, 2812-2815.
106. Ishizu, K.; Kakinuma, H. *J. Polym. Sci. Part A: Polym. Chem.* **2005,** *43*, 63-70.
107. Pakula, T.; Zhang, Y.; Matyjaszewski, K.; Lee, H.-i.; Boerner, H.; Qin, S.; Berry, G. C. *Polymer* **2006,** *47*, 7198-7206.
108. Yuan, J.; Xu, Y.; Walther, A.; Bolisetty, S.; Schumacher, M.; Schmalz, H.; Ballauff, M.; Müller, A. H. E. *Nat. Mater.* **2008,** *7*, 718-722.
109. Tang, H.; Li, Y.; Lahasky, S. H.; Sheiko, S. S.; Zhang, D. *Macromolecules* **2011,** *44*, 1491-1499.
110. Müllner, M.; Lunkenbein, T.; Breu, J.; Caruso, F.; Müller, A. H. E. *Chem. Mater.* **2012,** *24*, 1802-1810.

111. Tang, C.; Dufour, B.; Kowalewski, T.; Matyjaszewski, K. *Macromolecules* **2007,** *40*, 6199-6205.
112. Müllner, M.; Yuan, J.; Weiss, S.; Walther, A.; Förtsch, M.; Drechsler, M.; Müller, A. H. E. *J. Am. Chem. Soc.* **2010,** *132*, 16587-16592.
113. Müllner, M.; Lunkenbein, T.; Schieder, M.; Gröschel, A. H.; Miyajima, N.; Förtsch, M.; Breu, J.; Caruso, F.; Müller, A. H. E. *Macromolecules* **2012,** *45*, 6981-6988.
114. Ishizu, K.; Satoh, J.; Sogabe, A. *J. Colloid Interface Sci.* **2004,** *274*, 472-479.
115. Wu, D.; Zhao, C.; Tian, J.; Zhao, H. *Polym. Int.* **2009,** *58*, 1335-1340.
116. Lee, H.-i.; Matyjaszewski, K.; Yu-Su, S.; Sheiko, S. S. *Macromolecules* **2008,** *41*, 6073-6080.
117. Rzayev, J. *Macromolecules* **2009,** *42*, 2135-2141.
118. Bolton, J.; Rzayev, J. *ACS Macro Lett.* **2011,** *1*, 15-18.
119. Li, Z.; Ma, J.; Cheng, C.; Zhang, K.; Wooley, K. L. *Macromolecules* **2010,** *43*, 1182-1184.
120. Walther, A.; Drechsler, M.; Rosenfeldt, S.; Harnau, L.; Ballauff, M.; Abetz, V.; Müller, A. H. E. *J. Am. Chem. Soc.* **2009,** *131*, 4720-4728.
121. Wolf, A.; Walther, A.; Müller, A. H. E. *Macromolecules* **2011,** *44*, 9221-9229.
122. Stephan, T.; Muth, S.; Schmidt, M. *Macromolecules* **2002,** *35*, 9857-9860.
123. Ishizu, K.; Sawada, N.; Satoh, J.; Sogabe, A. *J. Mater. Sci. Lett.* **2003,** *22*, 1219-1222.
124. Hans, M.; Keul, H.; Heise, A.; Moeller, M. *Macromolecules* **2007,** *40*, 8872-8880.
125. Hans, M.; Xiao, Y.; Keul, H.; Heise, A.; Moeller, M. *Macromol. Chem. Phys.* **2009,** *210*, 736-746.
126. Neugebauer, D.; Theis, M.; Pakula, T.; Wegner, G.; Matyjaszewski, K. *Macromolecules* **2005,** *39*, 584-593.
127. Neugebauer, D. *Polymer* **2007,** *48*, 4966-4973.
128. Schappacher, M.; Deffieux, A. *Macromolecules* **2000,** *33*, 7371-7377.
129. Matyjaszewski, K.; Qin, S.; Boyce, J. R.; Shirvanyants, D.; Sheiko, S. S. *Macromolecules* **2003,** *36*, 1843-1849.
130. Schappacher, M.; Deffieux, A. *Science* **2008,** *319*, 1512-1515.
131. Lahasky, S. H.; Serem, W. K.; Guo, L.; Garno, J. C.; Zhang, D. *Macromolecules* **2011,** *44*, 9063-9074.
132. Uhrig, D.; Mays, J. W. *Macromolecules* **2002,** *35*, 7182-7190.
133. Sheiko, S. S.; da Silva, M.; Shirvaniants, D.; LaRue, I.; Prokhorova, S.; Moeller, M.; Beers, K.; Matyjaszewski, K. *J. Am. Chem. Soc.* **2003,** *125*, 6725-6728.
134. Gunari, N.; Schmidt, M.; Janshoff, A. *Macromolecules* **2006,** *39*, 2219-2224.
135. Subbotin, A.; Saariaho, M.; Stepanyan, R.; Ikkala, O.; ten Brinke, G. *Macromolecules* **2000,** *33*, 6168-6173.
136. Terao, K.; Farmer, B. S.; Nakamura, Y.; Iatrou, H.; Hong, K.; Mays, J. W. *Macromolecules* **2005,** *38*, 1447-1450.
137. Subbotin, A.; Saariaho, M.; Ikkala, O.; ten Brinke, G. *Macromolecules* **2000,** *33*, 3447-3452.
138. Feuz, L.; Leermakers, F. A. M.; Textor, M.; Borisov, O. *Macromolecules* **2005,** *38*, 8891-8901.
139. Rouault, Y.; Borisov, O. V. *Macromolecules* **1996,** *29*, 2605-2611.
140. Saariaho, M.; Subbotin, A.; Szleifer, I.; Ikkala, O.; ten Brinke, G. *Macromolecules* **1999,** *32*,

4439-4443.

141. Theodorakis, P. E.; Paul, W.; Binder, K. *Macromolecules* **2010,** *43*, 5137-5148.
142. Gerle, M.; Fischer, K.; Roos, S.; Müller, A. H. E.; Schmidt, M.; Sheiko, S. S.; Prokhorova, S.; Möller, M. *Macromolecules* **1999,** *32*, 2629-2637.
143. Terao, K.; Nakamura, Y.; Norisuye, T. *Macromolecules* **1999,** *32*, 711-716.
144. Lecommandoux, S.; Chécot, F.; Borsali, R.; Schappacher, M.; Deffieux, A.; Brûlet, A.; Cotton, J. P. *Macromolecules* **2002,** *35*, 8878-8881.
145. Müllner, M. *Bayreuth, Univ., Diss.* **2012**.
146. Saariaho, M.; Ikkala, O.; Szleifer, I.; Erukhimovich, I.; ten Brinke, G. *J. Chem. Phys.* **1997,** *107*, 3267-3276.
147. Zhang, B.; Gröhn, F.; Pedersen, J. S.; Fischer, K.; Schmidt, M. *Macromolecules* **2006,** *39*, 8440-8450.
148. van der Schoot, P. *J. Chem. Phys.* **1996,** *104*, 1130-1139.
149. Polotsky, A.; Charlaganov, M.; Xu, Y.; Leermakers, F. A. M.; Daoud, M.; Müller, A. H. E.; Dotera, T.; Borisov, O. *Macromolecules* **2008,** *41*, 4020-4028.
150. Djalali, R.; Li, S.-Y.; Schmidt, M. *Macromolecules* **2002,** *35*, 4282-4288.
151. Panyukov, S.; Zhulina, E. B.; Sheiko, S. S.; Randall, G. C.; Brock, J.; Rubinstein, M. *J. Phys. Chem. B* **2009,** *113*, 3750-3768.
152. Zhang, M.; Drechsler, M.; Müller, A. H. E. *Chem. Mater.* **2004,** *16*, 537-543.
153. Yamamoto, S.-i.; Pietrasik, J.; Matyjaszewski, K. *Macromolecules* **2007,** *40*, 9348-9353.
154. Li, C.; Gunari, N.; Fischer, K.; Janshoff, A.; Schmidt, M. *Angew. Chem. Int. Ed.* **2004,** *43*, 1101-1104.
155. Pietrasik, J.; Sumerlin, B. S.; Lee, R. Y.; Matyjaszewski, K. *Macromol. Chem. Phys.* **2007,** *208*, 30-36.
156. Xu, Y.; Bolisetty, S.; Drechsler, M.; Fang, B.; Yuan, J.; Ballauff, M.; Müller, A. H. E. *Polymer* **2008,** *49*, 3957-3964.
157. Wang, M.; Zou, S.; Guerin, G.; Shen, L.; Deng, K.; Jones, M.; Walker, G. C.; Scholes, G. D.; Winnik, M. A. *Macromolecules* **2008,** *41*, 6993-7002.
158. Lee, H.-i.; Boyce, J. R.; Nese, A.; Sheiko, S. S.; Matyjaszewski, K. *Polymer* **2008,** *49*, 5490-5496.
159. Xu, Y.; Bolisetty, S.; Drechsler, M.; Fang, B.; Yuan, J.; Harnau, L.; Ballauff, M.; Müller, A. H. E. *Soft Matter* **2009,** *5*, 379-384.
160. Xu, Y.; Bolisetty, S.; Ballauff, M.; Müller, A. H. E. *J. Am. Chem. Soc.* **2009,** *131*, 1640-1641.
161. Xu, Y.; Borisov, O. V.; Ballauff, M.; Müller, A. H. E. *Langmuir* **2010,** *26*, 6919-6926.
162. Lord, S. J.; Sheiko, S. S.; LaRue, I.; Lee, H.-I.; Matyjaszewski, K. *Macromolecules* **2004,** *37*, 4235-4240.
163. Potemkin, I. I.; Khokhlov, A. R.; Prokhorova, S.; Sheiko, S. S.; Möller, M.; Beers, K. L.; Matyjaszewski, K. *Macromolecules* **2004,** *37*, 3918-3923.
164. Lee, H.-i.; Pietrasik, J.; Matyjaszewski, K. *Macromolecules* **2006,** *39*, 3914-3920.
165. Zhang, Y.; Costantini, N.; Mierzwa, M.; Pakula, T.; Neugebauer, D.; Matyjaszewski, K. *Polymer* **2004,** *45*, 6333-6339.
166. Bolton, J.; Bailey, T. S.; Rzayev, J. *Nano Lett.* **2011,** *11*, 998-1001.

167. Han, W.; Byun, M.; Zhao, L.; Rzayev, J.; Lin, Z. *J. Mater. Chem.* **2011,** *21*, 14248-14253.
168. Yu-Su, S. Y.; Sheiko, S. S.; Lee, H.-i.; Jakubowski, W.; Nese, A.; Matyjaszewski, K.; Anokhin, D.; Ivanov, D. A. *Macromolecules* **2009,** *42*, 9008-9017.
169. Sun, F.; Sheiko, S. S.; Möller, M.; Beers, K.; Matyjaszewski, K. *J. Phys. Chem. A* **2004,** *108*, 9682-9686.
170. Sheiko, S. S.; Prokhorova, S. A.; Beers, K. L.; Matyjaszewski, K.; Potemkin, I. I.; Khokhlov, A. R.; Möller, M. *Macromolecules* **2001,** *34*, 8354-8360.
171. Xu, H.; Sheiko, S. S.; Shirvanyants, D.; Rubinstein, M.; Beers, K. L.; Matyjaszewski, K. *Langmuir* **2005,** *22*, 1254-1259.
172. Xu, H.; Shirvanyants, D.; Beers, K.; Matyjaszewski, K.; Rubinstein, M.; Sheiko, S. S. *Phys. Rev. Lett.* **2004,** *93*, 206103.
173. Xu, H.; Sun, F. C.; Shirvanyants, D. G.; Rubinstein, M.; Shabratov, D.; Beers, K. L.; Matyjaszewski, K.; Sheiko, S. S. *Adv. Mater.* **2007,** *19*, 2930-2934.
174. Sheiko, S. S.; Sun, F. C.; Randall, A.; Shirvanyants, D.; Rubinstein, M.; Lee, H.-i.; Matyjaszewski, K. *Nature* **2006,** *440*, 191-194.
175. Boyce, J. R.; Shirvanyants, D.; Sheiko, S. S.; Ivanov, D. A.; Qin, S.; Börner, H.; Matyjaszewski, K. *Langmuir* **2004,** *20*, 6005-6011.
176. Yuan, J.; Drechsler, M.; Xu, Y.; Zhang, M.; Müller, A. H. E. *Polymer* **2008,** *49*, 1547-1554.
177. Zhang, M.; Estournès, C.; Bietsch, W.; Müller, A. H. E. *Adv. Funct. Mater.* **2004,** *14*, 871-882.
178. Xu, Y.; Yuan, J.; Fang, B.; Drechsler, M.; Müllner, M.; Bolisetty, S.; Ballauff, M.; Müller, A. H. E. *Adv. Funct. Mater.* **2010,** *20*, 4182-4189.
179. Yuan, J.; Lu, Y.; Schacher, F.; Lunkenbein, T.; Weiss, S.; Schmalz, H.; Müller, A. H. E. *Chem. Mater.* **2009,** *21*, 4146-4154.
180. Yuan, J.; Schacher, F.; Drechsler, M.; Hanisch, A.; Lu, Y.; Ballauff, M.; Müller, A. H. E. *Chem. Mater.* **2010,** *22*, 2626-2634.
181. Jana, N. R.; Gearheart, L.; Murphy, C. J. *Adv. Mater.* **2001,** *13*, 1389-1393.
182. Murphy, C. J.; Jana, N. R. *Adv. Mater.* **2002,** *14*, 80-82.
183. Kijima, T.; Yoshimura, T.; Uota, M.; Ikeda, T.; Fujikawa, D.; Mouri, S.; Uoyama, S. *Angew. Chem. Int. Ed.* **2004,** *43*, 228-232.
184. Gao, C.; Lu, Z.; Yin, Y. *Langmuir* **2011,** *27*, 12201-12208.
185. Duxin, N.; Liu, F.; Vali, H.; Eisenberg, A. *J. Am. Chem. Soc.* **2005,** *127*, 10063-10069.
186. Wang, H.; Patil, A. J.; Liu, K.; Petrov, S.; Mann, S.; Winnik, M. A.; Manners, I. *Adv. Mater.* **2009,** *21*, 1805-1808.
187. Zhang, K.; Gao, L.; Chen, Y. *Macromolecules* **2008,** *41*, 1800-1807.
188. Zhang, K.; Gao, L.; Chen, Y. *Macromolecules* **2007,** *40*, 5916-5922.
189. Walther, A.; Yuan, J.; Abetz, V.; Müller, A. H. E. *Nano Lett.* **2009,** *9*, 2026-2030.
190. Yan, X.; Liu, G.; Liu, F.; Tang, B. Z.; Peng, H.; Pakhomov, A. B.; Wong, C. Y. *Angew. Chem. Int. Ed.* **2001,** *40*, 3593-3596.

191. Wang, H.; Lin, W.; Fritz, K. P.; Scholes, G. D.; Winnik, M. A.; Manners, I. *J. Am. Chem. Soc.* **2007,** *129*, 12924-12925.

192. Geng, Y.; Dalhaimer, P.; Cai, S.; Tsai, R.; Tewari, M.; Minko, T.; Discher, D. E. *Nat. Nano.* **2007,** *2*, 249-255.

193. Johnson, J. A.; Lu, Y. Y.; Burts, A. O.; Xia, Y.; Durrell, A. C.; Tirrell, D. A.; Grubbs, R. H. *Macromolecules* **2010,** *43*, 10326-10335.

Chapter 2

Overview of the Thesis

This thesis consists of six chapters including four publications, which are presented in Chapters 3 to 6.

The common theme that connects the individual chapters of this thesis is the unique highly branched architecture of cylindrical polymer brushes (CPBs). My research efforts have focused on (i) investigating the scission behavior of polyelectrolyte CPBs on different surfaces, (ii) developing novel synthetic pathways for well-defined CPBs *via* RAFT polymerization, (iii) the design and preparation of complex and functional CPBs for light-harvesting and energy transfer, and (iv) the application of CPBs as templates for the synthesis of novel 1D organic/inorganic hybrid nanostructures.

The polymer backbone of core-shell CPBs can be ruptured upon drying on solid surfaces, when sufficient Coulombic interactions between the shell block and the surface are formed (**Chapter 3**). A facile "CTA-shuttled" R-group approach overcomes the entrapment of active free radicals within individual growing CPBs, resulting in well-defined CPBs with narrow molecular weight distribution (**Chapter 4**). Single-molecular rod-like nano-light harvesters (NLH) on the basis of CPBs were fabricated by tethering block copolymer side chains carrying light absorbing antennae groups (energy donors) to a linear polymer backbone containing emitting groups (energy acceptors). These NLHs provide very efficient energy absorption and tunable energy transfer from antennae to energy acceptors (**Chapter 5**). Core-shell CPBs provide excellent templates for the preparation of various rare-earth metal cations (Ln^{3+}) incorporated silica hybrid nanoparticles which obtain unique and diverse properties from the incorporated Ln^{3+} ions (**Chapter 6**).

In the following, an overview of the main results detailed in this thesis is presented.

2.1 Scission Behavior of Polymer Brushes

The carbon-carbon covalent bond with bond energy of 348 kJ mol^{-1} is difficult to be challenged, except under some extreme conditions, such as ultrasonic field and single molecular stretching. Yet, in this chapter we work out a strategy to teach hundreds and thousands of intermolecular attractions to directly combat carbon-carbon covalent bonds under ambient conditions by employing core-shell CPBs.

Poly[2-(2-bromoisobutyryloxy)ethyl methacrylate] (PBIEM) with a number-average degree of polymerization (DP_n) of 1500 was used as polyinitiator backbone to grow side chains *via* the 'grafting from' approach. As illustrated in Scheme 2–1, three different CPBs were synthesized, carrying side chains of poly[oligo(ethylene glycol) methacrylate] (POEGMA), POEGMA-*block*-poly[2-(dimethylamino)ethyl methacrylate] (POEGMA-*b*-PDMAEMA) and POEGMA-*block*-poly[2-(methacryloyloxy)ethyl trimethylammonium iodide] (POEGMA-*b*-PMETAI), respectively.

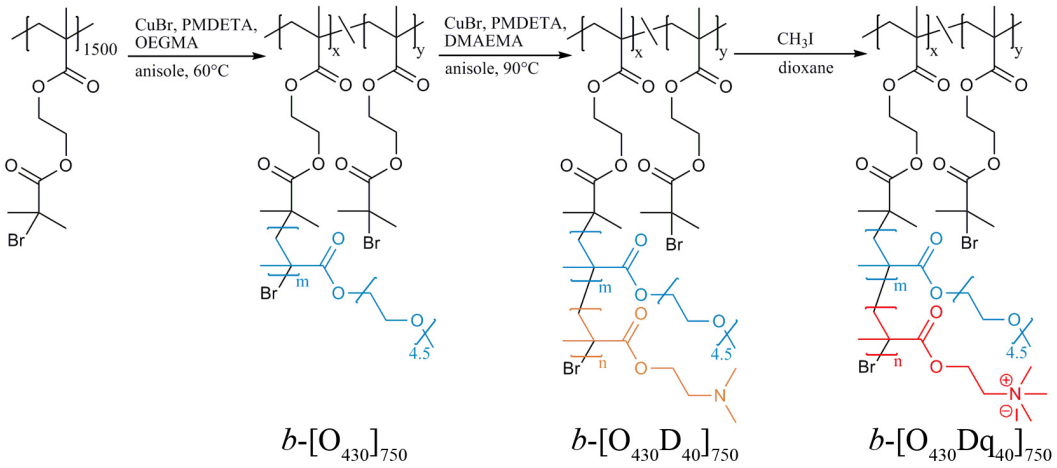

Scheme 2-1. Synthetic route to homopolymer CPB *b*-$[O_{430}]_{750}$, core-shell CPB *b*-$[O_{430}D_{40}]_{750}$ and *b*-$[O_{430}Dq_{40}]_{750}$. Reprinted with permission of ACS.

An atomic force microscopy (AFM) investigation of the CPBs on mica shows that the backbone of the core-shell CPB with POEGMA-*b*-PDMAEMA or POEGMA-*b*-PMETAI branches can be ruptured upon spin-coating (Figures 2–1 B and C), while the homopolymer CPB with POEGMA side chains stays stable (Figure 2–1A). The

ruptured CPB shows a non-continuous conformation with several small beads with a width of *ca.* 45 nm in the core part. The cross-sectional analysis shows obvious gaps (up to 30 nm in width) between two adjacent beads, as shown in Figure 2–1D.

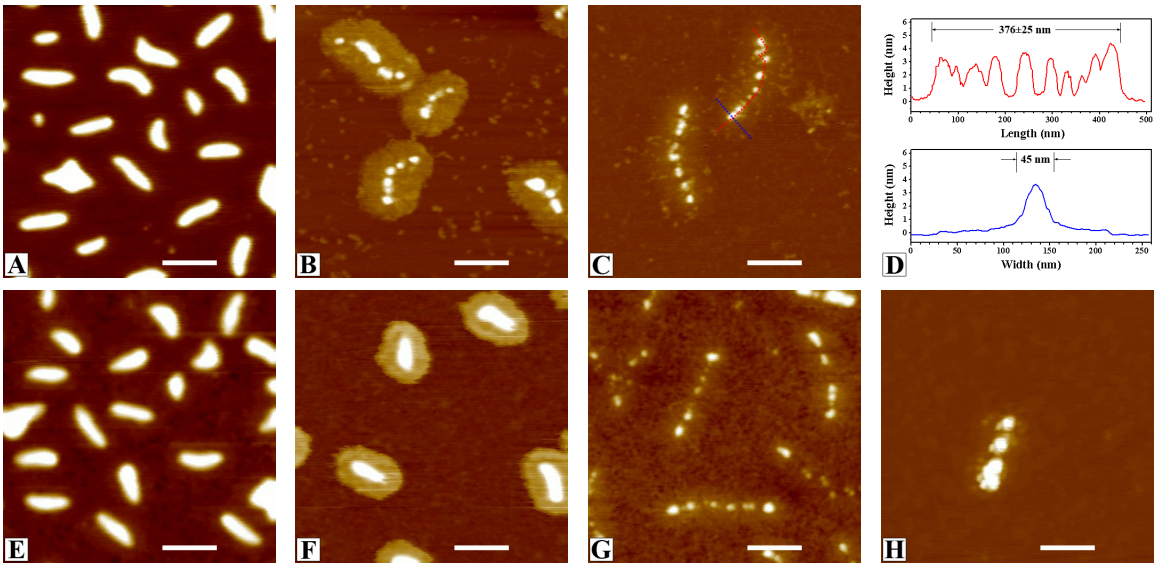

Figure 2-1. Tapping-mode AFM height image of CPBs: *b*-$[O_{430}]_{750}$ on mica (A) and on silicon (E), *b*-$[O_{430}D_{40}]_{750}$ on mica (B) and on silicon (F), as well as *b*-$[O_{430}Dq_{40}]_{750}$ on mica (C) and on silicon (G). (D) shows the corresponding height cross-section analysis of the marked CPB in (C). (H) demonstrates the CPB *b*-$[O_{430}Dq_{40}]_{750}$ containing 7.8 μM of $K_3[Co(CN)_6]$. All CPBs were spin-coated onto surfaces from 0.02 g L^{-1} aqueous solution (pH 5.5). Z-range is 8 nm. The scale bars correspond to 200 nm. Reprinted with permission of ACS.

A mechanism of this scission behavior is proposed and illustrated in Figure 2–2. Upon the instant contact of the CPB with the mica surface during spin-coating, a large number of functional groups in the outside shell layer anchor onto the charged solid surface, producing Coulombic interactions between the shell and the surface. This combined interaction is stronger than one or more carbon-carbon single bonds. Subsequently, as the inner core part contracts by drying, serving as a fast responsive driving force, the carbon-carbon covalent bonds in the backbone are ruptured.

This scission behavior is successfully controlled by tuning the surface interactions through switching the surface nature (Figures 2–1 F and G), varying pH, or adding multivalent counterions (Figure 2–1H). This study demonstrates that core-shell CPB serves as a template to directly compare the weak intermolecular forces with the strong carbon-carbon covalent bonds.

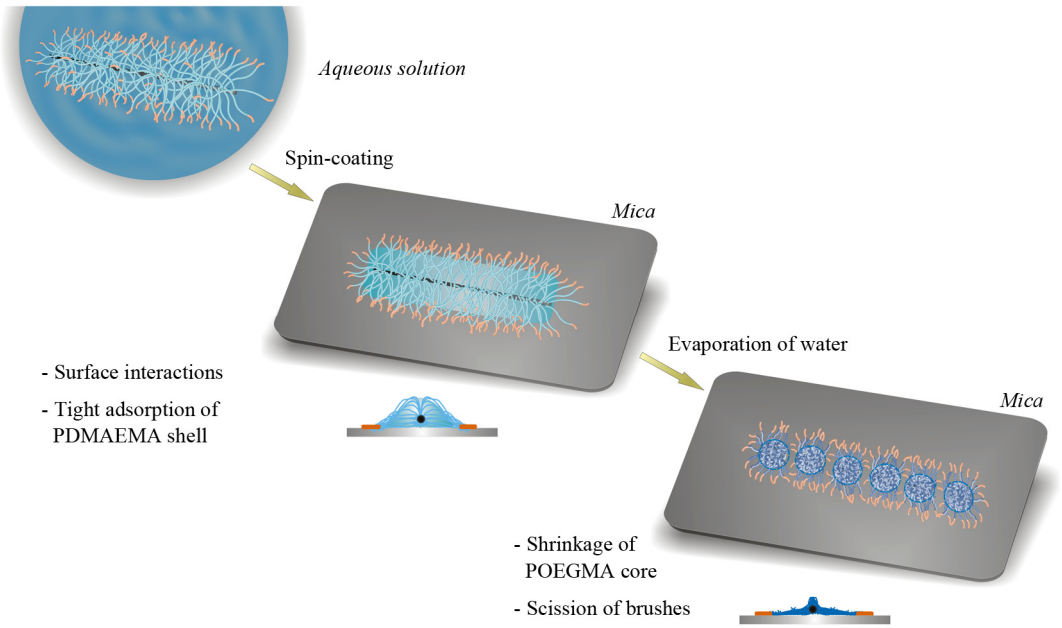

Figure 2-2. Illustration of scission behavior of the core-shell CPB *b*-$[O_{430}D_{40}]_{750}$ on mica surface. Reprinted with permission of ACS.

2.2 "CTA-shuttled" Grafting-from Approach

Well-defined complex polymer architectures, such as star polymers, comb polymers and cylindrical polymer brushes (CPBs), have received much attention in the polymer synthesis research. Controlled free-radical polymerization (CRP), such as atom transfer radical polymerization (ATRP) and reversible addition-fragmentation chain transfer (RAFT) polymerization, is most frequently applied for synthesizing CPBs and star polymers. However, the R-group 'grafting from' approach *via* RAFT is inferior in controlling the grafting of side chains from a densely functionalized backbone, poly(chain transfer agent) (polyCTA), except for few examples of rapidly propagating monomers, as the resulting CPBs showed multimodal molecular weight distribution (MWD).

So far, the unsuitability of the conventional R-group approach for the synthesis of well-defined CPBs has only been explained to be induced by the brush-brush coupling during the grafting polymerization. In this chapter, another reason for the broad MWD of the CPBs is proposed, which is the hindered transfer of the active radicals from one growing CPB to other CPBs. In a typical RAFT process, an addition-fragmentation equilibrium between the active propagating radical and the dormant radical intermediate ensures an equal growing probability of all polymer chains and thus a narrow MWD. In the case of grafting polymer branches from highly densely functionalized linear polyCTA, the transfer of an active radical on a CPB to a CTA on another CPB (intermolecular transfer) is critically limited (Scheme 2–2B). This is attributed to the densely branched architecture of CPBs, as the active radicals are trapped within individual CPBs. Thus, the CPBs carrying more active radicals grow faster, leading to a broad MWD of the CPBs (high polydispersity index, PDI).

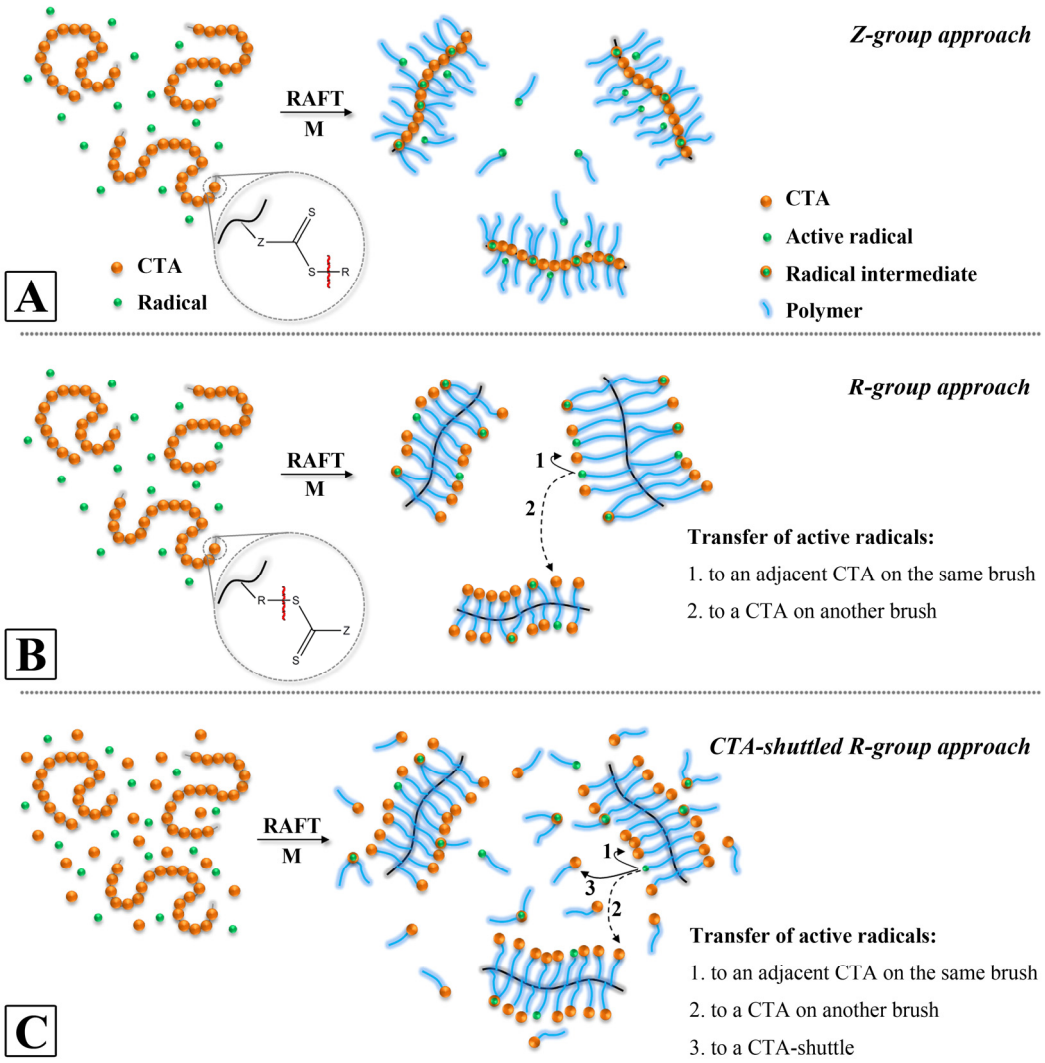

Scheme 2-2. Proposed mechanism of the Z-group approach (A), the conventional R-group approach (B) and the "CTA-shuttled" R-group approach (C). Reprinted with permission of Wiely-VCH.

A facile "CTA-shuttled" R-group approach is developed to overcome the entrapment effect. A certain amount of added low-molecular-weight CTA (LMW-CTA) into the polymerization system (Scheme 2–2C) can serve as "shuttles" for active radicals among different propagating CPBs. In this "CTA-shuttled" R-group approach, active radicals on the CPBs now have one highly possible transfer pathway, as they can add to a nearby CTA-shuttle to form a brush-shuttle radical intermediate (Scheme 2–2C), which can fragment into a dormant CTA on the CPB and a linear polymer carrying an active radical. This linear polymeric radical can transfer further to a surrounding CTA-shuttle or a CPB, resulting in an efficient transfer of the active radicals among different CPBs and thus a homogeneous propagation of the CPBs with a narrow MWD.

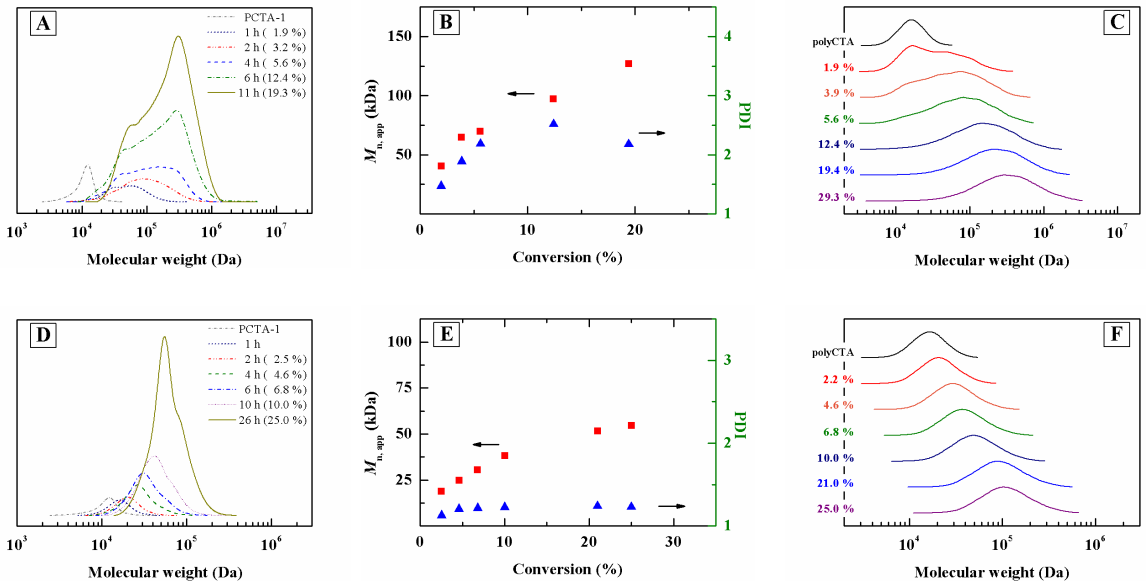

Figure 2-3. Evolution of MWD with time, development of $M_{n,app}$ and PDI with conversion and the corresponding Monte Carlo simulation of preparation of CPB with PS branches *via* conventional R-group approach (A–C) and *via* "CTA-shuttled" R-group approach (D–F). The numbers in parentheses in (A) and (D) refer to the corresponding conversions. All the samples were measured by SEC in THF with PS calibration. Reprinted with permission of Wiely-VCH.

This facile "CTA-shuttled" R-group approach provides much better defined CPBs with polystyrene (PS) branches (PDI = 1.23, Figures 2–3 D and E) than the conventional R-group approach (PDI = 2.18, Figures 2–3 A and B). Monte Carlo simulations confirm that the advantage of the "CTA-shuttled" R-group approach consists in the release of the active radicals from trapping CPB systems. Further well-defined CPBs with poly(*tert*-butyl acrylate) branches and core-shell CPBs with PS-*block*-poly(*N*-isopropylacrylamide) branches were successfully synthesized *via* the "CTA-shuttled" R-group approach.

2.3 Rod-like Nano-light Harvester

The producers in the biological world have been harvesting, transferring and storing solar light energy for millions of years. In a natural light-harvesting and energy transfer system with high efficiency, one fundamental concept is the "energy cascade" architecture, *i.e.*, pigments acting as light absorbing antennae surrounding the reaction center. Solar energy is absorbed by the antennae and transferred into the center where it is then transformed into chemical energy for use in the photosynthesis process. In the last decades, researchers have been encouraged to design different compounds mimicking living nature to harvest and store solar energy. However, the reported synthetic light-harvesting architectures suffer from some problems, such as instable energy transfer process and serious quenching induced by aggregation.

In this chapter, a novel rod-like nano-light harvester (NLH) architecture based on a core-shell cylindrical polymer brush (CPB) mimicking the natural "energy cascade" system is designed and prepared. In this architecture, light absorbing antennae, (9,9-diethylfluoren-2-yl)methyl methacrylate (FlMA) units, are located in a cylinder "wrapping" the backbone embedded with dilute energy acceptors, 9-anthracenemethyl methacrylate (AnMA) units, as illustrated in Scheme 2–3. The energy is absorbed by FlMA units and concentrated into the center by Förster resonance energy transfer (FRET).

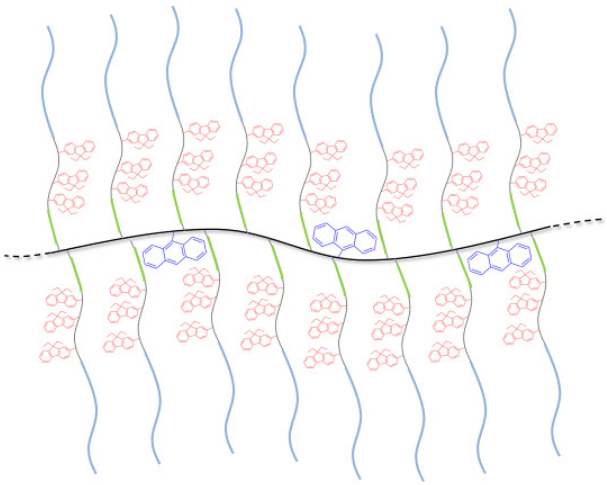

Scheme 2-3. Structure of rod-like nano-light harvester based on core-shell CPB. Reprinted with permission of Wiely-VCH.

As shown in Scheme 2–4, the polyinitiator backbone for preparing NLHs was synthesized *via* a random RAFT copolymerization of BIEM and AnMA. The ratio of BIEM to AnMA was kept as 4.6 / 1 to dilute the energy acceptors among the ATRP initiators. Three different NLHs (composition shown in Scheme 2–4) were prepared *via* sequential grafting of side chains from the backbone. The NLH-2 and NLH-3 has 5 and 15 methyl methacrylate (MMA) units between the backbone and the light absorbing antennae, respectively.

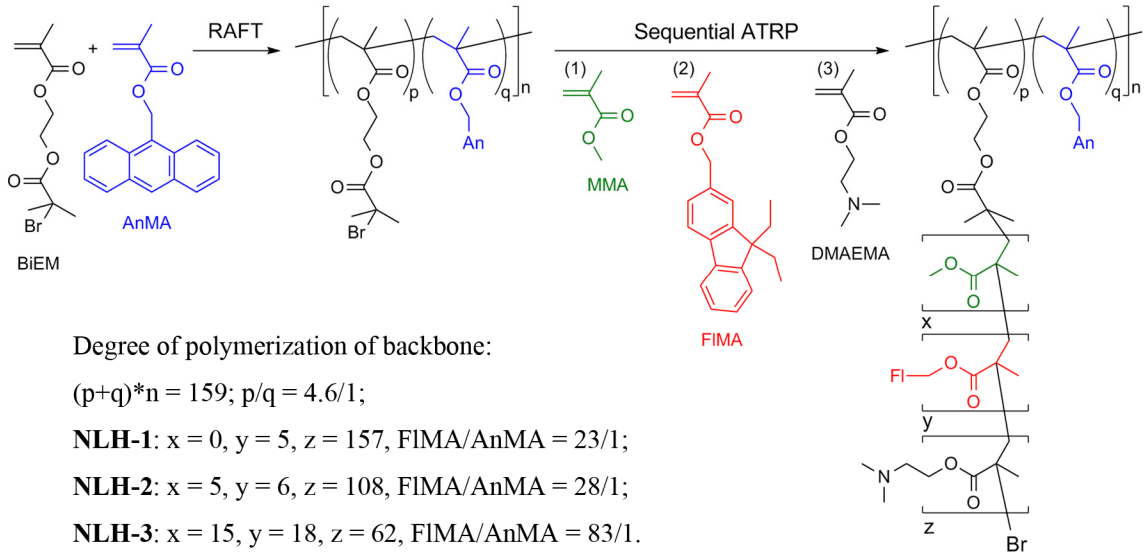

Scheme 2-4. Synthetic route to rod-like nano-light harvester. Reprinted with permission of Wiely-VCH.

Upon excitation at 305 nm, where FlMA has the maximal absorption and AnMA has a very low one, NLH-1 shows a strong emission of AnMA rather than that of FlMA in THF solution, as shown in Figure 2–4A. However, in the photoluminescence spectrum of a comparison mixture of 9,9-diethyl-2-hydroxymethylfluorene (FlOH) and 9-anthracenemethanol (AnOH) at the same concentrations, only emission from FlOH is observed (Figure 2–4C). This indicates that NLH-1 can realize efficient energy harvesting and fast energy transfer from FlMA to AnMA. Furthermore, the FRET can be varied by tuning the distance between the antennae and energy acceptors in either physical or chemical ways by means of changing solvents or adding inert spacer units, respectively. This CPB-based rod-like NLH concept provides a novel solution for light harvesting materials.

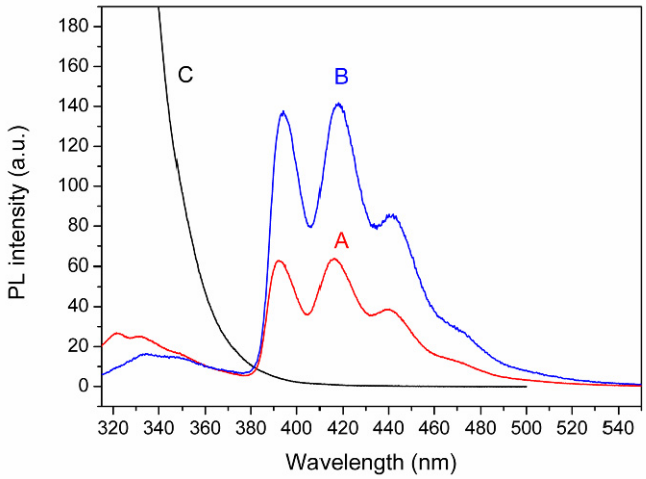

Figure 2-4. Photoluminescence spectra of **NLH-1** with 1×10^{-5} mol/L of FlMA units in THF (A, red) and water (B, blue), as well as a mixture of FlOH and AnOH ([FlOH] / [AnOH] = 24) in THF (C, black) with the same concentration as comparison. Reprinted with permission of Wiely-VCH.

2.4 Rare-earth Metal Cations Incorporated Silica Hybrid Nanoparticles

Rare-earth metals, *i.e.* the lanthanides from lanthanum (La) to lutetium (Lu), constitute a series of inner transition elements ("f-elements"). Their trivalent cations, Ln^{3+}, possessing unique and diverse properties, are of particular interest in constructing specific functional materials, such as photonic and magnetic materials. Gd^{3+} ions can significantly decrease the relaxation time of water protons and are thus widely used as contrast agents for magnetic resonance imaging (MRI). However, Gd^{3+} ions are highly toxic and must thus be chelated within ligands or embedded in nanoparticles to avoid the cytotoxicity. In the last decade, core-shell(-corona) cylindrical polymer brushes (CPBs), providing a large number of chelating sites within their branched architectures, have been employed as templates for the preparation of various rod-like hybrid nanoparticles (NPs), which demonstrate high dimensional stability and excellent solubility.

In this chapter, we designed core-shell CPBs with poly(acrylic acid)-*block*-poly[2-(dimethylamino)ethyl methacrylate] (PAA-*b*-PDMAEMA) side chains, short as *b*-[AD], for the first time as templates for the preparation of rare-earth metal cations (Ln^{3+}) incorporated hybrid NPs. As illustrated in Scheme 2–5, the CPB template *b*-[AD] was obtained *via* acidic hydrolysis of the CPB precursor with poly(*tert*-butyl acrylate)-*block*-PDMAEMA (P*t*BA-*b*-PDMAEMA) side chains (*b*-[TD]). Subsequently, various Ln^{3+} ions, *i.e.* gadolinium (Gd^{3+}), neodymium (Nd^{3+}), europium (Eu^{3+}), terbium (Tb^{3+}) and their mixtures, were incorporated into the PAA-core through chelating. A further localized deposition and condensation of tetramethyl orthosilicate (TMOS) molecules onto the PDMAEMA-shell yields hybrid NPs with a crosslinked silica shell.

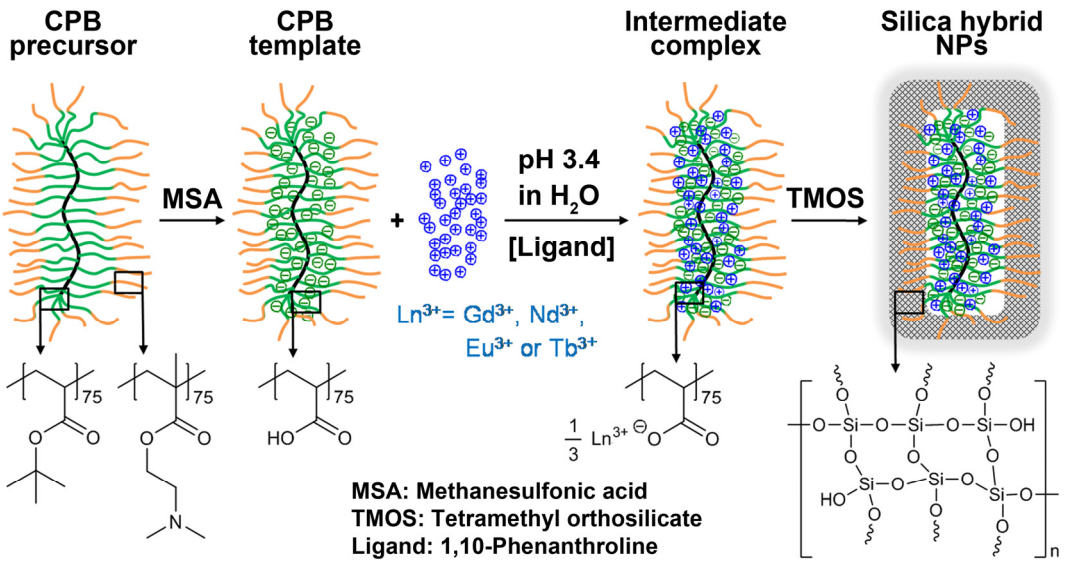

Scheme 2-5. Preparation of well-defined rare-earth metal cations (Ln^{3+}) incorporated silica hybrid nanoparticles *via* the template-directed approach based on core-shell cylindrical polymer brushes. Reprinted with permission of ACS.

AFM images confirm the successful synthesis of well-defined CPB precursors with different brush lengths, as illustrated in Figures 2–5 A and B. By employing the CPB templates, single-component silica hybrid NPs *h*-Gd_{3200}, *h*-Gd_{270}, *h*-Nd_{3200}, *h*-Nd_{270} and *h*-Tb_{3200}, ligand-coordinating ones *h*-Tb-L_{3200} and *h*-Eu-L_{3200} (1,10-phenanthroline as ligand), as well as multicomponent ones *h*-Tb/Gd_{3200} and *h*-Tb/Nd_{3200} (loaded with Ln^{3+} mixtures) were prepared. The obtained silica hybrid NPs maintain the cylindrical worm-like conformations from the templates as demonstrated in the TEM images (Figures 2–5 D–F). A core-shell nanostructure with a dark Ln^{3+}-containing core and a grey silica shell is observed in the silica hybrid NPs (Figures 2–5 D and F for *h*-Tb_{3200} and *h*-Tb/Gd_{3200}), while the intermediate of Gd^{3+}-loaded template without deposition of TMOS shows only a homogeneous dark nanostructure (Figure 2–5C).

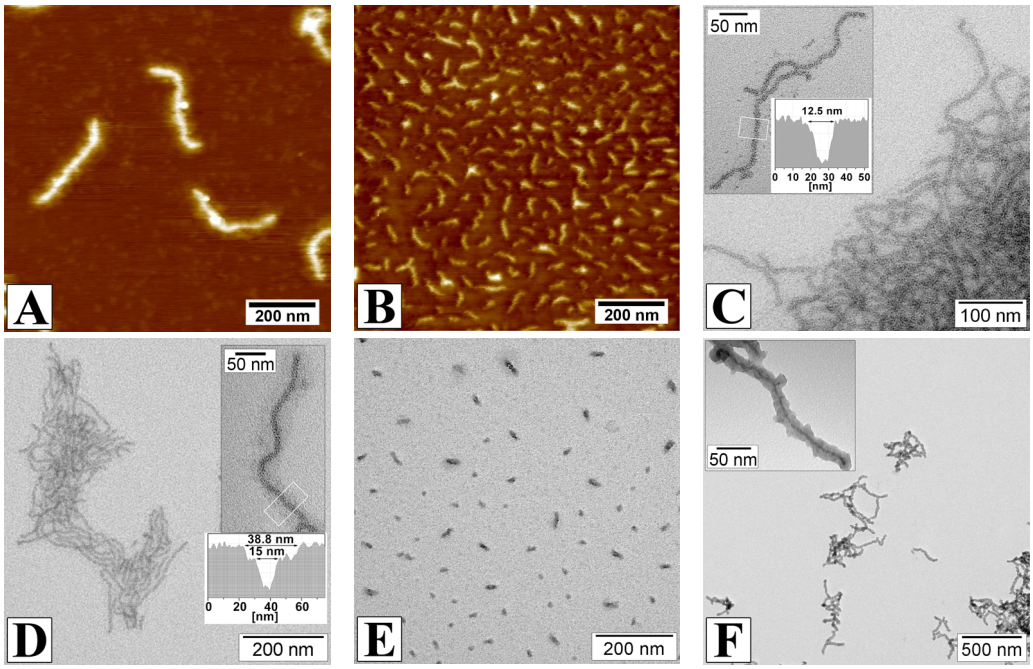

Figure 2-5. Tapping-mode AFM height image of the longer CPB precursor *b*-$[T_{75}D_{75}]_{3200}$ (A) and the shorter CPB precursor *b*-$[T_{80}D_{77}]_{270}$ (B). TEM image of the Gd^{3+}-loaded template intermediate without silicate deposition (C), the Ln^{3+}-incorporated silica hybrid NPs *h*-Tb_{3200} (D), *h*-Gd_{270} (E), and the multicomponent silica hybrid NP *h*-Tb/Gd_{3200} (F). The insets in (C) and (D) show the grayscale analysis of the marked areas. Reprinted with permission of ACS.

Besides a high stability of the encapsulation of Ln^{3+} ions and a satisfying solubility in water and alcohols, the silica hybrid NPs obtain unique and diverse properties from the incorporated Ln^{3+} ions. That is, the hybrid NPs with Tb^{3+} or Eu^{3+} incorporation exhibit characteristic visible photoluminescence upon excitation with UV light (Figure 2–6), which is sensitized by ligand or metal-metal energy transfer. The Gd^{3+}- and Nd^{3+}-containing hybrid NPs show paramagnetic behavior (Figure 2–7A). Especially, the Gd^{3+}-containing silica hybrid NPs show much higher longitudinal relaxivity, r_1, and stronger contrast enhancement in T_1-weighted MRI images than the commercial contrast agent Gd-DPTA (Figures 2–7 B and C). This remarkable T_1 shortening effect combined with a minimal cytotoxicity towards different human cells and a promising EPR effect suggests the potential application of the Gd^{3+}-containing silica hybrid NPs as effective MRI contrast agents for tumor diagnosis. The multicomponent hybrid NPs with a combination of different functional centers, *e.g.* Tb^{3+} and Gd^{3+}, possess both visible photoluminescence and T_1 contrast enhancement and can thus be applied as multimodal bioimaging

probes.

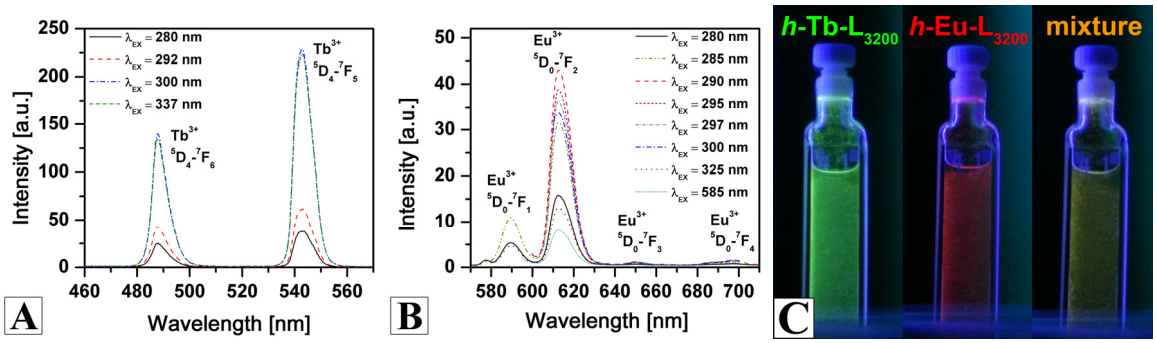

Figure 2-6. Photoluminescence emission spectra of the silica hybrid NPs in ethanol solution upon exciting at different wavelengths: *h*-Tb-L_{3200} with 1,10-phenanthroline as ligand, c_{Tb}= 160 mg L^{-1} (A) and *h*-Eu-L_{3200} with c_{Eu}= 82 mg L^{-1} (B). Luminescence image of the ethanol solutions of *h*-Tb-L_{3200}, *h*-Eu-L_{3200} and their mixture with c_{Tb}= 47 mg L^{-1} and c_{Gd}= 45 mg L^{-1} under excitation at 266 nm (C). Reprinted with permission of ACS.

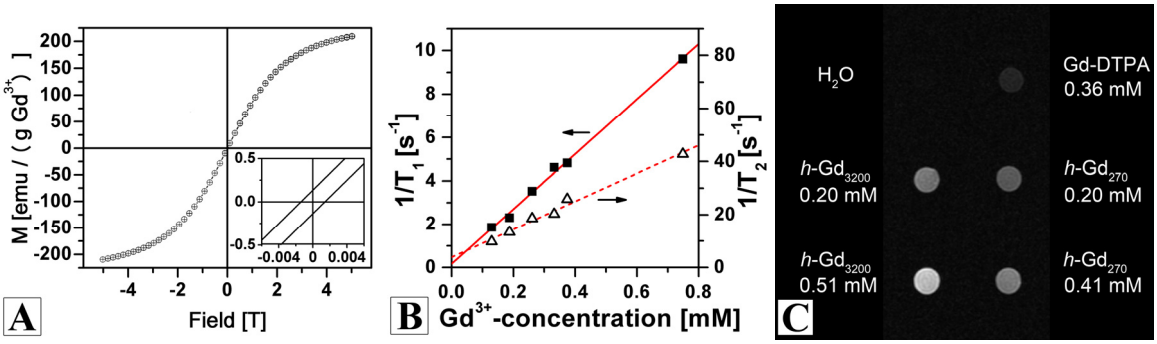

Figure 2-7. Magnetization curves at 5 K for the silica hybrid NP *h*-Gd_{3200} (A). Plots of longitudinal ($1/T_1$) and transverse relaxation rate ($1/T_2$) *versus* Gd^{3+}-concentration of the silica hybrid NP *h*-Gd_{3200} in D_2O at 37 °C and 7 T (B). T_1-weighted MRI images of *h*-Gd_{3200} and *h*-Gd_{270} with different Gd^{3+}-concentrations (C). Deionized water and commercial contrast agent Gd-DTPA were measured as references. Reprinted with permission of ACS.

2.5 Individual Contributions to Joint Publications

The results presented in this thesis were obtained in collaboration with others, and have been published or submitted to publication as indicated below. In the following, the contributions of all the co-authors to the different publications are specified. The asterisk denotes the corresponding author(s).

Chapter 3

This work is published in the journal *ACS Nano*, **2013**, *7*, 2284–2291, under the title:

"Surface Interactions Surpass Carbon-Carbon Bond: Understanding and Control of the Scission Behavior of Core-Shell Polymer Brushes on Surfaces"

by Zhicheng Zheng, Markus Müllner, Jun Ling* and Axel H. E. Müller*

I conducted all experiments and wrote the publication, except that:

- M. Müllner was involved in early experiments;
- J. Ling and A. H. E. Müller were involved in scientific discussions and correcting the publication.

Chapter 4

This work is in press in the journal *Macromolecular Rapid Communications*, **2013**, DOI: 10.1002/marc.201300578, under the title:

"Revival of the R-Group Approach: A 'CTA-shuttled' Grafting-from Approach for Well-defined Cylindrical Polymer Brushes *via* RAFT Polymerization"

by Zhicheng Zheng, Jun Ling* and Axel H. E. Müller*

I conducted all experiments and wrote the publication, except that:

- J. Ling conducted the Monte Carlo simulations and was involved in scientific discussions and correcting the manuscript;

- A. H. E. Müller was involved in scientific discussions and correcting the manuscript.

Chapter 5

This work is in press in the journal *Macromolecular Rapid Communications*, **2013**, DOI: 10.1002/marc.201300785, under the title:

"Rod-like Nano-Light Harvester"

by Jun Ling,* Zhicheng Zheng, Anna Köhler and Axel H. E. Müller*

I conducted all polymerizations, performed some photoluminescence measurements and was involved in scientific discussions and writing the manuscript.

- J. Ling conducted the syntheses of monomers, performed the remaining characterizations and wrote the manuscript;
- A. Köhler conducted the calculations and was involved in scientific discussions and correcting the manuscript;
- A. H. E. Müller was involved in scientific discussions and correcting the manuscript.

Chapter 6

This work is published in the journal *Chemistry of Materials*, **2013**, *25*, 4585–4594, under the title:

"Rare-Earth Metal Cations Incorporated Silica Hybrid Nanoparticles Templated by Cylindrical Polymer Brushes"

by Zhicheng Zheng, Alexander Daniel, Wei Yu, Birgit Weber, Jun Ling* and Axel H. E. Müller*

I conducted all experiments, interpreted the results of all measurements and wrote the manuscript, except that:

- A. Daniel conducted the loading of hybrid nanoparticles and performed characterizations;
- W. Yu conducted the cytotoxicity measurements;
- B. Weber was involved in the evaluation and discussion of the magnetic measurements;
- J. Ling was involved in scientific discussions and correcting the manuscript;
- A. H. E. Müller was involved in scientific discussions and correcting the manuscript.

Chapter 3

Scission Behavior of Core-Shell Cylindrical Polymer Brushes on Solid Surfaces

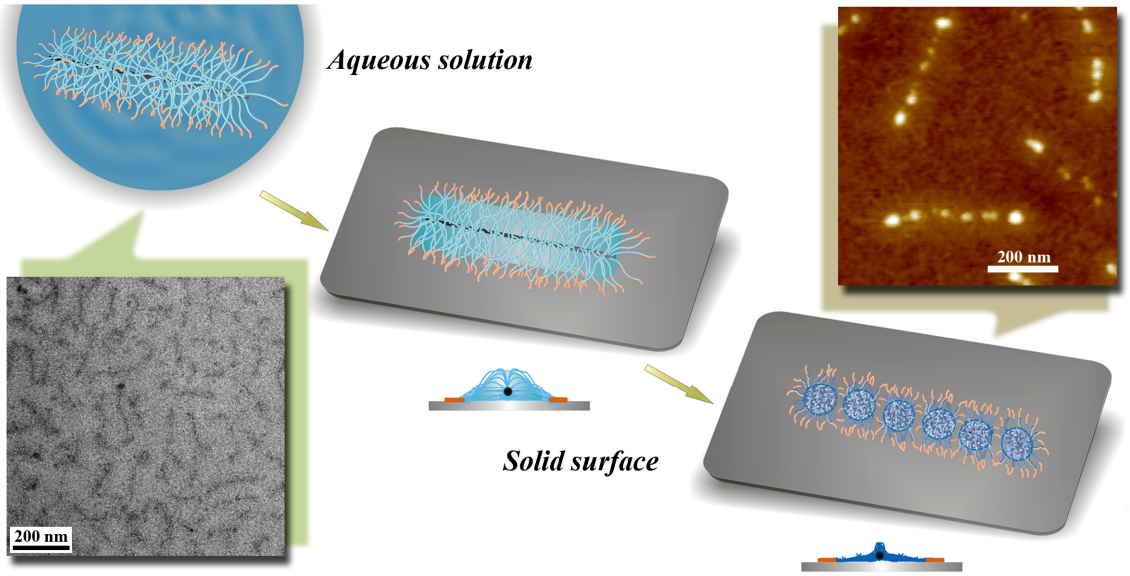

The results of this chapter have been published as:

"Surface Interactions Surpass Carbon-Carbon Bond: Understanding and Control of the Scission Behavior of Core-Shell Polymer Brushes on Surfaces"

by Zhicheng Zheng, Markus Müllner, Jun Ling* and Axel H. E. Müller*

in *ACS Nano*, **2013**, *7*, 2284–2291. Reprinted with permission of ACS.

Abstract

A tapping-mode AFM investigation of core-shell cylindrical polymer brushes (CPBs) on mica shows that they can be ruptured upon spin-coating. Three different CPBs were synthesized, having a methacrylate backbone, carrying branches of poly[oligo(ethylene glycol) methacrylate] (POEGMA), POEGMA-*block*-poly[2-(dimethylamino)ethyl methacrylate] (POEGMA-*b*-PDMAEMA) and POEGMA-*block*-poly[2-(methacryloyloxy)ethyl trimethylammoniumiodide] (POEGMA-*b*-PMETAI). The polymer backbone of core-shell CPB with POEGMA-*b*-PDMAEMA or POEGMA-*b*-PMETAI branches is ruptured upon drying on mica surface, while they are stable in aqueous solution. We propose that the scission behavior is induced by Coulomb interactions between PDMAEMA or PMETAI corona and the solid surface and that this interaction is stronger than one or more carbon-carbon single bonds. We control this scission behavior by tuning the surface interactions through switching the surface nature, varying pH, or adding multivalent counterions. Our study demonstrates that core-shell CPB serves as a template to directly compare the weak intermolecular forces with the strong carbon-carbon covalent bonds.

Keywords

Cylindrical polymer brushes, polyelectrolytes, surface charges, intermolecular attractions, surface interaction energy, carbon-carbon bond energy, scission behavior

3.1 Introduction

It is an ingenious strategy to mobilize a group of many dwarves to defeat a giant. Intermolecular attraction, *the dwarf*, possesses an energy of 2 to 12 kJ mol^{-1}, less by one to two orders of magnitude than the carbon-carbon covalent bond, *the giant*, with an energy of 348 kJ mol^{-1}. Under some extreme conditions the carbon-carbon covalent bond can be challenged, such as ultrasonic field,[1] clashing flow,[2] receding interface[3] and single molecular stretching.[4,5] Yet, in this contribution we work out a strategy to teach hundreds and thousands of intermolecular attractions to directly combat carbon-carbon covalent bonds under ambient conditions. We employ a branched polymer architecture, *i.e.* a core-shell cylindrical polymer brush (CPB), which consists of a single linear polymer backbone and a large number of polymer chains with functional groups in the outside shell layer.[6,7] When they cooperate to anchor on a solid surface producing enough intermolecular attractions and then the inner core part contracts by drying, serving as a fast responsive driving force, the carbon-carbon covalent bonds in the backbone are ruptured within minutes. The CPB residues after scission meet the situation that the remaining dwarfs are just insufficient in number to beat a giant. Therefore, the control of the extent and the position of the scission of the backbone is feasible by means of tuning the intermolecular attractions between the functional groups and the surface. Our design differs from the report of a random scission of a CPB backbone by Sheiko *et al*.,[8] where the CPB was transformed *via* very slow expansion (in hours or in days) from a 3-dimentional cylindrical conformation into a 2-dimentional flat one driven by a confinement-induced passive exclusion of densely grafted side chains.

3.2 Experimental Section

3.2.1 Preparation of CPBs

The synthesis of the polyinitiator poly[2-(2-bromoisobutyryloxy)ethyl methacrylate] (PBIEM) (DP_n=1500, PDI=1.08) by anionic polymerization, acidic cleavage of the trimethylsilyl groups, and an esterification to attach the ATRP initiating sites was reported previously.[9] The homopolymer CPB *b*-$[O_{430}]_{750}$ was synthesized *via* ATRP from PBIEM backbone. A flask equipped with CuBr and polyinitiator PBIEM was degassed with argon for 30 min. Then degassed monomer OEGMA and solvent anisole were added by syringe. The mixture was stirred and heated to 60 °C. Finally, the degassed ligand, *N,N,N′,N″,N″*-pentamethyldiethylenetriamine (PMDETA), was injected to start the polymerization, and an initial sample was taken for ^{1}H NMR measurement. The polymerization was monitored by withdrawing samples for ^{1}H NMR measurements. When a desired conversion was achieved, the reaction was quenched by cooling the reaction mixture to room temperature and exposing it to air. The reaction mixture was purified by passing through a silica gel column, followed by precipitating into cold *n*-hexane.

The core-shell CPB *b*-$[O_{430}D_{40}]_{750}$ was obtained *via* ATRP of DMAEMA from the homopolymer CPB *b*-$[O_{430}]_{750}$. A round-bottom was charged with CuBr, *b*-$[O_{430}]_{750}$ and anisole. The mixture was degassed with argon for 30 min. After that, the degassed monomer DMAEMA was added by syringe into the flask, which was then heated to 90 °C. The degassed ligand PMDETA was injected to start the polymerization. As described above, the polymerization was monitored by ^{1}H NMR measurements. After achiving a desired conversion, the reaction was quenched by cooling the reaction mixture to room temperature and exposing it to air. The reaction mixture was purified by passing through a silica gel column, followed by precipitating into cold *n*-hexane for twice.

The core-shell CPB *b*-$[O_{430}Dq_{40}]_{750}$ carrying polyelectrolyte PMETAI segments was synthesized *via* quaternization of the PDMAEMA segments of the CPB *b*-$[O_{430}D_{40}]_{750}$. Here, *b*-$[O_{430}D_{40}]_{750}$ was dissolved in dioxane (about 10 mg/mL). Methyl iodide was

added at room temperature at a molar ratio of 2 compared to amino groups. After around 20 min, the solution became turbid. Stirring was continued for 2 days to ensure the full reaction. Then the turbid reaction mixture was transferred into a dialysis membrane and dialyzed against pure water for one week.

3.2.2 Determination of the initiating efficiency

The initiating efficiency of the polyinitiator PBIEM toward OEGMA was determined by cleaving POEGMA side chains from the CPB *b*-$[O_{430}]_{750}$ under alkaline conditions. The obtained PMAA linear polymers were methylated into PMMA, which was characterized by SEC. The procedure was detailed in our earlier work.[10]

3.2.3 Characterization methods

Size Exclusion Chromatography. SEC was conducted using dimethyl acetamide (DMAc) with 0.05% lithium bromide as eluent at an elution rate of 0.8 mL/min. The equipment consists of one pre-column and two analytical columns (PSS GRAM, 10^2 and 10^3 Å pore size, 7 mm particle size) and an Agilent 1200 RI detector. The measurements were performed at 60 °C. PDMAEMA calibration curve was used to calibrate the columns.

^{1}H Nuclear Magnetic Resonance Spectroscopy. ^{1}H NMR measurements were carried out on a Bruker AC-300 instrument at room temperature in $CDCl_3$ or D_2O.

Tapping-mode Atomic Force Microscopy. AFM images were recorded on a Digital Instruments Dimension 3100 microscope operated in tapping mode. The samples were prepared by spin-coating (3000 rpm, 1 min) diluted aqueous solutions onto mica or silicon surface.

Contact-mode Atomic Force Microscopy in liquid. AFM images were recorded on a JPK Nanowizard I equipment. The sample was prepared by dipping diluted aqueous solution onto mica which was glued on a glass dish containing Milli-Q pure water.

3.3 Results and Discussion

3.3.1 Synthesis of cylindrical polymer brushes (CPBs)

The "grafting from" synthetic route to different core-shell CPBs follows an established protocol[11,12] and is illustrated in Scheme 3–S1. Poly[2-(2-bromo-isobutyryloxy)ethyl methacrylate] (PBIEM) with the degree of polymerization, DP, of 1500 and a polydispersity index, PDI, of 1.08 was used as polyinitiator. The homopolymer CPB with poly[oligo(ethylene glycol) methacrylate] (POEGMA) side chains was prepared *via* ATRP of OEGMA from the PBIEM backbone. This well-defined CPB has an apparent PDI of 1.35. The initiating efficiency of the PBIEM polyinitiator toward OEGMA was determined as 0.50. Therefore, each CPB has 750 POEGMA side chains with a DP of 430 (short as *b*-$[O_{430}]_{750}$), as shown in Scheme 3–1A. A sequential grafting of the poly[2-(dimethylamino)ethyl methacrylate] (PDMAEMA) block from the homopolymer CPB *b*-$[O_{430}]_{750}$ generated the core-shell CPB with diblock copolymer side chains of POEGMA-*b*-PDMAEMA (short as *b*-$[O_{430}D_{40}]_{750}$, shown in Scheme 3–1B and 3–1D). The core-shell CPB *b*-$[O_{430}D_{40}]_{750}$ is also well-defined and has an apparent PDI of 1.28. The DP of the PDMAEMA block was determined as 40, and thus the weight fraction (wt-%) of PDMAEMA segments in the CPB *b*-$[O_{430}D_{40}]_{750}$ is only 4.6 %. Quaternization of the PDMAEMA block with iodomethane led to core-shell CPBs with a POEGMA core and a polyelectrolyte shell of poly[2-(methacryloyloxy)ethyl trimethylammoniumiodide] (PMETAI) (short as *b*-$[O_{430}Dq_{40}]_{750}$, shown in Scheme 3–1C). The characterization of different CPBs by proton nuclear magnetic resonance (^{1}H NMR) and size exclusion chromatography (SEC) is given in Figures 3–S1 and 3–S2.

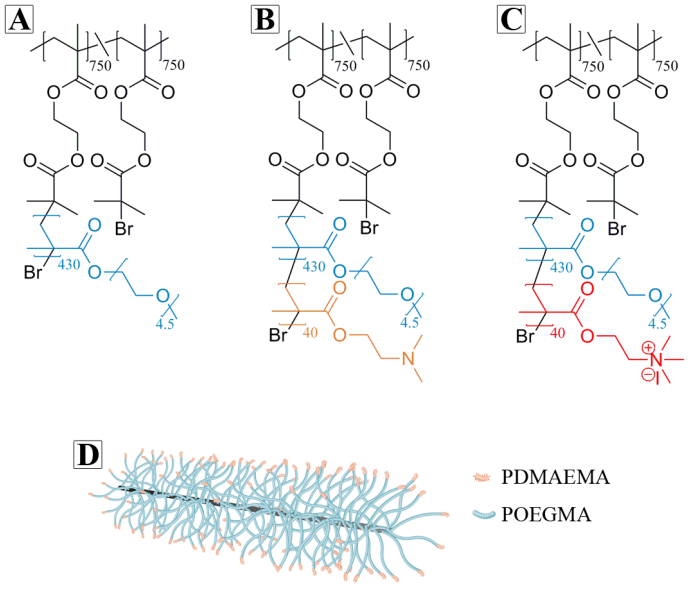

Scheme 3-1. Chemical structures of the homopolymer CPB *b*-$[O_{430}]_{750}$ (A), the core-shell CPB *b*-$[O_{430}D_{40}]_{750}$ (B) and the core-shell CPB *b*-$[O_{430}Dq_{40}]_{750}$ (C). Schematic illustration of the core-shell CPB *b*-$[O_{430}D_{40}]_{750}$ (D).

3.3.2 Scission of CPBs on mica surface

After being spin-coated onto mica surface from dilute aqueous solution (pH 5.5), tapping-mode AFM images of the core-shell CPB *b*-$[O_{430}D_{40}]_{750}$ showed a completely different conformation than that of the homopolymer CPB *b*-$[O_{430}]_{750}$, even though the fraction of PDMAEMA segments is very low (4.6 %) (Figures 3–1 A–F and 3–S3 A–C). In the core part of CPB *b*-$[O_{430}D_{40}]_{750}$ with the number-average length L_n = 261 ± 21 nm, mainly five or six separated small beads with a width of *ca.* 50 nm are observed. The cross-sectional analysis shows obvious gaps (up to 30 nm in width) between two adjacent beads, which reach the surface basis as shown in Figure 1F. In contrast, the homopolymer CPB *b*-$[O_{430}]_{750}$ has a homogeneous and continuous conformation with L_n = 172 ± 20 nm and a width of *ca.* 70 nm (Figure 1A–C) on mica surface. In the case of CPB *b*-$[O_{430}Dq_{40}]_{750}$ which carries quaternized PDMAEMA segments in the periphery, a non-continuous conformation is observed with even more small beads (mainly nine or ten) with a width of *ca.* 45 nm in the core part, as shown in Figures 3–1 G–I and 3–S3 D–F. the average length, L_n, of the CPB *b*-$[O_{430}Dq_{40}]_{750}$ was measured as 376 ± 25 nm, which

equals to the contour length (375 nm) of the PBIEM backbone with a DP of 1500. This non-continuous and fully stretched conformation as well as the obvious gaps between adjacent beads indicate that the core-shell CPBs had ruptured.

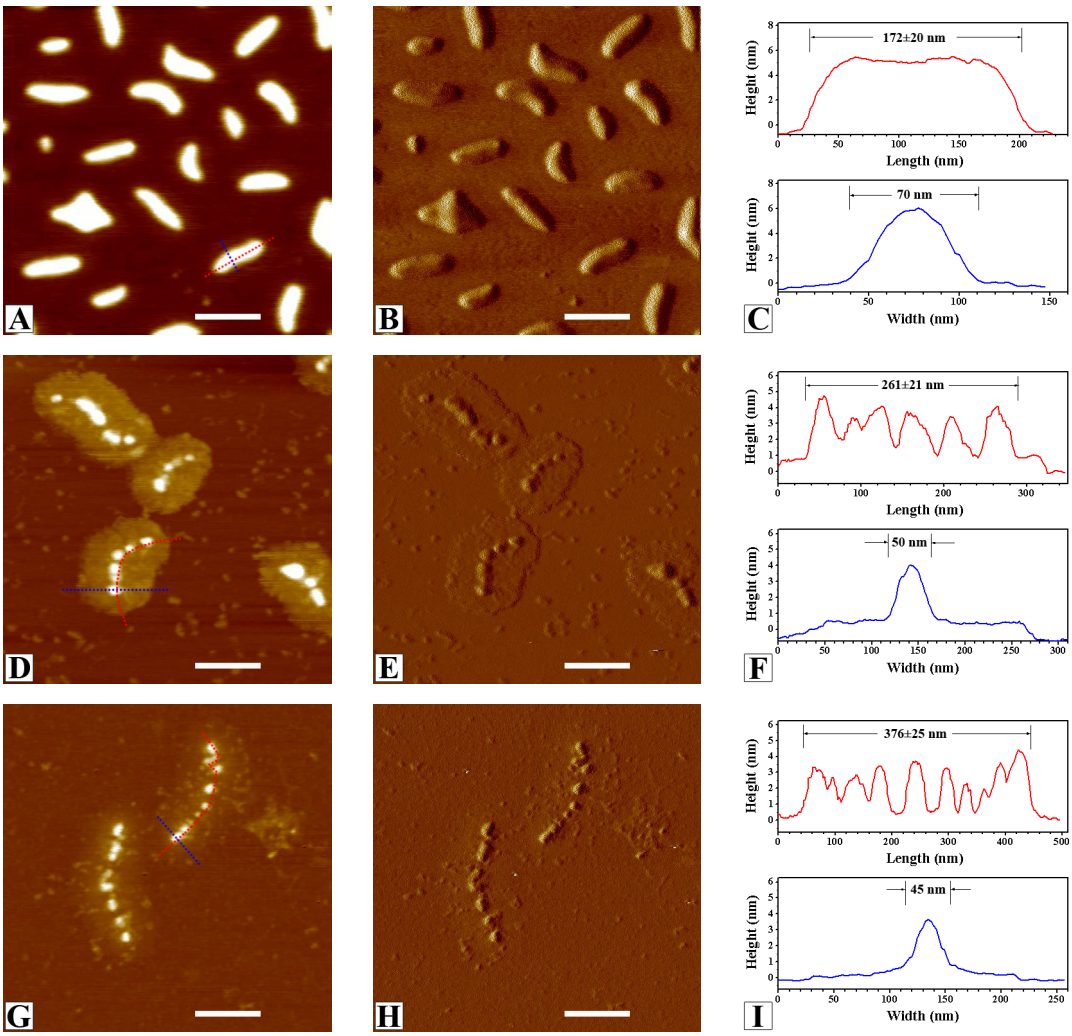

Figure 3-1. Tapping-mode AFM height image, phase image and the corresponding height cross-section analysis of CPBs *b*-$[O_{430}]_{750}$ (A–C), *b*-$[O_{430}D_{40}]_{750}$ (D–F) and *b*-$[O_{430}Dq_{40}]_{750}$ (G–I). CPBs were spin-coated on freshly cleaved mica surface from 0.02 g L^{-1} aqueous solution (pH 5.5). Z-ranges are 8 nm for height images and 10° for phase images. The scale bars correspond to 200 nm.

3.3.3 CPBs in aqueous solution

To prove that the scission of core-shell CPBs happens only after spin-coating onto surfaces rather than in the previous aqueous solution, aqueous solution (pH 5.5) of different CPBs were characterized by dynamic light scattering (DLS) and cryogenic transmission electron microscopy (cryo-TEM). Although DLS measurements only give an apparent

dimension for wormlike CPBs, the apparent hydrodynamic radius, $R_{h,app}$, reflects the overall changes of CPBs in aqueous solution.[13] The monomodal and narrow $R_{h,app}$ distributions of different CPBs (Figure 3–2A) indicate that the CPBs were well dissolved and stayed stable in aqueous solution without detectable constitution changes. Furthermore, only continuous wormlike conformations observed for both CPBs *b*-$[O_{430}D_{40}]_{750}$ and *b*-$[O_{430}Dq_{40}]_{750}$ in cryo-TEM (Figure 3–2 B and C) directly confirm that the core-shell CPBs were not ruptured in aqueous solution. The L_n values of CPBs *b*-$[O_{430}D_{40}]_{750}$ and *b*-$[O_{430}Dq_{40}]_{750}$ are underestimated in the measurement as 172 and 265 nm, respectively, since wormlike CPBs stay tilt in the specimen film with a thickness of *ca.* 200 nm for cryo-TEM and only the projection is measured. Assuming an average tilting angle of 40°, L_n values of CPBs *b*-$[O_{430}D_{40}]_{750}$ and *b*-$[O_{430}Dq_{40}]_{750}$ are corrected to 226 and 348 nm, respectively, and they are in good agreement with the dimensions measured from AFM images (Figures 3–1 and 3–S3). In addition, a sample of the CPB *b*-$[O_{430}Dq_{40}]_{750}$ was prepared by applying its aqueous solution onto mica, which was then kept in water for contact-mode AFM in liquid. The height image also shows a continuous wormlike conformation (Figure 3–S4), indicating the CPB is stable even after being adsorbed on mica as long as it is not dried. The scission behavior observed in Figure 1 thus is related to the drying process during spin-coating.

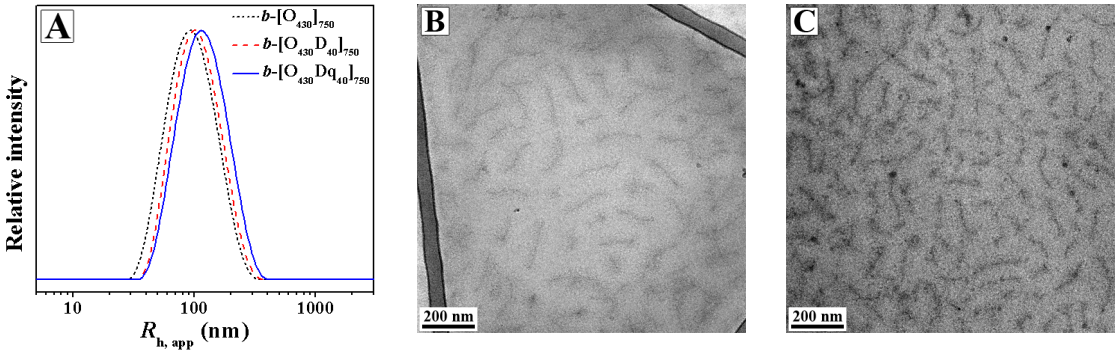

Figure 3-2. Intensity-weighted DLS CONTIN plots for CPBs in 0.2 g L^{-1} aqueous solution (pH 5.5) (A), $\langle R_{h,app}\rangle_z$ = 92, 102 and 112 nm, PDI = 1.16, 1.15 and 1.16, for *b*-$[O_{430}]_{750}$ (black), *b*-$[O_{430}D_{40}]_{750}$ (red) and *b*-$[O_{430}Dq_{40}]_{750}$ (blue), respectively. Cryo-TEM images of CPBs *b*-$[O_{430}D_{40}]_{750}$ (B) and *b*-$[O_{430}Dq_{40}]_{750}$ (C) in 0.24 g L^{-1} aqueous solution (pH 5.5), L_n = 172 ± 23 and 265 ± 38 nm for *b*-$[O_{430}D_{40}]_{750}$ and *b*-$[O_{430}Dq_{40}]_{750}$, respectively.

3.3.4 Understanding the scission behavior of CPB *b*-[$O_{430}D_{40}$]$_{750}$ on mica

On the basis of the above experimental results, we propose a scission mechanism of the core-shell CPB *b*-[$O_{430}D_{40}$]$_{750}$ on mica surface as illustrated in Figure 3–3. In aqueous solution, the well-dissolved CPB extends side-chains in all directions. Upon the instant contact of the CPB with the mica surface during spin-coating, the PDMAEMA segments tightly anchor to mica as telechelic claws due to the Coulombic interactions between the tertiary amino-groups and the negatively charged mica surface (2×10^6 negative charges/μm^2),[14,15] whereas the POEGMA segments of the core carry water molecules within their ethylene ether units.[16] Subsequently, the water molecules begin to evaporate from the CPB, resulting in a contraction of the POEGMA core, both along and perpendicular to the backbone. Hence, in order to fulfill the volume change during the drying-induced shrinking process, either the PDMAEMA-mica interactions or the carbon-carbon covalent single bonds of the backbone have to be destroyed. If the energy of interactions between PDMAEMA segments and the mica surface, $E_{D,S}$, are *n* times as strong as that of carbon-carbon covalent single bond, E_{CB}, *n* carbon-carbon covalent single bonds will break and the CPB will be ruptured into *n+1* small beads. We found that the CPB *b*-[$O_{430}D_{40}$]$_{750}$ was ruptured into mainly five or six small beads in the core part (Figures 3–1 D–F and 3–S3 A–C) after being spin-coated onto mica, which indicates the energy of the combined surface interactions, $E_{D,S}$, is in the range of four to five times of the carbon-carbon covalent single bond energy, E_{CB}. The dependence of the number of small beads, N_{beads}, in the ruptured CPB on the energy of combined surface interactions, E_{SI}, can be described as Equation (3–1),

$$N_{\text{beads}} - 1 = \frac{E_{\text{SI}}}{E_{\text{CB}}} = \frac{\sum_i E_{\text{P},i}}{E_{\text{CB}}} = \frac{\sum_i (-\int \boldsymbol{F}_i \cdot \mathrm{d}\boldsymbol{S}_i)}{E_{\text{CB}}} \qquad (3\text{–}1)$$

where $E_{p,i}$, $\boldsymbol{F}_i$ and $\mathrm{d}\boldsymbol{S}_i$ are the PDMAEMA-substrate attractive potential energy of a single DMAEMA unit, the corresponding intermolecular attractive force and differential replacement, respectively. In the case of CPB *b*-[$O_{430}Dq_{40}$]$_{750}$ carrying polyelectrolyte PMETAI segments, the intermolecular attraction, $\boldsymbol{F}_{Dq,S}$ is higher than that of PDMAEMA, $\boldsymbol{F}_{D,S}$, since the densely positively charged PMETAI segments have stronger electrostatic interactions with the negative charges on mica.[17] Assuming that the number of METAI

units which contact the mica surface in CPB *b*-$[O_{430}Dq_{40}]_{750}$ is the same as that of DMAEMA units in the precursor CPB *b*-$[O_{430}D_{40}]_{750}$, Equation (3–1) predicts that CPB *b*-$[O_{430}Dq_{40}]_{750}$ should be ruptured into more small beads on mica than the CPB *b*-$[O_{430}D_{40}]_{750}$. This is confirmed by the observation of mainly nine or ten small beads in the AFM images (Figures 3–1 G–I and 3–S3 D–F). Therefore, the above theory can be applied to control the scission behavior of core-shell CPBs on surfaces by tuning the intermolecular attraction, $\boldsymbol{F}$, and thus the surface interaction energy.

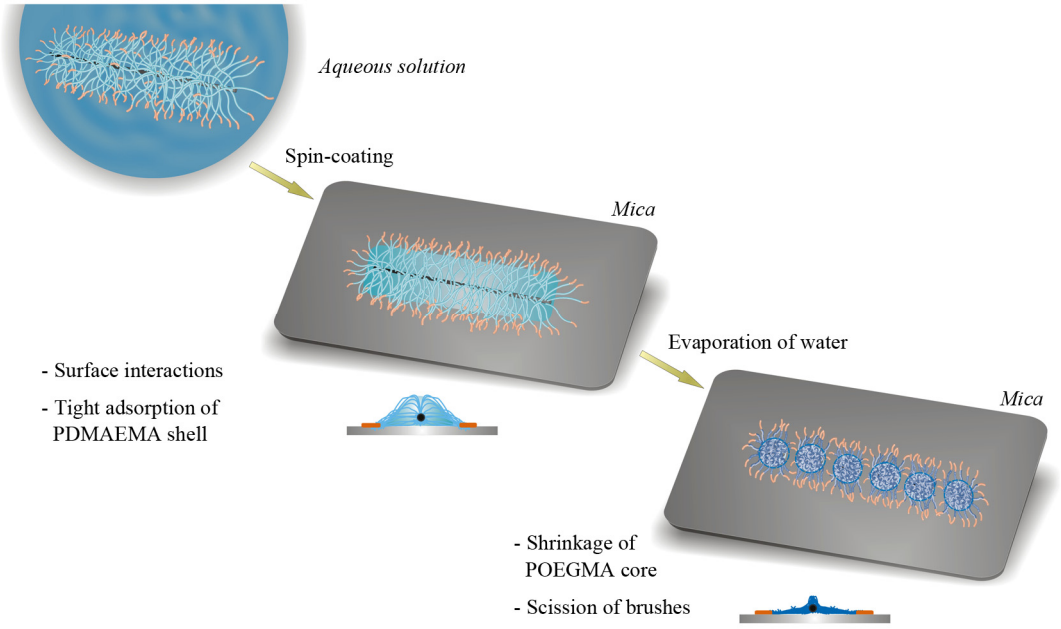

Figure 3-3. Illustration of scission behavior of the core-shell CPB *b*-$[O_{430}D_{40}]_{750}$ on mica surface.

3.3.5 Scission of CPBs on silicon surface

An alternate way to tune the intermolecular attraction, $\boldsymbol{F}$, is to change nature of the surface. The surface of silicon is very slightly charged at pH 5.5,[18] providing weaker attraction than mica with either PDMAEMA or PMETAI segments, *i.e.* $\boldsymbol{F}_{D,Si}<\boldsymbol{F}_{D,mica}$ and $\boldsymbol{F}_{Dq,Si}<\boldsymbol{F}_{Dq,mica}$. As shown in Figures 3–4 A–C and 3–S5 A–B, in contrast to the scission conformation on mica (Figure 3–1 D–F), the CPB *b*-$[O_{430}D_{40}]_{750}$ shows a "fried egg"-like conformation with a continuous homogeneous core on silicon (Figure 3–4 D–F). The core of CPB *b*-$[O_{430}D_{40}]_{750}$ was measured as 134 and 9 nm in length and height, respectively, which is shorter but higher than that on mica (261 and 4 nm). This conformation of CPB *b*-$[O_{430}D_{40}]_{750}$ is explained by the weaker interaction energy. During the drying-induced volume contraction process of the POEGMA core, the PDMAEMA telechelic claws are

sliding rather than anchoring on silicon surface, leading to a shorter but more compact and continuous core part in the final conformation. Taking CPB *b*-$[O_{430}Dq_{40}]_{750}$ carrying strongly positively charged PMETAI segments on silicon into account, $\boldsymbol{F}_{Dq,Si}>\boldsymbol{F}_{D,Si}$ but $\boldsymbol{F}_{Dq,Si}<\boldsymbol{F}_{Dq,mica}$, leading to a non-continuous conformation with mainly five or six small beads in the core part as observed in Figures 3–4 G–I and 3–S5 C–E. Therefore, the energy of surface interactions between PMETAI segments and silicon, $E_{Dq\text{-}Si}$, is in the range of four to five times of the carbon-carbon covalent single bond energy, E_{CB}.

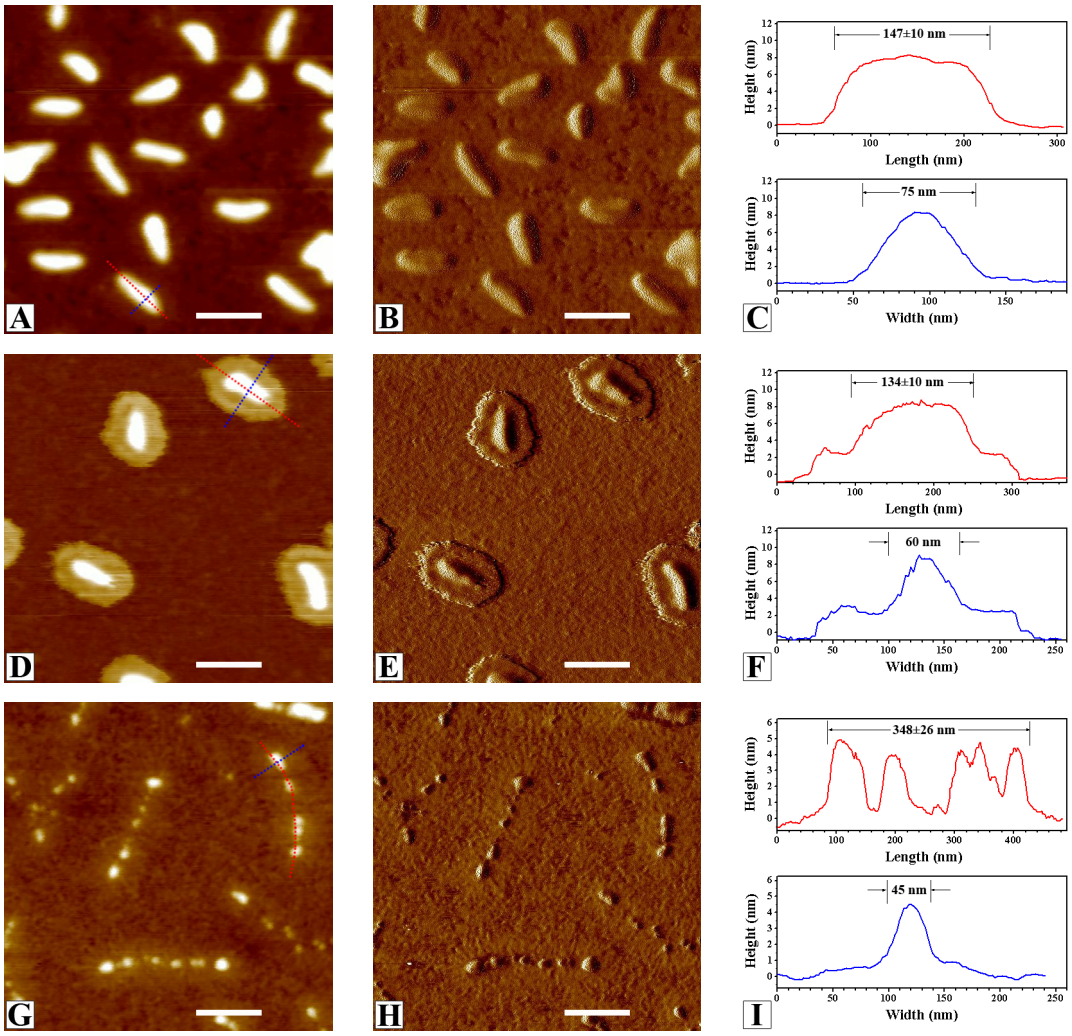

Figure 3-4. Tapping-mode AFM height image, phase image and the corresponding height cross-section analysis of CPBs *b*-$[O_{430}]_{750}$ (A–C), *b*-$[O_{430}D_{40}]_{750}$ (D–F) and *b*-$[O_{430}Dq_{40}]_{750}$ (G–I). CPBs were spin-coated on silicon surface from 0.02 g L^{-1} aqueous solution (pH 5.5). Z-ranges are 12 nm for height images and 10° for phase images. The scale bars correspond to 200 nm.

3.3.6 pH value as a trigger to control the scission of the CPB *b*-$[O_{430}D_{40}]_{750}$ on mica

The pH dependent protonation degree of the PDMAEMA segments of the CPB *b*-$[O_{430}D_{40}]_{750}$ affects the intermolecular attraction, ***F***, between the outside shell layer and the negatively charged mica surface. Based on Equation (3–1), tuning the pH value of the aqueous solution of CPB *b*-$[O_{430}D_{40}]_{750}$ is a way to control its scission behavior. For instance, elevated PDMAEMA protonation at low pH increases surface interactions, $E_{D,S}$, between PDMAEMA segments and mica, and thus should increase the number of small beads, N_{beads}, in the ruptured CPB. The samples in Figures 1 and 4 were prepared from aqueous solutions at pH 5.5, resulting in a *ca.* 50 % protonation of the CPB *b*-$[O_{430}D_{40}]_{750}$ (the star polymer $(PDMAEMA_{240})_{24}$ has pK_a = 5.8[19]). Two samples of CPB *b*-$[O_{430}D_{40}]_{750}$ were prepared from 0.02 g L^{-1} aqueous solutions at pH 1.9 and 10.0, where the PDMAEMA segments are fully protonated and fully deprotonated, respectively. In the case of pH 1.9, the core part was ruptured into mainly six or seven small beads (Figures 3–5 A–C and 3–S6 A–C), more than that at pH 5.5 (Figure 3–1 D–F). In contrast, upon increasing the pH to 10.0, only three or four beads were observed in the core part of CPB (Figures 3–5 D–F and 3–S6 D–F).

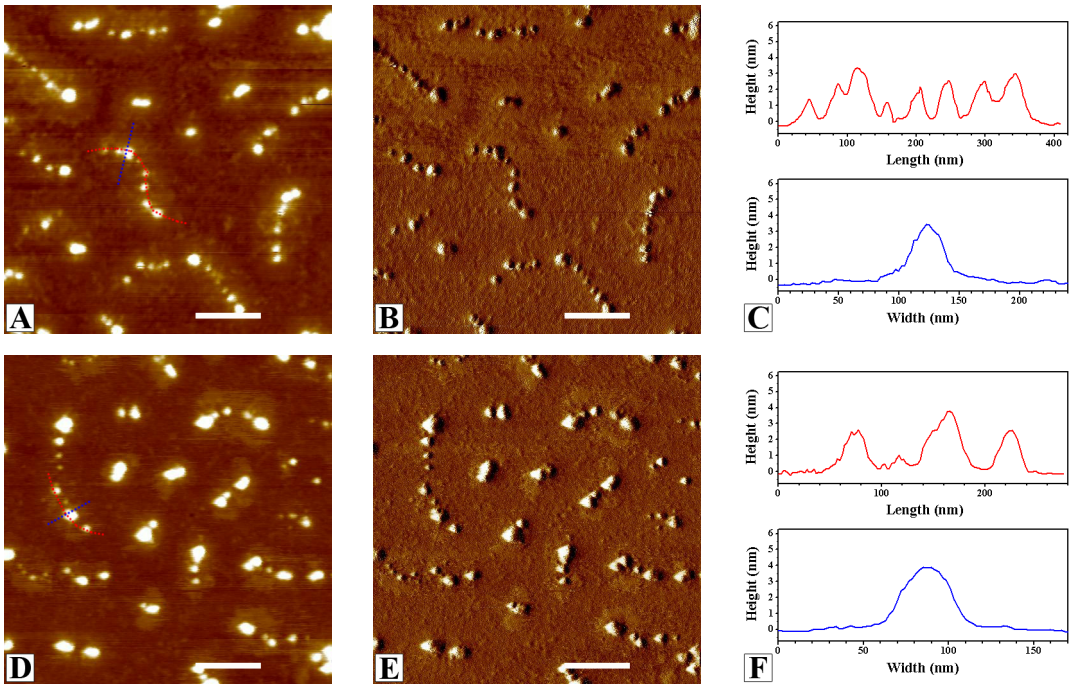

Figure 3-5. Tapping-mode AFM height image, phase image and the corresponding height cross-section analysis of the CPB *b*-$[O_{430}D_{40}]_{750}$ spin-coated on mica surface from 0.02 g L^{-1} aqueous solution at pH 1.9 (A–C) and at pH 10.0 (D–F). Z-ranges are 8 nm for height images and 10° for phase images. The scale bars correspond to 200 nm.

3.3.7 Multivalent counterion as a trigger to control the scission of CPB *b*-$[O_{430}Dq_{40}]_{750}$

Homopolymer CPBs with PMETAI side chains conformationally respond to multivalent counterions in aqueous solution as reported in our previous work.[13] Exchanging some monovalent iodide counterions of the PMETAI segments by multivalent counterions decreases the osmotic pressure within the brush, screening the electrostatic interactions between the positively charged telechelic segments of the CPB *b*-$[O_{430}Dq_{40}]_{750}$ and the negative charges on mica. Accordingly, intermolecular attraction, ***F***, should decrease. Referring to Equation (3–1), the core part of CPB is expected to be ruptured into fewer small beads on mica. To confirm this, we prepared 0.02 g L^{-1} aqueous solutions (pH 5.5) of the CPB *b*-$[O_{430}Dq_{40}]_{750}$, (containing 5.7 μM iodide ions) and added $K_3[Co(CN)_6]$ to reach 3.9 and 7.8 μM concentrations of $[Co(CN)_6]^{3-}$ ions, respectively. As predicted, the core part of CPB was ruptured into mainly six or seven small beads as observed in the tap-

ping-mode AFM images of *b*-$[O_{430}Dq_{40}]_{750}$ containing 3.9 μM of $K_3[Co(CN)_6]$ on mica (Figures 3–6 A–C and 3–S7 A–C). In the sample containing 7.8 μM of $K_3[Co(CN)_6]$, the core part of CPB was broken into even fewer small beads (three or four) on mica (Figures 3–6 D–F and 3–S7 D–F), as intermolecular attraction, ***F***, between the telechelic segments and mica is lower than that with 3.9 μM salt.

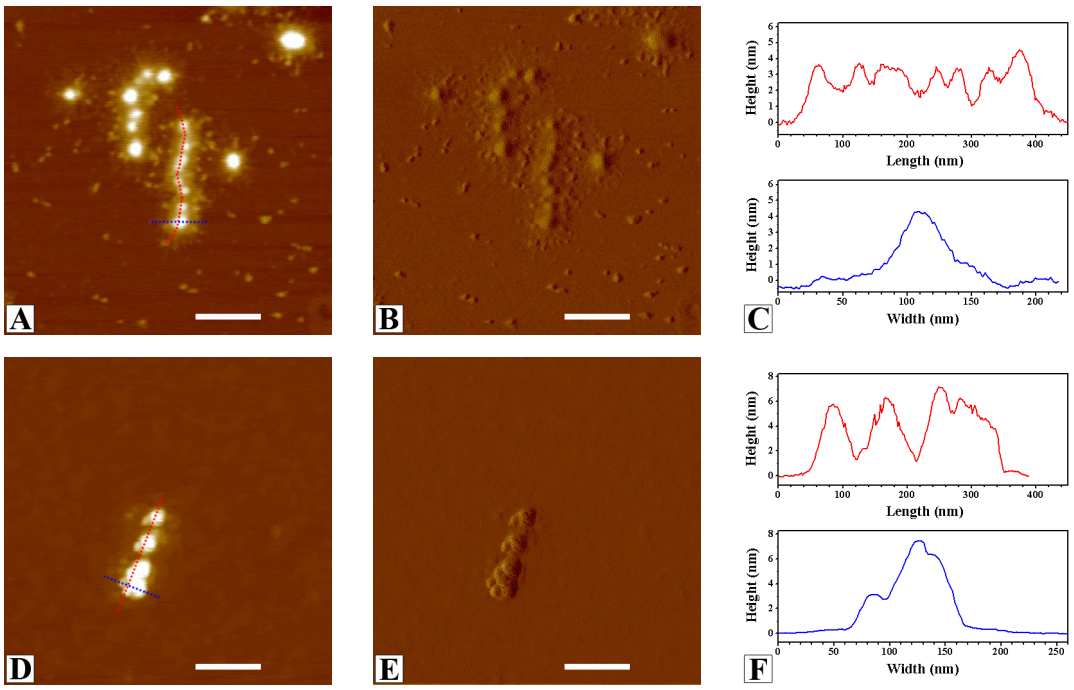

Figure 3-6. Tapping-mode AFM height image, phase image and the corresponding height cross-section analysis of CPBs *b*-$[O_{430}Dq_{40}]_{750}$ (0.02 g L^{-1} aqueous solution, pH 5.5) containing 3.9 μM of $K_3[Co(CN)_6]$ (A–C), and 7.8 μM of $K_3[Co(CN)_6]$ (D–F). CPBs were spin-coated on freshly cleaved mica surface. Z-ranges are 8 nm for height images and 10° for phase images. The scale bars correspond to 200 nm.

3.3.8 Comparison of surface interaction energies of different CPBs

By employing Equation (3–1), we estimate the ratio of combined surface interaction energy, E_{SI}, of CPBs to the carbon-carbon covalent single bond energy, E_{CB}, from the number of small beads, N_{beads}, in the core part. According to the statistic results (Figures 3–1, 3–4, 3–5, 3–6, 3–S3, 3–S5, 3–S6, and 3–S7), we summarize the ratio $E_{SI}/E_{CB} = N_{beads}$-1 of different CPBs on surfaces in Figure 3–7. For the homopolymer CPB *b*-$[O_{430}]_{750}$, the surface interactions energy, E_{SI}, is lower than the carbon-carbon covalent bond energy, E_{CB}, on both mica and silicon, where the CPB is not ruptured. In all cases of

core-shell CPBs on surfaces, except *b*-$[O_{430}D_{40}]_{750}$ on silicon, the surface interactions surpass the carbon-carbon covalent bond, *i.e.* the ratio $E_{SI}/E_{CB}>1$, resulting in the scission of CPBs on surfaces. Comparing to the CPB *b*-$[O_{430}D_{40}]_{750}$, the CPB *b*-$[O_{430}Dq_{40}]_{750}$ with a high density of positive charges in polyelectrolyte PMETAI segments shows stronger surface interactions on both mica and silicon. However, silicon as a nearly neutral surface gives weaker interactions than mica with either PDMAEMA or PMETAI segments. The surface interactions between PDMAEMA segments and mica increase with decreasing pH values, *i.e.* increasing protonation. Adding multivalent counterions into the aqueous solution of the CPB *b*-$[O_{430}Dq_{40}]_{750}$ reduces the electrostatic interactions between the positively charged PMETAI segments and the negative charges on mica, thus decreasing the ratio E_{SI}/E_{CB}.

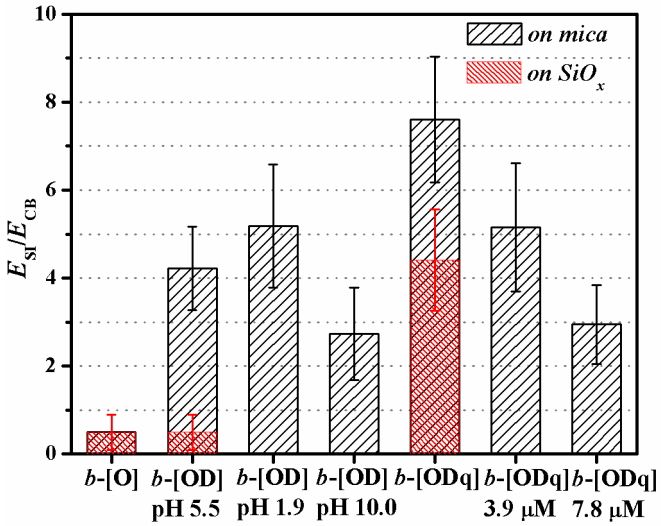

Figure 3-7. Comparison of combined surface interactions energy, E_{SI}, of different CPBs on various surfaces (mica, black, and silicon, red) relative to the carbon-carbon covalent bond energy, E_{CB}. The last two samples contain the given concentration of $[Co(CN)_6]^{3-}$ ions.

3.4 Conclusions

The polymer backbone of core-shell CPB is ruptured upon drying under ambient conditions, when the functional groups in the outside shell produce enough intermolecular interactions with a solid surface. We successfully tune the surface interactions to control this scission behavior of different core-shell CPBs by means of switching the surface nature, quaternization, varying the pH value or adding multivalent counterions. Our study demonstrates that core-shell CPB as a branched polymer architecture provides a platform for a direct dialogue between the weak intermolecular forces and the strong carbon-carbon covalent bonds.

Acknowledgement

Z. Zheng appreciates a scholarship from the Elite Support Program of Bavaria. J. Ling sincerely thanks the Alexander von Humboldt Foundation for granting him a research fellowship. We thank Melanie Förtsch for Cryo-TEM measurements and Dr. Oleg Borisov for helpful discussions.

Supporting Information Available

Synthetic route, ^{1}H NMR spectra, SEC profiles, AFM images with larger scan sizes and histograms can be found in the supporting information. This material is available free of charge *via* the Internet at http://pubs.acs.org.

3.5 References

1. Basedow, A.; Ebert, K., Ultrasonic degradation of polymers in solution. In *Physical Chemistry*, Springer Berlin Heidelberg: **1977**; Vol. 22, pp 83-148.
2. Odell, J. A.; Keller, A.; Rabin, Y. *J. Chem. Phys.* **1988**, *88*, 4022-4028.
3. Bensimon, A.; Simon, A.; Chiffaudel, A.; Croquette, V.; Heslot, F.; Bensimon, D. *Science* **1994**, *265*, 2096-2098.
4. Kishino, A.; Yanagida, T. *Nature* **1988**, *334*, 74-76.
5. Mehta, A. D.; Rief, M.; Spudich, J. A.; Smith, D. A.; Simmons, R. M. *Science* **1999**, *283*, 1689-1695.
6. Zhang, M.; Müller, A. H. E. *J. Polym. Sci. Part A: Polym. Chem.* **2005**, *43*, 3461-3481.
7. Sheiko, S. S.; Sumerlin, B. S.; Matyjaszewski, K. *Prog. Polym. Sci.* **2008**, *33*, 759-785.
8. Sheiko, S. S.; Sun, F. C.; Randall, A.; Shirvanyants, D.; Rubinstein, M.; Lee, H.-i.; Matyjaszewski, K. *Nature* **2006**, *440*, 191-194.
9. Zhang, M.; Breiner, T.; Mori, H.; Müller, A. H. E. *Polymer* **2003**, *44*, 1449-1458.
10. Plamper, F. A.; Schmalz, A.; Penott-Chang, E.; Drechsler, M.; Jusufi, A.; Ballauff, M.; Müller, A. H. E. *Macromolecules* **2007**, *40*, 5689-5697.
11. Yuan, J.; Xu, Y.; Walther, A.; Bolisetty, S.; Schumacher, M.; Schmalz, H.; Ballauff, M.; Müller, A. H. E. *Nat. Mater.* **2008**, *7*, 718-722.
12. Müllner, M.; Yuan, J.; Weiss, S.; Walther, A.; Förtsch, M.; Drechsler, M.; Müller, A. H. E. *J. Am. Chem. Soc.* **2010**, *132*, 16587-16592.
13. Xu, Y.; Bolisetty, S.; Drechsler, M.; Fang, B.; Yuan, J.; Harnau, L.; Ballauff, M.; Müller, A. H. E. *Soft Matter* **2009**, *5*, 379-384.
14. Güven, N. *Z. Kristallogr.* **1971**, *134*, 196-212.
15. Rojas, O. J.; Ernstsson, M.; Neuman, R. D.; Claesson, P. M. *Langmuir* **2002**, *18*, 1604-1612.
16. Keefe, A. J.; Jiang, S. *Nature Chem.* 2012, *4*, 59-63.

17. Dahlgren, M. A. G.; Claesson, P. M.; Audebert, R. *J. Colloid Interface Sci.* **1994**, *166*, 343-349.
18. Buron, C. C.; Filiâtre, C.; Membrey, F.; Bainier, C.; Charraut, D.; Foissy, A. *J. Colloid Interface Sci.* **2007**, *314*, 358-366.
19. Plamper, F. A.; Ruppel, M.; Schmalz, A.; Borisov, O.; Ballauff, M.; Müller, A. H. E. *Macromolecules* **2007**, *40*, 8361-8366.

3.6 Supporting Information

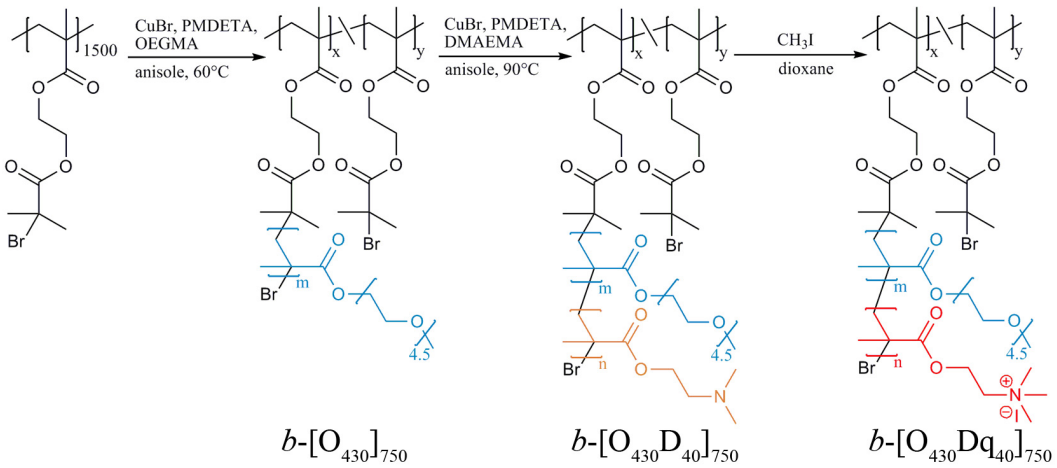

Scheme 3-S1. Synthetic route to CPBs *b*-$[O_{430}]_{750}$, *b*-$[O_{430}D_{40}]_{750}$ and *b*-$[O_{430}Dq_{40}]_{750}$.

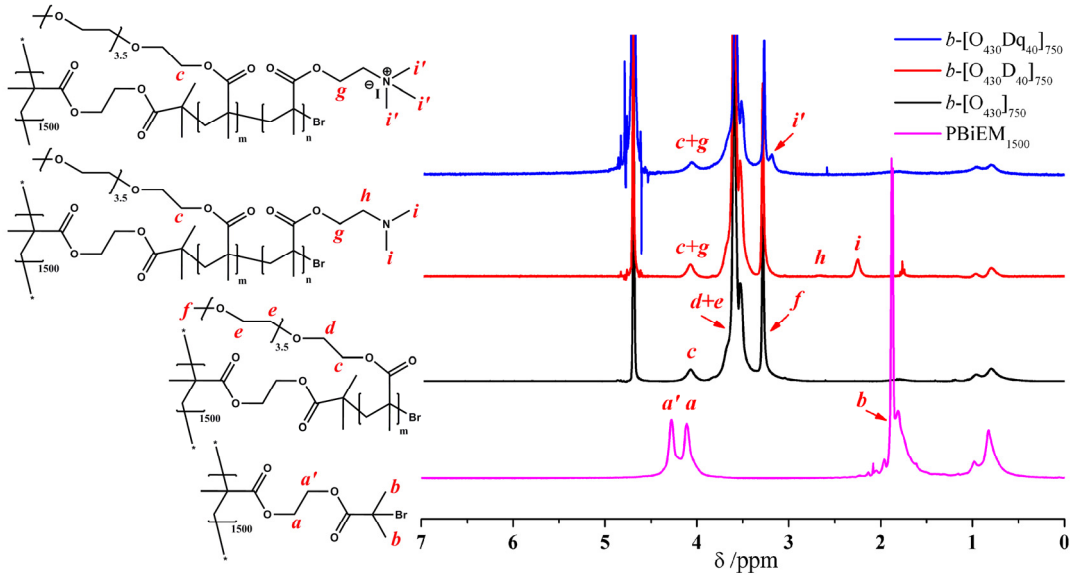

Figure 3-S1. ^{1}H NMR spectra of PBIEM polyinitiator backbone (pink), CPBs *b*-$[O_{430}]_{750}$ (black), *b*-$[O_{430}D_{40}]_{750}$ (red) and *b*-$[O_{430}Dq_{40}]_{750}$ (blue). PBIEM was measured in $CDCl_3$ and all CPBs in D_2O.

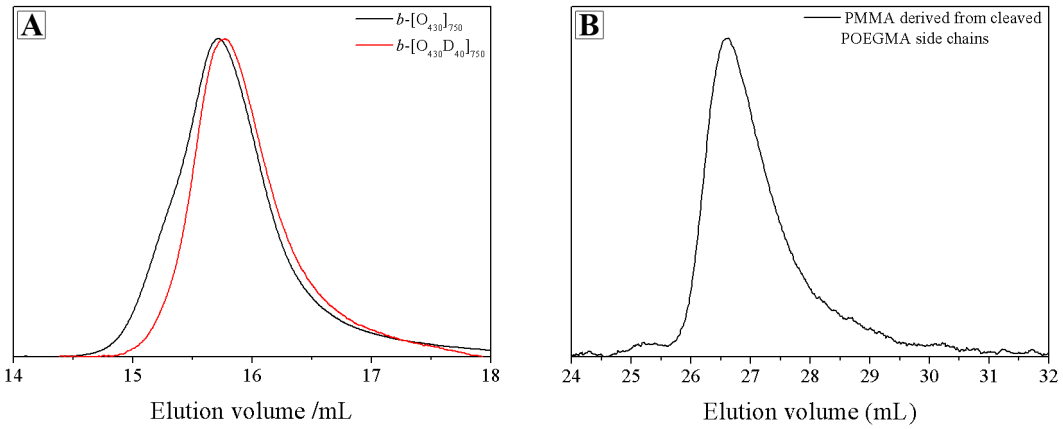

Figure 3-S2. SEC elution traces of CPBs *b*-$[O_{430}]_{750}$ (black) and *b*-$[O_{430}D_{40}]_{750}$ (red) (A) using DMAc with 0.05% lithium bromide as eluent. SEC elution trace of PMMA derived from cleaved POEGMA side chains from CPB *b*-$[O_{430}]_{750}$ (B) using THF as eluent for the determination of the initiating efficiency of the PBIEM polyinitiator.

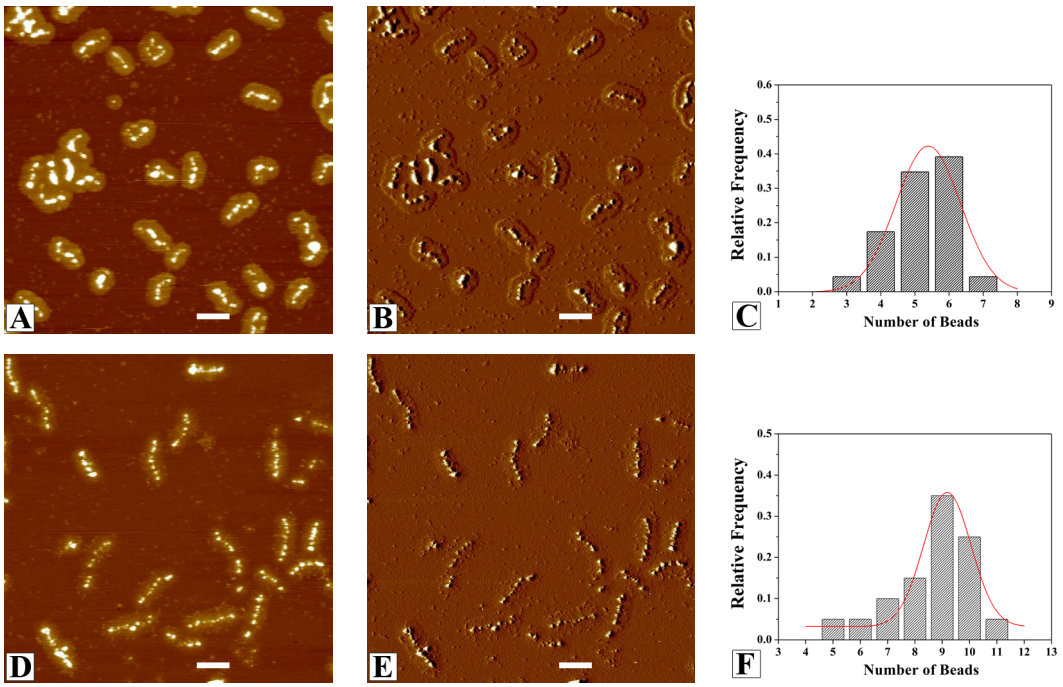

Figure 3-S3. Tapping-mode AFM height image, phase image and the corresponding histogram of N_{beads} distribution (for *ca.* 20 counted CPBs) of CPBs *b*-$[O_{430}D_{40}]_{750}$ (A–C) and *b*-$[O_{430}Dq_{40}]_{750}$ (D–F). CPBs were spin-coated on freshly cleaved mica surface from 0.02 g L^{-1} aqueous solution. Z-ranges are 8 nm for height images and 10° for phase images. The scale bars correspond to 300 nm.

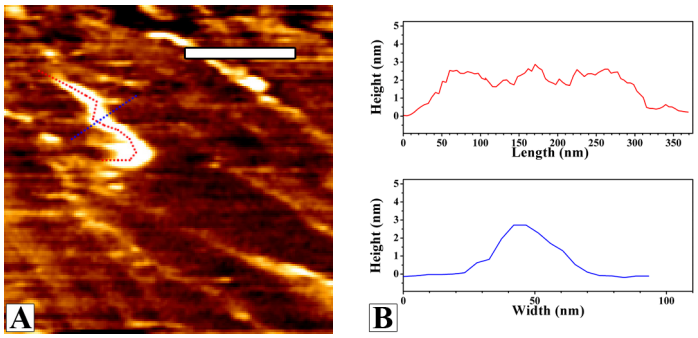

Figure 3-S4. Contact-mode AFM in liquid height image (A) and the corresponding height cross-section analysis (B) of the CPB *b*-$[O_{430}Dq_{40}]_{750}$. A 0.02 g L^{-1} aqueous solution (pH 5.5) of CPB was dipped onto a freshly cleaved mica surface which was glued on a glass dish containing Milli-Q pure water. The scale bar corresponds to 200 nm.

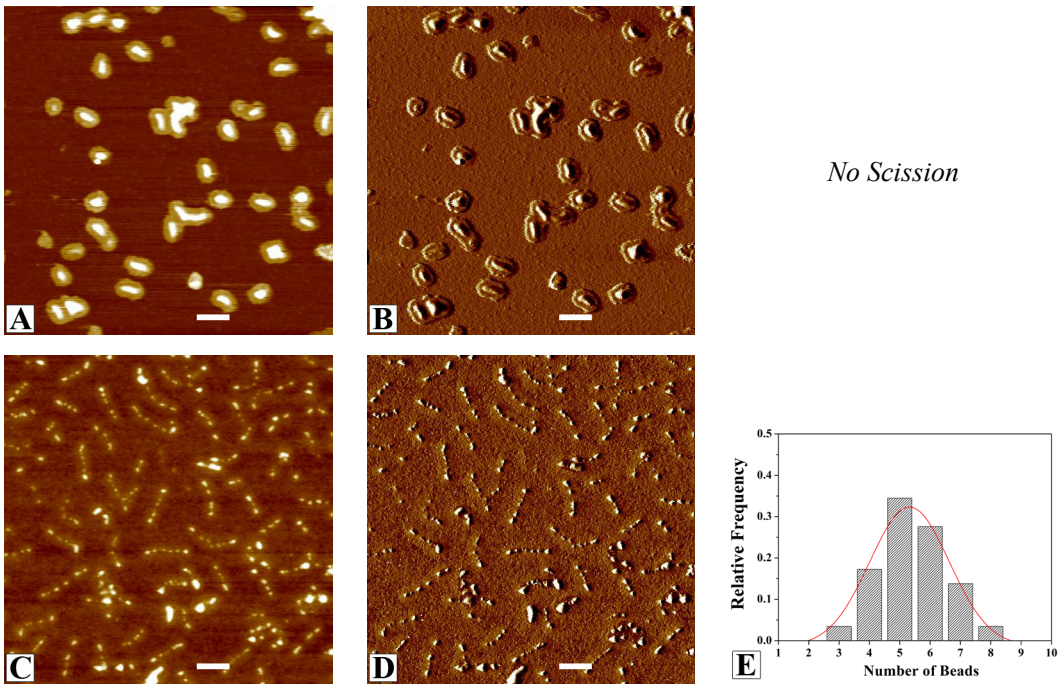

Figure 3-S5. Tapping-mode AFM height image, phase image and the corresponding histogram of N_{beads} distribution (bottom, for *ca.* 20 counted CPBs) of CPBs *b*-$[O_{430}D_{40}]_{750}$ (A, B) and *b*-$[O_{430}Dq_{40}]_{750}$ (C–E). CPBs were spin-coated on silicon surface from 0.02 g L^{-1} aqueous solution. Z-ranges are12 nm for height images and 10° for phase images. The scale bars correspond to 300 nm.

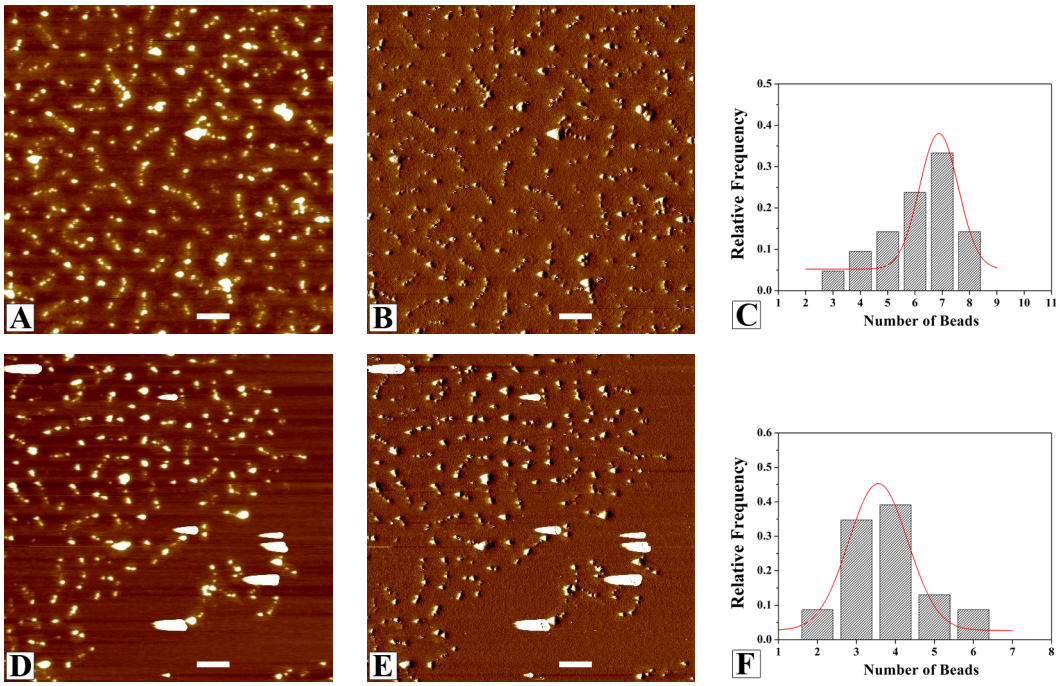

Figure 3-S6. Tapping-mode AFM height image, phase image and the corresponding histogram of N_{beads} distribution (for *ca.* 20 counted CPBs) of the CPB *b*-$[O_{430}D_{40}]_{750}$ spin-coated on mica surface from 0.02 g L^{-1} aqueous solution at pH 1.9 (A–C) and at pH 10.0 (D–F). Z-ranges are 8 nm for height images and 10° for phase images. The scale bars correspond to 300 nm.

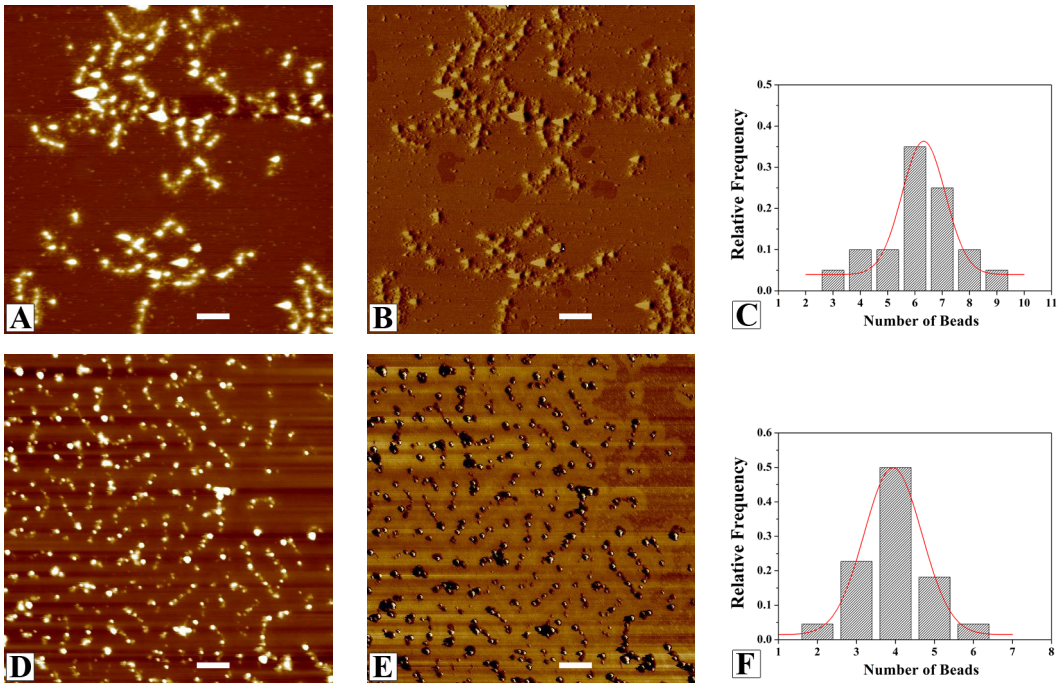

Figure 3-S7. Tapping-mode AFM height image, phase image and the corresponding histogram of N_{beads} distribution (for *ca.* 20 counted CPBs) of CPBs *b*-$[O_{430}Dq_{40}]_{750}$ (0.02 g L^{-1} aqueous solution, pH 5.5) containing 3.9 µM of $K_3[Co(CN)_6]$ (A–C), and 7.8 µM of $K_3[Co(CN)_6]$ (D–F). CPBs were spin-coated on freshly cleaved mica surface. Z-ranges are 8 nm for height images and 10° for phase images. The scale bars correspond to 300 nm.

Chapter 4

"CTA-shuttled" Grafting from Approach for Well-defined Cylindrical Polymer Brushes

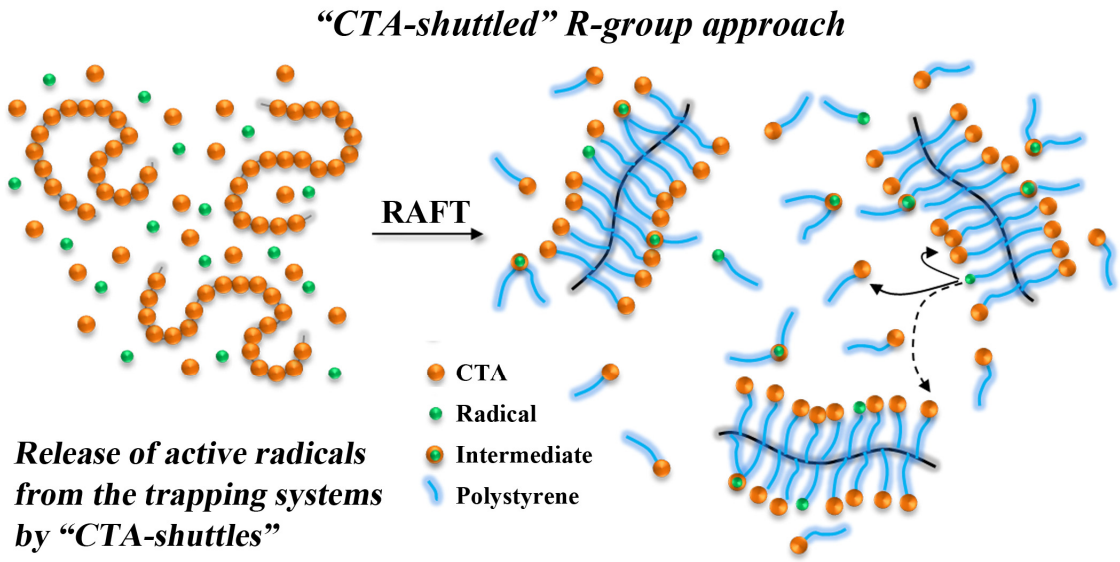

The results of this chapter have been published as:

"Revival of the R-Group Approach: A 'CTA-shuttled' Grafting from Approach for Well-defined Cylindrical Polymer Brushes *via* RAFT Polymerization"

by Zhicheng Zheng, Jun Ling* and Axel H. E. Müller*

in *Macromolecular Rapid Communications*, **2013**, DOI: 10.1002/marc.201300578. Re-printed with permission of Wiely-VCH.

Abstract

The synthesis of well-defined cylindrical polymer brushes (CPBs) from a linear polymer backbone with a high density of RAFT functionalities ("grafting from" approach) is challenging when the chain transfer agent (CTA) is attached to the backbone *via* its R-group. We propose here that the difficulties of the R-group approach in controlling the grafting polymerization are induced by the "entrapment" of active free radicals within individual growing CPBs. A facile "CTA-shuttled" R-group approach overcoming this entrapment effect is developed, and used to synthesize well-defined CPBs with polystyrene or poly(*tert*-butyl acrylate) branches and core-shell CPBs with polystyrene-*block*-poly(*N*-isopropylacrylamide) branches. The polydispersity index (PDI = 1.23) of the obtained CPBs with polystyrene branches is much lower than that from the conventional R-group approach (PDI = 2.18). Monte Carlo simulations confirm that the advantage of the "CTA-shuttled" R-group approach consists in the release of the active radicals from the trapping CPB systems. Based on the same principle, this approach is suitable for the synthesis of star polymers in the core-first strategy.

Keywords

Cylindrical polymer brushes, entrapment of active radicals, graft copolymer, reversible addition-fragmentation chain transfer (RAFT), R-group approach

4.1 Introduction

In recent years, well-defined branched polymer architectures, such as star polymers, comb polymers and cylindrical polymer brushes (CPBs), have received great research attention. CPBs consist of a linear backbone with densely tethered grafts.[1,2] The synthesis methods of star polymers involve the core-first and the arm-first strategy.[3] Similar to the star polymers, there are three general approaches to synthesize CPBs: "grafting from", "grafting onto" and "grafting through".[1,2]

Controlled free-radical polymerization (CRP) is most frequently applied for synthesizing CPBs and star polymers. Most commonly the "grafting from" (or core-first) approach is used *via* atom transfer radical polymerization (ATRP) by attaching initiator groups onto a linear backbone or small core. In contrast, reversible addition-fragmentation chain transfer (RAFT) polymerization is much less popular for preparing CPBs or stars. Here, the situation is complicated by two ways how to attach a RAFT chain transfer agent (CTA) on a backbone or core. In the Z-group approach, CTAs are tethered to a backbone or core *via* the stabilizing group (Z-group), whereas in the R-group approach the reinitiating group (R-group) is employed for this attachment.[3,4] As a consequence, the propagating radicals are either leaving the backbone and core during the grafting polymerization in the Z-group approach or being carried on in the R-group approach (Scheme 4–1 A and B).

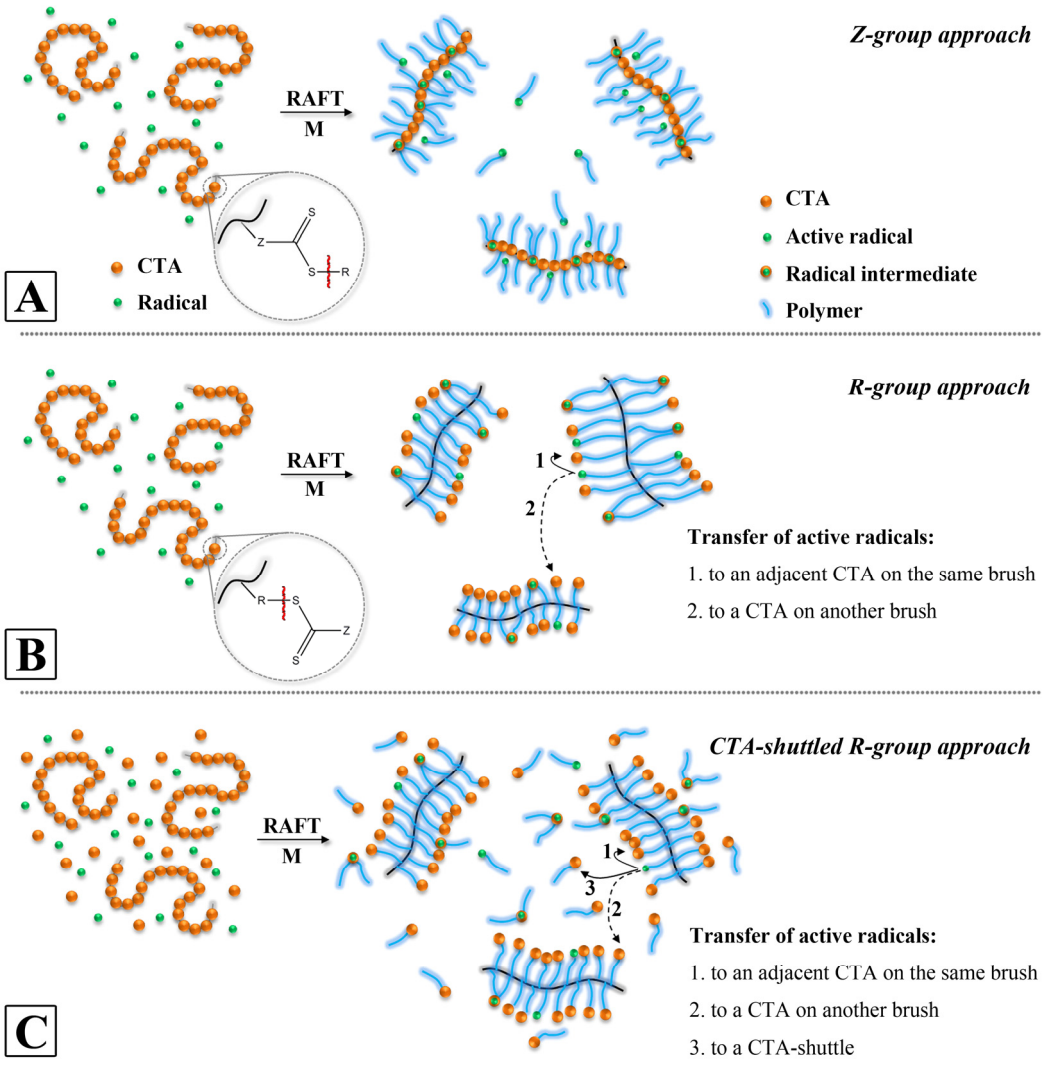

Scheme 4-1. Proposed mechanisms of the Z-group approach (A), the R-group approach (B) and the "CTA-shuttled" R-group approach (C) to synthesize CPBs. The red wavy line indicates where monomer will be inserted.

In the synthesis of star polymers the Z-group approach has been proven to provide better control over the grafting polymerization,[3,4] while the R-group approach is inferior except for few examples of rapidly propagating monomers, like vinyl acetate (VAc)[5,6] or *N*-vinylpyrrolidone (NVP).[7] However, in the synthesis of CPBs the Z-group approach suffers from steric shielding effect and shows limited control over the grafting of branches, and thus very few CPB systems have been synthesized *via* the Z-group approach.[3,8] Davis and coworkers have first employed the R-group approach to graft polystyrene (PS) branches from a densely CTA-functionalized backbone (polyCTA).[9] The resulting CPBs showed multimodal molecular weight distribution (MWD). After this at-

tempt, the R-group approach has been seldom used in synthesizing CPBs except several reports of loosely grafted systems[10-12] and CPBs with specific branches, like PVAc or PNVP.[13,14]

So far, the reason for the unsuitability of the conventional R-group approach for the synthesis of well-defined CPBs is still under debate. One straightforward explanation is the bi-radical brush-brush coupling during the grafting polymerization.[3,9,15] However, a significant amount of termination events is avoided by RAFT polymerization as a controlled radical polymerization technique,[16] as the grafting polymerization of PS has followed pseudo-first-order kinetics.[9] Furthermore, if the bi-radical coupling is the most critical reason for the broad MWD of CPBs, any kind of radical polymerization techniques should not be able to control the grafting of polymer branches from the backbone. However, the ATRP technique has demonstrated very good control over grafting processes resulting in well-defined CPBs with even more complex architectures.[1] Therefore, we propose here that the different polymerization mechanisms of ATRP and RAFT induce different capabilities of controlling the "grafting from" process. In an ATRP-based "grafting from" procedure, the catalysts, copper halides, can easily diffuse into and out of individual growing CPBs and thus ensure an effective "transfer" and an even distribution of the propagating sites among the CPBs. In contrast, in an R-group "grafting from" approach *via* RAFT, the transfer of the active radicals from one growing CPB to other CPBs is hindered, resulting in a broad MWD of the CPBs. It is well-known that the addition-fragmentation equilibrium between active propagating radicals and dormant radical intermediates in a typical RAFT process ensures that all polymer chains have equal probability to grow, resulting in a narrow MWD.[17] To fulfill this equilibrium, the active radicals must transfer efficiently among all CTAs. In the case of grafting polymer branches from a densely functionalized linear polyCTA, an active radical on a CPB can either transfer to an adjacent CTA on the same CPB (intramolecular transfer) or to a CTA on another CPB (intermolecular transfer), however, the latter is critically limited (Scheme 4–1B). This is attributed to the densely branched architecture of CPBs. When two different CPBs encounter, the sparse active radicals on one CPB are shielded among the poly-

mer branches rather than adding to CTAs on the other CPB. Therefore, the active radicals are trapped within individual CPBs, once they transfer onto the polyCTAs at the initial stage of the grafting polymerization. Thus, the CPBs carrying more active radicals grow faster, leading to a broad MWD of the CPBs.

To release the active radicals from the trapping CPB systems, we propose to add a certain amount of low-molecular-weight CTA (LMW-CTA) with the same structure of the pendant CTA units of the polyCTA into the polymerization system (Scheme 4–1C). These LMW-CTAs and their deriving linear polymers can serve as "shuttles" for active radicals among different propagating CPBs. In this "CTA-shuttled" R-group approach, active radicals on CPBs now have one highly possible transfer pathway, as they can add to a nearby CTA-shuttle to form a brush-shuttle radical intermediate (Scheme 4–1C). This radical intermediate can either fragment back to an active radical on the CPB and a dormant CTA-shuttle or into a dormant CTA on the CPB and a linear polymer carrying an active radical. This linear polymeric radical can transfer further to a surrounding CTA-shuttle instead of back to the original CPB. As a result, the active radicals will be transferred efficiently by the CTA-shuttles among different CPBs rather than being trapped within individual CPBs. The CPBs can propagate homogeneously leading to a narrow MWD, namely a satisfying control of the grafting polymerization.

To the best of our knowledge, the adding of extra ("free", "sacrificial") LMW-CTAs into grafting polymerization systems was, so far, only applied to overcome the heterogeneous nature of substrates in the synthesis of planar polymer brushes (polymers grafted on surfaces).[18-20] In such heterogeneous cases, without the free LMW-CTAs, the RAFT agents fragmented from the substrate were diluted in solution, resulting in a very low effective concentration of RAFT agents near the surface and thus an uncontrolled growth of polymer branches from the surface.[21] Thereby, the added free LMW-CTAs compensate and maintain the effective concentration of RAFT agents. This kind of heterogeneous challenge was also observed in the synthesis of planar polymer brushes using other polymerization techniques, such as ATRP[22] and nitroxide mediated radical polymerization (NMP),[23] where the adding of "sacrificial" initiators and nitroxides is required to keep the

effective concentration of the corresponding species, respectively. Generally, all the heterogeneous issues differ significantly from the "entrapment" effect in the synthesis of CPBs *via* the conventional R-group approach mentioned above. In our "CTA-shuttled" approach, we are utilizing an apparently similar method to overcome a different mechanism challenge.

In this article, the facile "CTA-shuttled" R-group approach is proven to be better than the conventional one in controlling the grafting of polymer branches from linear polyCTA with a high density of RAFT functionalities. The developed "grafting from" method is able to control the grafting polymerization of common monomers, such as styrene (S) and *tert*-butyl acrylate (*t*BA). Our proposed mechanism of the "CTA-shuttled" R-group approach is further confirmed by Monte Carlo simulations.

4.2 Results and Discussion

4.2.1 Synthesis of polyCTAs

Well-defined linear polyCTAs with high density of RAFT functionalities were successfully synthesized *via* two reaction steps (Scheme 4–2; for experimental details see Supporting Information). First, two poly(4-vinylbenzyl chloride) (PVBC) homopolymers with DPs of 30 and 120 as precursors were prepared *via* RAFT polymerization (Table 4–S1). The obtained PVBC precursors showed monomodal and narrow MWDs (PDI = 1.17, Figure 4–S1). Trithiocarbonate RAFT functionalities were then introduced *via* a subsequent polymer-analogous reaction of the PVBC precursors, where the chlorine was substituted by dodecyl trithiocarbonate. The ^{1}H-NMR spectra (Figure 4–S2) of the purified substituted products confirm a high functionalization degree of the polyCTAs (>90%, Table 4–S1). Nearly every repeating unit of the polyCTAs is a trithiocarbonate RAFT agent, with the benzyl group and the dodecyl group serving as the R-group and the Z-group, respectively. SEC analysis indicates that the obtained polyCTAs possess narrow MWDs (Figure 4–S1, PDI = 1.12 ~ 1.13). The high functionalization degree and the low polydispersity of the polyCTAs ensure their application in the preparation of CPBs *via* “grafting from” approach.

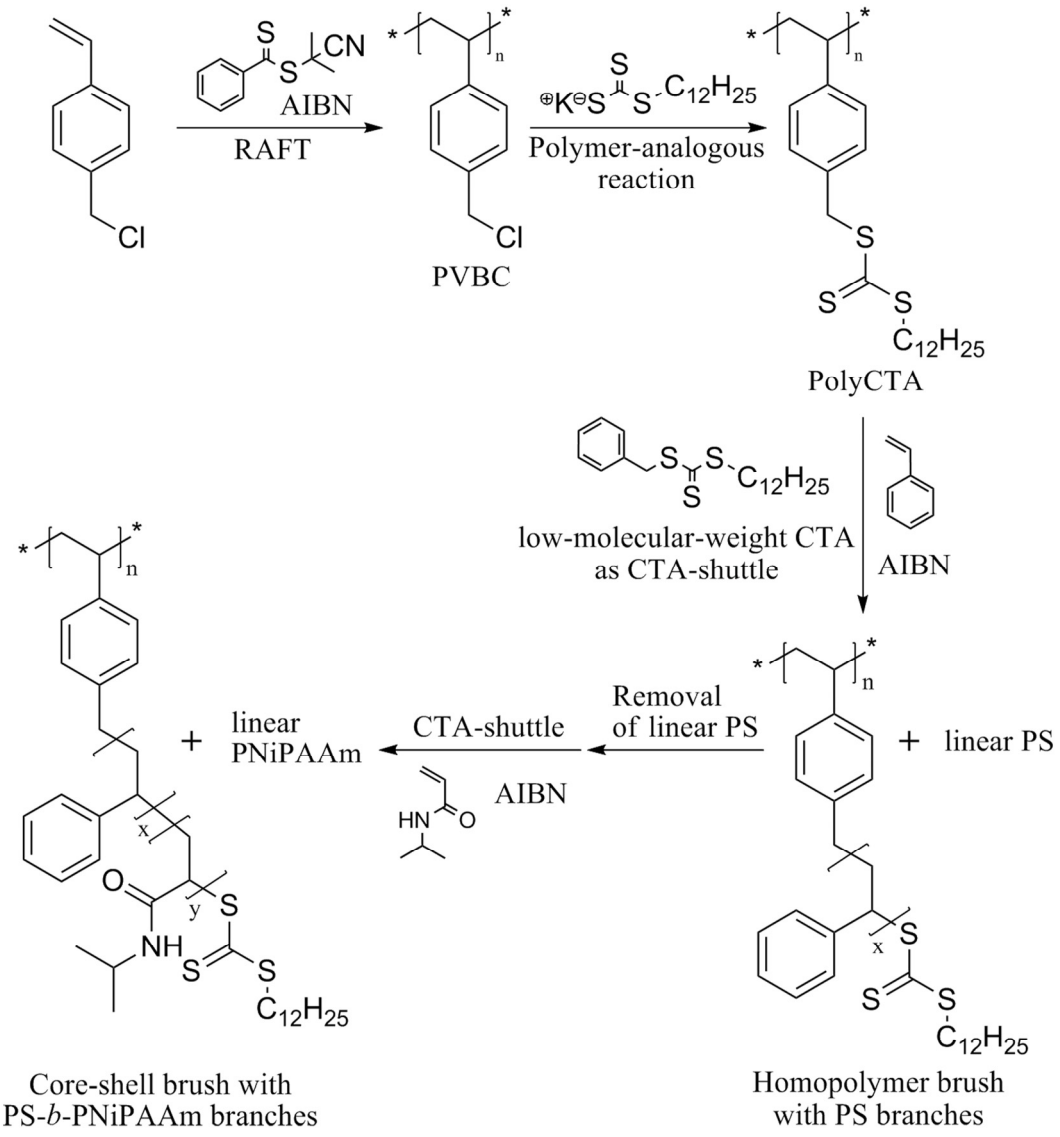

Scheme 4-2. Synthetic route to homopolymer CPB with PS branches (*b*-[S]) and core-shell CPB with PS-*b*-PNiPAAm branches (*b*-[SN]) from linear highly densely functionalized polyCTA *via* the "CTA-shuttled" R-group approach.

4.2.2 Grafting of polymer branches via the conventional R-group approach

The synthesis of CPBs using the conventional R-group approach was demonstrated in the grafting of polystyrene (PS) branches from the polyCTA with DP of 30 (PCTA-1), yielding brush *b*-$[S_{38}]_{30}$ having 30 side chains with an average DP of 38 (Table 4–1). We used AIBN as radical generator, PCTA-1 as polyCTA and anisole as solvent at 70°C. The con-

centrations of polyCTA and monomer were kept low to minimize the radical-radical coupling reaction and the Trommsdorf effect. The polymerization followed pseudo-first-order kinetics (Figure 4–1A), showing the character of a living radical polymerization. However, the evolution of the MWD measured by SEC did not obey the trend of a controlled radical polymerization (Figure 4–1B), as the distribution showed significant broadening even after a short polymerization time. The development of the apparent number-average molecular weight, $M_{n,app}$, and the PDI (linear PS standards) is shown in Figure 4–1C. The high PDI (above 2) of the obtained CPBs indicates that the conventional R-group approach cannot control the grafting of polymer branches from linear polyCTA with a high density of RAFT functionalities, which agrees with the results reported before.[9]

Table 4-1. Grafting of different polymer branches from polyCTAs by RAFT Polymerization.

brush	polyCTA	monomer	[M]:[CTA units]:[LMW-CTA]:[I][b]	time /h	brush polymers		linear polymers[c]	
					M_n (PDI)[d] /kDa	M_n[e] /kDa	M_n (PDI)[d] /kDa	M_n[e] /kDa
b-$[S_{38}]_{30}$[a]	PCTA-1	Styrene	200:1:0:0.3	11	127.2 (2.18)	--	--	--
b-$[S_{25}]_{30}$	PCTA-1	Styrene	200:1:1:0.3	26	54.5 (1.23)	144.9	3.8 (1.19)	5.1
b-$[S_{22}]_{120}$	PCTA-2	Styrene	200:1:1:0.3	22	113.1 (1.29)	408.5	3.3 (1.20)	3.8
b-$[T_{41}]_{30}$	PCTA-1	*t*BA	200:1:1:0.3	5	72.6 (1.07)	125.9	6.4 (1.24)	5.7
b-$[T_{46}]_{120}$	PCTA-2	*t*BA	200:1:1:0.3	5	163.9 (1.12)	503.6	8.0 (1.23)	6.8
b-$[S_{25}N_{11}]_{30}$	*b*-$[S_{25}]_{30}$	NiPAAm	200:1:1:0.3	8	47.4 (1.29)	--	1.4 (1.13)	--
b-$[S_{25}N_{300}]_{30}$	*b*-$[S_{25}]_{30}$	NiPAAm	1200:1:1:0.3	10	473.1 (1.20)	--	33.0 (1.16)	--

[a] without CTA-shuttle (low-molecular-weight CTA, LMW-CTA). [b] T = 70 °C (60 °C for *b*-$[S_{25}N_{11}]_{30}$); AIBN and benzyl dodecyl trithiocarbonate were used as initiator and LMW-CTA, respectively. [CTA units] indicates the total amount of CTA units carried on polyCTA. [c] Linear polymer chains growing from the LMW-CTAs. [d] Measured by SEC in THF (DMAc for *b*-[SN]) with a RI-detector using PS, P*t*BMA and PNiPAAm calibration for *b*-[S], *b*-[T] and *b*-[SN], respectively. [e] Measured by SEC in THF with a light scattering detector.

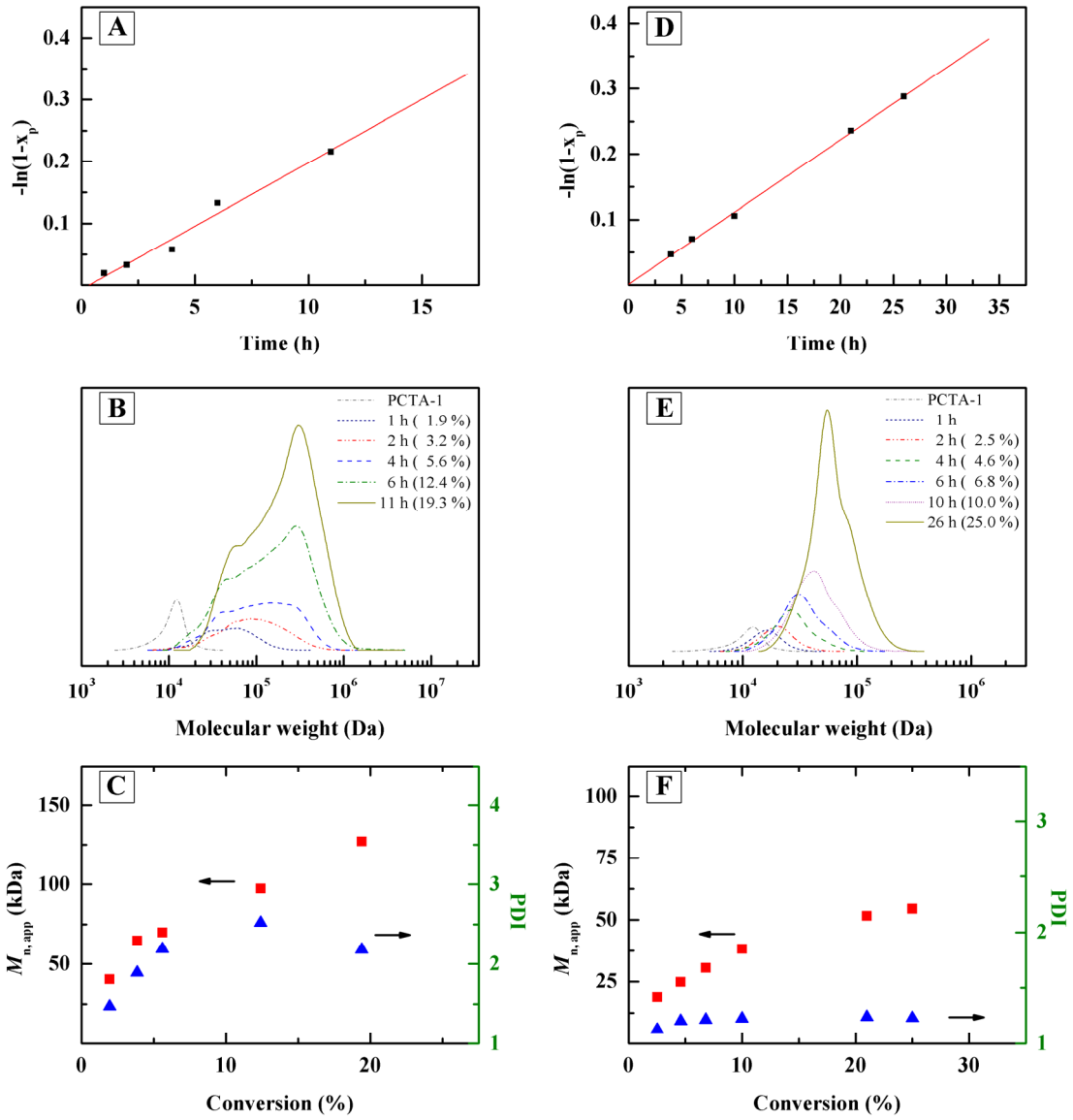

Figure 4-1. Preparation of CPB with PS branches *b*-$[S_{38}]_{30}$ *via* conventional R-group approach and *b*-$[S_{25}]_{30}$ *via* "CTA-shuttled" R-group approach. Pseudo-first-order plot for *b*-$[S_{38}]_{30}$ (A) and *b*-$[S_{25}]_{30}$ (D). Evolution of apparent MWD with time for *b*-$[S_{38}]_{30}$ (B) and *b*-$[S_{25}]_{30}$ (E), with the numbers in parentheses referring to the corresponding conversions. Development of $M_{n,app}$ and PDI with conversion for *b*-$[S_{38}]_{30}$ (C) and *b*-$[S_{25}]_{30}$ (F). Feed ratio [M]:[CTA units]:[LMW-CTA]:[I] = 200:1:0:0.3 and 200:1:1:0.3 for *b*-$[S_{38}]_{30}$ and *b*-$[S_{25}]_{30}$, respectively. All the samples were measured by SEC in THF with linear PS calibration. The results in (E) and (F) represent the brush part in the polymerization system.

4.2.3 Grafting of polymer branches via the "CTA-shuttled" R-group approach

Well-defined CPBs with different polymer branches were successfully prepared *via* the "CTA-shuttled" R-group approach. First, this was applied to graft PS branches from PCTA-1 (*b*-$[S_{25}]_{30}$, Table 4–1), as shown in Scheme 4–2. The only difference is the presence of one equivalent (relative to the total amount of CTAs on the polyCTA) of LMW-CTA with the same structure as the repeating unit of the polyCTA (Scheme 4–2). This "CTA-shuttled" grafting polymerization of PS also adheres to pseudo-first-order kinetics (Figure 4–1D), indicating a living radical polymerization. Excitingly, the evolution of the MWD is completely different from that of the conventional approach (Figure 4–1E). The MWD of the CPB part maintained monomodal and narrow, with only a small shoulder appearing at longer reaction times. The $M_{n,app}$ value increased with conversion, whereas the PDI stayed at a low level with the final value of 1.23 at a conversion of 25% (Figure 4–1F). The curvature in the $M_{n,app}$-conversion profile is attributed to the SEC separation mechanism, as highly branched polymers possess smaller hydrodynamic volume than linear ones with the same molecular weight. As expected, linear PS polymers were growing from the LMW-CTA during the "CTA-shuttled" grafting polymerization. These well-defined polymers with M_n = 3.8 kDa and PDI = 1.19 (Table 4–1) could be easily removed from the CPB *via* fractional precipitation (Figure 4–S3). The branching density of the CPB was estimated as 95% based on the M_n measured by SEC using a light scattering detector (see Supporting Information). By applying the same "CTA-shuttled" R-group approach, another CPB with PS branches was successfully grafted from the longer PCTA-2 (*b*-$[S_{22}]_{120}$, Table 4–1). The obtained well-defined CPBs indicate that the "CTA-shuttled" R-group approach is able to control the grafting of polymer branches from highly densely functionalized linear polyCTA.

In a similar way, well-defined CPBs with poly(*tert*-butyl acrylate) (P*t*BA) branches were prepared under even better control from different linear polyCTAs *via* the

"CTA-shuttled" R-group approach (*b*-$[T_{41}]_{30}$ and *b*-$[T_{46}]_{120}$, Table 4–1, Figure 4–S4 and Supporting Information). The final PDIs are 1.07 and 1.13, respectively, indicating the application potential of the "CTA-shuttled" R-group approach in the grafting of diverse polymer branches from linear polyCTA.

We then expanded the application of our new approach to the preparation of well-defined core-shell CPBs with block copolymer branches (Scheme 4–2, *b*-$[S_{25}N_{11}]_{30}$ and *b*-$[S_{25}N_{300}]_{30}$, Table 4–1). The homopolymer CPB *b*-$[S_{25}]_{30}$ with PS branches was selected as precursor for this more complex architecture. The monomer chosen for achieving the shell part was *N*-isopropylacrylamide (NiPAAm), which is known as a challenging monomer for ATRP. Both PNiPAAm grafting polymerizations succeeded, resulting in monomodal and narrow MWDs (Figure 4–S5). The $M_{n,app}$ of the core-shell CPB *b*-$[S_{25}N_{11}]_{30}$ with shorter PNiPAAm segments shows a slight increase from the homopolymer CPB precursor, while the *b*-$[S_{25}N_{300}]_{30}$ with longer PNiPAAm has an extremely high $M_{n,app}$ of 473.1 kDa (PNiPAAm calibration). The comparison of the ^{1}H-NMR spectrum of the core-shell CPB *b*-$[S_{25}N_{300}]_{30}$ (Figure 4–S2, line D) with that of the precursor *b*-$[S_{25}]_{30}$ (Figure 4–S2, line C) indicates the successful chain extension of the PS branches to PS-*b*-PNiPAAm ones. This confirms the capability of the "CTA-shuttled" R-group approach to prepare complex grafted polymer architectures. Due to the rather short backbone and long branches the CPB *b*-$[S_{25}N_{300}]_{30}$ is more star-like but serves as a proof of principle.

4.2.4 Monte Carlo simulation

To confirm the polymerization mechanisms discussed above, we applied the Monte Carlo method to simulate the kinetics of grafting PS branches *via* different approaches. The Monte Carlo method has been proven very powerful in studying various polymerization mechanisms including ATRP,[24] RAFT,[25,26] radical addition-coupling polymerization (RACP),[27] coordination polymerization[28] and ring-opening polymerization.[29]

The basic Monte Carlo algorithm applied in this work is the same as reported[24-27]

except a slight modification described as follows. In every "elemental reaction", known as a single Monte Carlo step, an active free radical is randomly selected to carry out propagation (with a monomer), chain transfer (with a further randomly selected CTA) or termination (with another randomly selected active radical) according to the reaction probabilities calculated by the set of Equations (4–1),

$$
\begin{aligned}
P_p &= \frac{N(\mathrm{M})}{N(\mathrm{M}) + C_{tr} \cdot N(\mathrm{Z}) + C_{term} \cdot N(\mathrm{R})} \\
P_{tr} &= \frac{C_{tr} \cdot N(\mathrm{Z})}{N(\mathrm{M}) + C_{tr} \cdot N(\mathrm{Z}) + C_{term} \cdot N(\mathrm{R})} \\
P_{term} &= \frac{C_{term} \cdot N(\mathrm{R})}{N(\mathrm{M}) + C_{tr} \cdot N(\mathrm{Z}) + C_{term} \cdot N(\mathrm{R})} \\
C_{tr} &= \frac{k_{tr}}{k_p} \\
C_{term} &= \frac{k_{term}}{k_p}
\end{aligned}
\tag{4–1}
$$

where P, N, k, M, Z and R stand for reaction probability, species amount, reaction rate constant, monomer, CTA and active radical, respectively. In the latter two cases, the location of the further selected CTA or active radical decides whether the occurring transfer or termination reaction is intramolecular or intermolecular. In an intermolecular reaction of an active radical locating on a CPB, the "entrapment effect" discussed above should be considered. Therefore, the collision (to perform an intermolecular reaction) of a CPB, where the selected active radical or CTA locates, with another molecule is divided by the number of branches on the CPB, as shown in Equation (4–2),

$$
X\left(\mathrm{Z\ or\ R@CPB}\right) = \frac{N\left(\mathrm{Z\ or\ R@CPB}\right)}{N\left(\mathrm{branches@CPB}\right)} \tag{4–2}
$$

where X is the corrected species amount. The same algorithm and parameters (see Supporting Information) were applied to simulate both the grafting of PS branches from a polyCTA (DP = 30) *via* the conventional R-group approach and that *via* the "CTA-shuttled" one, where the only difference is that the initial concentration ratio of the LMW-CTA-shuttles to the pendant CTAs on polyCTAs is 0:1 and 1:1, respectively.

Figure 4–2 summarizes the Monte Carlo simulation results at various conversions (noted on the left margin). The conversion-dependent M_n and PDI obtained from Monte Carlo simulations agree well with the experimental results as shown in Figure 4–2 B and D. It is to note that the simulation results are absolute molecular weights, which are reasonably becoming larger than the experimental apparent ones obtained from SEC measurements based on the hydrodynamic volume exclusion mechanism.

In the case of the conventional R-group approach, the simulated MWD becomes broad even at a low conversion of 1.9%. The PDI stays above 2 with increasing conversion (Figure 4–2 A and B), indicating the inhomogeneous growth of the CPBs. Additionally, we conducted another Monte Carlo simulation without termination reactions for the conventional R-group approach. The results (Figure 4–S6) are nearly the same as the simulation considering terminations, indicating that the "entrapment effect" is the major reason for the broad MWD.

In contrast, the simulation of the "CTA-shuttled" R-group approach illustrates narrow and monomodal MWD (PDI < 1.3) throughout the grafting polymerization with conversion of up to 28.0% (Figure 4–2 C and D), indicating the CPBs are propagating homogeneously. At this conversion, the linear PS chains deriving from the CTA-shuttles have also a narrow MWD with a PDI of 1.05. The Monte Carlo simulation confirms that the CTA-shuttles succeed in releasing active radicals from the trapping CPB systems and thus controlling the grafting polymerization.

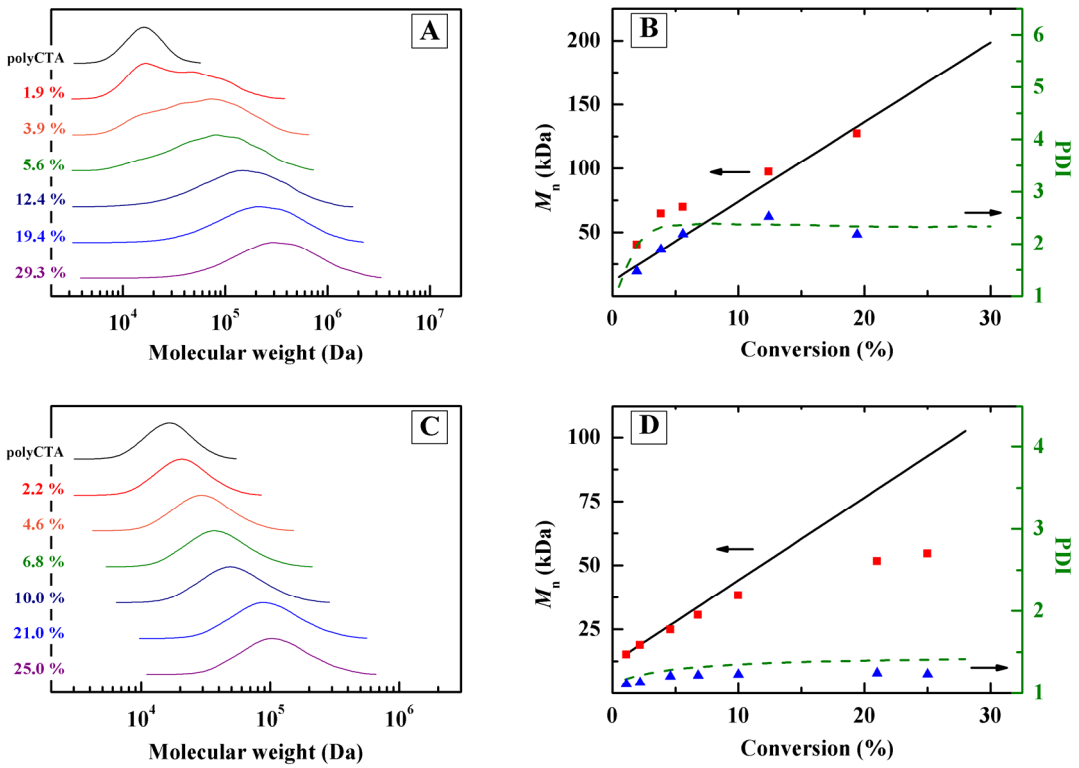

Figure 4-2. Evolution of MWD with conversion according to Monte Carlo simulations and the comparison between experimental values (M_n: square; PDI: triangle) and simulated ones (M_n: solid line; PDI: dashed line) for CPB with PS branches prepared *via* conventional R-group approach (A, B) and *via* “CTA-shuttled” one (C, D).

4.3 Conclusions

In the synthesis of CPBs with branches of common monomers *via* RAFT polymerization from linear polyCTAs, the conventional R-group approach suffers from an "entrapment effect" of active free radicals within individual propagating CPBs, which is responsible for broad MWDs of the CPBs. We have developed a facile "CTA-shuttled" R-group approach to release the entrapped active radicals from CPB systems and thus to prepare well-defined CPBs. Both the grafting polymerization experiment and the Monte Carlo simulation confirm the advantage of the "CTA-shuttled" R-group approach. Various well-defined complex polymer architectures including homopolymer CPBs with PS or P*t*BA branches and core-shell CPBs with PS-*b*-PNiPAAm branches are successfully synthesized by using the "CTA-shuttled" R-group approach. Furthermore, the idea of "CTA-shuttling" provides potential solutions for the control of other trapping polymerization systems, like the grafting of branches from a densely functionalized core in the synthesis of star polymers.

Acknowledgement

Z. Zheng appreciates a scholarship from the Elite Support Program of Bavaria. J. Ling sincerely thanks the Alexander von Humboldt Foundation for granting him a research fellowship. We thank Marietta Böhm (University of Bayreuth, MCII) for SEC measurements.

Supporting Information Available

Experimental section, details of polyCTA synthesis, ^{1}H-NMR spectra, SEC profiles of *b*-$[T_{41}]_{30}$, *b*-$[T_{46}]_{120}$, *b*-$[S_{25}N_{11}]_{30}$ and *b*-$[S_{25}N_{300}]_{30}$ brushes as well as Monte Carlo simulation details. This material is available from the Wiley Online Library or from the authors.

4.4 References

1. Sheiko, S. S.; Sumerlin, B. S.; Matyjaszewski, K. *Prog. Polym. Sci.* **2008,** *33*, 759-785.
2. Zhang, M.; Müller, A. H. E. *J. Polym. Sci. Part A: Polym. Chem.* **2005,** *43*, 3461-3481.
3. Gregory, A.; Stenzel, M. H. *Prog. Polym. Sci.* **2012,** *37*, 38-105.
4. Barner, L.; Davis, T. P.; Stenzel, M. H.; Barner-Kowollik, C. *Macromol. Rapid Commun.* **2007,** *28*, 539-559.
5. Bernard, J.; Favier, A.; Zhang, L.; Nilasaroya, A.; Davis, T. P.; Barner-Kowollik, C.; Stenzel, M. H. *Macromolecules* **2005,** *38*, 5475-5484.
6. Chaffey-Millar, H.; Stenzel, M. H.; Davis, T. P.; Coote, M. L.; Barner-Kowollik, C. *Macromolecules* **2006,** *39*, 6406-6419.
7. Nguyen, T. L. U.; Eagles, K.; Davis, T. P.; Barner-Kowollik, C.; Stenzel, M. H. *J. Polym. Sci. Part A: Polym. Chem.* **2006,** *44*, 4372-4383.
8. Mespouille, L.; Nederberg, F.; Hedrick, J. L.; Dubois, P. *Macromolecules* **2009,** *42*, 6319-6321.
9. Quinn, J. F.; Chaplin, R. P.; Davis, T. P. *J. Polym. Sci. Part A: Polym. Chem.* **2002,** *40*, 2956-2966.
10. Vosloo, J. J.; Tonge, M. P.; Fellows, C. M.; D'Agosto, F.; Sanderson, R. D.; Gilbert, R. G. *Macromolecules* **2004,** *37*, 2371-2382.
11. Carter, S. R.; England, R. M.; Hunt, B. J.; Rimmer, S. *Macromol. Biosci.* **2007,** *7*, 975-986.
12. Wu, D.; Song, X.; Tang, T.; Zhao, H. *J. Polym. Sci. Part A: Polym. Chem.* **2010,** *48*, 443-453.
13. Nese, A.; Kwak, Y.; Nicolaÿ, R.; Barrett, M.; Sheiko, S. S.; Matyjaszewski, K. *Macromolecules* **2010,** *43*, 4016-4019.
14. Nese, A.; Li, Y.; Averick, S.; Kwak, Y.; Konkolewicz, D.; Sheiko, S. S.; Matyjaszewski, K. *ACS Macro Lett.* **2011,** *1*, 227-231.

15. Cheng, C.; Khoshdel, E.; Wooley, K. L. *Macromolecules* **2007,** *40*, 2289-2292.
16. Moad, G.; Rizzardo, E.; Thang, S. H. *Aust. J. Chem.* **2005,** *58*, 379-410.
17. Litvinenko, G.; Müller, A. H. E. *Macromolecules* **1997,** *30*, 1253-1266.
18. Semsarilar, M.; Ladmiral, V.; Perrier, S. *J. Polym. Sci. Part A: Polym. Chem.* **2010,** *48*, 4361-4365.
19. Liu, J.; Zhang, L.; Shi, S.; Chen, S.; Zhou, N.; Zhang, Z.; Cheng, Z.; Zhu, X. *Langmuir* **2010,** *26*, 14806-14813.
20. Rowe, M. D.; Hammer, B. A. G.; Boyes, S. G. *Macromolecules* **2008,** *41*, 4147-4157.
21. Moad, G.; Chen, M.; Haussler, M.; Postma, A.; Rizzardo, E.; Thang, S. H. *Polym. Chem.* **2011,** *2*, 492-519.
22. Ohno, K.; Morinaga, T.; Koh, K.; Tsujii, Y.; Fukuda, T. *Macromolecules* **2005,** *38*, 2137-2142.
23. Rybak, A.; Warde, M.; Beyou, E.; Chaumont, P.; Bechelany, M.; Brioude, A.; Toury, B.; Cornu, D.; Miele, P.; Guiffard, B.; Seveyrat, L.; Guyomar, D. *Nanotechnology* **2010,** *21*, 145610.
24. He, J.; Zhang, H.; Chen, J.; Yang, Y. *Macromolecules* **1997,** *30*, 8010-8018.
25. Drache, M.; Schmidt-Naake, G. *Macromol. Chem. Phys.* **2012,** *213*, F74.
26. Drache, M.; Schmidt-Naake, G. *Macromol. Symp.* **2007,** *259*, 397-405.
27. Zhang, C.; Ling, J.; Wang, Q. *Macromolecules* **2011,** *44*, 8739-8743.
28. Ling, J.; Ni, X.; Zhang, Y.; Shen, Z. *Polymer* **2000,** *41*, 8703-8707.
29. Ling, J.; Chen, W.; Shen, Z. *J. Polym. Sci. Part A: Polym. Chem.* **2005,** *43*, 1787-1796.

4.5 Supporting Information

4.5.1 Experimental section

4.5.1.1 Materials

2-Cyano-2-propyl benzodithioate (CPrB, RAFT agent, 97%, aldrich), 1-dodecanethiol (DdSH, 98%, Aldrich), carbon disulfide (CS_2, 99%, Fluka) and potassium hydroxide (KOH, 85%, Roth) was purchased and used without further treatment. Benzyl dodecyl trithiocarbonate (BDdTT, RAFT agent) was synthesized according to literature method. 2, 2'-Azoisobutyronitrile (AIBN, 98%, Aldrich) was recrystallized from methanol. 4-Vinylbenzyl chloride (VBC, 90%, Aldrich), styrene (S, 99% Aldrich) and *tert*-butyl acrylate (*t*BA, 98%, Aldrich) were purified by passing through basic alumina columns before polymerizations. *N*-isopropylacrylamide (NiPAAm, 97%, aldrich) was recrystallized from a mixture of benzene and hexane (2:1). All solvents were of analytical grade and used as received.

4.5.1.2 Synthesis of PVBC precursors

In the preparation of PVBC with a degree of polymerization (DP) of 30, VBC (3.0 g, 19.7 mmol), CPrB (21.8 mg, 9.9×10^{-2} mmol) and AIBN (4.1 mg, 2.5×10^{-2} mmol) were placed in a flask and dissolved in 3 mL of anisole. The mixture was degassed with argon for 30 min. After an initial sample was taken for ^{1}H-NMR measurement, the mixture was heated to 80 °C. When a desired conversion was achieved, the polymerization was stopped by cooling the reaction mixture to room temperature. The contents were precipitated in methanol for twice. The polymer was filtered, redissolved in dioxane and freeze-dried overnight. Yield = 420 mg; THF-SEC (RI, PS calibration): M_n = 4.5 kDa, PDI = 1.17. In a similar procedure, PVBC with a DP of 120 was prepared with yield = 550 mg; THF-SEC (RI, PS calibration): M_n = 17.4 kDa, PDI = 1.17.

4.5.1.3 Synthesis of poly(4-vinylbenzyl dodecyl trithiocarbonate) (PVBDdTT) polyCTAs

KOH (85%, 216.3 mg, 3.3 mmol) was dissolved in 1 mL H_2O and added into an acetone solution (5 mL) of DdSH (663.0 mg, 3.3 mmol), with a white precipitate forming immediately. CS_2 (249.4 mg, 3.3 mmol) was added dropwise into the solution and the mixture became homogeneous with a yellow color. Then 10 mL THF solution of PVBC (DP = 30, 250 mg) was added dropwise. A precipitate of KBr formed immediately. The solution was stirred for 4 h, filtered and precipitated in methanol (twice). The polymer was collected, redissolved in dioxane and freeze-dried overnight. Yield = 620 mg; THF-SEC (RI, PS calibration): M_n = 10.2 kDa, PDI = 1.13. In a similar procedure, PVBDdTT polyCTA with a DP of 120 was prepared with yield = 600 mg; THF-SEC (RI, PS calibration): M_n = 32.1 kDa, PDI = 1.12.

4.5.1.4 Synthesis of homopolymer CPB with PS branches from polyCTA via conventional R-group approach

Styrene (1.0 g, 9.6 mmol), PVBDdTT polyCTA (DP = 30, 18.9 mg, containing 4.8×10^{-2} mmol CTA units) and AIBN (2.4 mg, 1.4×10^{-2} mmol) were placed in a flask and dissolved in 16 mL anisole. The mixture was degassed with argon for 30 min. After an initial sample was taken for ^{1}H-NMR measurement, the mixture was heated to 70 °C. The kinetics of polymerization was monitored by withdrawing samples for ^{1}H-NMR and THF-SEC measurements. When a desired conversion was achieved, the polymerization was stopped by cooling the reaction mixture to room temperature. The contents were precipitated in methanol for twice. The polymer was filtered, redissolved in dioxane and freeze-dried overnight. Yield = 180 mg; THF-SEC (RI, PS calibration): M_n = 127.2 kDa, PDI = 2.18.

4.5.1.5 Synthesis of homopolymer CPB with PS branches from polyCTA via "CTA-shuttled" R-group approach

Styrene (1.5 g, 14.4 mmol), PVBDdTT polyCTA (DP = 30, 28.4 mg, containing 7.2×10^{-2} mmol CTA units), low-molecular-weight CTA BDdTT as CTA-shuttle (26.5 mg, 7.2×10^{-2} mmol) and AIBN (3.6 mg, 2.2×10^{-2} mmol) were placed in a flask and dissolved in 21 mL anisole. The further treatment was the same as that *via* conventional R-group approach described above. Yield = 350 mg; THF-SEC (RI, PS calibration, CPB part): M_n = 54.5 kDa, PDI = 1.23; THF-SEC (RI, PS calibration, linear polymer part): M_n = 3.8 kDa, PDI = 1.19. Furthermore, the CPB part was separated by slowly adding methanol into a THF solution of the freeze-dried polymer (50 mg/mL), leading to a fractional precipitation of the brush. In a similar procedure, PS branches were grafted from PVBDdTT polyCTA with a DP of 120 with yield = 220 mg; THF-SEC (RI, PS calibration, CPB part): M_n = 113.1 kDa, PDI = 1.29; THF-SEC (RI, PS calibration, linear polymer part): M_n = 3.3 kDa, PDI = 1.20.

4.5.1.6 Synthesis of homopolymer CPB with P*t*BA branches from polyCTA via "CTA-shuttled" R-group approach

*t*BA (0.85 g, 6.6 mmol), PVBDdTT polyCTA (DP = 30, 13.1 mg, containing 3.3×10^{-2} mmol CTA units), low-molecular-weight CTA BDdTT as CTA-shuttle (12.2 mg, 3.3×10^{-2} mmol) and AIBN (1.7 mg, 1.0×10^{-2} mmol) were placed in a flask and dissolved in 12 mL anisole. The further treatment was similar to that in the grafting of PS branches *via* "CTA-shuttled" R-group approach described above, with a methanol/H_2O (1/1) mixture added into a THF solution. Yield = 320 mg; THF-SEC (RI, P*t*BMA calibration, CPB part): M_n = 72.6 kDa, PDI = 1.07; THF-SEC (RI, P*t*BMA calibration, linear polymer part): M_n = 6.4 kDa, PDI = 1.24. In a similar procedure, P*t*BA branches were grafted from PVBDdTT polyCTA with a DP of 120 with yield = 380 mg; THF-SEC (RI, P*t*BMA calibration, CPB part): M_n = 163.9 kDa, PDI = 1.12; THF-SEC (RI, P*t*BMA calibration, linear polymer part): M_n = 8.0 kDa, PDI = 1.23.

4.5.1.7 Synthesis of core-shell CPB with PS-*b*-PNiPAAm branches via "CTA-shuttled" R-group approach

NiPAAm (400 mg, 3.5 mmol), homopolymer CPB with PS branches ($DP_{backbone}$ = 30, 60 mg, containing 1.8×10^{-2} mmol CTA units), low-molecular-weight CTA BDdTT as CTA-shuttle (6.5 mg, 1.8×10^{-2} mmol) and AIBN (0.9 mg, 5.3×10^{-3} mmol) were placed in a flask and dissolved in 4 mL dioxane. The mixture was degassed with argon for 30 min and then heated to 60 °C. When a desired conversion was achieved, the polymerization was stopped by cooling the reaction mixture to room temperature. The contents were precipitated in diethyl ether for twice. The polymer was filtered, redissolved in dioxane and freeze-dried overnight. Yield = 80 mg; DMAc-SEC (RI, PNiPAAm calibration, CPB part): M_n = 47.4 kDa, PDI = 1.29; DMAc-SEC (RI, PNiPAAm calibration, linear polymer part): M_n = 1.4 kDa, PDI = 1.13. In a similar procedure (T = 70 °C), block copolymer branches with a longer PNiPAAm block were grafted from homopolymer CPB with PS branches ($DP_{backbone}$ = 30) with yield = 300 mg; DMAc-SEC (RI, PNiPAAm calibration, CPB part): M_n = 473.1 kDa, PDI = 1.20; DMAc-SEC (RI, PNiPAAm calibration, linear polymer part): M_n = 33.0 kDa, PDI = 1.16.

4.5.1.8 Characterization methods

Size exclusion chromatography (SEC) using tetrahydrofuran (THF) as eluent (THF-SEC) was performed at a flow rate of 1.0 mL/min at room temperature. Column set: 5 µm SDV gel, 10^2, 10^3, 10^4, and 10^5 Å, 30 cm each (PSS, Mainz); detectors: refractive index (RI), UV (254 nm). PS and poly(*tert*-butyl methacrylate) (P*t*BMA) calibration curves were used to calibrate the columns. SEC using dimethyl acetamide (DMAc) with 0.05% lithium bromide as eluent (DMAc-SEC) was conducted at an elution rate of 0.8 mL/min at 60 °C. Columns include one pre-column and two analytical columns (PSS GRAM, 10^2 and 10^3 Å pore size, 7 µm particle size). PNiPAAm calibration curve was used to calibrate the columns. SEC equipped with a light scattering detector (SEC-LS) was running at a flow rate of 0.8 mL/min at 26 °C using THF as eluent. Column set: 5 µm SDV gel,

10^3, 10^5 and 10^8 Å, 30 cm each (PSS, Mainz).

^{1}H-nuclear magnetic resonance spectroscopy (^{1}H-NMR) measurements were carried out on a Bruker AC-300 instrument at room temperature in $CDCl_3$.

4.5.2 Synthesis of polyCTAs

Table 4-S1. Synthesis of well-defined polyCTAs based on PVBC.

polymer	precusor	[M]:[CTA]:[I]	time /h	M_n[c] /kDa	PDI[c]	DP[d]	$f_{mod.}$[e]
PVBC-1	--	200:1:0.25[a]	4	4.5	1.17	30	--
PVBC-2	--	600:1:0.25[a]	12	17.4	1.17	120	--
PCTA-1	PVBC-1[b]	--	4	10.2	1.13	30	0.95
PCTA-2	PVBC-2[b]	--	6	32.1	1.12	120	0.90

[a] RAFT polymerization at 80 °C; 2-cyano-2-propyl benzodithioate (CPrB) and AIBN were used as CTA and initiator, respectively. [b] Polymer-analogous reaction of PVBC with $C_{12}H_{25}SC(=S)S^-K^+$ at RT. [c] Measured by SEC in THF with polystyrene calibration. [d] DP of PVBC was calculated from the conversion measured by ^{1}H-NMR. [e] Modification degree of the polymer-analogous reaction was calculated from ^{1}H-NMR data of PCTA.

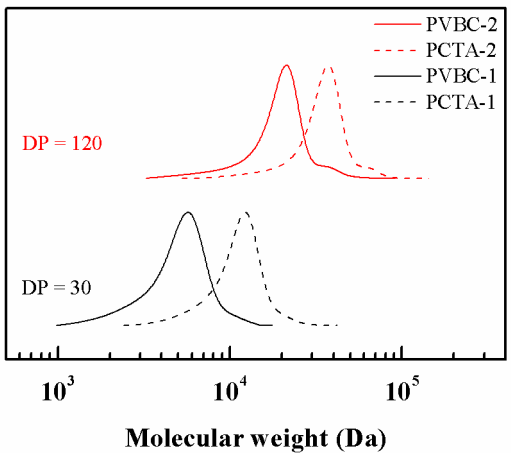

Figure 4-S1. MWDs for PVBC precursors and polyCTAs measured by SEC in THF with PS calibration.

4.5.3 ^{1}H-NMR spectra of precursor, polyCTA and CPBs

The signals of dodecyl protons (e) are observed in spectrum B (PCTA-1). The ratio of the integral of the signal at 3.2 ppm (methylene protons of dodecyl group adjacent to thiocarbonyl group) to that at 4.4 ppm (methylene protons of benzyl group) indicates a functionalization degree of the polyCTAs of 95%.

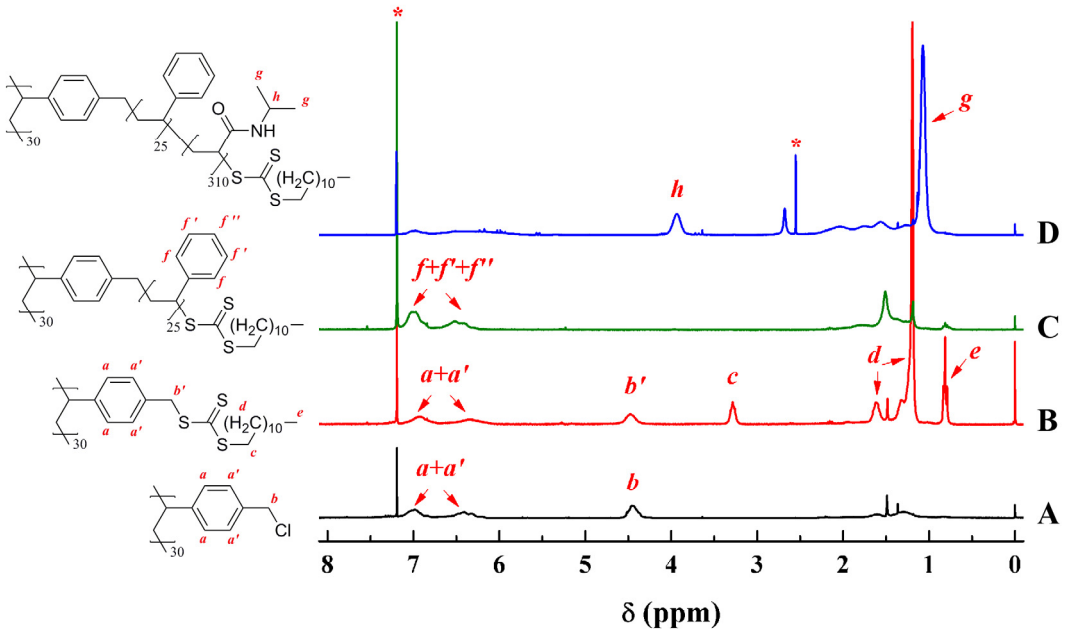

Figure 4-S2. ^{1}H-NMR spectra of precursor PVBC-1 (A), linear polyCTA PCTA-1 (B), homopolymer CPB *b*-$[S_{25}]_{30}$ (C) and core-shell CPB *b*-$[S_{25}N_{300}]_{30}$ (D). All the samples were measured in $CDCl_3$.

4.5.4 Removal of linear polymers from CPBs

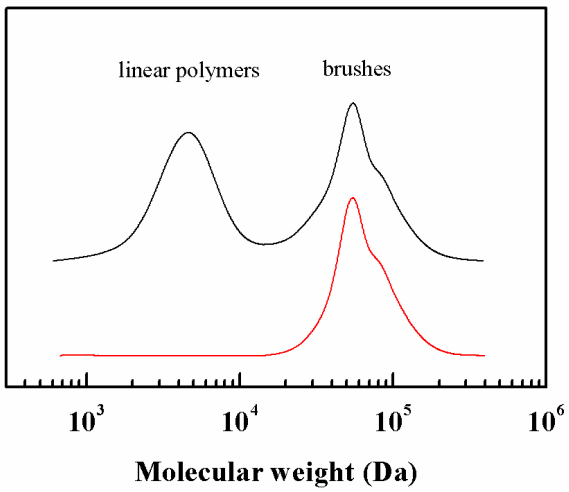

Figure 4-S3. Removal of linear polymers growing from CTA-shuttles from the CPBs *via* fractional precipitation. Black line: *b*-$[S_{25}]_{30}$ before fractional precipitation; red line: *b*-$[S_{25}]_{30}$ after fractional precipitation.

4.5.5 Calculation of branching density of CPBs

The branching density is calculated based on M_n measured by SEC using a multi-angle light scattering (MALS) detector according to Equation (4–S1),

$$\text{branching density} = \frac{M_{\text{n, brush}}}{M_{\text{n, linear}} \cdot DP_{\text{n, backbone}}} \qquad (4\text{–S1})$$

where $M_{n,brush}$ and $M_{n,linear}$ are the MALS-SEC measured number-averaged molecular weight of CPBs and linear polymers growing from CTA-shuttles, respectively. A premise is that the polymer branches on the CPBs have the same length as the linear polymers deriving from CTA-shuttles.

4.5.6 Grafting of P*t*BA branches via the "CTA-shuttled" R-group approach

In both P*t*BA grafting procedures, the MWD retained a monomodal, sharp peak throughout the polymerization (Figure 4–S4 A and B), with no shoulder observed even at higher

conversions (above 40%). Figure 4–S4C shows the $M_{n,app}$- and PDI-conversion profiles of both the grafting polymerizations. As expected, the $M_{n,app}$ of the CPBs increased with the conversion, with the PDI remaining low. The final PDI of the CPB *b*-$[T_{41}]_{30}$ and *b*-$[T_{46}]_{120}$ is 1.07 and 1.13, respectively.

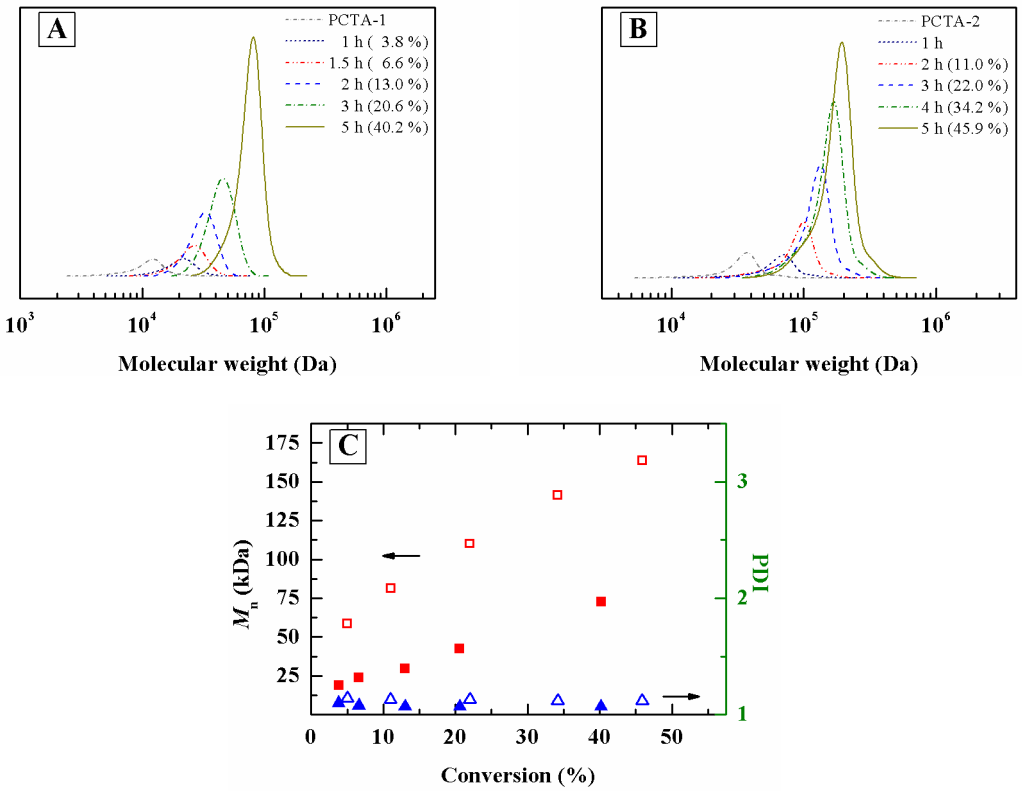

Figure 4-S4. Preparation of CPBs with P*t*BA branches *via* "CTA-shuttled" R-group approach. Evolution of MWD with time for *b*-$[T_{41}]_{30}$ (A) and for *b*-$[T_{46}]_{120}$ (B), with the numbers in parentheses referring to the corresponding conversions. Development of $M_{n,app}$ and PDI with conversion (C), with the solid and open symbols referring to *b*-$[T_{41}]_{30}$ and *b*-$[T_{46}]_{120}$, respectively. All the samples were measured by SEC in THF with P*t*BMA calibration (PS calibration for polyCTAs).

4.5.7 Grafting of PS-*b*-PNiPAAm branches via the "CTA-shuttled" R-group approach

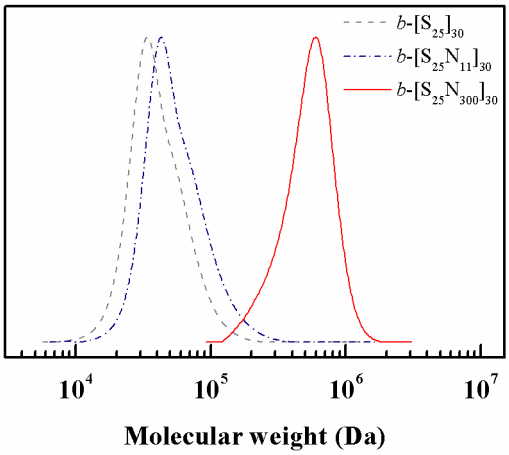

Figure 4-S5. Apparent MWDs for core-shell CPB *b*-$[S_{25}N_{11}]_{30}$ and *b*-$[S_{25}N_{300}]_{30}$ prepared *via* "CTA-shuttled" R-group approach. The homopolymer CPB precursor *b*-$[S_{25}]_{30}$ is shown for comparison. All samples were measured by SEC in DMAc with PNiPAAm calibration.

4.5.8 Monte Carlo simulation

Monte Carlo simulation was programmed in a MATLAB environment according to the reported algorithm with the modification mentioned in manuscript. Three types of reactions are shown in Equation 4–S2 - S4, where P*, CTA, PCTA*P and P represent active free radicals, trithiocarbonate CTA species, dormant radical intermediate, and terminated polymers with neither free radicals nor CTA groups, respectively. The subscripts *n* and *m* denote the DPs of styrene units in the polymeric chain.

$$P_n^* + M \longrightarrow P_{n+1}^* \qquad (4\text{–}S2)$$

$$P_n^* + P_mCTA \rightleftharpoons P_mCTA^*P_n \rightleftharpoons P_m^* + P_nCTA \qquad (4\text{–}S3)$$

$$P_n^* + P_n^* \longrightarrow P_{n+m} \qquad (4\text{–}S4)$$

All parameters are using experimental ones. The reaction rate constant ratios of k_{tr} (transfer) and k_d (termination) to k_p (propagation) are expressed as $C_{tr}=k_{tr}/k_p=460$[2-5] and $C_d=k_d/k_p=2$. The value of C_d was the only tunable parameter in the simulation and it was optimized to be 2 in simulation. Simulation scale, *i.e.* the initial number of styrene mo-

nomers, is $N(M)=3.3\times10^{7}$ to 1.1×10^{8}, which involves a reaction volume on the order of 10^{-16} L. The simulated results are reproducible and parallel when repeating running the Monte Carlo program, which indicates very good convergence in the scale used.

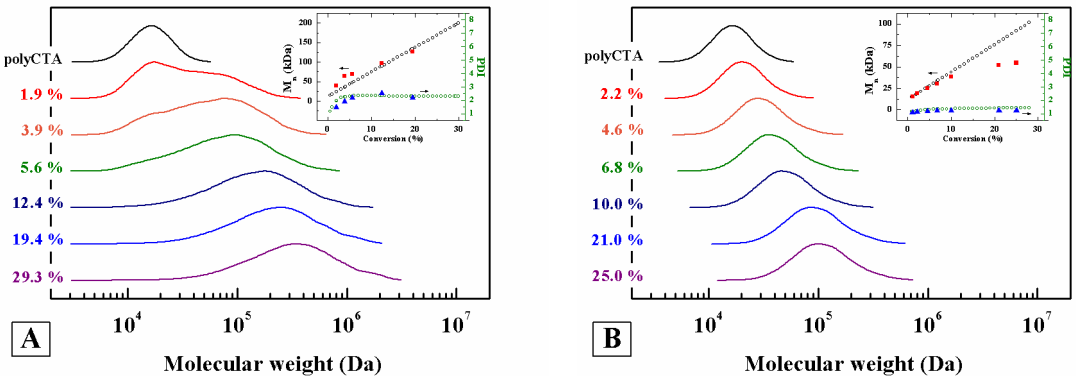

Figure 4-S6. Evolution of molecular weight distribution with conversion for CPB with PS branches prepared *via* conventional R-group approach (A) and *via* CTA-shuttled one (B) according to Monte Carlo simulations without termination reactions. Insets show the comparison between experimental values (from *b*-$[S_{38}]_{30}$ and *b*-$[S_{25}]_{30}$; M_n: red solid square; PDI: blue solid triangle) and those from Monte Carlo simulations (M_n: black hollow circle; PDI: green hollow circle).

4.5.9 References

1. Harrisson, S. *Macromolecules* **2009,** *42*, 897-898.
2. Drache, M.; Schmidt-Naake, G. *Macromol. Chem. Phys.* **2012**, *213*, F74.
3. Konkolewicz, D.; Siauw, M.; Gray-Weale, A.; Hawkett, B. S.; Perrier, S. *J. Phys. Chem. B* **2009**, *113*, 7086-7094.
4. Drache, M.; Schmidt-Naake, G. *Macromol. Symp.* **2007**, *259*, 397-405.
5. Drache, M.; Schmidt-Naake, G. *Macromol. Symp.***2008**, *271*, 129-136.

Chapter 5

Rod-like Nano-Light Harvester

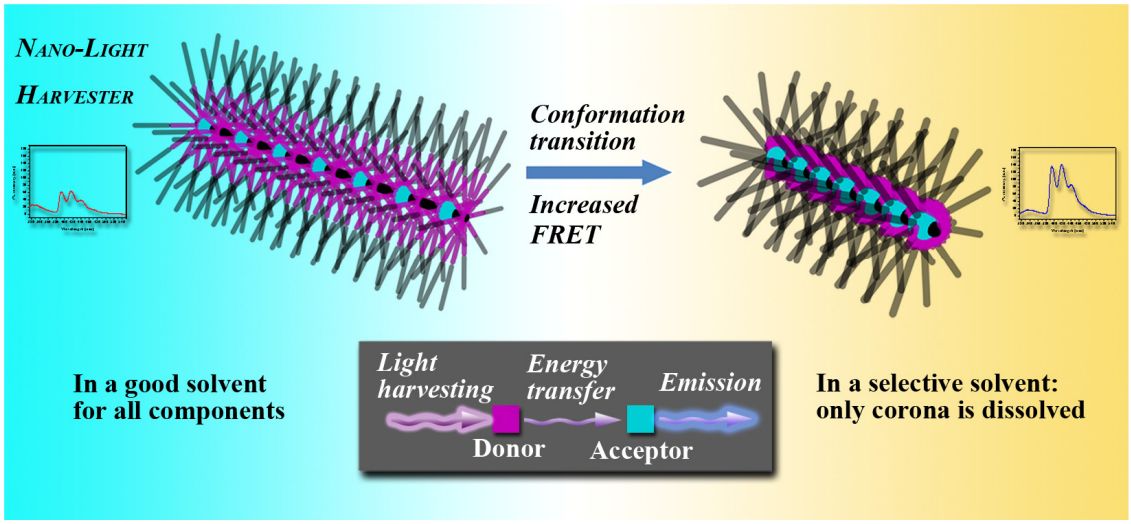

The results of this chapter have been published as:

"Rod-like Nano-Light Harvester"

by Jun Ling,* Zhicheng Zheng, Anna Köhler and Axel H. E. Müller*

in *Macromolecular Rapid Communications*, **2013**, DOI: 10.1002/marc.201300785. Reprinted with permission of Wiely-VCH.

Abstract

Imitating the natural "energy cascade" architecture, we present a single-molecular rod-like nano-light harvester (NLH) based on a cylindrical polymer brush. Block copolymer side chains carrying (9,9-diethylfluoren-2-yl)methyl methacrylate units as light absorbing antennae (energy donors) are tethered to a linear polymer backbone containing 9-anthracenemethyl methacrylate units as emitting groups (energy acceptors). These NLHs exhibit very efficient energy absorption and transfer. Moreover, we successfully manipulate the energy transfer by tuning the donor-acceptor distance.

Keywords

Light harvesting, Förster resonance energy transfer, cylindrical polymer brushes, graft copolymer, atom transfer radical polymerization (ATRP)

5.1 Introduction

Energy is the currency in the universe. As producers in the biological world, bacteria and plants have been harvesting, transferring and storing solar light energy for millions of years. In a natural light-harvesting and energy transfer system with high efficiency, one fundamental concept is the "energy cascade" architecture, *i.e.,* pigments acting as light absorbing antennae surrounding the reaction center with a distance up to 2 nm (Figure 5–S1 in Supporting Information).[1-4] In such ring-like geometries, solar energy is absorbed and transferred into the center where it is then transformed into chemical energy for use in the next step in photosynthesis process.[1-4] In the last decades, the continuously growing demand for energy encouraged researchers to design molecules mimicking living nature to harvest and store solar energy. Some synthetic light-harvesting compounds have been reported,[5] including linear molecules,[6,7] star-shaped and dendritic polymers,[8-10] macro-cyclic polymers,[11] non-covalent bonding self-assembled compounds,[12,13] and supramole-cular nano-tubes.[14]

Here we report a novel rod-like nano-light harvester (NLH) architecture based on a cylindrical core-shell polymer brush (CPB)[15,16] mimicking a natural "energy cascade" system. In this architecture, light absorbing antennae, (9,9-diethylfluoren-2-yl)methyl methacrylate (FlMA) units, are located in a cylinder "wrapping" the backbone embedded with dilute energy acceptors, 9-anthracenemethyl methacrylate (AnMA) units (Figure 5–S1 and Scheme 5–1). The FlMA units absorb energy and concentrate it into the center by Förster resonance energy transfer (FRET) instead of releasing or consuming it in the antenna layer. This architecture builds a string of natural "energy cascade" structures. As a most promising advantage, it combines both a fixed concentric location of antennae and dilutes the energy acceptors.

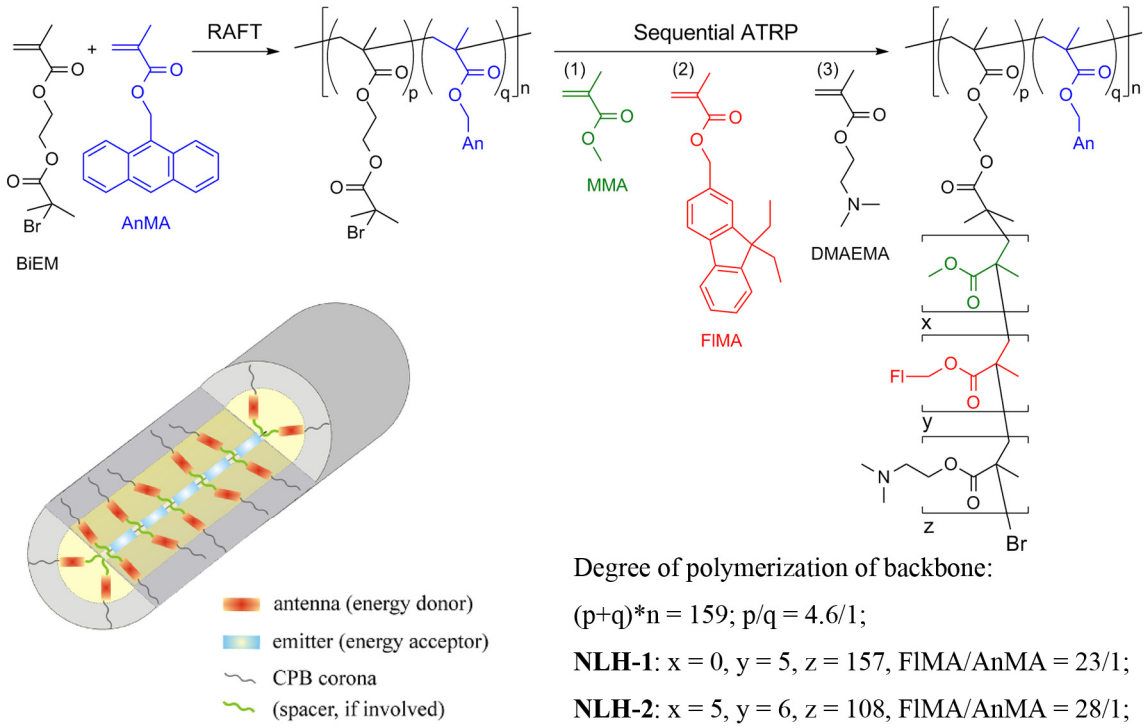

Scheme 5-1. Synthesis and illustration of rod-like nano-light harvester $(PBIEM_{0.82}$-*co*-$PAnMA_{0.18})_{159}$-*g*-($PMMA_x$-*b*-$PFlMA_y$-*b*-$PDMAEMA_z$).

5.2 Results and Discussion

Three NLH systems were synthesized and characterized as summarized in Table 5–1. The polymer synthesis is outlined in Scheme 5–1, and more details are given in the Supporting Information. Taking **NLH-1** as an example, AnMA units acting as energy acceptors and light emitters are distributed along the backbone by a controlled random copolymerization with 2-(2-bromoisobutyryloxy)ethyl methacrylate (BIEM). The molar fraction of AnMA is less than 1/5.6 which does not reduce the density of side chains of the final CPB architecture. FlMA units as light absorbers and energy donors, building the inner block of the side chains, generate a dense layer "wrapping" the backbone because of the density of CPB side chains. The outer corona of 2-(dimethylamino)ethyl methacrylate (DMAEMA) segments was configured long enough to ensure good solubility in various solvents including water and, more importantly, to induce steric repulsion among side chains which results in a stretching of the backbone and thus a one-dimensional rod-like conformation

of the NLH.[15,16] Both RuO_4-stained transmission electron microscopy (TEM) and atomic force microscopy (AFM) images confirm the rod-like one-dimensional conformation of NLH molecules with stretched backbone length of *ca.* 40 nm (Figure 5–S2 in Supporting Information).

Table 5-1. Rod-like nano-light harvester samples.

Sample	Composition[a]	M_n[b] (kDa)	PDI[b]
NLH-1	$(PBIEM_{0.82}$-*co*-$PAnMA_{0.18})_{159}$-*g*-$(PFlMA_5$-*b*-$PDMAEMA_{157})$	554	1.22
NLH-2	$(PBIEM_{0.82}$-*co*-$PAnMA_{0.18})_{159}$-*g*-$(PMMA_5$-*b*-$PFlMA_6$-*b*-$PDMAEMA_{108})$	767	1.22
NLH-3	$(PBIEM_{0.82}$-*co*-$PAnMA_{0.18})_{159}$-*g*-$(PMMA_{15}$-*b*-$PFlMA_{18}$-*b*-$PDMAEMA_{62})$	381	1.35

[a] BIEM = 2-(2-bromoisobutyryloxy)ethyl methacrylate; AnMA = 9-anthracenemethyl methacrylate; FlMA = 2-(9,9-diethylfluorene)methyl methacrylate; DMAEMA = 2-(dimethylamino)ethyl methacrylate.
[b] Measured by SEC in dimethylacetamide with 0.05% LiBr using PDMAEMA calibration.

Figure 5–1 shows the absorption and fluorescence spectra of the donor, FlMA, and the acceptor, AnMA. The spectra indicate that there is sufficient overlap between the FlMA emission and the AnMA absorption to allow for Förster type resonance energy transfer. In addition, the spectral range of the FlMA and the AnMA emission are well separated thus facilitating a clear data analysis.

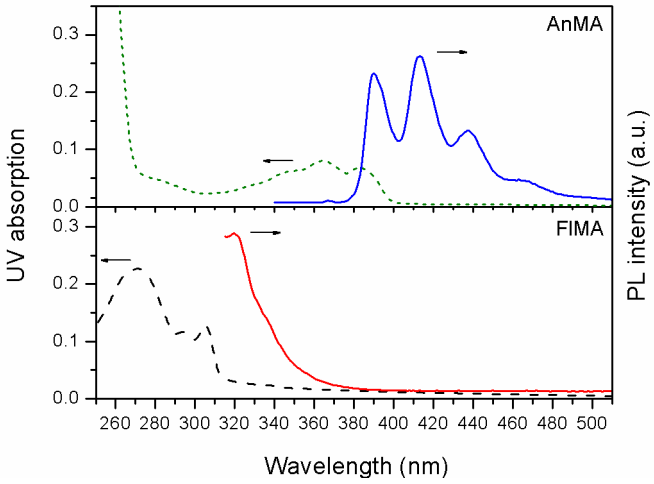

Figure 5-1. Absorption (optical density) and emission spectra of FlMA and AnMA taken at 1×10^{-5} mol/L in THF.

Figures 5–2 A and B show the emission from **NLH-1** in THF and in water for excitation at 305 nm. At this wavelength, the donor absorption has a maximum and exceeds the acceptor absorption by a factor of 10. By comparison with Figure 5–1, the band from 380 to 500 nm can be assigned to emission from AnMA units, while the band from 310 nm to 380 nm is due to emission from FlMA.[11,17,18] For comparison, the emission resulting from a mixture of 9,9-diethyl-2-hydroxymethylfluorene (FlOH) and 9-anthracenemethanol (AnOH), the precursors of FlMA and AnMA, at the same concentrations is also shown (Figure 5–2C). When FlOH and AnOH are not connected, only emission from FlOH is observed. This is due to the fact that at 305 nm, almost exclusively FlOH can be excited and without connection (Figure 5–1), the distances between FlOH and AnOH in solution are too large for energy transfer to occur.[1-4] When AnMA is attached to the antennae FlMA, the relative intensity of the FlMA emission is strongly reduced while emission from AnMA appears. This is a first clear indication that energy transfer takes place from FlMA to AnMA. When changing the solvent from THF to water, the relative ratio of FlMA to AnMA emission decreases further, implying more energy transfer to occur when **NLH-1** is in water than in THF (Figure 5–2B). According to the above observation, the FlMA units work collectively to absorb light and then quantitatively transfer the energy to the inner AnMA units. Therefore, our rod-like NLH architecture successfully realizes the

"energy cascade" concept.

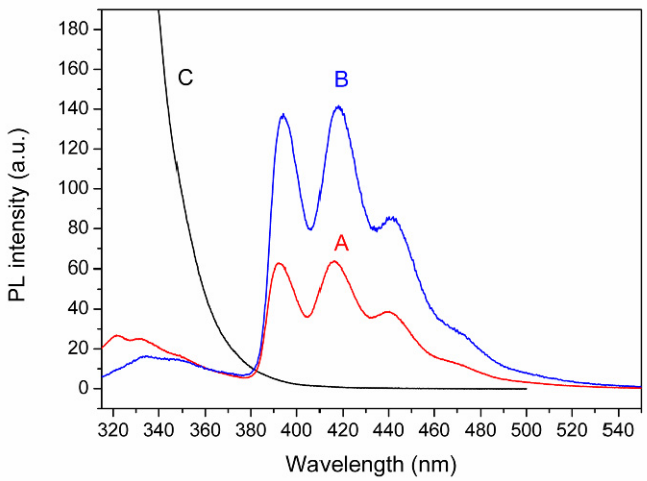

Figure 5-2. Photoluminescence spectra of **NLH-1** with 1×10^{-5} mol/L of FlMA units in THF (A, red) and water (B, blue), as well as a mixture of FlOH and AnOH ([FlOH] / [AnOH] = 24) in THF (C, black) with the same concentration as comparison.

Inserting an inert spacer between the energy donor and the energy acceptor in a chemical way, we have developed two NLHs (**NLH-2** and **NLH-3**) with 5 and 15 methyl methacrylate (MMA) units, respectively, as the inner block of side chains, thus extending the structure to a core-shell-corona brush (Scheme 5–1). The MMA spacer provides an increase of the antennae-emitter distance and may thus decrease the energy transfer, *i.e.*, strong FlMA fluorescence remains while only weak emission of AnMA is observed (Figures 5–3 B and C). When replacing the solvent THF by water (Figures 5–4 B and C), a qualitatively similar reduction in the acceptor fluorescence and concomitant increase in donor fluorescence is observed upon introduction of the MMA spacer. The comparison of the ratio of integrated emission intensities of AnMA to that of FlMA of these NLH systems in solvents is summarized in Table 5–2. The samples were excited at 305 nm, and the concentration of FlMA units is 1×10^{-5} mol/L for all compounds. It is evident that in both solvents, THF and water, less of the AnMA acceptor emission is observed relative to the emission from the constant concentration of FlMA donor when going from **NLH-1** to **NLH-2** and **NLH-3**. According to Förster theory, the rate of energy transfer depends only linearly on the number of chromophores, yet with the 6th power on the donor-acceptor distance. Since the relative molar acceptor concentration remains nearly constant when

going from **NLH-1** to **NLH-2** (from 4.3% to 3.6% of the acceptor AnMA relative to the donor FlMA), we attribute the reduced relative acceptor emission to the effect of increasing spacer lengths in **NLH-2**. Whereas the relative acceptor emission decreases by a factor of 10 (from 3.4 to 0.35) from **NLH-1** to **NLH-2** in THF, it reduces only by about a factor of 5 in water, implying that the introduction of a spacer with 5 MMA units has less effect if the **NLH-2** is in water. Such a pronounced difference is not found when further 10 MMA units are inserted.

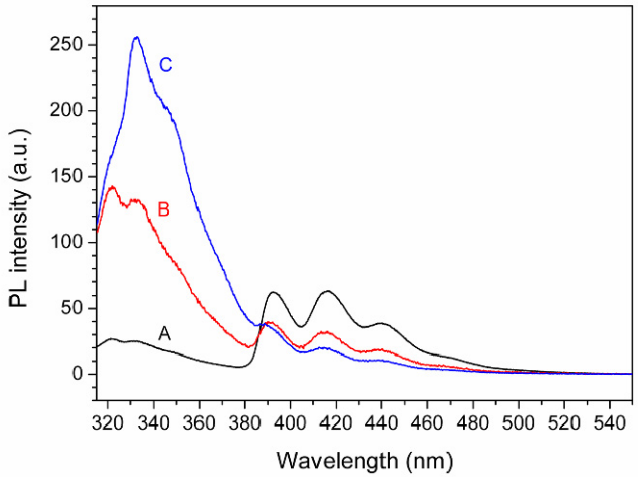

Figure 5-3. Photoluminescence spectra of **NLH-1** (A, black), **NLH-2** (B, red) and **NLH-3** (C, blue) in THF with the excitation light wavelength of 305 nm. The concentrations of FlMA units are 1×10^{-5} mol/L.

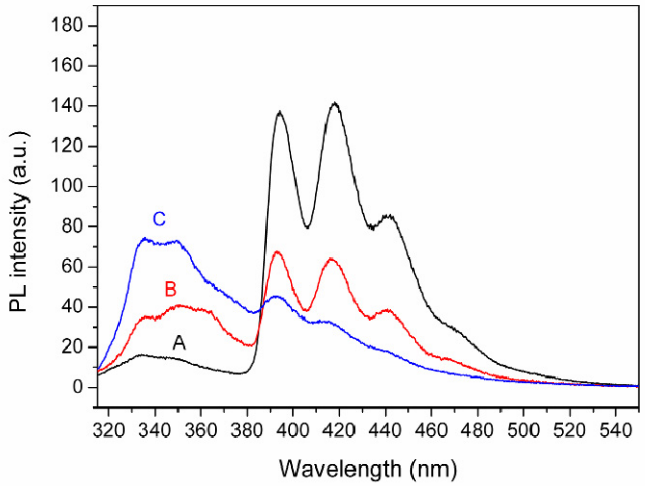

Figure 5-4. Photoluminescence spectra of **NLH-1** (A, black), **NLH-2** (B, red) and **NLH-3** (C, blue) in water with the excitation light wavelength of 305 nm. The concentrations of FlMA units are 1×10^{-5} mol/L.

Table 5-2. Ratio of donor emission to acceptor emission of NLH samples in different solvents.

Solvent	Sample	Em(FlMA)[a] (a.u.)	Em(AnMA)[b] (a.u.)	Em(AnMA)/Em(FlMA)
THF	**NLH-1**	1063	3566	3.4
THF	**NLH-2**	5569	1942	0.35
THF	**NLH-3**	10157	1524	0.15
water	**NLH-1**	736	7874	10.7
water	**NLH-2**	1921	3713	1.9
water	**NLH-3**	3432	2418	0.70

[a] FlMA emission calculated as the integral area of 315–380 nm in the PL spectra. [b] AnMA emission calculated as the integral area of 380–500 nm in the PL spectra.

5.3 Conclusions

In conclusion, our rod-like NLHs successfully mimic the natural "energy cascade" concept, exhibiting efficient energy harvesting. The fluorescence resonance energy transfer (FRET) can be varied by tuning the distance between the antennae and energy acceptors in either physical or chemical ways by means of changing solvents or adding inert spacer units, respectively. This CPB-based rod-like NLH concept provides a novel solution for light harvesting materials. Moreover, it is quite open to be transplanted to any energy capture applications by modifying energy absorbing antenna and acceptor units.

Acknowledgement

Financial support from the Alexander von Humboldt Foundation is acknowledged. J.L. acknowledges support by National Natural Science Foundation of China (21374093). Z.Z. appreciates a scholarship from the Elite Support Program of Bavaria. A.K. acknowledges financial support from the German Science Foundation (DFG/GRK 1640) and the Bavarian State Ministry of Science, Research, and the Arts for the Collaborative Research Network "Solar Technologies go Hybrid".

Supporting Information Available

Experimental details, structural illustrations of natural light-harvesting complex from purple bacteria and our rod-like NLH molecules, TEM and AFM images of NLH samples are included. This material is available from the Wiley Online Library or from the authors.

5.4 References

1. Mackowski, S. *J. Phys.: Condens. Matter* **2010**, *22*, 193102.
2. McDermott, G.; Prince, S. M.; Freer, A. A.; Hawthornthwaite-Lawless, A. M.; Papiz, M. Z.; Cogdell, R. J.; Isaacs, N. W. *Nature* **1995**, *374*, 517-521.
3. van Oijen, A. M.; Ketelaars, M.; Köhler, J.; Aartsma, T. J.; Schmidt, J. *Science* **1999**, *285*, 400-402.
4. Hofmann, E.; Wrench, P. M.; Sharples, F. P.; Hiller, R. G.; Welte, W.; Diederichs, K. *Science* **1996**, *272*, 1788-1791.
5. Popere, B. C.; Pelle, A. M. D.; Poe, A.; Thayumanavan, S. *Phys. Chem. Chem. Phys.* **2012**, *14*, 4043-4057.
6. Harriman, A.; Mallon, L. J.; Elliot, K. J.; Haefele, A.; Ulrich, G.; Ziessel, R. *J. Am. Chem. Soc.* **2009**, *131*, 13375-13386.
7. Häussler, M.; Lok, Y. P.; Chen, M.; Jasieniak, J.; Adhikari, R.; King, S. P.; Haque, S. A.; Forsyth, C. M.; Winzenberg, K.; Watkins, S. E.; Rizzardo, E.; Wilson, G. J. *Macromolecules* **2010**, *43*, 7101-7110.
8. Albrecht, K.; Kasai, Y.; Yamamoto, K. *J. Inorg. Organomet. Polym.* **2009**, *19*, 118-123.
9. Furuta, P.; Fréchet, J. M. J. *J. Am. Chem. Soc.* **2003**, *125*, 13173-13181.
10. Kostereli, Z.; Ozdemir, T.; Buyukcakir, O.; Akkaya, E. U. *Org. Lett.* **2012**, *14*, 3636-3639.
11. Chen, R.; Ling, J.; Hogen-Esch, T. E. *Macromolecules* **2009**, *42*, 6015-6022.
12. Branchi, B.; Ceroni, P.; Balzani, V.; Klärner, F.-G.; Vögtle, F. *Chem.-Eur. J.* **2010**, *16*, 6048-6055.
13. Zhang, X.; Chen, Z.-K.; Loh, K. P. *J. Am. Chem. Soc.* **2009**, *131*, 7210-7211.
14. Eisele, D. M.; Cone, C. W.; Bloemsma, E. A.; Vlaming, S. M.; van der Kwaak, C. G. F.; Silbey, R. J.; Bawendi, M. G.; Knoester, J.; Rabe, J. P.; Vanden Bout, D. A. *Nature Chem.* **2012**, *4*, 655-662.
15. Zhang, M.; Müller, A. H. E. *J. Polym. Sci. Part A: Polym. Chem.* **2005**, *43*,

3461-3481.

16. Yuan, J.; Xu, Y.; Walther, A.; Bolisetty, S.; Schumacher, M.; Schmalz, H.; Ballauff, M.; Müller, A. H. E. *Nat. Mater.* **2008**, *7*, 718-722.
17. Chen, R.; Zhang, X.; Hogen-Esch, T. E. *Macromolecules* **2003**, *36*, 7477-7483.
18. Chen, R.; Johnson, J. M.; Bradforth, S. E.; Hogen-Esch, T. E. *Macromolecules* **2003**, *36*, 9966-9970.

5.5 Supporting Information

5.5.1 Materials

9-Anthracenemethanol (AnOH, Aldrich-Sigma, 97%), methacryloyl chloride (Aldrich, 97%), 2-bromofluorene (Sinopharm Chemical Reagent), iodoethane (Sinopharm Chemical Reagent), sodium borohydride ($NaBH_4$, Sinopharm Chemical Reagent), potassium iodide (Shantou Xilong Chemical), n-BuLi/Hexane (J&K Scientific Ltd.), 1,1,4,7,10,10-hexamethyltriethylenetetraamine (HMTETA, Aldrich, 97%) and 2-cyano-2-propyl benzodithioate (CPrB, Aldrich, >97%) were used as received.

2-(2-Bromoisobutyryloxy)ethyl methacrylate (BIEM) was synthesized according to literature.[1] 9-Anthracenemethyl methacrylate (AnMA) was synthesized according to literature.[2] Methyl methacrylate (MMA, Aldrich, >98.5%) and 2-(dimethylamino)ethyl methacrylate (DMAEMA, Aldrich, >98%) were purified by passing through a column of basic aluminum oxide to remove the inhibitors.

Dimethyl formamide (DMF) and triethylamine (TEA) were distilled over CaH_2 under reduced pressure and stored in argon atmosphere at room temperature. Tetrahydrofuran (THF) was refluxed over potassium-benzophenone ketyl prior to use. CuBr (Aldrich, 98%) was purified by stirring with acetic acid overnight. After filtration, it was washed with ethanol and diethylether and then dried in vacuum oven. 2,2'-Azoisobutyronitrile (AIBN, Aldrich, 98%) was recrystallized from methanol.

5.5.2 Synthesis of (9,9-diethylfluoren-2-yl)methyl methacrylate (FlMA) monomer

The synthesis of FlMA monomer includes four steps as shown in Scheme 5–S1. The 2-bromofluorene was dialkylated by reaction with iodoethane in order to obtain protection at 9-fluorenyl position. The bromine was converted to the hydroxymethyl group after formylation and subsequent reduction under standard conditions. FlMA was obtained by esterification of 9,9-diethyl-2-hydroxymethylfluorene (FlOH) with methacryloyl chloride.

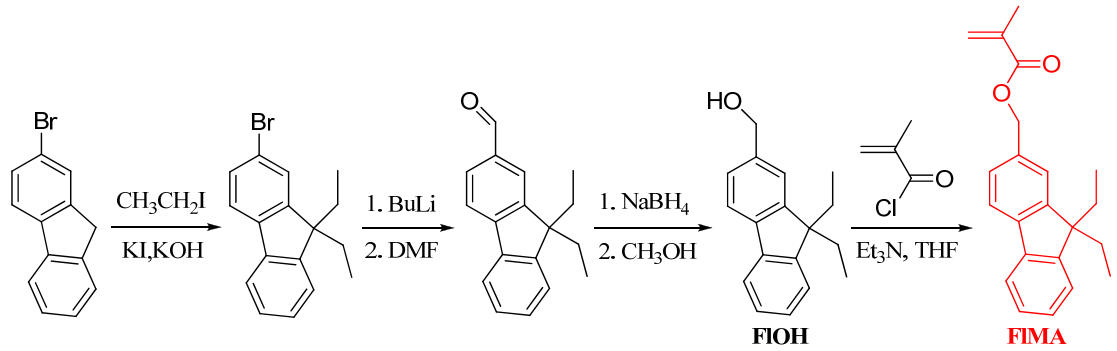

Scheme 5-S1. Synthesis of (9,9-diethylfluoren-2-yl)methyl methacrylate monomer.

5.5.3 Synthesis of 2-bromo-9,9-diethylfluorene

2-Bromofluorene (11.77 g, 48.0 mmol) dissolved in 90 mL dimethyl sulfoxide at 60 °C. Potassium iodide (0.81 g, 4.8 mmol), iodoethane (8.9 mL, 110.0 mmol) and powdered potassium hydroxide (11.75 g, 209.0 mmol) were added and stirred overnight at room temperature. The reaction mixture was precipitated from 600 mL water. The solid was filtered, washed with water and dried under vacuum. The light yellow crude product was purified by recrystallization from methanol to give white crystals (16.50 g, 95.9%), m.p. = 56 °C. ESI-MS: *m/z* 301.22 (calculated for $C_{17}H_{17}Br$: 301.22). Analytical calculated for $C_{17}H_{17}Br$: C = 67.78%, H = 5.69%; found: C = 67.56%, H = 5.65%. ^1H NMR (500 MHz, $CDCl_3$, δ in ppm): 7.45-7.67 (m, 7H, ArH), 2.01 (m, 2H, CH_2), 0.31 (t, 3H, CH_3). ^{13}C NMR (125 MHz, $CDCl_3$, δ in ppm): 152.16, 149.48, 140.55, 140.44, 129.95, 127.47, 127.01, 126.22, 122.92, 120.97, 119.72, 77.27, 77.02, 76.76, 56.40, 32.66, 8.42. FT-IR (cm^{-1}): 2950, 1200 (ν_{C-H} of CH_3), 2850, 720 (ν_{C-H} of CH_2), 913 (ν_{C-Br}).

5.5.4 Synthesis of 9,9-diethyl-2-formyl-fluorene

2-Bromo-9,9-diethylfluorene (29.31 g, 97.3 mmol) was dissolved in 140 mL dry THF, and cooled to -78 °C under argon atmosphere. n-BuLi/hexane solution (46.7 mL, 116.8 mmol) was added dropwise. The reaction was carried out at -78 °C for 1 h and a yellow precipitate was formed. DMF (13.5 mL, 166 mmol) was then added dropwise and the solution was stirred for additional 2 h at -78 °C. After warmed up to room temperature, 1 mol/L HCl was added to quench the reaction. The product was extracted by ethyl acetate and dried under vacuum. A yellow viscous liquid was obtained (23.39 g, 96.0%). ESI-MS: *m/z* 250.33 (calculated for $C_{18}H_{18}O$: 250.14). Analytical calculated for $C_{18}H_{18}O$: C =

86.13%, H = 7.25%; found: C = 86.36%, H = 7.82%. ^{1}H NMR (500 MHz, $CDCl_3$, δ in ppm): 10.08 (s, 2H, CHO), 7.35-7.92 (m, 7H, ArH), 2.10 (m, 4H, CH_2), 0.31 (t, 6H, CH_3). ^{13}C NMR (125 MHz, $CDCl_3$, δ in ppm): 151.35, 150.73, 147.97, 139.97, 135.36, 130.53, 128.83, 127.23, 126.98, 126.76, 123.19, 122.87, 120.94, 119.93, 119.60, 77.30, 77.05, 76.79, 56.29, 32.71, 32.57, 8.42, 1.03. FT-IR (cm^{-1}): 2950, 1200 (ν_{C-H} of CH_3), 2850, 720 (ν_{C-H} of CH_2), 2601 ($\nu_{C=O}$ of CHO), 1697 (ν_{C-H} of CHO).

5.5.5 Synthesis of 9,9-diethyl-2-hydroxymethylfluorene (FlOH)

9,9-Diethyl-2-formyl-fluorene (9.1 g, 36.38 mmol) was dissolved in 50 mL methanol followed by adding $NaBH_4$ (2.06 g, 54.57 mmol) in 30 mL methanol solution. The reaction was stirred at room temperature for 30 min monitored by thin layer chromatography. HCl (3 mol/L) was added to discompose the excess $NaBH_4$. After evaporation, the product was extracted 2 times by ethyl ether, vacuum dried and recrystallized in hexane to give light yellow crystals (8.3 g, 91.5%). ESI-MS (EI): *m/z* 274.1 (calculated for $C_{18}H_{20}ONa$: 275.35). Analytical calculated for $C_{18}H_{20}O$: C = 85.67%, H = 7.99%; found: C = 85.78%, H = 8.22%. ^{1}H NMR (500 MHz, $CDCl_3$, δ in ppm): 7.25-7.75 (m, 7H, ArH), 4.75 (s, 2H, $C\underline{H}_2OH$), 2.01 (m, 4H, CH_2), 1.7 (s, 1H, $CH_2O\underline{H}$), 0.31 (t, 6H, CH_3). ^{13}C NMR (125 MHz, $CDCl_3$, δ in ppm): 150.38, 150.00, 141.19, 141.17, 139.81, 127.02, 1 26.80, 125.85, 122.91, 121.59, 119.63, 77.30, 77.04, 76.79, 56.05, 32.69, 31.58, 22.65, 14.12, 8.50. FT-IR (cm^{-1}): 2950, 1200 (ν_{C-H} of CH_3), 2850.

5.5.6 Synthesis of (9,9-diethylfluoren-2-yl)methyl methacrylate (FlMA)

FlOH (2.18 g, 8.6 mmol) was dissolved in 15 mL dry THF followed by adding TEA (2.0 mL, 21.6 mmol). A 15 mL THF solution of methacryloyl chloride (3.25 mL, 21.6 mmol) was added dropwise at 0 °C and the reaction was carried out for 30 min followed by another 3 h at 25 °C. A dilute ammonia solution was added till the pH value reached 8. After stirred for another 1 h, the mixture was evaporated, extracted 2 times with ethyl ether and washed with 1 mol/L HCl, saturated sodium bicarbonate and water, successively. The organic layer was dried by sodium sulfate and evaporated. The final product was obtained as a colorless viscous liquid (2.47 g, 89.3%). ESI-MS (EI): *m/z* 343.42 (calculated

for $C_{22}H_{24}O_2Na$: 343.42). Analytical calculated for $C_{22}H_{24}O_2$: C = 82.46%, H = 7.55%; found: C = 82.09%, H = 7.68%. ^{1}H NMR (500 MHz, $CDCl_3$, δ in ppm): 7.25-7.75 (m, 7H, ArH), 5.60 and 6.18 (s, 2H, $C\underline{H}_2$=CCH_3), 5.27 (s, 2H, CH_2OCO), 2.01 (m, 4H, CH_2), 1.98 (s, 1H, CH_2=$CC\underline{H}_3$), 0.33 (t, 6H, CH_3). ^{13}C NMR (125 MHz, $CDCl_3$, δ in ppm): 167.34, 150.29, 150.14, 141.64, 141.04, 136.40, 134.89, 127.23, 127.00, 126.89, 125.71, 122.95, 122.79, 119.78, 119.67, 77.34, 77.09, 76.84, 66.90, 56.07, 37.67, 26.95, 18.40, 8.52. FT-IR (cm^{-1}): 2950, 2850, 1720 ($\nu_{C=O}$ of COO), 1635 ($\nu_{C=C}$), 1200 (ν_{C-H} of CH_3), 1157 (ν_{C-O} of COO), 720 (ν_{C-H} of CH_2).

5.5.7 Synthesis of polymers

5.5.7.1 Polymer backbone ($PBIEM_{0.82}$-*co*-$PAnMA_{0.18}$)$_{159}$

Random copolymer of BIEM with AnMA was synthesized *via* reversible addition-fragmentation chain transfer (RAFT) polymerization using CPrB as the chain transfer agent (CTA) and AIBN as the initiator. BIEM (1.0 g, 3.58 mmol), AnMA (247.5 g, 0.90 mmol), CPrB (2.64 mg, 1.2×10^{-2} mmol) and AIBN (0.5 mg, 3×10^{-3} mmol) were dissolved in 2 mL anisole to form a crimson transparent solution. After deoxygenated by bubbling with argon for 30 min, the flask was sealed and immersed into a 70°C oil bath to start the polymerization. After a predetermined time, the reaction mixture was cooled to room temperature and precipitated into cold hexane. The precipitate was separated by filtration and dried in vacuum for 24 h. According to the ^{1}H NMR intensities the molar ratio of [BIEM]/[AnMA] was calculated as 4.6 and therefore the fractions of BIEM and AnMA are 82 and 18 mol%, respectively. SEC (in THF with poly(*tert*-butyl methacrylate) standards): M_n = 47 kDa, PDI = 1.24.

5.5.7.2 CPB ($PBIEM_{0.82}$-*co*-$PAnMA_{0.18}$)$_{159}$-*g*-($PFlMA_5$)

Grafting polymerization of FlMA from ($PBIEM_{0.82}$-*co*-$PAnMA_{0.18}$)$_{159}$ backbone was carried out *via* atom transfer radical polymerization (ATRP).

A flask equipped with CuBr, FlMA and polyinitiator was dissolved in anisole and degassed with argon for 30 min. The mixture was stirred and heated to 40 °C before the degassed ligand HMTETA was injected into the flask to start the polymerization. The polymerization was monitored by ^{1}H-NMR measurements. After a desired conversion, the

polymerization was quenched by cooling the reaction mixture to room temperature and exposing it to air. The reaction mixture was passed through a silica gel column to remove the catalyst and then precipitated into cold *n*-hexane.

5.5.7.3 CPB ($PBIEM_{0.82}$-*co*-$PAnMA_{0.18}$)$_{159}$-*g*-($PFlMA_5$-*b*-$PDMAEMA_{157}$) (NLH-1)

The synthesis of DMAEMA corona *via* ATRP "grafting from" method on CPB ($PBIEM_{0.82}$-*co*-$PAnMA_{0.18}$)$_{159}$-*g*-($PFlMA_5$) was similar to the procedure described in Section 5.5.7.2 above.

5.5.7.4 NLH-2 and NLH-3

The syntheses of **NLH-2** and **NLH-3** were the same as that of **NLH-1** mentioned above *via* controlled/living ATRP "grafting from" method using the same linear polymer ($PBIEM_{0.82}$-*co*-$PAnMA_{0.18}$)$_{159}$ backbone (Section 5.5.7.1), except for an additional MMA segments were involved.

5.5.8 Measurements

Fourier transform infrared (FT-IR) spectra were recorded on a Bruker VECTOR-22 IR spectrometer using a KBr salt plate. Elemental analysis was performed on Flash EA 1112.Nuclear magnetic resonance (NMR) spectra were recorded on a Bruker Avance DMX 500 (^{1}H: 500 MHz and ^{13}C: 125 MHz) or a Bruker AC-300 (^{1}H: 300 MHz) spectrometer using $CDCl_3$ as solvent and tetramethyl silane as internal reference. Number-average molecular weights (M_ns) and polydispersity indices (PDIs) were determined by size-exclusion chromatography (SEC) using dimethyl acetamide (DMAc) with 0.05% lithium bromide (LiBr) as eluent at an elution rate of 0.8 mL/min at 60 °C. Columns include one pre-column and two analytical columns (PSS GRAM, 10^2 and 10^3 Å pore size, 7 μm particle size). Poly(*tert*-butyl methacrylate) or PDMAEMA with narrow PDI was used to calibrate the columns. UV-Vis and steady-state fluorescence emission measurements were carried out on a Hitachi U-3000 spectrometer and a Shimadzu RF-5301 PC spectrofluorometer, respectively. Spectra were recorded at a concentration of 1.0×10^{-5}mol/L in HPLC-grade THF or Milli-Q ultra-pure water (pH = 5.5). The excitation wavelength for the fluorescence measurements was 305 nm. Transmission electron microscopy (TEM) images were recorded on a Zeiss LEO 922 OMEGA electron microscope

operated at 200 kV. A 2 µL droplet of the THF solution of NLHs was dropped onto a copper grid coated with carbon film, followed by a removal of the redundant solution using a filter paper. The grid was stained by RuO_4 before imaging. Tapping-mode atomic force microscopy (AFM) images were recorded on a Digital Instruments Dimension 3100 microscope operated in tapping mode. The samples were prepared by spin-coating (3000 rpm, 1 min) diluted THF solutions of NLHs onto mica surface.

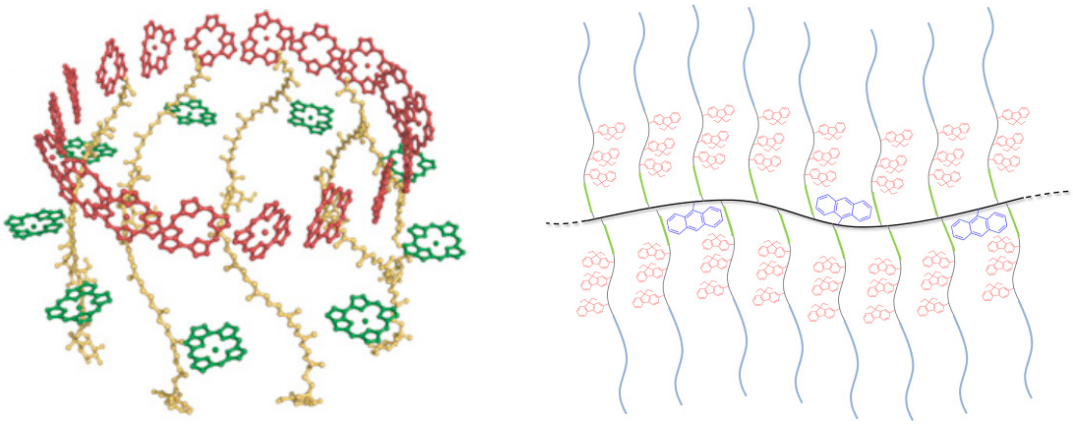

Figure 5-S1. Structure of a natural light-harvesting complex from purple bacteria[3] (left) [reprinted with permission of IOP Publishing], and of our rod-like nano-light harvester molecules (right).

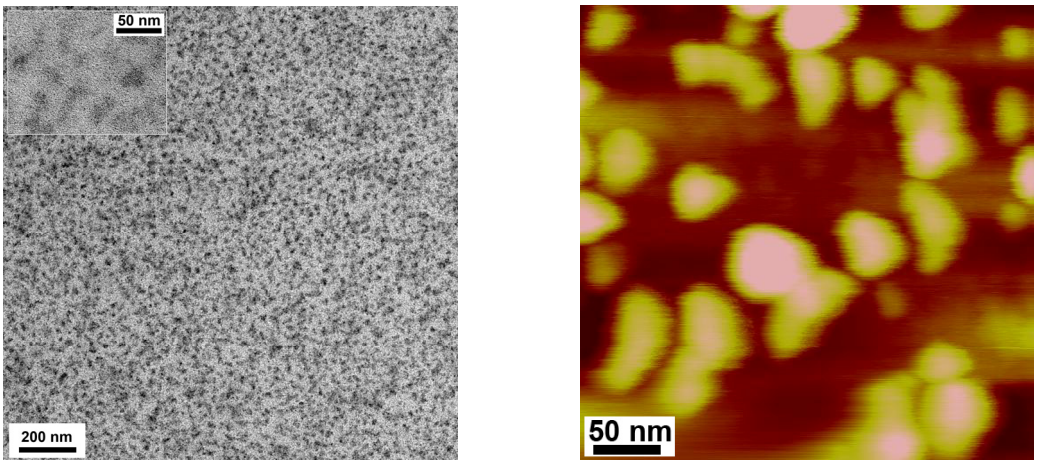

Figure 5-S2. TEM (left) and AFM height (right) images of **NLH-1** from THF solution.

5.5.9 References

1. R. Venkatesh, L. Yajjou, C. E. Koning, B. Klumperman, *Macromol. Chem. Phys.* **2004**, *205*, 2161-2168.
2. D. A. Holden, J. E. Guillet, *Macromolecules* **1980**, *13*, 289-295.
3. Mackowski, S. *J. Phys.: Condens. Matter* **2010**, *22*, 193102.

Chapter 6

Rare-Earth Metal Cations Incorporated Silica Hybrid Nanoparticles Templated by Cylindrical Polymer Brushes

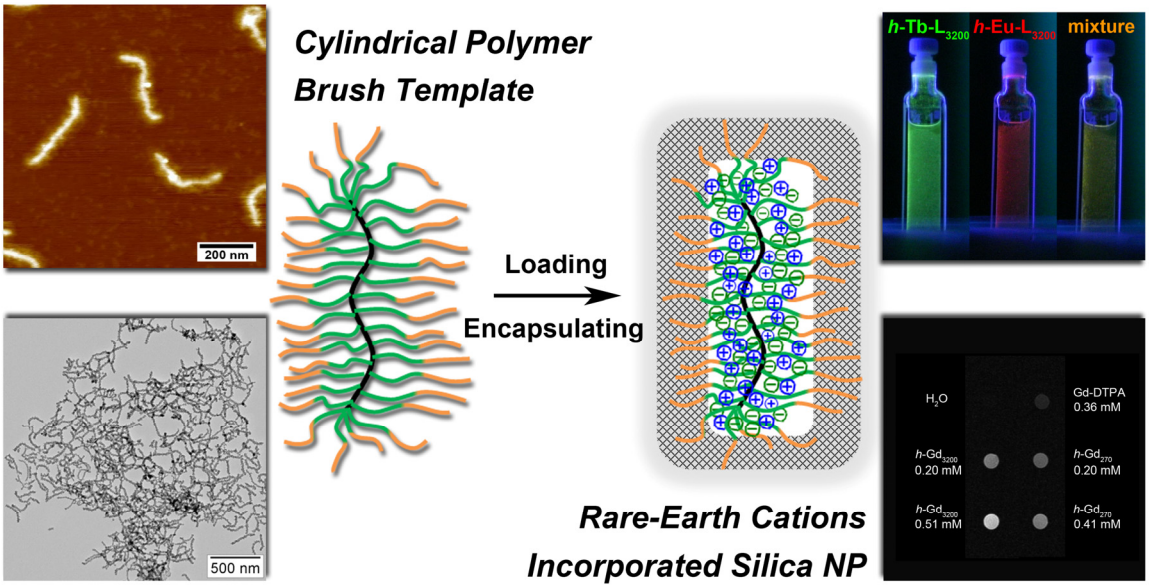

The results of this chapter have been published as:

"Rare-Earth Metal Cations Incorporated Silica Hybrid Nanoparticles Templated by Cylindrical Polymer Brushes"

by Zhicheng Zheng, Alexander Daniel, Wei Yu, Birgit Weber, Jun Ling* and Axel H. E. Müller*

in *Chemistry of Materials*, **2013**, *25*, 4585–4594. Reprinted with permission of ACS.

Abstract

A novel template-directed approach based on core-shell cylindrical polymer brushes (CPBs) has been developed to prepare rare-earth metal cations (Ln^{3+}) incorporated silica hybrid nanoparticles (NPs) with predictable dimensions. Tight chelation of Ln^{3+} ions in the core of the CPB template and a crosslinked silica layer deposited on the shell provide a very stable encapsulation of Ln^{3+} ions within the hybrid NPs and thus a high biocompatibility. As expected, the silica hybrid NPs obtain unique and diverse properties from the incorporated Ln^{3+} ions. That is, the hybrid NPs with Tb^{3+} or Eu^{3+} incorporation exhibit characteristic photoluminescence in visible light range, while the Gd^{3+}- and Tb^{3+}-containing hybrid NPs show paramagnetic behavior. Especially, the Gd^{3+}-containing silica hybrid NPs show a remarkable longitudinal relaxation time (T_1) shortening effect as well as minimal cytotoxicity, suggesting the application potential of these NPs as effective magnetic resonance imaging (MRI) contrast agents. This novel template-directed approach succeeds in combining different functional centers *via* loading *in-situ* mixed Ln^{3+} ions, *e.g.* Tb^{3+} and Gd^{3+}, into individual CPBs resulting in multicomponent hybrid NPs, which possess both visible photoluminescence and T_1 contrast enhancement and can thus be applied as multimodal bioimaging probes.

Keywords

Rare-earth cations, cylindrical polymer brushes, template-directed, photoluminescence, paramagnetic, MRI contrast agent, cytotoxicity

6.1 Introduction

Rare-earth metals, *i.e.* the lanthanides from lanthanum (La) to lutetium (Lu), constitute a series of inner transition elements ("f-elements"). In the case of their trivalent cations (Ln^{3+}), the 4*f* orbital is filled in a completely regular manner from $4f^0$ for La^{3+} to $4f^{14}$ for Lu^{3+}. The shielding of the 4*f* electrons by the occupied $5s^2$ and $5p^6$ orbitals is responsible for the unique and diverse properties of the Ln^{3+} ions, which have encouraged scientists to use them as functional centers for constructing specific functional materials.[1,2] One important application is demonstrated in photonics, such as phosphors for displays and labels for bioimaging, since the luminescence of Ln^{3+} ions covers the spectral range from the ultraviolet to the near-infrared wavelength.[3-5] Lanthanide-doped luminescent nano-materials possess high photostability,[6,7] no blinking,[8] sharp emission lines,[9] large Stokes shifts[10] and long lifetimes of the emitting state.[10] Another well-known contribution of rare-earth ions is the application in developing magnetic materials, as several Ln^{3+} ions have a large number of unpaired electrons and thus provide high magnetic moments in a magnetic field.[11] Gd^{3+} ions with seven unpaired electrons can significantly decrease the relaxation time of water protons and are thus widely used as contrast agents for magnetic resonance imaging (MRI).[12] However, Gd^{3+} ions are highly toxic and must thus be che-lated within ligands[13,14] or embedded in nanoparticles[15-20] to avoid the cytotoxicity for the MRI application.

In the last decade, core-shell(-corona) cylindrical polymer brushes (CPBs), providing a large number of chelating sites within their branched architectures, have been employed as templates for the preparation of various rod-like hybrid nanoparticles (NPs), such as magnetic hybrid NPs,[21,22] water-soluble organo-silica hybrid nanowires[23] and nanotubes,[24,25] cadmium sulfide hybrid NPs,[26] platinum-functionalized nanowires[27] and titania hybrid NPs.[28,29] These template-directed prepared hybrid NPs obtain high dimen-sional stability from the core of the CPB, while the shell and/or corona protects them from agglomeration and precipitation in solution. In this work, we designed core-shell CPBs with poly(acrylic acid)-*block*-poly[2-(dimethylamino)ethyl methacrylate]

(PAA-*b*-PDMAEMA) side chains, short as *b*-[AD], for the first time as templates for the preparation of rare-earth metal cations (Ln^{3+}) incorporated hybrid NPs. As illustrated in Scheme 6–1, the CPB precursor with poly(*tert*-butyl acrylate)-*block*-PDMAEMA (P*t*BA-*b*-PDMAEMA) side chains, short as *b*-[TD], is converted into the CPB template *b*-[AD] *via* hydrolysis by methanesulfonic acid. Subsequently, various Ln^{3+} ions, *i.e.* gadolinium (Gd^{3+}), neodymium (Nd^{3+}), europium (Eu^{3+}), terbium (Tb^{3+}) and their mixtures, are incorporated into the PAA-core through an exchange between Ln^{3+} ions and hydrogen ions. A further localized deposition of tetramethyl orthosilicate (TMOS) molecules onto the PDMAEMA-shell and their subsequent condensation yield hybrid NPs with a crosslinked silica shell. The tight bonding of Ln^{3+} ions by the carboxylate ions in the PAA-core combined with the crosslinked silica shell ensures an isolating encapsulation of the toxic Ln^{3+} ions and thus a minimized cytotoxicity and a satisfying biocompatibility of the hybrid NPs.

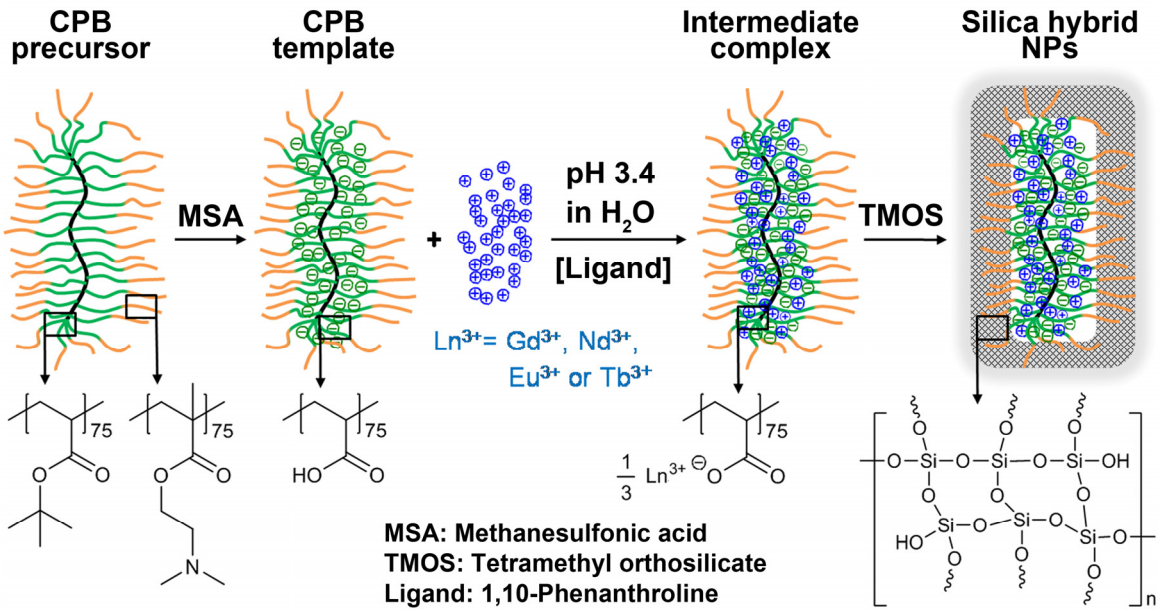

Scheme 6-1. Preparation of well-defined rare-earth metal cations (Ln^{3+}) incorporated silica hybrid nanoparticles *via* the template-directed approach based on core-shell cylindrical polymer brushes.

6.2 Experimental Section

6.2.1 Materials

The synthesis of the macroinitiator poly[2-(2-bromoisobutyryloxy)ethyl methacrylate] (PBIEM, DP_n=3200, PDI=1.14) by anionic polymerization, acidic cleavage of the trimethylsilyl groups, and an esterification to attach the ATRP initiating sites was reported previously.[30] The monomer BIEM for synthesis of the other macroinitiator PBIEM with a DP_n of 270 was prepared according to literature method.[31] 2,2'-Azoisobutyronitrile (AIBN, 98%, Aldrich) was recrystallized from methanol. 2-Cyano-2-propyl benzodithioate (CPrB, RAFT agent, 97%, Aldrich), methanesulfonic acid (MSA, 99.5%, Aldrich) and tetramethyl orthosilicate (TMOS, 98%, Aldrich) were purchased and used without further treatment. CuBr (98%, Aldrich) was purified by stirring with acetic acid overnight. After filtration, it was washed with ethanol and diethyl ether and then dried in vacuum oven. *tert*-Butyl acrylate (*t*BA, 98%, Aldrich) and 2-(dimethylamino)ethyl methacrylate (DMAEMA, 98%, Aldrich) were purified by passing through basic alumina columns before polymerizations. Rare earth metal oxides (Nd_2O_3, Gd_2O_3, Eu_2O_3 and Tb_4O_7) were purchased from Beijing Founde Star Science and Technology Co. Ltd. and transformed to corresponding cations (Ln^{3+}) through reaction with acid at elevated temperature. All other solvents and chemicals were of analytical grade and used as received. Water was obtained from a Milli-Q PLUS (Millipore) apparatus.

6.2.2 Synthesis of macroinitiator $PBIEM_{270}$

The macroinitiator $PBIEM_{270}$ was synthesized *via* RAFT polymerization of 2-(2-bromoisobutyryloxy)ethyl methacrylate (BIEM). RAFT agent 2-cyano-2-propyl benzodithioate (CPrB) (1.98 mg, 9.0×10^{-3} mmol), monomer BIEM (1.5 g, 5.4 mmol) and initiator AIBN (0.37 mg, 2.2×10^{-3} mmol) were dissolved in anisole. The reaction mixture was stirred and degassed with argon for 30 min and then heated to 70 °C. The polymerization was monitored by withdrawing samples for ^{1}H NMR measurements. When a de-

sired conversion was achieved, the reaction was quenched by cooling the reaction mixture to room temperature and exposing it to air. The reaction mixture was purified by precipitating into cold *n*-hexane. DMAc-SEC (RI, PMMA calibration): M_n = 30.0 kDa, PDI = 1.21. ^{1}H NMR (300 MHz, $CDCl_3$, δ in ppm): 4.30 (s, 2H, $OCOCH_2C\underline{H}_2OCOC(CH_3)_2Br$), 4.14 (s, 2H, $OCOC\underline{H}_2CH_2OCOC(CH_3)_2Br$), 1.90 (s, 6H, $C(C\underline{H}_3)_2Br$), 1.25-0.70 (m, 3H, $CH_2CHC\underline{H}_3$).

6.2.3 Preparation of CPB precursors *b*-[TD]

The homopolymer CPB *b*-$[T_{80}]_{270}$ was synthesized *via* ATRP from a $PBIEM_{270}$ backbone. A flask equipped with CuBr (15.4 mg, 1.07×10^{-1} mmol) and polyinitiator PBIEM (40 mg, 1.43×10^{-1} mmol initiating sites) was degassed with argon for 30 min. Then degassed monomer *t*BA (7.35 g, 53.7 mmol) and solvent anisole were added by syringe. The mixture was stirred and heated to 60 °C. Finally, the degassed ligand, *N,N,N′,N″,N″*-pentamethyldiethylenetriamine (PMDETA, 18.6 mg, 1.07×10^{-1} mmol), was injected to start the polymerization, and an initial sample was taken for ^{1}H NMR measurement. The polymerization was monitored by withdrawing samples for ^{1}H NMR measurements. When a desired conversion was achieved, the reaction was quenched by cooling the reaction mixture to room temperature and exposing it to air. The reaction mixture was purified by passing through a silica gel column, followed by precipitating into cold methanol/water mixture (8:1) for twice. The initiating efficiency of the polyinitiator PBIEM toward *t*BA was determined as 65%. The procedure was detailed in our earlier work.[32] Based on the monomer conversion and the initiating efficiency, the DP_n of the P*t*BA block was calculated as 80. ^{1}H NMR (300 MHz, $CDCl_3$, δ in ppm): 1.38 (s, 9H, $OC(C\underline{H}_3)_3$).

The core-shell CPB *b*-$[T_{80}D_{77}]_{270}$ was obtained *via* ATRP of DMAEMA from the homopolymer CPB *b*-$[T_{80}]_{270}$. A round-bottom flask was charged with CuBr (3.32 mg, 2.32×10^{-2} mmol), *b*-$[T_{80}]_{270}$ (300 mg) and anisole. The mixture was degassed with argon for 30 min. After that, the degassed monomer DMAEMA (1.09 g, 6.95 mmol) was added by syringe into the flask, which was then heated to 90 °C. The degassed ligand PMDETA

(4.01 mg, 2.32×10^{-2} mmol) was injected to start the polymerization. As described above, the polymerization was monitored by ^{1}H NMR measurements. After achieving a desired conversion, the reaction was quenched by cooling the reaction mixture to room temperature and exposing it to air. The reaction mixture was purified by passing through a silica gel column, followed by precipitating into cold *n*-hexane for twice. The DP_n of the PDMAEMA block was calculated as 77 from the ^{1}H NMR spectrum by comparing the *t*BA protons with the DMAEMA protons. ^{1}H NMR (300 MHz, $CDCl_3$, δ in ppm): 4.00 (s, 2H, $OC\underline{H}_2CH_2N(CH_3)_2$), 2.50 (s, 2H, $OCH_2C\underline{H}_2N(CH_3)_2$), 2.22 (s, 6H, $OCH_2CH_2N(C\underline{H}_3)_2$), 1.38 (s, 9H, $OC(C\underline{H}_3)_3$).

The core-shell CPB *b*-$[T_{75}D_{75}]_{3200}$ was prepared *via* the same approach as *b*-$[T_{80}D_{77}]_{270}$, with a $PBIEM_{3200}$ macroinitiator used as the backbone.

6.2.4 Preparation of CPB templates *b*-[AD]

The core-shell CPB template *b*-$[A_{80}D_{77}]_{270}$ with a polyelectrolyte poly(acrylic acid) (PAA) core was synthesized *via* hydrolysis of the P*t*BA segments of the CPB precursor *b*-$[T_{80}D_{77}]_{270}$. Herein, *b*-$[A_{80}D_{77}]_{270}$ was dissolved in dichloromethane (about 15 mg/mL) and methanesulfonic acid (MSA)[33] was added at room temperature at a molar ratio of 20 compared to *t*BA units. After around 30 min, the solution became turbid. Stirring was continued for 24 h to ensure the full reaction. After evaporation of the organic solvent, the reaction product was dissolved in pure water.

The core-shell CPB template *b*-$[A_{75}D_{75}]_{3200}$ was prepared *via* the same approach as *b*-$[A_{80}D_{77}]_{270}$, with *b*-$[T_{75}D_{75}]_{3200}$ used as CPB precursor.

6.2.5 Preparation of rare earth metal cations incorporated silica hybrid NPs

The Gd^{3+}-incorporated silica hybrid NP *h*-Gd_{270} was prepared *via* the template-directed approach. 1 mL aqueous solution of Gd^{3+} (0.22 mmol mL^{-1}) was added into 3.4 mL aqueous solution of CPB template *b*-$[A_{80}D_{77}]_{270}$ (1.0 mg mL^{-1}) under stirring. The

pH-value and the temperature of the solution were kept at 3.4 – 3.6 and 15 °C, respectively. 0.2 mL of tetramethyl orthosilicate (TMOS) was added into the solution under stirring.[34,35] The deposition and crosslinking procedure of TMOS on the PDMAEMA segments was running for 20 min. The achieved silica hybrid NP *h*-Gd_{270} was purified by ultracentrifugation. The precipitates were washed with ethanol, redissolved in ethanol using ultrasonic bath and ultracentrifuged for three times.

The silica hybrid NPs *h*-Gd_{3200}, *h*-Nd_{3200}, *h*-Nd_{270}, *h*-Tb_{3200} and *h*-Tb_{270} were prepared *via* the same template-directed approach as *h*-Gd_{270}, with corresponding CPB template and Ln^{3+} aqueous solution being applied. In the preparation of the ligand-coordinating hybrid NPs *h*-Tb-L_{3200} and *h*-Eu-L_{3200}, 1,10-phenanthroline (50 mg, 0.28 mmol) as ligand was added into the reaction solution before the adding of TMOS. In the case of multicomponent hybrid NPs *h*-Tb/Gd_{3200} and *h*-Tb/Nd_{3200}, corresponding Ln^{3+} mixture was used for the template-directed synthesis.

6.2.6 Characterization methods

Size Exclusion Chromatography. SEC was conducted by using dimethyl acetamide (DMAc) with 0.05% lithium bromide as eluent at an elution rate of 0.8 mL min^{-1}. The equipment consists of one pre-column and two analytical columns (PSS GRAM, 10^2 and 10^3 Å pore size, 7 mm particle size) and an Agilent 1200 RI detector. The measurements were performed at 60 °C. PMMA calibration curve was used to calibrate the columns.

^{1}H Nuclear Magnetic Resonance Spectroscopy. ^{1}H NMR measurements were carried out on a Bruker AC-300 instrument at room temperature in $CDCl_3$.

Tapping-mode Atomic Force Microscopy. AFM images were recorded on a Digital Instruments Dimension 3100 microscope operated in tapping mode. The samples were prepared by spin-coating (3000 rpm, 1 min) diluted aqueous solutions onto freshly cleaved mica surface.

Transmission Electron Microscopy. TEM images of silica hybrid NPs were recorded on Zeiss CEM 902 and LEO 922 OMEGA electron microscopes operated at 80 kV and

200 kV, respectively. Data evaluation and processing was carried out with Soft Imaging Viewer and Image Tool. A 2 µL droplet of the ethanol solution of silica hybrid NPs was dropped onto a copper grid coated with carbon film, followed by a removal of the redundant solution using a filter paper.

Scanning Electron Microscopy and *Energy Dispersive X-ray Analysis*. SEM was performed by using a Zeiss Leo 1530 instrument equipped with a field emission cathode with a lateral resolution of approximately 2 nm. The sample was measured after sputtering a thin layer (1 – 2 nm) of platinum. EDX analysis was performed by using an Oxford EDX INCA 400 detector and a Thermo Fischer Scientific Noran System 7 with corresponding NSS 3 X-Ray MicroAnalysis software.

Thermogravimetric Analysis. TGA was conducted on a Mettler Toledo TGA/SDTA 85 instrument under a constant air flow of 60 mL min^{-1}. The measurements were scanned in the temperature range of 30 – 700 °C at a heating rate of 10 K min^{-1}.

Inductively Coupled Plasma Optical Emission Spectrometry. ICP-OES was applied to determine the rare earth metal cation (Ln^{3+}) contents of the silica hybrid NPs. The measurements were conducted on a Varian Vista-Pro Radial instrument. Standard solutions of free rare earth metal cations (1 g L^{-1}) were prepared as the references for the measurements.

Leaching Study of Ln^{3+} from Silica Hybrid NPs. The stability of the encapsulation of Ln^{3+} within the silica hybrid NPs *h*-Gd_{3200} and *h*-Tb_{3200} was determined by performing a complexometric titration of free Ln^{3+} leaching from the hybrid NPs, using xylenol orange as indicator. Xylenol orange gives a yellow color in a non-complex form (λ_{max} = 432 nm in UV-Vis absorption spectrum), while a red color is observed from the complex of xylenol orange with Ln^{3+}. By measuring the absorption at the wavelength of 432 nm, a quantitative analysis of free Ln^{3+} is feasible. Xylenol orange solution was prepared by dissolving 36 mg of xylenol orange tetrasodium salt (3,3′-bis[*N,N*-bis(carboxymethyl) aminomethyl]-*o*-cresolsulfonephthalein tetrasodium salt) in 100 mL acetate puffer (sodium acetate/acetic acid, pH 5.8). The obtained xylenol orange solution was kept in 1 mL por-

tion in 1.5 mL Eppendorf PCR centrifuge vials at -30 °C. The procedure of the complexometric titration: 1.5 mL of *h*-Gd_{3200} solution (output [Gd^{3+}] = 0.7 mM) was centrifuged for 10 min. The precipitates were isolated and redissolved in 1.5 mL water. The start of the redissolving is defined as the zero point of the kinetic measurement of the leaching study of Ln^{3+}. After a time period *t* (1 h, 1 d, 3d, 7 d or 14 d), an 250 µL aliquot solution was taken, diluted in 1 mL water and centrifuged for 10 min. Now, 250 µL of the supernatant solution was taken and diluted in 5 mL water. The obtained solution was filtered through a 0.2 µm nylon filter. Then, 100 µL of the filtrate was added into a mixture of 2.8 mL acetate puffer and 100 µL xylenol orange indicator solution. The obtained solution was transferred completely into a quartz cuvette and measured for its adsorption in the range of 200 – 800 nm by using a Hitachi U-3000 UV-Vis spectrometer. A control sample containing acetate puffer and xylenol orange indicator but without hybrid NP was also measured. A working curve of the adsorption depending on the Tb^{3+}-concentration was measured previously from a concentration series of free Tb^{3+} in water (0.3 – 9 µM). The complexometric titration *h*-Tb_{3200} solution (output [Tb^{3+}] = 0.5 mM) was performed in the same way.

Photoluminescence Spectroscopy. PL excitation and emission spectra of the ethanol solutions of the Tb^{3+}- and Eu^{3+}-containing silica hybrid NPs were recorded by using a Shimadzu RF-5301 PC fluorescence spectrometer. The Ln^{3+}-concentration of each sample was previously determined by ICP-OES as described above. A UV lamp operating at 266 nm was applied to record the luminescence images of the ethanol solutions of hybrid NPs.

Superconducting Quantum Interference Device Magnetometer. SQUID measurements of the Gd^{3+}- and Tb^{3+}-containing silica hybrid NPs were performed on a Quantum Design MPMS-XL-5 SQUID magnetometer. About 10 mg of hybrid NPs was dried in a gelatin capsule for the measurement. The magnetizations of the hybrid NPs were measured as function of the applied magnetic field with a maximal strength of 5 T at 5 K in the hysteresis mode. Temperature-dependent magnetizations of the hybrid NPs were scanned in the temperature range of 2 – 300 K with an applied magnetic field strength of 1 T.

Relaxivity Measurements of Gd^{3+}-containing Silica Hybrid NPs. The longitudinal T_1

and transverse relaxation time T_2 of Gd^{3+}-containing silica hybrid NPs were measured on a Brucker Ultrashield 300 MHz instrument at 37 °C and 7.0 T. For each type of hybrid NPs, a concentration series (0.01 – 0.8 mM of Gd^{3+} in D_2O) was prepared and previously determined by ICP-OES as described above. T_1 and T_2 were determined for three times by applying Inversion-Recovery pulse sequence and Car-Purcell-Meilboom-Gill pulse sequence, respectively. The inverses of the mean of T_1 and that of T_2, namely the relaxation rates $1/T_1$ and $1/T_2$, were plotted *versus* the Gd^{3+}-concentration of the hybrid NPs to calculate their relaxivities r_1 and r_2, *i.e.* the slopes of the plots.

MRI Phantom Study of Gd^{3+}-containing Silica Hybrid NPs. The T_1-weighted MRI images of Gd^{3+}-containing silica hybrid NPs were acquired on a GE Signa MRI 3.0 T Scanner at room temperature. Samples of *h*-Gd_{270} and *h*-Gd_{3200} were prepared in deionized water with concentrations of 0.20, 0.41 mM and 0.20, 0.51 mM of total Gd^{3+}, respectively. A sample of pure deionized water and another sample of commercial contrast agent gadopentetate dimeglumine (Gd-DTPA) with a Gd^{3+}-concentration of 0.36 mM in deionized water were measured as references. The parameters of the measurements are given as follows: a repetition time (TR) of 60 ms, an echo time (TE) of 11 ms, a slice thickness of 1.0 mm, a spacing of 0.5 mm, a FOV read of 70 mm and an 8 h brain small coil with an inner diameter of 50 mm.

Cell Culture. The human bronchoalveolar carcinoma derived cell line A549 cells were obtained from Cell Bank of Typical Culture Collection of Chinese Academy of Sciences (Shanghai, China) and maintained in regular growth medium consisting of high glucose DMEM supplemented with 10% fetal bovine serum (FBS), 100 μL penicillin, and 100 μg mL^{-1} streptomycin at 37 ℃, in a 5% CO_2 humidified incubator. The human endothelial cells (CRL-1730) were obtained from American Type Culture Collection (ATCC, USA) and maintained with regular growth medium consisting of high-glucose RPMI 1640 supplemented with 10% FBS, 100 μL penicillin, and 100 μg mL^{-1} streptomycin, and cultured at 37 °C in a 5% CO_2 humidified environment. The cells were routinely passaged until 80 – 90% confluence. Briefly, the culture medium was removed and the cells were carefully washed three times with phosphate buffered saline (PBS) to remove all traces of

serum which contains trypsin inhibitor. The cells were then incubated with 1 mL trypsin/ethylenediaminetetraacetic acid disodium salt (EDTA, 0.25%) in PBS until the cell layer was dispersed (usually within 5 min). The trypsin was blocked by adding 6.0 – 8.0 mL complete growth medium and the cells were aspirated by gentle pipetting. The cells were isolated by centrifugation at 1000 rpm for 5 min and then dispersed in fresh culture medium and incubated at 37 ^{o}C.

Cytotoxicity Study of Gd^{3+}-containing Silica Hybrid NPs. The A549 cells were plated at a density of 1×10^{4} cells per well on a 96-well plate and cultured for 16 h for the cell viability assay. The medium was replaced with fresh one containing the hybrid NPs of variable concentrations. To determine the cell viability, after co-incubation with the hybrid NPs for determined time intervals (24 or 72 h), 20 μL 3-[4,5-dimethylthiazol-2-yl]-2,5-diphenyltetrazolium bromide (MTT, 5 mg mL^{-1}) was added to each well and the cells were continuously cultured at 37 ℃ for 4 h. The dark blue formazan crystals generated by the mitochondria dehydrogenase in viable cells were dissolved in dimethyl sulphoxide (DMSO), whose absorbance was measured at 570 nm by a microplate reader (Biorad Model 680). Three parallel experiments were conducted, and the data were normalized to that of the hybrid NP-free control. The endothelial cells were cultured in a 96-well plate until 80 – 90% confluence for cell viability study. The medium was replaced with fresh one containing the hybrid NPs of variable concentrations. To determine the cell viability, after the cells were co-incubated with the hybrid NPs for 24 or 72 h, 20 μL MTT (5 mg mL^{-1}) was added to each well and the cells were further cultured at 37 °C for 4 h. The cell viability was determined with the same method as that for A549 cells.

6.3 Results and Discussion

6.3.1 Synthesis of Ln^{3+} incorporated hybrid NPs

Two core-shell CPB precursors *b*-[TD] with different lengths were synthesized *via* sequential grafting of P*t*BA and PDMAEMA blocks using ATRP from well-defined polyinitiators poly[2-(2-bromoisobutyryloxy)ethyl methacrylate] (PBIEM) with degrees of polymerization, DP, of 3200 (polydispersity index, PDI=1.14) and 270 (PDI=1.21), respectively. The synthetic route is illustrated in Scheme 6–S1 (Supporting Information). The longer CPB precursor was determined to have 75 P*t*BA and 75 PDMAEMA units in its block copolymer side chains (short as *b*-$[T_{75}D_{75}]_{3200}$), whereas the shorter CPB precursor was defined as *b*-$[T_{80}D_{77}]_{270}$ according to ^{1}H NMR analyses shown in Figure 6–S1. Tapping-mode atomic force microscopy (AFM) shows that the CPB precursors *b*-$[T_{75}D_{75}]_{3200}$ and *b*-$[T_{80}D_{77}]_{270}$ have worm-like conformations with the number-average length, $L_{n,}$ of 313 ± 62 nm (Figures 6–1A and 6–S2B) and 52 ± 9 nm (Figures 6–1B and 6–S2E), respectively. Acidic hydrolysis of the CPB precursors *b*-[TD] formed CPB templates with PAA-*b*-PDMAEMA side chains, *b*-$[A_{75}D_{75}]_{3200}$ and *b*-$[A_{80}D_{77}]_{270}$, whose AFM images are shown in Figures 6–S2C and 6–S2F.

By employing the CPB templates, various Ln^{3+}-incorporated hybrid NPs were successfully prepared *via* a loading and encapsulation process, as given in Table 6–1. They are single-component silica hybrid NPs *h*-Gd_{3200}, *h*-Gd_{270}, *h*-Nd_{3200}, *h*-Nd_{270}, *h*-Tb_{3200}, and *h*-Tb_{270}, ligand-coordinating ones *h*-Tb-L_{3200} and *h*-Eu-L_{3200} (1,10-phenanthroline as ligand), as well as multicomponent ones *h*-Tb/Gd_{3200} and *h*-Tb/Nd_{3200} (loaded with Ln^{3+} mixtures). In the loading process, the pH was kept at 3.4, where the PDMAEMA segments are almost completely protonated and strongly positively charged. Therefore, their ability to form complex with metal cations (also positively charged) is strongly reduced. In contrast, the PAA units are still capable to chelate the metal cations at this pH. In the silica encapsulation, the partially negatively charged silicate precursor TMOS is first adsorbed on the positively charged PDMAEMA segments, which catalyze the hydrolysis of

TMOS to orthosilicic acid ($Si(OH)_4$). A following condensation into silica finishes the encapsulation. Since we conducted this loading and encapsulation process in excess of Ln^{3+} ions and TMOS, every template brush adsorbed sufficient silicate precursor on its shell and underwent a complete encapsulation. Both the silica hybrid NPs derived from *b*-$[A_{75}D_{75}]_{3200}$ and that from *b*-$[A_{80}D_{77}]_{270}$ maintain the cylindrical worm-like conformations from the templates as demonstrated in the transmission electron microscopy (TEM) images (Figures 6–1 D-I), with the former and the latter NPs having $L_n \approx 200$ nm and 50 nm, respectively (Table 6–1). The silica hybrid NPs have a core-shell nanostructure with a dark Ln^{3+}-containing core (more electron-dense) and a grey silica shell (Figures 6–1 F and I for *h*-Tb_{3200} and *h*-Tb/Gd_{3200}), while the intermediate of Gd^{3+}-loaded *b*-$[A_{75}D_{75}]_{3200}$ without deposition of TMOS shows only a homogeneous dark nanostructure (Figure 6–1C).

The Ln^{3+}-contents of the silica hybrid NPs were determined by inductively coupled plasma optical emission spectrometry (ICP-OES) as 9% – 12% for the NPs derived from the CPB template *b*-$[A_{75}D_{75}]_{3200}$ and 6% – 7% for the ones from *b*-$[A_{80}D_{77}]_{270}$ (Table 6–1). This lower Ln^{3+}-content of the shorter NPs is attributed to the increased surface-to-volume ratio, which shifts the silica-to-Ln^{3+} ratio in favor of silica, as more silicate precursors deposited and condensed on the shell. It is to note that in the multicomponent hybrid NPs *h*-Tb/Gd_{3200} and *h*-Tb/Nd_{3200}, each component has almost the same content. By combining the ICP-OES results with the TGA measurements (Figure 6–S3), the weight fraction of the silica shell in the silica hybrid NPs was determined as *ca.* 11%. Furthermore, scanning electron microscopy (SEM) images with combined energy-dispersive X-ray (EDX) analysis of the silica hybrid NPs also qualitatively confirms the Ln^{3+}-loading and the silica encapsulation of the hybrid NPs, as shown in Figure 6–S4. The stability of the encapsulation of Ln^{3+} ions within the silica hybrid NPs was confirmed by measuring the leaching kinetic of Ln^{3+} ions from the NPs *via* a complexometric titration using xylenol orange as indicator. After dissolving in water for 14 d, the concentration of free Ln^{3+} ions in the solutions of hybrid NPs *h*-Gd_{3200} (output $[Gd^{3+}] = 0.7$ mmol L^{-1}) and *h*-Tb_{3200} (output $[Tb^{3+}] = 0.5$ mmol L^{-1}) maintained below the detection limit of

0.01 mmol L^{-1} (Figure 6–S6). Compared with other reported Ln^{3+}-nanosystems,[16,36] our silica hybrid NPs provide a very stable encapsulation of the toxic Ln^{3+} ions, indicating application potential as stable and safe nanomaterials. In addition, the silica shell ensures excellent solubility of the silica hybrid NPs in water and alcohols. This is confirmed by the dynamic light scattering (DLS) measurement of the hybrid NP *h*-Tb_{3200} in aqueous solution, which demonstrates a monomodal and narrow particle size distribution with average apparent hydrodynamic radius ($R_{h,app}$) of 247 nm and PDI of 1.18, as shown in Figure 6–S5.

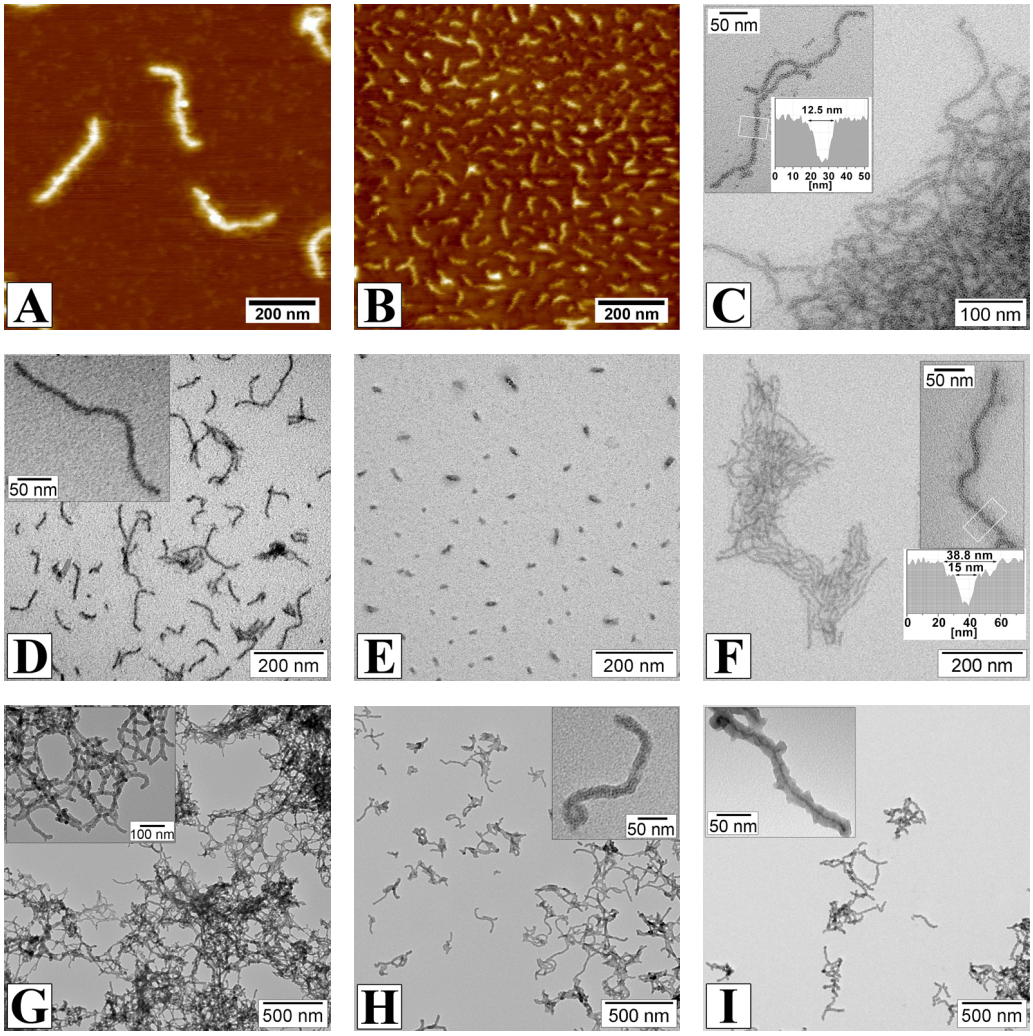

Figure 6-1. Tapping-mode AFM height image of the longer CPB precursor *b*-$[T_{75}D_{75}]_{3200}$ (A) and the shorter CPB precursor *b*-$[T_{80}D_{77}]_{270}$ (B). TEM image of the Gd^{3+}-loaded template intermediate without silicate deposition (C), the Ln^{3+}-incorporated silica hybrid NPs *h*-Gd_{3200} (D), *h*-Gd_{270} (E), *h*-Tb_{3200} (F), the ligand-coordinating silica hybrid NPs *h*-Tb-L_{3200} (G) and *h*-Eu-L_{3200} (H), and the multicomponent silica hybrid NP *h*-Tb/Gd_{3200} (I). The insets in (C) and (F) show the grayscale analysis of the marked areas.

Table 6-1. Silica hybrid nanoparticles with different rare-earth metal cations (Ln^{3+}) incorporations and dimensions

Hybrid	Brush template	Length[b] [nm]	Ln^{3+} content[c] [wt-%]
h-Gd_{3200}	*b*-$[A_{75}D_{75}]_{3200}$	194 ± 24	12.0
h-Gd_{270}	*b*-$[A_{80}D_{77}]_{270}$	51 ± 5	6.5
h-Nd_{3200}	*b*-$[A_{75}D_{75}]_{3200}$	191 ± 30	10.0
h-Nd_{270}	*b*-$[A_{80}D_{77}]_{270}$	46 ± 5	6.8
h-Tb_{3200}	*b*-$[A_{75}D_{75}]_{3200}$	196 ± 57	12.0
h-Tb-L_{3200}[a]	*b*-$[A_{75}D_{75}]_{3200}$	221 ± 51	8.1
h-Eu-L_{3200}[a]	*b*-$[A_{75}D_{75}]_{3200}$	212 ± 37	8.4
h-Tb/Gd_{3200}	*b*-$[A_{75}D_{75}]_{3200}$	238 ± 38	5.2/4.3
h-Tb/Nd_{3200}	*b*-$[A_{75}D_{75}]_{3200}$	194 ± 31	4.6/4.2

[a] L stands for 1,10-phenanthroline as ligand. [b] Measured from TEM images. [c] Determined by ICP-OES.

6.3.2 Visible photoluminescence of the hybrid NPs with Tb^{3+} or Eu^{3+} incorporation

Nanoparticles with visible luminescence (wavelength from 390 to 700 nm) are of great interest in the research and development of display screens, sensors and light-emitting diodes. The prepared silica hybrid NPs with Tb^{3+} or Eu^{3+} incorporation are expected to be photoluminescent in the visible range. Upon excitation at 292 nm, *h*-Tb_{3200} emits much stronger luminescence in ethanol solution (c_{Tb}= 80 mg L^{-1}) at the Tb^{3+} characteristic wavelengths of 488 nm (energy level transition: $^5D_4 \rightarrow {}^7F_6$) and 543 nm ($^5D_4 \rightarrow {}^7F_5$) than free Tb^{3+} ions (c_{Tb}= 3600 mg L^{-1}), as shown in Figure 6–2A. This means the bonding of Tb^{3+} in the PAA-core and the isolation by the silica shell in the hybrid NP are able to avoid solvent-induced quenching. Several wavelengths chosen from the excitation spectrum (Figure 6–S7A) were applied to excite *h*-Tb_{3200} and we found that the excitation wavelengths of 280 and 300 nm induce the highest luminescence. The emission spectrum

of *h*-Tb-L_{3200} in ethanol solution (c_{Tb}= 160 mg L^{-1}) indicates that the introduction of a ligand, 1,10-phenanthroline, enhances the luminescence of Tb^{3+} ions (Figure 6–2B), especially for the excitation at 300 and 337 nm, as the luminescence is 10 times higher than that of the *h*-Tb_{3200} solution. This sensitization effect is attributed to a more efficient light absorption of the Tb^{3+} ions coordinated by the ligand.[37,38] Furthermore, since 1,10-phenanthroline is a neutral ligand, there is no interaction between the ligand and the brushes so that it does not influence the Coulomb interaction between the Ln^{3+} ions and the PAA core. Another silica hybrid NP, *h*-Eu-L_{3200}, succeeds in emitting luminescence of Eu^{3+} ions in ethanol solution (c_{Eu}= 82 mg L^{-1}) at the characteristic wavelengths of 590 nm ($^5D_0 \rightarrow {}^7F_1$), 615 nm ($^5D_0 \rightarrow {}^7F_2$), 650 nm ($^5D_0 \rightarrow {}^7F_3$) and 702 nm ($^5D_0 \rightarrow {}^7F_4$), with 290 and 295 nm being the most effective excitation wavelengths (Figure 6–2C).

Mixing the hybrid NPs *h*-Tb-L_{3200} and *h*-Eu-L_{3200} in ethanol solution (c_{Tb}:c_{Eu}= 1:2) demonstrates a straightforward way to combine different functional centers. In the emission spectrum of this mixed solution, both the luminescence of Tb^{3+} ions (488 nm, 543 nm) and that of Eu^{3+} ions (590 nm, 615 nm) are observed (Figure 6–2D), indicating that the separated encapsulation of Tb^{3+} and Eu^{3+} ions avoids interference between their photoluminescent behavior. The luminescence image confirms the functionality combination, as *h*-Tb-L_{3200} and *h*-Eu-L_{3200} in ethanol solution shows a green and a red color, respectively, while a further yellow color was observed in the mixed solution (Figure 6–2E). Another way to combine different functional centers is demonstrated by the multicomponent hybrid NP *h*-Tb/Gd_{3200} with incorporation of a mixture of Tb^{3+} and Eu^{3+} ions. This multicomponent hybrid NP with a lower Tb^{3+} concentration (c_{Tb}= 47 mg L^{-1} and c_{Gd}= 45 mg L^{-1}) in ethanol solution exhibits the same high luminescence as the *h*-Tb_{3200} solution (Figure 6–2F *vs*. 6–2A). This luminescence sensitization effect induced by an effective metal-to-metal energy transfer (Gd^{3+}: $^6P_J \rightarrow Tb^{3+}$: ^5H_J)[39] indicates that the *in-situ* mixed loading of various Ln^{3+} ions into individual NP provides possibilities for interactions among different functional centers.

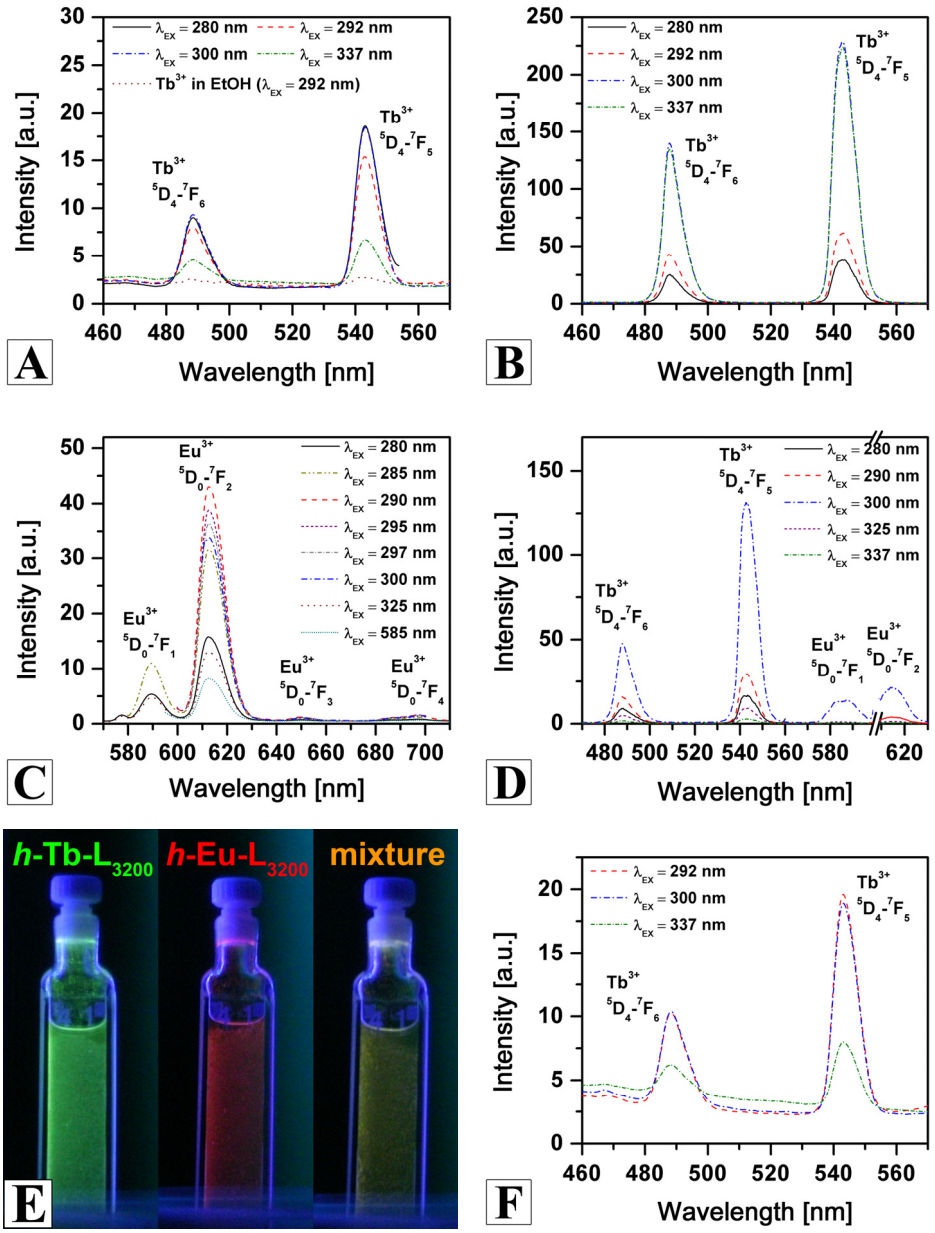

Figure 6-2. Photoluminescence emission spectra of the silica hybrid NPs in ethanol solution upon exciting at different wavelengths: *h*-Tb_{3200} with c_{Tb}= 80 mg L^{-1} (A), *h*-Tb-L_{3200} with 1,10-phenanthroline as ligand, c_{Tb}= 160 mg L^{-1} (B), *h*-Eu-L_{3200} with c_{Eu}= 82 mg L^{-1} (C), a mixed solution of *h*-Tb-L_{3200} and *h*-Eu-L_{3200} with c_{Tb}= 32 mg L^{-1}, c_{Eu}= 65 mg L^{-1} (D) and the multicomponent hybrid NPs *h*-Tb/Gd_{3200} with c_{Tb}= 47 mg L^{-1}, c_{Gd}= 45 mg L^{-1} (F). The brown dash line in (A) corresponds to the emission spectrum of an ethanol solution of free Tb^{3+} cations with c_{Tb}= 3600 mg L^{-1}. Luminescence image of the ethanol solutions of *h*-Tb-L_{3200}, *h*-Eu-L_{3200} and their mixture under excitation at 266 nm (E).

By comparing the excitation and the emission spectra of the longer NP *h*-Tb_{3200} (Figures 6–S7A and 6–2A) with that of the shorter NP *h*-Tb_{270} (Figures 6–S7 E and F), the influence of the NP size on the photoluminescence behavior was investigated. Both NPs

possess excitation and luminescence at the same wavelengths, suggesting no effect of the NP size on the energy band gap and thus the luminescence behavior. That is due to the same chemical environment of Ln^{3+} ions within various NPs, which is independent of the NP size.

6.3.3 Magnetic behavior of the Gd^{3+}- and Tb^{3+}-containing hybrid NPs

The Gd^{3+}- and Tb^{3+}-containing silica hybrid NPs were investigated for their potential magnetic properties by superconducting quantum interference device (SQUID) measurements. The magnetization curves at a temperature of 5 K and the temperature dependence of the molar magnetic susceptibility (χ_M) at an external field of 1 T for *h*-Gd_{3200}, *h*-Tb/Gd_{3200} and *h*-Tb/Nd_{3200} are shown in Figure 6–3, with the main results given in Table 6–2. The magnetization of *h*-Gd_{3200} rises with increasing applied field strength without any hysteresis indicating a paramagnetic behavior at 5 K (Figure 6–3A). Fitting with the Langevin function (Figure 6–S8A) leads to a saturation magnetization, M_s = 266.1 emu/(g Ln^{3+}), which coincides with the theoretical value for free Gd^{3+} ions (249 emu/(g Ln^{3+})). The plot of the $\chi_M T$ product as a function of temperature in the range of 2 to 300 K (Figure 6–3B) suggests a classic paramagnetic behavior of *h*-Gd_{3200}. The effective magnetic moment, μ_{eff}, at 300 K was determined as 6.80μ_B, which is slightly lower than the theoretical value for free Gd^{3+} ions (7.94μ_B). The inverse susceptibility, χ_M^{-1}, of *h*-Gd_{3200} shows a perfect linear dependence on the temperature over the full range (Figure 6–3B, inset). A Curie fitting of this plot suggests a Curie constant C = 7.58 cm^3 K/(mol Ln^{3+}) and a Weiss constant θ = -0.8 K (Table 6–2). This almost negligible Weiss constant also indicates an ideal paramagnetic Curie behavior of *h*-Gd_{3200}. All the magnetic properties of *h*-Gd_{3200} discussed above imply that the individual Gd^{3+} ions in the NP are isolated from each other possessing independent atomic moments. In the case of multicomponent hybrid NPs *h*-Tb/Gd_{3200} and *h*-Tb/Nd_{3200}, the magnetization curves at 5 K also follow a paramagnetic manner (Figures 6–3 C and E). Compared with *h*-Gd_{3200}, the incorporation of Tb^{3+} in *h*-Tb/Gd_{3200} slows down the increase of magnetization with increasing field strength (Figure 3C). An M_s of 210.2 emu/(g Ln^{3+}) is extrapolated using the Langevin

function (Figure 6–S8B), which is lower than the theoretical value for independently acting Tb^{3+} and Gd^{3+} ions (285 emu/(g Ln^{3+})). This could be an indication for some cooperative interactions between the ions in the NP at 5 K, which could be communicated through the carboxylate groups. This phenomenon is also observed in other multicomponent hybrid NP *h*-Tb/Nd_{3200}, as an M_s of 145.2 emu/(g Ln^{3+}) is expected (Figures 6–3E and 6–S8C), which is lower than the theoretical value (225 emu/(g Ln^{3+})). However, the effect is very small as the characteristics, μ_{eff} at 300 K, C and θ, determined from the temperature dependence of $\chi_M T$ and χ_M^{-1} (Figures 6–3 D and F, Table 6–2) confirm an almost ideal Curie paramagnetic behavior of *h*-Tb/Gd_{3200} and *h*-Tb/Nd_{3200}.

Table 6-2. Magnetic properties of the Gd^{3+}- and Nd^{3+}-containing silica hybrid NPs.

Hybrid	M_s [a]	C [b]	θ [b]	μ_{eff} [c]
	[emu/(g Ln^{3+})]	[cm^3 K/(mol Ln^{3+})]	[K]	[μ_B]
h-Gd_{3200}	266.1	7.58	-0.8	6.80
h-Tb/Gd_{3200}	210.2	8.65	-3.5	6.44
h-Tb/Nd_{3200}	145.2	7.50	-6.9	5.88

[a] Saturation magnetization at 5 K obtained by fitting the magnetization curve with the Langevin function. [b] Curie constant (C) and Weiss constant (θ) determined by fitting the inverse susceptibility (χ_M^{-1}) *vs.* temperature curve at 1 T. [c] Effective magnetic moment calculated from the product of molar susceptibility and temperature (χ_MT) at 300 K.

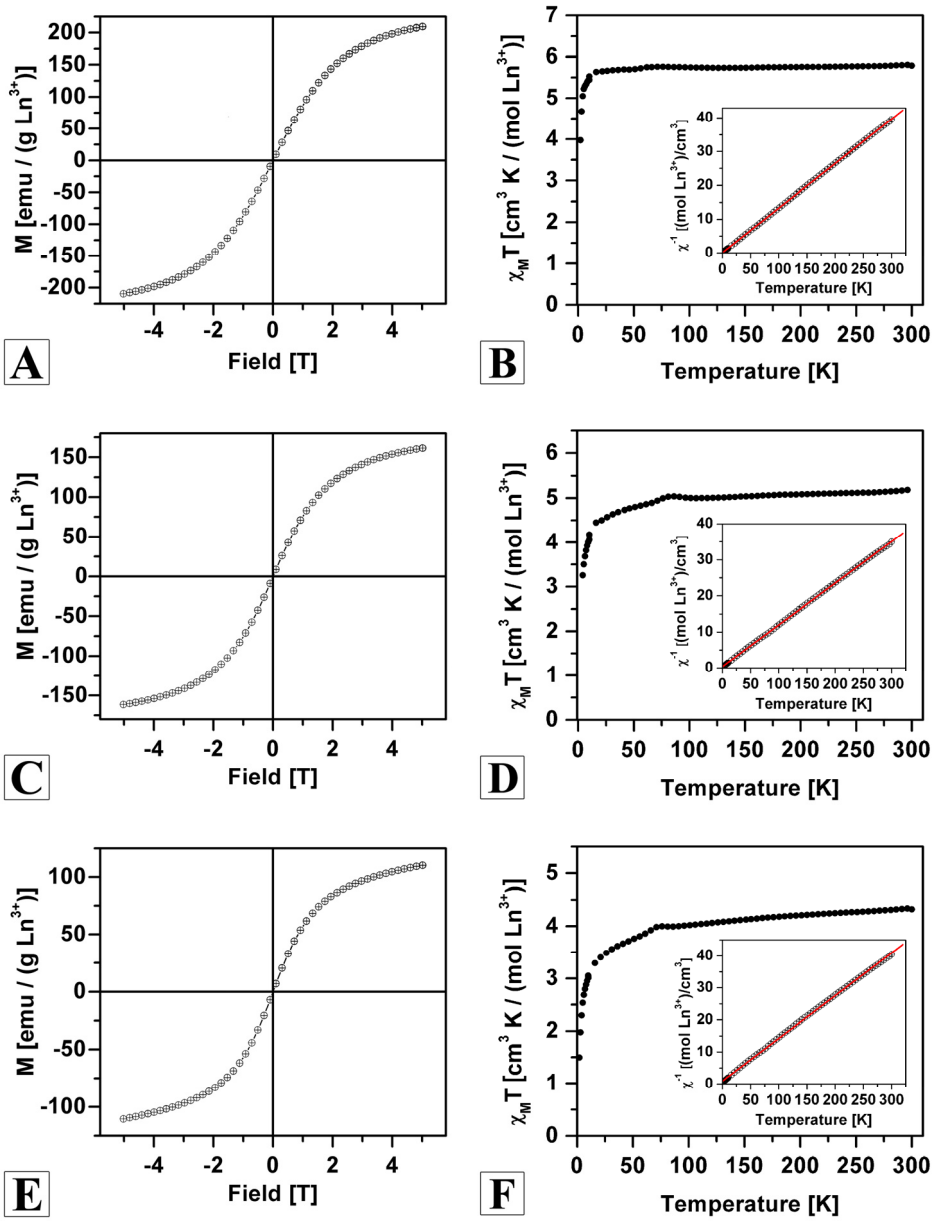

Figure 6-3. Magnetization curves at 5 K for the silica hybrid NPs *h*-Gd_{3200} (A), the multicomponent hybrid NPs *h*-Tb/Gd_{3200} (C) and *h*-Tb/Nd_{3200} (E). Temperature dependence of the product of molar susceptibility and temperature ($\chi_M T$) at 1 T for *h*-Gd_{3200} (B), *h*-Tb/Gd_{3200} (D) and *h*-Tb/Nd_{3200} (F). The inset shows the temperature dependence of the inverse susceptibility (χ_M^{-1}). Black cycles: experimental results; red line: Curie fitting result.

6.3.4 Relaxation time shortening effect of the Gd^{3+}-containing hybrid NPs

Gadolinium species with seven unpaired electrons are well-known candidates as positive contrast agents for magnetic resonance imaging (MRI) technique, as they can shorten the relaxation time of nearby water protons. By measuring the concentration-dependent longitudinal (T_1) and transverse relaxation time (T_2) at 37 °C and 7 T, the Gd^{3+}-containing silica hybrid NPs were investigated for their potential applications as contrast agents. From the plots of the longitudinal relaxation rate, $1/T_1$, against the Gd^{3+}-concentration (Figures 6–4 A and B), the longitudinal relaxivity, r_1, of *h*-Gd_{3200} and *h*-Gd_{270} was determined as 12.7 and 12.2 $mmol^{-1}$ L S^{-1}, respectively (Table 6–3). Compared with the commercial contrast agent gadopentetate dimeglumine (Gd-DTPA) possessing an r_1 value of 3.3 $mmol^{-1}$ L S^{-1} under the same conditions,[20] both *h*-Gd_{3200} and *h*-Gd_{270} exhibit much better T_1 contrast efficacy and can be used at a lower dose to achieve a comparable T_1 contrast enhancement. In the case of the multicomponent hybrid NP *h*-Tb/Gd_{3200} (Figure 6–4C), an r_1 value of 11.9 $mmol^{-1}$ L S^{-1} indicates that the incorporation of Tb^{3+} does not reduce the T_1 shortening effect and is harmless for potential MRI application. Combined with the Tb^{3+}-photoluminescence sensitized by Gd^{3+} (Figure 6–2F), *h*-Tb/Gd_{3200} can be used as dual imaging probe for MRI and fluorescence microscopy. It is to note that both T_1 and T_2 shortening effects can be observed in paramagnetic and superparamagnetic nanosystems, while the r_2/r_1 ratio is the most important factor to evaluate whether the material should be preferably applied as a positive contrast agent (T_1 shortening) or a negative one (T_2 shortening).[40] In general, the materials with low r_2/r_1 ratio are prevailing T_1 contrast agents. On the basis of the concentration-dependent T_1 and T_2 measurements, the r_2/r_1 ratio of *h*-Gd_{3200}, *h*-Gd_{270} and *h*-Tb/Gd_{3200} was determined as 4.1, 3.6 and 5.8, respectively (Table 6–3). Compared with other reported gadolinium-containing nanomaterials (r_2/r_1 = 3.8 – 24.8),[20,40] our hybrid NPs have relatively low r_2/r_1, indicating that they are efficient T_1 contrast agents. Combined with their adequate solubility in water, the hybrid NPs are expected to exhibit a nice signal-to-noise ratio and a satisfying anatomical

resolution in T_1-weighted MRI scans. MRI phantom images of water samples containing the hybrid NPs were recorded at 37 °C and 3 T to confirm their T_1 contrast efficacy. As shown in Figure 6–4D, the samples contrasted by *h*-Gd_{3200} or *h*-Gd_{270} were clearly detected, while a sample of pure water hardly demonstrated a T_1 signal. A comparison between the hybrid NPs and the commercial contrast agent Gd-DTPA was also performed. Even at a lower concentration of Gd^{3+} ions (0.20 mmol L^{-1}), both *h*-Gd_{3200} and *h*-Gd_{270} showed stronger T_1 contrast enhancement than the Gd-DTPA ([Gd^{3+}] = 0.36 mmol L^{-1}), suggesting the application perspective of the hybrid NPs as efficient MRI contrast agents. A comparison between the two hybrid NPs shows that the *h*-Gd_{3200} provides a slightly brighter signal at the same concentration (0.20 mmol L^{-1}), suggesting that a longer particle length results in a stronger T_1 contrast enhancement. In both cases of *h*-Gd_{3200} and *h*-Gd_{270}, the T_1 contrast effect increases expectedly with increasing concentration of the NPs.

Table 6-3. Longitudinal (r_1) and transverse relaxivity (r_2) of the Gd^{3+}-containing silica hybrid NPs measured in D_2O at 37 °C and 7 T.

Hybrid	r_1 [$mmol^{-1}$ L S^{-1}]	r_2 [$mmol^{-1}$ L S^{-1}]	r_2/r_1
h-Gd_{3200}	12.7	52.8	4.1
h-Gd_{270}	12.2	44.6	3.6
h-Tb/Gd_{3200}	11.9	69.7	5.8

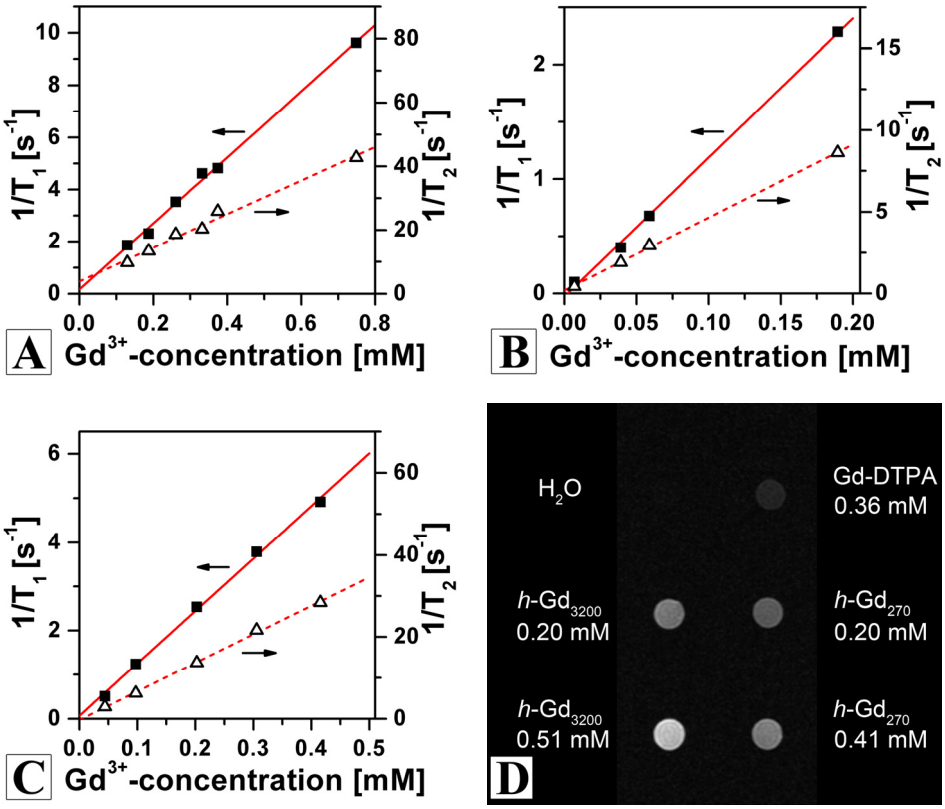

Figure 6-4. Plots of longitudinal ($1/T_1$) and transverse relaxation rate ($1/T_2$) *versus* Gd^{3+}-concentration of the silica hybrid NPs *h*-Gd_{3200} (A), *h*-Gd_{270} (B) and the multicomponent hybrid NPs *h*-Tb/Gd_{3200} (C) in D_2O at 37 °C and 7 T. T_1-weighted MRI images of *h*-Gd_{3200} and *h*-Gd_{270} with different Gd^{3+}-concentrations (D). Deionized water and commercial contrast agent Gd-DTPA were measured as references.

6.3.5 Cytotoxicity of the Gd^{3+}-containing hybrid NPs

The cytotoxicity of the silica hybrid NPs *h*-Gd_{3200} and *h*-Gd_{270} was determined by cell culture using the human bronchoalveolar carcinoma derived cell line A549 as the tested cells. The MTT assay was used to assess the viability of the A549 cells after exposure to the hybrid NPs for 24 h or 72 h at various concentrations of NP (10, 50, 150 µg mL^{-1}). As shown in Figure 6–5, the cell viability is not significantly altered (stays above 90%) after being incubated with *h*-Gd_{270} in the whole experimental period (72 h) regardless of the sample concentrations. The cell viability is slightly reduced when the cells were incubated with *h*-Gd_{3200} for 24 h. It is maintained above 80% of the NP-free control, although slightly decreased at higher concentrations. The cell viability stays relatively stable when the incubation time with *h*-Gd_{3200} extends to 72 h. All the results suggest that the silica

hybrid NPs have a minimal toxicity to A549 cells. Another MTT assay of the human endothelial cells (CRL-1730) under incubation with the silica hybrid NPs *h*-Gd_{3200} and *h*-Gd_{270} was performed with an experimental period of 72 h. The results are shown in Figure 6–S9. With a NP concentration of up to 150 μg mL^{-1}, the *h*-Gd_{270} shows only a minimal toxicity to endothelial cells. In the case of the *h*-Gd_{3200}, a very low toxicity to endothelial cells was observed at concentrations lower than 50 μg mL^{-1}. Furthermore, a MTT assay of a control sample of free Gd^{3+} ions was conducted by using the cell line A549, which indicates that the cell viability after exposure to free Gd^{3+} ions for 24 h at corresponding concentrations (10, 50, 150 μg mL^{-1}) is strongly reduced to *ca.* 65%. Therefore, the encapsulated hybrid NPs possess much lower cytotoxicity than the free Gd^{3+} ions. This minimal cytotoxicity of the silica hybrid NPs *h*-Gd_{3200} and *h*-Gd_{270} is attributed to the fact that all the toxic Gd^{3+} ions are tightly chelated in the PAA-core of the CPB template and are completely isolated by the crosslinked silica shell from the outside surrounding.

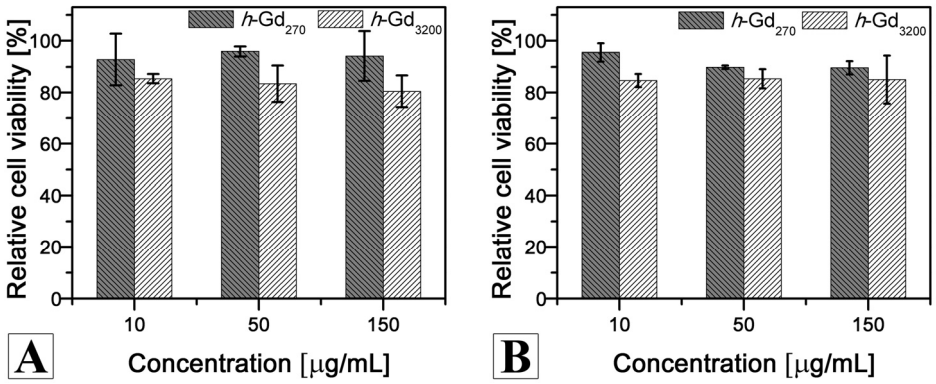

Figure 6-5. Relative viability of A549 cells incubated with the silica hybrid NPs *h*-Gd_{3200} and *h*-Gd_{270} of varying NP concentration with an incubation period of 24 h (A) and 72 h (B). The results are expressed as a percentage of the control cell culture.

Another important characteristic of the silica hybrid NPs *h*-Gd_{3200} and *h*-Gd_{270} is the particle size and shape. As mentioned above, the *h*-Gd_{3200} and *h*-Gd_{270} has a mean particle length of 194 and 51 nm, respectively. NPs in this range of dimension not only extravasate from the leaky tumor vasculature to a higher degree than healthy tissue, but also remain in the tumor issue by the enhanced permeability and retention (EPR) effect.[41-43]

Under fluid flow conditions, due to the one-dimensional (1D) cylindrical shape of the hybrid NPs, they are taken up by cells less readily and more persistent than spheres, because the former are extended by the flow.[44] A combination of the adequate solubility in water, the significant T_1-shortening efficacy, the minimal cytotoxicity and the promising EPR effect suggests that the silica hybrid NPs *h*-Gd_{3200} and *h*-Gd_{270} can be applied as effective T_1 contrast agents for early-stage cancer diagnose. Furthermore, it is noteworthy that the multicomponent hybrid NP *h*-Tb/Gd_{3200} with combined visible photoluminescence and T_1 shortening effect is potential candidate for multimodal bioimaging.

6.4 Conclusions

Various well-defined rare-earth metal cations (Ln^{3+}) incorporated silica hybrid nanoparticles (NPs) with different particle sizes were successfully prepared *via* a template-directed approach based on core-shell cylindrical polymer brushes. The crosslinked silica shell deposited on the PDMAEMA segments ensures a high stability of the encapsulation of Ln^{3+} ions within the hybrid NPs, as well as a satisfying solubility in water and alcohols. Upon excitation with UV light, the silica hybrid NPs with Tb^{3+} or Eu^{3+} incorporation exhibit characteristic visible photoluminescence, which is sensitized by ligand or metal-metal energy transfer. SQUID measurements confirm the paramagnetic properties of the Gd^{3+} and Tb^{3+} containing silica hybrid NPs. Especially, the multicomponent hybrid NP incorporated with a mixture of Tb^{3+} and Gd^{3+} possesses both the visible photoluminescence and the paramagnetic property. The Gd^{3+}-containing silica hybrid nanoparticles show much higher longitudinal relaxivity, r_1, and stronger contrast enhancement in T_1-weighted MRI images than the commercial contrast agent Gd-DPTA. This remarkable T_1 shortening effect combined with a minimal cytotoxicity towards different human cells and a promising EPR effect suggests the potential application of the Gd^{3+}-containing silica hybrid NPs as effective MRI contrast agents for tumor diagnosis.

Acknowledgement

Z. Zheng appreciates a scholarship from the Elite Support Program of Bavaria. J. Ling sincerely thanks the Alexander von Humboldt Foundation for granting him a research fellowship and the National Science Foundation of China (No. 21174122). We thank Stephan Schlamp for SQUID measurements and Dr. Zhengwei Mao for cytotoxicity measurements.

Supporting Information Available

Supporting Information Available: synthetic route, ^{1}H NMR spectra, AFM images, SEM images, EDX analysis, TGA results, *etc.*, can be found in the supporting information. This material is available free of charge *via* the Internet at http://pubs.acs.org.

6.5 References

1. McGill, I., Rare Earth Elements. In *Ullmann's Encyclopedia of Industrial Chemistry*, Wiley-VCH Verlag GmbH & Co. KGaA: **2000**.
2. Bünzli, J.-C. G.; André, N.; Elhabiri, M.; Muller, G.; Piguet, C. *J. Alloy. Compd.* **2000**, *303–304*, 66-74.
3. Ma, Y.; Wang, Y. *Coordin. Chem. Rev.* **2010**, *254*, 972-990.
4. Blasse, G.; Grabmaier, B. C., *Luminescent materials*. Springer-Verlag: **1994**.
5. Moeller, T. *J. Chem. Edu.* **1970**, *47*, 417-423.
6. Zhang, H.; Xu, Y.; Yang, W.; Li, Q. *Chem. Mater.* **2007**, *19*, 5875-5881.
7. Carlos, L. D.; Ferreira, R. A. S.; Bermudez, V. d. Z.; Ribeiro, S. J. L. *Adv. Mater.* **2009**, *21*, 509-534.
8. Zhou, J.; Sun, Y.; Du, X.; Xiong, L.; Hu, H.; Li, F. *Biomaterials* **2010**, *31*, 3287-3295.
9. Kenyon, A. J. *Prog. Quant. Electron.* **2002**, *26*, 225-284.
10. Bunzli, J.-C. G.; Piguet, C. *Chem. Soc. Rev.* **2005**, *34*, 1048-1077.
11. Bouzigues, C.; Gacoin, T.; Alexandrou, A. *ACS Nano* **2011**, *5*, 8488-8505.
12. Bottrill, M.; Kwok, L.; Long, N. J. *Chem. Soc. Rev.* **2006**, *35*, 557-571.
13. Carr, D. H.; Brown, J.; Bydder, G. M.; Steiner, R. E.; Weinmann, H.-J.; Speck, U.; Hall, A. S.; Young, I. R. *Am. J. Roentgenol.* **1984**, *143*, 215-224.
14. Ye, M.; Qian, Y.; Shen, Y.; Hu, H.; Sui, M.; Tang, J. *J. Mater. Chem.* **2012**, *22*, 14369-14377.
15. Bridot, J.-L.; Faure, A.-C.; Laurent, S.; Rivière, C.; Billotey, C.; Hiba, B.; Janier, M.; Josserand, V.; Coll, J.-L.; Vander Elst, L.; Muller, R.; Roux, S.; Perriat, P.; Tillement, O. *J. Am. Chem. Soc.* **2007**, *129*, 5076-5084.
16. Hifumi, H.; Yamaoka, S.; Tanimoto, A.; Citterio, D.; Suzuki, K. *J. Am. Chem. Soc.* **2006**, *128*, 15090-15091.
17. Park, Y. I.; Kim, J. H.; Lee, K. T.; Jeon, K.-S.; Na, H. B.; Yu, J. H.; Kim, H. M.; Lee, N.; Choi, S. H.; Baik, S.-I.; Kim, H.; Park, S. P.; Park, B.-J.; Kim, Y. W.; Lee, S. H.;

Yoon, S.-Y.; Song, I. C.; Moon, W. K.; Suh, Y. D.; Hyeon, T. *Adv. Mater.* **2009**, *21*, 4467-4471.

18. Hifumi, H.; Yamaoka, S.; Tanimoto, A.; Akatsu, T.; Shindo, Y.; Honda, A.; Citterio, D.; Oka, K.; Kuribayashi, S.; Suzuki, K. *J. Mater. Chem.* **2009**, *19*, 6393-6399.
19. Liu, Q.; Sun, Y.; Li, C.; Zhou, J.; Li, C.; Yang, T.; Zhang, X.; Yi, T.; Wu, D.; Li, F. *ACS Nano* **2011**, *5*, 3146-3157.
20. Zhou, Z.; Wang, L.; Chi, X.; Bao, J.; Yang, L.; Zhao, W.; Chen, Z.; Wang, X.; Chen, X.; Gao, J. *ACS Nano* **2013**, *7*, 3287-3296.
21. Zhang, M.; Estournès, C.; Bietsch, W.; Müller, A. H. E. *Adv. Funct. Mater.* **2004**, *14*, 871-882.
22. Xu, Y.; Yuan, J.; Fang, B.; Drechsler, M.; Müllner, M.; Bolisetty, S.; Ballauff, M.; Müller, A. H. E. *Adv. Funct. Mater.* **2010**, *20*, 4182-4189.
23. Yuan, J.; Xu, Y.; Walther, A.; Bolisetty, S.; Schumacher, M.; Schmalz, H.; Ballauff, M.; Müller, A. H. E. *Nat. Mater.* **2008**, *7*, 718-722.
24. Müllner, M.; Yuan, J.; Weiss, S.; Walther, A.; Förtsch, M.; Drechsler, M.; Müller, A. H. E. *J. Am. Chem. Soc.* **2010**, *132*, 16587-16592.
25. Müllner, M.; Lunkenbein, T.; Breu, J.; Caruso, F.; Müller, A. H. E. *Chem. Mater.* **2012**, *24*, 1802-1810.
26. Zhang, M.; Drechsler, M.; Müller, A. H. E. *Chem. Mater.* **2004**, *16*, 537-543.
27. Yuan, J.; Schacher, F.; Drechsler, M.; Hanisch, A.; Lu, Y.; Ballauff, M.; Müller, A. H. E. *Chem. Mater.* **2010**, *22*, 2626-2634.
28. Yuan, J.; Lu, Y.; Schacher, F.; Lunkenbein, T.; Weiss, S.; Schmalz, H.; Müller, A. H. E. *Chem. Mater.* **2009**, *21*, 4146-4154.
29. Müllner, M.; Lunkenbein, T.; Schieder, M.; Gröschel, A. H.; Miyajima, N.; Förtsch, M.; Breu, J.; Caruso, F.; Müller, A. H. E. *Macromolecules* **2012**, *45*, 6981-6988.
30. Zhang, M.; Breiner, T.; Mori, H.; Müller, A. H. E. *Polymer* **2003**, *44*, 1449-1458.
31. Venkatesh, R.; Yajjou, L.; Koning, C. E.; Klumperman, B. *Macromol. Chem. Phys.* **2004**, *205*, 2161-2168.
32. Plamper, F. A.; Schmalz, A.; Penott-Chang, E.; Drechsler, M.; Jusufi, A.; Ballauff, M.;

Müller, A. H. E. *Macromolecules* **2007**, *40*, 5689-5697.

33. Retsch, M.; Walther, A.; Loos, K.; Müller, A. H. E. *Langmuir* **2008**, *24*, 9421-9429.
34. Yuan, J.-J.; Mykhaylyk, O. O.; Ryan, A. J.; Armes, S. P. *J. Am. Chem. Soc.* **2007**, *129*, 1717-1723.
35. Li, Y.; Du, J.; Armes, S. P. *Macromol. Rapid Commun.* **2009**, *30*, 464-468.
36. Huang, C.-C.; Liu, T.-Y.; Su, C.-H.; Lo, Y.-W.; Chen, J.-H.; Yeh, C.-S. *Chem. Mater.* **2008**, *20*, 3840-3848.
37. Liu, D.; Yu, H.; Wang, Z.; Nie, Q. *Polym. Int.* **2010**, *59*, 937-944.
38. Li, H. R.; Lin, J.; Zhang, H. J.; Fu, L. S.; Meng, Q. G.; Wang, S. B. *Chem. Mater.* **2002**, *14*, 3651-3655.
39. Li, Y.-C.; Chang, Y.-H.; Chang, Y.-S.; Lin, Y.-J.; Laing, C.-H. *J. Phys. Chem. C* **2007**, *111*, 10682-10688.
40. Kim, B. H.; Lee, N.; Kim, H.; An, K.; Park, Y. I.; Choi, Y.; Shin, K.; Lee, Y.; Kwon, S. G.; Na, H. B.; Park, J.-G.; Ahn, T.-Y.; Kim, Y.-W.; Moon, W. K.; Choi, S. H.; Hyeon, T. *J. Am. Chem. Soc.* **2011**, *133*, 12624-12631.
41. Alexis, F.; Pridgen, E.; Molnar, L. K.; Farokhzad, O. C. *Mol. Pharm.* **2008**, *5*, 505-515.
42. Jokerst, J. V.; Lobovkina, T.; Zare, R. N.; Gambhir, S. S. *Nanomedicine* **2011**, *6*, 715-728.
43. Maeda, H.; Wu, J.; Sawa, T.; Matsumura, Y.; Hori, K. *J. Controlled Release* **2000**, *65*, 271-284.
44. Geng, Y.; Dalhaimer, P.; Cai, S.; Tsai, R.; Tewari, M.; Minko, T.; Discher, D. E. *Nat. Nano.* **2007**, *2*, 249-255.

6.6 Supporting Information

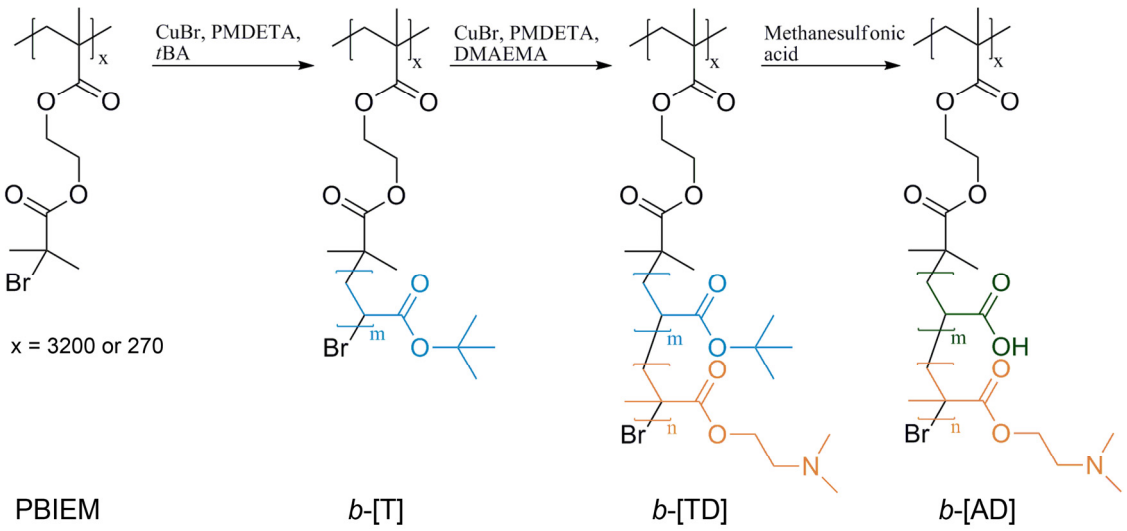

Scheme 6-S1. Synthetic route to CPB templates *b*-[AD].

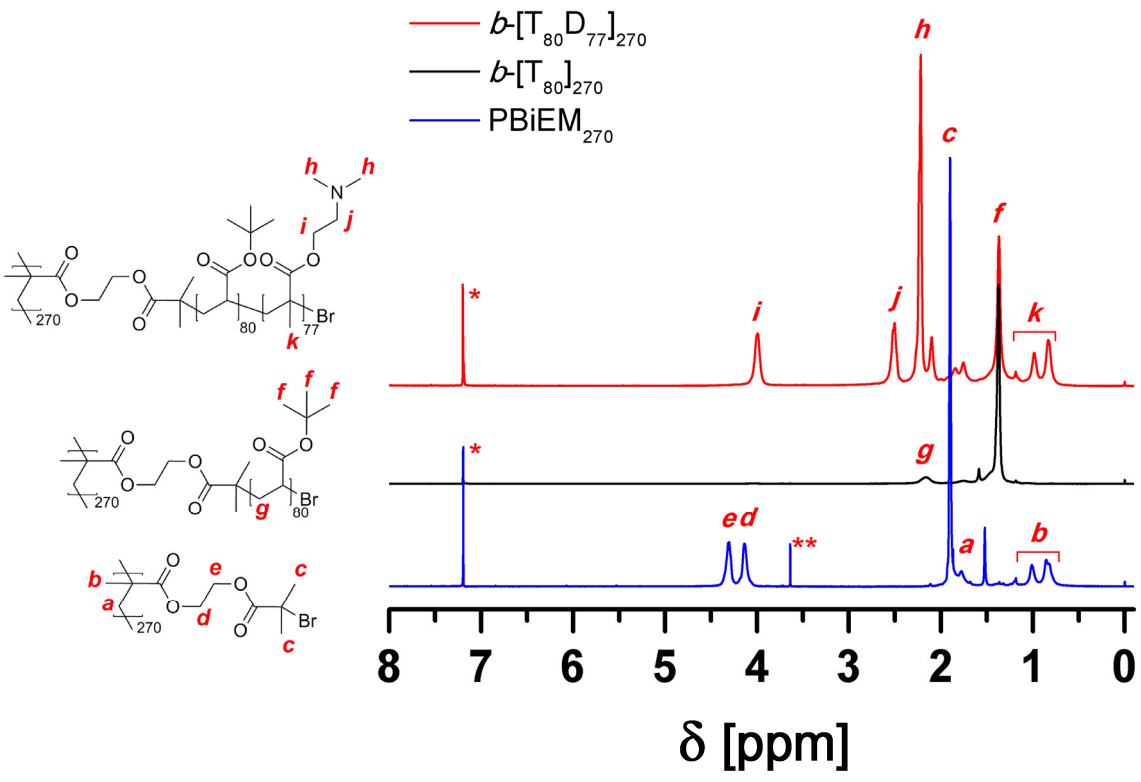

Figure 6-S1. ^{1}H NMR spectra of $PBIEM_{270}$ polyinitiator backbone (blue), CPBs *b*-$[T_{80}]_{270}$ (black) and *b*-$[T_{80}D_{77}]_{270}$ (red). All samples were measured in $CDCl_3$. *$CHCl_3$, **dioxane.

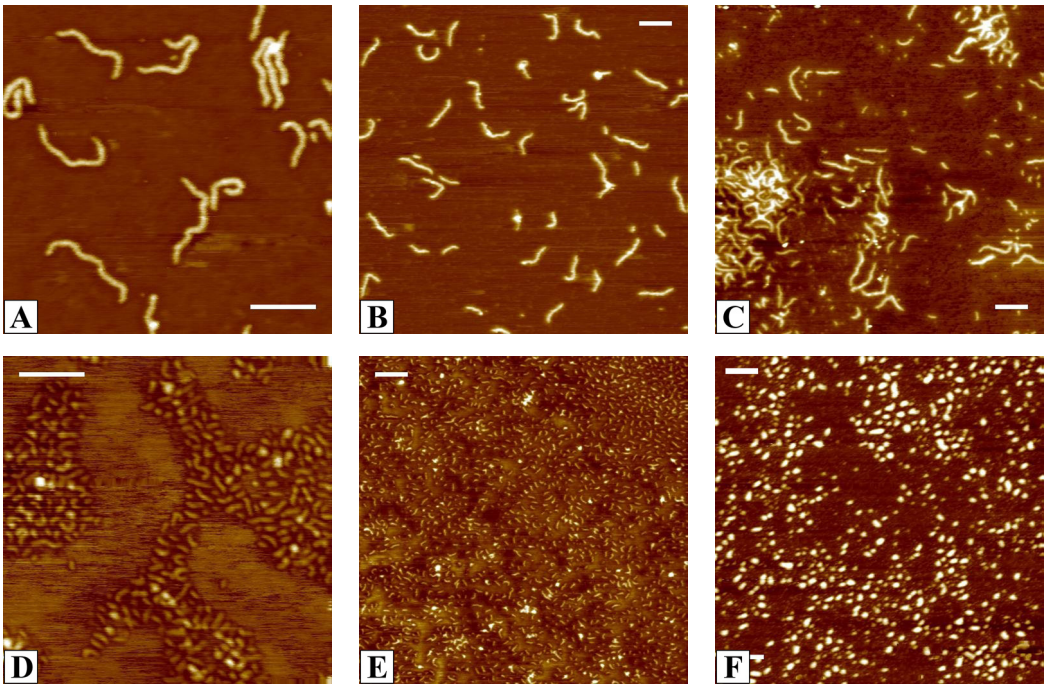

Figure 6-S2. Tapping-mode AFM height image of the CPB precursors *b*-$[T_{75}]_{3200}$ (A), *b*-$[T_{75}D_{75}]_{3200}$ (B), *b*-$[T_{80}]_{270}$ (D) *b*-$[T_{80}D_{77}]_{270}$ (E), and the CPB templates *b*-$[A_{75}D_{75}]_{3200}$ (C), *b*-$[A_{80}D_{77}]_{270}$ (F). Scale bars correspond to 200 nm for (A), (D) and 300 nm for (B), (C), (E), (F).

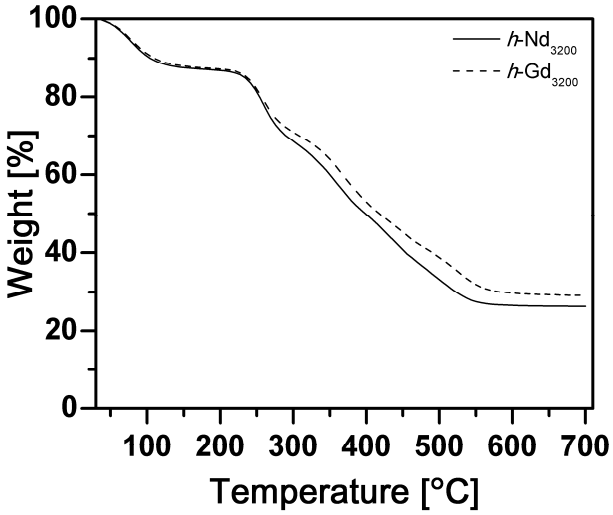

Figure 6-S3. TGA measurement of silica hybrid NPs *h*-Nd_{3200} and *h*-Gd_{3200}.

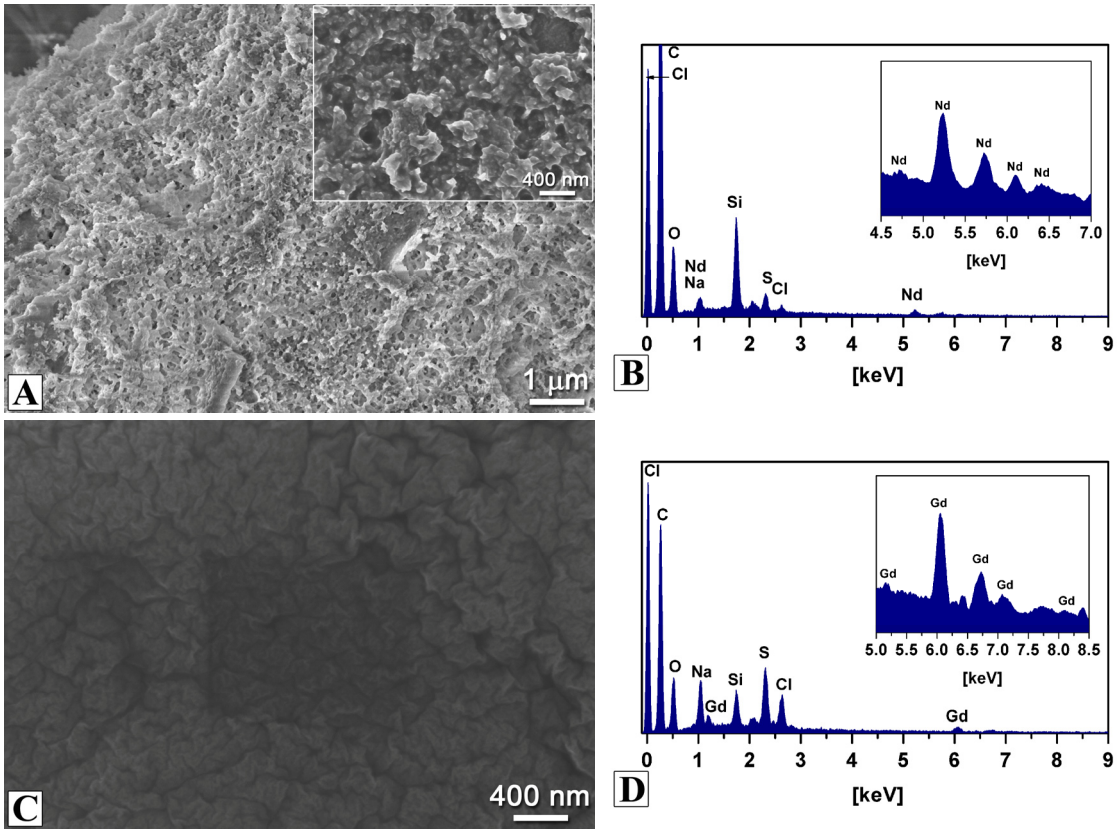

Figure 6-S4. SEM image and EDX analysis of silica hybrid NPs *h*-Nd_{3200} (A), (B) and *h*-Gd_{3200} (C), (D).

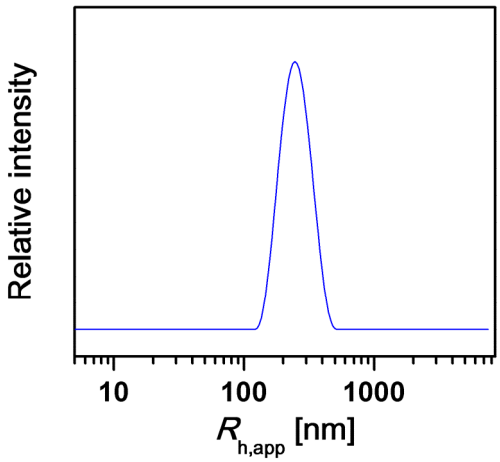

Figure 6-S5. Intensity-weighted DLS CONTIN plot for silica hybrid NP *h*-Tb_{3200} in aqueous solution. $\langle R_{h,app} \rangle_z$ = 247 nm, PDI = 1.18.

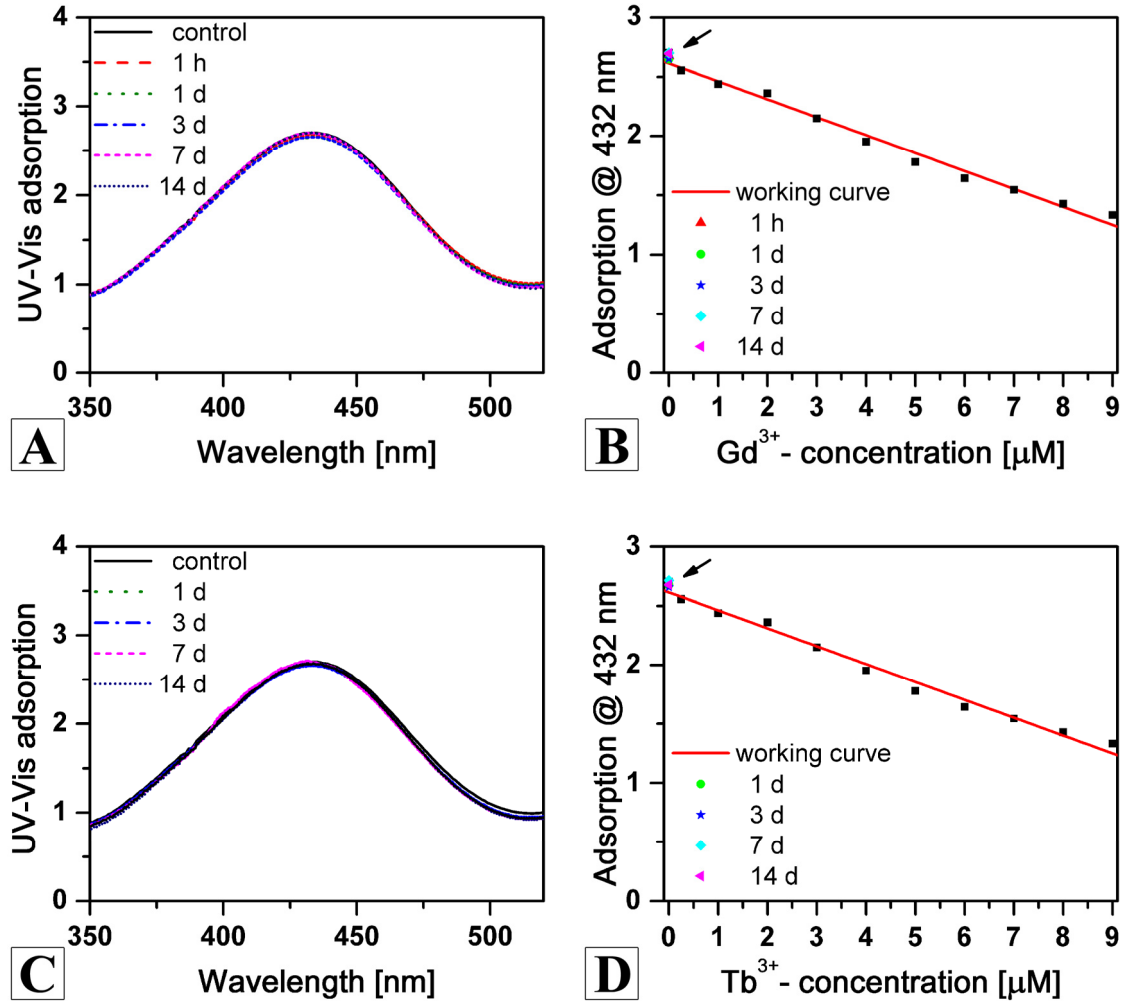

Figure 6-S6. Leaching study of Ln^{3+} from silica hybrid NPs. Time-dependent development of absorption spectrum of xylenol orange by Gd^{3+}-diffusion from *h*-Gd_{3200} (A) and by Tb^{3+}-diffusion from *h*-Tb_{3200} (C). A NP-free xylenol orange solution was measured as the control sample. Calibration curve for the complexometric titration of the concentration of free Gd^{3+}diffusing from *h*-Gd_{3200} (B) and Tb^{3+} diffusing from *h*-Tb_{3200} (D).

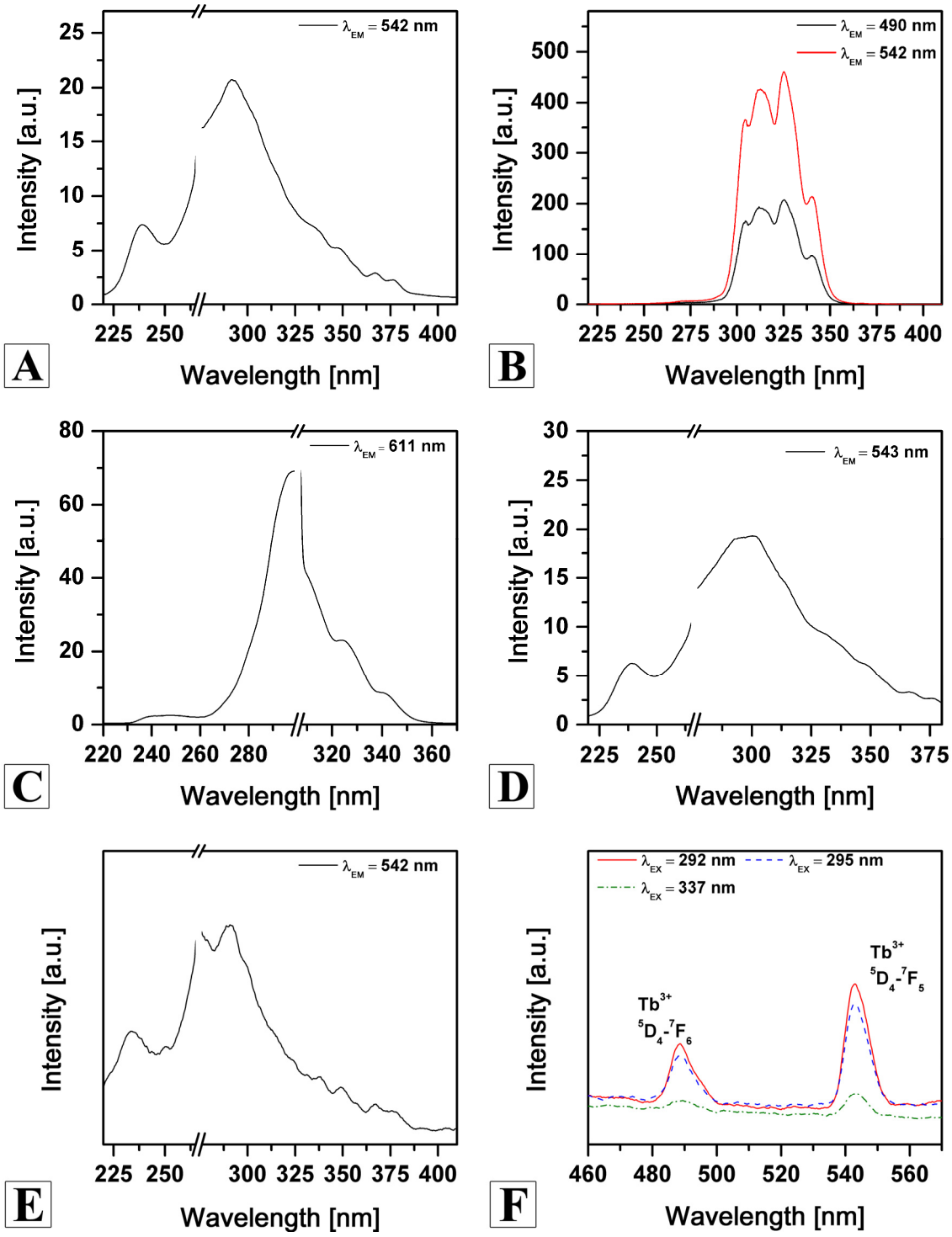

Figure 6-S7. Photoluminescence excitation spectrum of the silica hybrid NPs in ethanol solution: *h*-Tb_{3200} (A), *h*-Tb-L_{3200} (B), *h*-Eu-L_{3200} (C), the multicomponent hybrid NPs *h*-Tb/Gd_{3200} (D) and *h*-Tb_{270} (E). Photoluminescence emission spectrum of *h*-Tb_{270} in ethanol solution (F).

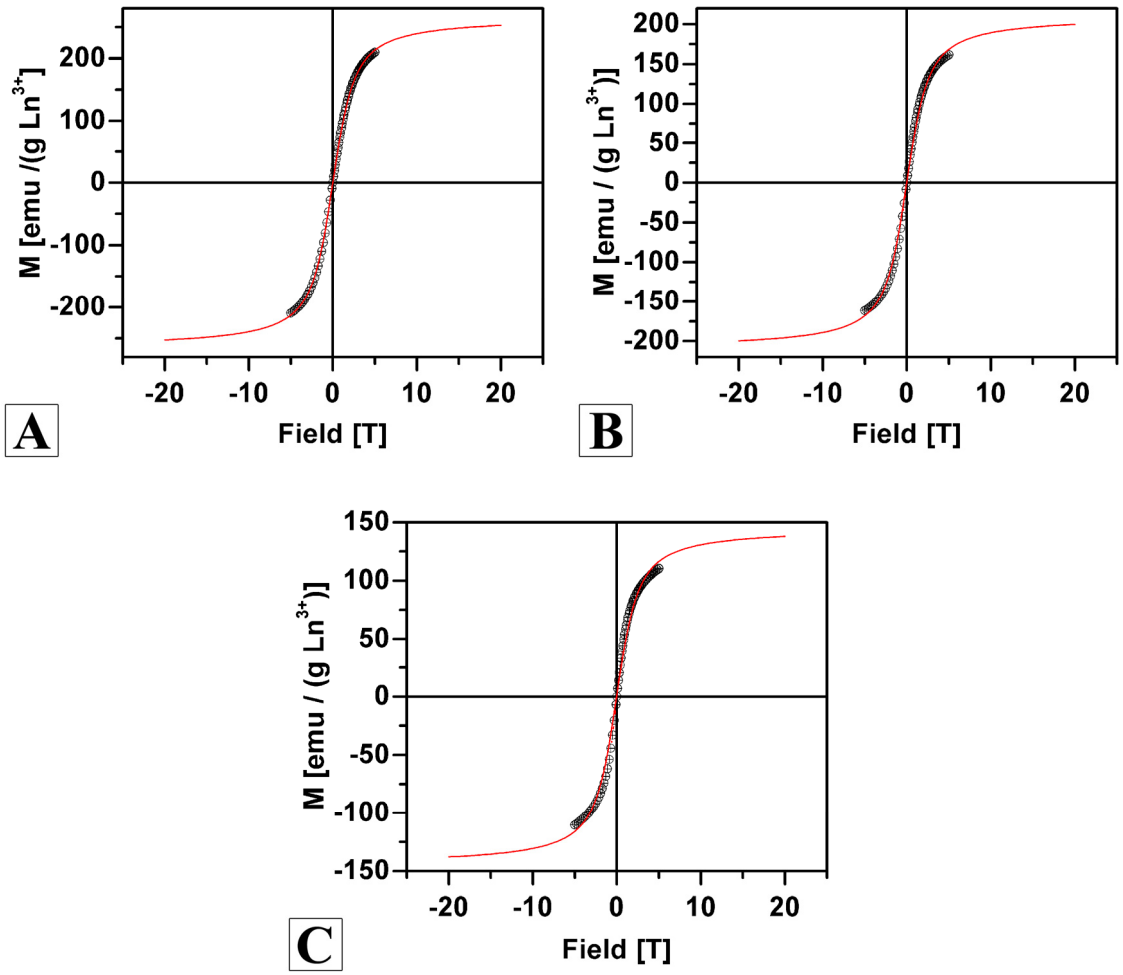

Figure 6-S8. Magnetization curves at 5 K for the silica hybrid NPs *h*-Gd_{3200} (A), the multicomponent hybrid NPs *h*-Tb/Gd_{3200} (B) and *h*-Tb/Nd_{3200} (C). Black cycles: experimental results; red lines: Langevin function fitting results.

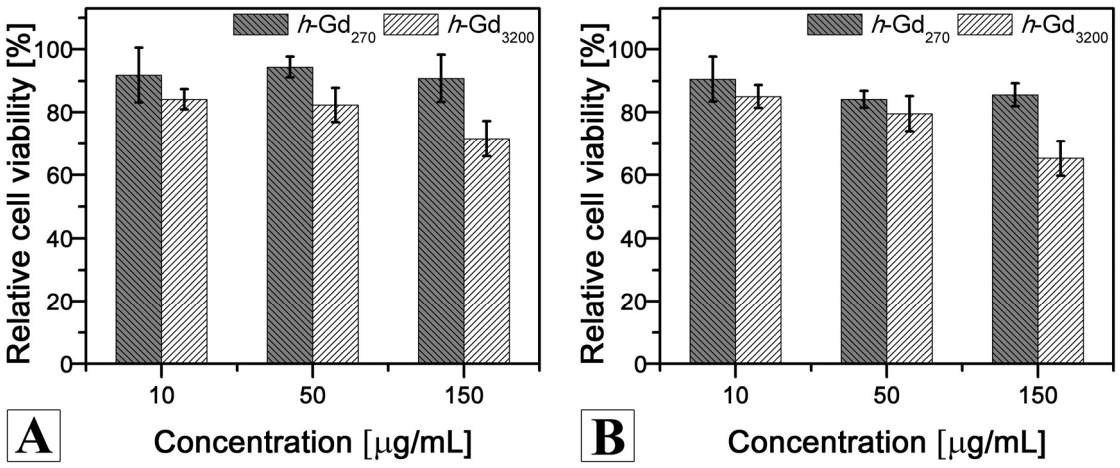

Figure 6-S9. Relative viability of human endothelial cells (CRL-1730) incubated with the silica hybrid NPs *h*-Gd_{3200} and *h*-Gd_{270} of varying NP concentration with an incubation period of 24 h (A) and 72 h (B). The results are expressed as a percentage of the control cell culture.

List of Publications

5. **Zheng, Z.**; Daniel, A.; Yu, W.; Weber, B.; Ling, J.; Müller, A. H. E.: Rare-Earth Metal Cations Incorporated Silica Hybrid Nanoparticles Templated by Cylindrical Polymer Brushes, *Chemistry of Materials*, **2013,** *25*, 4585–4594. DOI: 10.1021/cm402776d

4. Ling, J.; **Zheng, Z.**; Köhler, A.; Müller, A. H. E.: Rod-Like Nano-Light Harvester, *Macromol. Rapid Comm.*, in press, **2013**. DOI: 10.1002/marc.201300785

3. **Zheng, Z.**; Ling, J.; Müller, A. H. E.: Revival of the R-Group Approach: A "CTA-shuttled" Grafting from Approach for Well-defined Cylindrical Polymer Brushes via RAFT Polymerization, *Macromol. Rapid Comm.*, in press, **2013**. DOI: 10.1002/marc.201300578

2. **Zheng, Z.**; Müllner, M.; Ling, J.; Müller, A. H. E.: Surface Interactions Surpass Carbon-Carbon Bond: Understanding and Control of the Scission Behavior of Core-Shell Polymer Brushes on Surfaces, *ACS Nano*, **2013**, *7*, 2284–2291. DOI: 10.1021/nn3054347

1. Lin, Y.; **Zheng, Z.**; Hogen-Esch, T. E.; Ling, J.; Shen, Z.: Well-defined Novel Fluorene-containing Polymers: Synthesis, Fluorescent Properties, and Micellar Nanoparticles, *J. Colloid Interface Sci.*, **2013**, *390*, 105–113. DOI: 10.1016/j.jcis.2012.09.055

Conference Presentations

5. **Zheng, Z.**; Daniel, A.; Yu, W.; Ling, J.; Müller, A. H. E.: "Rare-Earth Metal Cations Incorporated Silica Hybrid Nanoparticles", poster presentation at *Bayreuth Polymer Symposium*, September 2013, Bayreuth, Germany

4. **Zheng, Z.**; Ling, J.; Müller, A. H. E.: "C-C Bond Scission of Cylindrical Polymer Brushes on Surfaces", poster presensation at *3rd International Symposium Frontiers in Polymer Science*, May 2013, Sitges, Spain

3. **Zheng, Z.**; Ling, J.; Müller, A. H. E.: "Novel Light-harvesting and Energy Transfer Molecular Architectures", oral presentation at *245th ACS National Meeting*, April 2013, New Orleans, Louisiana, USA

2. **Zheng, Z.**; Ling, J.; Müller, A. H. E.: "Syntheses and Surface Interactions of Well-Defined Cylindrical Polymer Brushes", poster presentation at *Belgian-German (Macro)Molecular Meeting*, December 2012, Houffalize, Belgium

1. **Zheng, Z.**; Ling, J.; Müller, A. H. E.: "Synthesis of Well-defined Complex Polymer Architectures via CTA-shuttled "Grafting from" RAFT Approach", oral presentation at *10th International Congress of Young Chemists*, October 2012, Gdansk, Poland

Acknowledgements

I would like to take this occasion to thank all the people who have helped and supported me during my thesis time in Bayreuth.

First and foremost, I would like to thank my supervisor and "Doktorvater" Prof. Axel Müller for giving me the opportunity to finish my PhD work in the group MCII. His kindness, patience and inspiring attitude encouraged me to overcome the scientific challenges and my personal weakness. I am very thankful for his numerous useful tips and helpful discussions throughout my thesis, contributing to the success of my research efforts. I am sincerely grateful for the multiple opportunities to present our research at national and international conferences. I also sincerely appreciate all the things that I have learnt from him during my master study and my PhD work in Bayreuth. Herzlichen Dank!

Special thanks also go to Prof. Jun Ling for his diverse cooperation and strong contribution to the success of my research. He has invested a lot of time for discussions and reviewing the manuscripts and presentations. I want to thank Jun for guiding me in the field of rare-earth metals and energy transfer architectures. Furthermore, I want to thank him for his patience and the nice working atmosphere. He is always smiling in the lab, in discussions, in conferences ;-)

I would also like to especially thank Prof. Georg Papastavrou, who was my other mentor within the graduate school. I thank him for all the time he spent in discussions and helping me conduct my research.

I want to thank Prof. Birgit Weber and Prof. Anna Köhler, who have been involved in joint projects and have helped me characterize and evaluate my research results as well as correct my manuscripts.

Most of all, I would like to thank the entire MCII group for the wonderful working atmosphere and supports from various aspects. Without them I could not reach my success. Therefore, I sincerely thank our helpful technical assistants who have helped me

with all kinds of analytical issues. They are Melanie Förtsch, Marietta Böhm, Annika Pfaffenberger, Annette Krökel, Dane Blasser and Susanne Edinger. In addition, I thank Gaby Oliver very much for all her patience and her help with all bureaucratic matters.

Many thanks also go to the present and former members and guests of the MCII team, who have given me an incredible and memorable time in Bayreuth. So in, no particular order, thank you Alexander Majweski, Alexander Schmalz, André Gröschel, André Pfaff, Andrea Wolf, Andreas Hanisch, Andreas Walther, Anja Goldmann, Annika Eckardt, Christopher Synatschke, Daniela Pirner, Eva Betthausen, Francesca Bennet, Holger Schmalz, Jiayin Yuan, Jie Kong, Joachim Schmelz, Kerstin Küspert, Lourdes Pastor-Pérez, Marina Krekhova, Markus Drechsler, Markus Müllner, Michael Witt, Oleg Borisov, Ramón Novoa-Carballal, Sandrine Tea, Stefan Döhler, Stefan Reinicke, Stephan Weiß, Thomas Ruhland, Tina Löbling, Tomohiro Hirano, Weian Zhang, Youyong Xu, and many more ...

I would also like to thank my students – Alexander Daniel, Hubertus Burchhardt and Tobias Honold – who have worked on several projects with me. Especially, I want to thank Alexander Daniel for his helping hands and strong contribution during his multiple lab courses and his master thesis.

I thank the Bayreuth graduate school of Mathematical and Natural Sciences (BayNAT) for a membership within the PhD program “Polymer Science”. For financial support, I am also thankful to the Bavarian State for having provided me a scholarship through the BayEFG.

Last but not least, I owe thousands of thanks to my family, my parents, and my fiancée Zhuying for their love and their overwhelming support throughout my whole study over the years. I deeply thank you for everything you gave me and did for me. I especially thank you Zhuying for all your love and patience. Your great confidence in me encouraged me to face tough times and keep going. Thank you so much, my darling!

Erklärung

Die vorliegende Arbeit wurde von mir selbstständig verfasst und ich habe dabei keine anderen als die angegebenen Hilfsmittel und Quellen benutzt.

Ferner habe ich nicht versucht, anderweitig mit oder ohne Erfolg eine Dissertation einzureichen oder mich der Doktorprüfung zu unterziehen.

Bayreuth, den 18.09.2013

Zhicheng Zheng